High Performance n-Type Polymer Semiconductors

for Printed Logic Circuits

by

Bin Sun

A thesis
presented at University of Waterloo
in fulfillment of the
thesis requirement for the degree of
Doctoral of Philosophy
in
Chemical Engineering

Waterloo, Ontario, Canada, 2016
© Bin Sun 2016

Author's Declaration

I hereby declare that this thesis consists of materials all of which I authored or co-authored: see Statement of Contributions included in the thesis. This is a true copy of the thesis, including any required final revisions, as accepted by my examiners.

I understand that my thesis may be made electronically available to the public.

Statement of Contribution

This thesis contains materials from several published or submitted papers, some of which resulted from collaboration with my colleagues in the group.

The content in Chapter 2 has been partially published in *Adv. Mater.* **2014**, *26*, 2636. B. Sun, W. Hong, Z. Yan, H. Aziz, Y. Li

The content in Chapter 3 has been partially published in *Polym. Chem.* **2015**, *6*, 938. B. Sun, W. Hong, H. Aziz, Y. Li

The content in Chapter 4 has been partially published in *Org. Electron.* **2014**, *15*, 3787. B. Sun, W. Hong, E. Thibau, H. Aziz, Z. Lu, Y. Li

The content in Chapter 5 has been partially published in *ACS Appl Mater Interfaces* **2015**, *7*, 18662. B. Sun, W. Hong, E. Thibau, H. Aziz, Z. Lu, Y. Li,

Abstract

Solution processable polymer semiconductors open up potential applications for radio-frequency identification (RFID) tags, flexible displays, electronic paper and organic memory due to their low cost, large area processability, flexibility and good mechanical properties. An inverter, providing the 'NOT' logic function, is a fundamental unit in these applications. A complementary inverter, which consists of both p-type and n-type transistors, offers low power consumption, higher voltage gain, and stronger immunity against noise, and thus is most widely studied and used for integrated circuits. A high-performance complementary logic circuit requires p-type and n-type transistors with high and balanced hole and electron mobilities. However, stable n-type polymer semiconductors are rare and the current level of electron mobility of n-type polymers remains much lower than that of p-type polymers.

In this work, a number of high-performance n-type polymer semiconductors were successfully developed using several approaches. In Chapter 2, a new polymer semiconductor with a record high electron mobility value of 6.30 $cm^2V^{-1}s^{-1}$ in OTFT devices was developed. This polymer contains a key new electron-accepting building block, **DBPy**, which consists of a DPP core flanked with two 2-pyridinyl substituents. The 2-pyridinyl substituents can effectively alleviate its steric interaction with the DPP core, resulting in a highly coplanar structure; meanwhile, the relatively electron deficient characteristic of pyridine helped to reduce the LUMO energy level. Our results demonstrate that **DBPy** is a highly promising new building block for polymer semiconductors for ambipolar complementary logic.

In Chapter 3, a **DBPy**-thieno[3,2-*b*]thiophene copolymer with a high ambipolar performance was synthesized. The source and drain electrodes of the OTFT devices were modified with a thin layer of polyethyleneimine (PEI) to convert the polymer into a unipolar n-type semiconductor,

achieving an electron mobility as high as 2.38 $cm^2V^{-1}s^{-1}$. This opens a door to ambipolar polymers to be used as n-type polymers for complementary circuits.

In Chapter 4, the surface modification of source and drain electrodes by an ultrathin layer (~ 2-5 nm) of polyethyleneimine (PEI) on source and drain electrodes utilized in Chapter 3, is further demonstrated to be an effective and universal way to convert other ambipolar polymers and even a p-type semiconductor into unipolar n-type semiconductors in OTFTs.

In Chapter 5, another general approach to converting ambipolar and even p-type polymer semiconductors into unipolar n-type semiconductor materials for high performance OTFTs was discovered by doping these polymers with a small amount of PEI. The PEI dopant was uniformly distributed throughout polymer semiconductors even when the blend films were annealed at high temperatures up to 200ºC. This general doping method is a significant step forward for making complementary circuits using ambipolar and even p-type polymer semiconductors in n-channel OTFTs.

In the Conclusion and Outlook, the fabrication of complementary inverters based on both p-type and n-type OTFTs using the general approach developed in Chapter 5 is discussed. The inverters demonstrate low power consumption, high voltage gain and strong robustness to noise.

Acknowledgements

I would like to express my sincerest appreciation to my supervisors, Prof. Yuning Li and Prof. Hany Aziz, for their helpful and invaluable mentorship, assistance, support and guidance. I also would like to thank all my committee members, Prof. Jun Yang, Prof. Bo Cui, Prof. Ali Elkamel, and Prof. Mark Pritzker for their suggestions and guidance on this work.

I also thank all my lab mates: Dr. Wei Hong, Dr. Jonathan Yuen, Dr. Chang Guo, Zhuangqing Yan, Dr. Yunfeng Deng, Yinghui He, Leanne Murphy, Jesse Quinn, Dr. Graeme Williams, Dr. Qi Wang, Baoling Tian, Yingjie Zhang, Dr. Yoshitaka Kajiyama, Sibi Sutty, Dr. Uyxing Vongsaysy, Tyler Davidson-Hall, Zhiyong Xiao, and Hossein Zamani for their great assistance and friendship. I send special gratitude to Dr. Joseph P. Thomas, Dr. Feng Chen, and Dr. Jian Zhang, and Melissa Chow, who helped me tremendously with my experiments.

Finally, I express my deepest gratitude to my family, who have been constantly providing support and help. Special thanks go to my wife for always being there for me.

Contents

Author's Declaration ii

Statement of Contribution iii

Abstract iv

Acknowledgements vi

Contents vii

List of Figures ix

List of Schemes xvi

List of Tables xvii

List of Abbreviations xviii

Chapter 1. Introduction 1

1.1 Overview 1

1.2 Organic Thin-film Transistors (OTFTs) 1

1.3 Integrated Circuits Based on Semiconducting Polymers 4

1.4 Organic Semiconductors 11

1.5 Polymer Semiconductors for OTFTs 15

1.5.1 p-Type Polymer Semiconductors 15

1.5.2 n-Type Polymer Semiconductors 18

1.6 Objective of This Work 24

Chapter 2. High Electron Mobility Polymer Semiconductors Based on DBPy 27

2.1 Introduction 27

2.2 Results and Discussion 28

2.3 Conclusion 42

2.4 Experimental 43

2.4.1 Materials and Instrumentation 43

2.4.2 Synthesis 44

2.4.3 Fabrication and Characterization of OTFT Devices 47

Chapter 3. Conversion of PDBPyTT Ambipolar Polymer into Unipolar n-Type and p-type Semiconductors in Organic Thin Film Transistors 50

3.1 Introduction 50

3.2 Results and Discussion 51

3.3 Conclusion 62

3.4 Experimental Section 62

3.4.1 Materials and Instrumentation 62
3.4.2 Synthesis 63
3.4.3 Device Fabrication 66

Chapter 4. n-Type Unipolar Conversion from Ambipolar and p-Type Polymer Semiconductors by PEI-modification of Au Electrodes 68

4.1 Introduction 68

4.2 Results and Discussion 68

4.3 Conclusion 82

4.4 Experimental 83

4.4.1 Materials and Methods. 83
4.4.2 Work Function Measurement. 84
4.4.3 OTFT Device Fabrication. 86

Chapter 5. Polyethylenimine (PEI) as an Effective Dopant for n-Type Unipolarization from Ambipolar and p-type Polymer Semiconductors 87

5.1 Introduction 87

5.2 Results and discussion 89

5.3 Conclusion 105

5.4 Experimental Section 105

5.4.1 Materials and Methods 105
5.4.2 Time-of-flight Secondary Ion Mass Spectrometry 108
5.4.3 OTFT Device Fabrication 109

Chapter 6. Chapter 6. Conclusion and Outlook 112

References 121

Appendix: 127

Part 1. Output and transfer characteristics of OTFT devices in Chapter 3 127

Part 2. Output and transfer characteristics of OTFT devices in Chapter 4 138

Part 3. Output and transfer characteristics of OTFT devices in Chapter 5 152

Part 4. Fabrication of Complementary Inverters in Chapter 6 155

List of Figures

Figure 1.1 A field effect transistor with a structure of bottom gate/ bottom contact (left), whose operation is analogous to the control of water flow by a tap (right). 2

Figure 1.2 OTFT device designs: a) bottom gate/top contact (BGTC); b) bottom gate/bottom contact (BGBC); c) top gate/top contact (TGTC); d) top gate/bottom contact/ (TGBC). 2

Figure 1.3. (a) The 3-D structure of a BGBC OTFT using PDQT-26. Typical output (b) and transfer (c) characteristics of hole accumulation regimes. OTFT was fabricated by employing BGBC (Au electrode) configuration on heavily doped n^{++}-silicon wafers with a 300 nm SiO_2 layer (capacitance 11 nF cm^{-2}) as the gate dielectric layer. The polymer film with a thickness of 40 nm was obtained by spin-coating a polymer solution on the substrate. Channel length L = 30 μm and channel width W = 1 mm. The saturation field effect mobility is 6.9 $cm^2V^{-1}s^{-1}$ at V_{DS} = -100 V.[5]................................ 3

Figure 1.4 Architecture of the five different inverter types: a) resistive load inverter, b) diode type, c) V_{GS}0 type, complementary type d) based on two unipolar semiconductors and e) based on ambipolar semiconductor.[11] 5

Figure 1.5. Voltage transfer characteristic (VTC) of an inverter. 7

Figure 1.6 (a) Schematic representation of a three-stage ring oscillator consisting of complementary inverters based on ambipolar PSeDPPBT. (b) Input-output characteristics, worst-case noise margin extraction and gain of constituent inverters at positive drive voltages of 10 V and 20 V.[18] Copyright 2012, John Wiley & Sons, Inc. 9

Figure 1.7. Optical image of inkjet-printed (a) P2100 and (b) N2200 TFTs and droplets (insets). Static inverter characteristics; (c) voltage transfer characteristics, (d) voltage gains, (e) corresponding power dissipation, and (f) noise margins of a complementary inverter at various V_{DD} [P2100:N2200, PMMA gate dielectric thickness 400 nm (2E solvent)].[19] Copyright 2011, John Wiley & Sons, Inc. 10

Figure 1.8. (a): atomic orbitals (left), formation of boding and antibonding (middle), energy level splitting (right); (b): energy bands in solid. 12

Figure 1.9. a) and b) are the geometry of the sp^3 and sp^2 orbital structures; c) shows the HOMO (highest occupied molecular orbital) and the LUMO (lowest occupied molecular orbital) with ethylene as the example. 13

Figure 1.10 A schematic diagram showing the band splitting of benzene. 14

Figure 1.11 Carbon p_z atomic orbitals (left), formation of π-boding and π*-antibonding (middle), energy level splitting (right). 15

Figure 1.12 Representative p-type polymer semiconductors.[39, 45-52] 16

Figure 1.13 Representative DPP-based polymer semiconductors for OTFTs with high hole mobility.[27, 29-31, 33, 37, 53-56] 17

Figure 1.14 Representative n-type polymer semiconductors for OTFTs with high electron mobility.[59-63] 20

Figure 1.15. Alternating donor–acceptor units lower the effective band gap by orbital overlap.[64] 21

Figure 1.16 Representative ambipolar polymer semiconductors for OTFTs with high electron mobility (μ_e is electron mobility; μ_h is hole mobility).[40, 78-80] 22

Figure 2.1. The optimized HUMO/LUMO electron distribution diagrams and geometry of 2,5-dimethyl-3,6-di(thiophen-2-yl)pyrrolo[3,4-*c*]pyrrole-1,4(2*H*,5*H*)-dione (DBT-Me), 2,5-dimethyl-3,6-diphenylpyrrolo[3,4-c]pyrrole-1,4(2*H*,5*H*)-dione (DBP-Me), and 2,5-dimethyl-3,6-di(pyridin-2-yl)pyrrolo[3,4-*c*]pyrrole-1,4(2*H*,5*H*)-dione (DBPy-Me) obtained by computer simulation with density functional theory (DFT) calculations. . 28

Figure 2.2. UV-vis absorption spectra of PDBPyBT solution (chloroform) and as-cast thin film on quartz. 32

Figure 2.3 Cyclic voltammetry diagrams of **PDBPyBT** and the reference ferrocene (Fc) in acetonitrile at a sweep rate of 50 mV s^{-1}. The HOMO and LUMO energy levels of **PDBPyBT** were determined from the oxidative and reductive onset potentials to be -5.69 eV and -4.33 eV, respectively. 33

Figure 2.4. (a) XRD patterns of spin-coated PDBPyBT thin films on bare SiO_2/Si substrates annealed at different annealing temperatures measured in a reflection mode using Cu Kα1 radiation. (b) XRD pattern of a stack of non-annealed PDBPyBT thin films in a transmission mode using Mo Kα radiation. (c) AFM images (2 μm × 2 μm each) of PDBPyBT thin films on bare SiO_2/Si substrates annealed at different temperatures: the root-mean square (RMS) roughness is 8.2 nm, 8.3 nm, and 11.7 nm for the as-spun (r.t.), 150 °C-annealed, and 200 °C-annealed thin films, respectively. Annealing of the thin film samples for both XRD and AFM was conducted on a hot plate for 10 min in nitrogen. 34

Figure 2.5 Photographs of water droplets on the surfaces of a bare SiO_2/Si substrate (a), DDTS-modified SiO_2/Si substrate, and gold film (c) by axisymmetric droplet shape analysis at 20 °C. The contact angles are (a) 28°, (b) 104°, and (c) 76°, indicating the wettability order of (a) > (c) > (b). 36

Figure 2.6. AFM images (2 μm × 2 μm each) of PDBPyBT thin films between gold source/drain contacts on (a) DDTS-modified bare SiO_2/Si substrates annealed at different temperatures: the root-mean square (RMS) roughness is 4.2 nm, 6.7 nm, and 6.7 nm for the as-spun (r.t.), 150 °C-annealed, and 200 °C-annealed thin films, respectively; (b) bare SiO_2/Si substrates annealed at different temperatures: the root-

mean square (RMS) roughness is 5.0 nm, 6.2 nm, and 8.2 nm for the as-spun (r.t.), 150 °C-annealed, and 200 °C-annealed thin films, respectively. 36

Figure 2.7. (a) Output, (b) leakage current through gate, and (c) transfer curves of a BGBC OTFT device using a PDBPyBT thin film annealed at 200 °C. Hole mobility: 0.46 $cm^2V^{-1}s^{-1}$. 37

Figure 2.8. Output (top) and transfer (bottom) curves of a typical top-gate, bottom-contact (TGBC) OTFT device with a PDBPyBT thin film annealed at 100 °C. Device dimensions: channel length $L = 30\ \mu m$; channel width $W = 1$ mm. 38

Figure 2.9. The chemical structure of Cytop. 41

Figure 2.10. Output (left) and transfer (right) curves of a top-gate, bottom-contact (TGBC) OTFT device using a PDQT (structure shown in Scheme 2.1 in the main text) thin film annealed at 100 °C. Hole mobility: 1.01 $cm^2V^{-1}s^{-1}$. 41

Figure 2.11. The 300 MHz ^1H NMR spectra of DBPyBr-20. 45

Figure 2.12. The 75 MHz ^{13}C NMR spectrum of DBPyBr-20. 46

Figure 2.13. The 300 MHz ^1H NMR spectrum of PDBPyBT. 47

Figure 3.1. Energy diagrams of PDBPyTT, Au, PEI-modified Au, and MoO_3-modified Au, where WF and E_F are work function and Fermi energy level, respectively. WF values of Au, PEI/Au (PEI modified Au), and MoO_3 are taken from the literature. 53

Figure 3.2. a) Output (top) and transfer (middle) curves of a typical ambipolar OTFT device (bottom) under hole and electron enhancement modes; b) Output (top, left) and transfer (top, right) curves of a typical OTFT device (bottom) with a PEI interlayer between the Au contacts and the PDBPyTT layer; c) Output (top, left) and transfer (top, right) curves of a typical OTFT device with a MoO_3 interlayer between the Au contacts and the PDBPyTT layer. The PDBPyTT thin films (~50 nm) in these devices were annealed at 150 °C for 15 min in nitrogen. 57

Figure 3.3. The dependences of electron and hole mobilities on the thickness of the PEI layer (top) and the MoO_3 layer (bottom). Mobility values were obtained from at least 5 OTFT devices for each data point. 58

Figure 3.4. Left: The reflection XRD diagrams of PDBPyTT thin films (~50 nm thick) spin-coated on SiO_2/Si substrates and annealed at difference temperatures. Right: The transmission XRD diagram of a stack of PDBPyTT thin films sandwiched between two Mylar substrates. The inserted graph in the middle represents the lamellar crystal structure with edge-on chain orientation in the polymer films. 60

Figure 3.5. AFM images (2 μm × 2 μm each) of PDBPyTT thin films (~50 nm) on SiO_2/Si substrates annealed at different temperatures. Root-mean-square (RMS) roughness: 11.8 nm (100 °C), 14.3 nm (150 °C), and 19.1 nm (200 °C). 61

Figure 3.6. UV-vis absorption spectra of PDBPyTT solution (chloroform) and as-cast thin film on quartz. 64

Figure 3.7. Cyclic voltammetry (CV) curves of PDBPyTT and ferrocene (Fc) (as a reference) in 0.1 M tetrabutylammonium hexafluorophosphate in anhydrous acetonitrile at a scan rate of 50 mVs^{-1}. 65

Figure 3.8 The 300 MHz ^{1}H NMR spectrum of PDBPyTT. 65

Figure 4.1. Effect of PEI thickness on the work function of gold (Au) modified by a layer of PEI. 69

Figure 4.2. Structures of polymer semiconductors studied in this work. 70

Figure 4.3. The top gate, bottom contact (TGBC) OTFT device configuration and the HOMO and LUMO energy levels of ambipolar semiconductors and the Fermi levels of pure Au and PEI-modified Au. 72

Figure 4.4 Mobility changes of **P4-1** with increasing PEI layer thickness on the surface of Au source and drain electrodes in OTFT devices. 74

Figure 4.5 Output (left) and transfer (right) curves of representative unipolar n-channel OTFT devices of P4-1 with PEI (3.9nm; μ_e = 1.03 $cm^2V^{-1}s^{-1}$) modified source and drain electrodes. 74

Figure 4.6 Mobility changes of P4-2 with increasing PEI layer thickness on the surface of Au source and drain electrodes in OTFT devices. 75

Figure 4.7 Output (left) and transfer (right) curves of representative unipolar n-channel OTFT devices of P4-2 with PEI (2.9nm; μ_e = 0.18 $cm^2V^{-1}s^{-1}$) modified source and drain electrodes. 76

Figure 4.8 Mobility changes of P4-3 with increasing PEI layer thickness on the surface of Au source and drain electrodes in OTFT devices. 77

Figure 4.9 Output (left) and transfer (right) curves of representative unipolar n-channel OTFT devices of P4-3 with PEI (2.2nm; μ_e = 0.091 $cm^2V^{-1}s^{-1}$) modified source and drain electrodes. 77

Figure 4.10 Mobility changes of P4-4 with increasing PEI layer thickness on the surface of Au source and drain electrodes in OTFT devices. 78

Figure 4.11 Output (left) and transfer (right) curves of representative unipolar n-channel OTFT devices of P4-4 with PEI (3.9nm; μ_e = 0.41 $cm^2V^{-1}s^{-1}$) modified source and drain electrodes. 78

Figure 4.12 Mobility changes of P4-5 with increasing PEI layer thickness on the surface of Au source and drain electrodes in OTFT devices. 79

Figure 4.13 Output (left) and transfer (right) curves of representative unipolar n-channel OTFT devices of P4-5 with PEI (4.7nm; μ_e = 0.0018 $cm^2V^{-1}s^{-1}$) modified source and drain electrodes. 80

Figure 4.14 Mobility changes of P4-6 with increasing PEI layer thickness on the surface of Au source and drain electrodes in OTFT devices. 81

Figure 4.15 Output (left) and transfer (right) curves of representative unipolar n-channel OTFT devices of P4-6 with PEI (4.7nm; μ_e = 0.036 $cm^2V^{-1}s^{-1}$) modified source and drain electrodes. 81

Figure 4.16. The AFM height images (2 μm × 2 μm each) of P4-1 thin films (~50 nm) on pure Au electrode (a) and modified Au electrodes (b-d) with different PEI thicknesses. 84

Figure 4.17. The PEI thicknesses at different PEI concentrations in isopropanol (IPA). The PEI thin films were spin coated on SiO_2/Si wafer substrates at 5000 rpm. Each data point was obtained from at least 3 samples. 85

Figure 4.18. UPS spectra of pure Au film and PEI-modified Au films with various PEI thicknesses. Work function (WF) values obtained from the UPS spectra were used to make the graph in Figure 4.1. 85

Figure 4.19 The AFM height image of the 40 nm-thick Au electrode film (3 nm of Cr as adhesion layer, thermally deposited at 0.01 nm s^{-1}) thermally evaporated on the SiO_2/Si wafer substrate with a deposition rate of 0.03 nm s^{-1} at a pressure of 5 × 10^{-6} bar using Intel Vac thermal deposition instrument. 85

Figure 5.1. Chemical structures of PEI (branched polyethylenimine) and polymer semiconductors PDBTAZ (P5-1)[119] (E_{HOMO}/E_{LUMO} = -5.67 eV/-4.24 eV), PPzDPDP-BT (P5-2)[134] (E_{HOMO}/E_{LUMO} = -5.59 eV/-4.17 eV), PDBPyBT (P5-3)[66] (E_{HOMO}/E_{LUMO} = -5.69 eV/-4.33 eV), and PDQT (P5-4)[31, 37] (E_{HOMO}/E_{LUMO} = -5.24 eV/-4.04 eV) used in this study. P5-1, P5-2, and P5-3 were previously reported to show typical ambipolar (ambi) charge transport performance, while P5-4 showed typical p-type hole-only transport performance when gold was used as source/drain contacts in an OTFT device. 88

Figure 5.2. (a) Top-gate bottom-contact (TGBC) OTFT device structure with a pristine polymer semiconductor (PSC) as the channel, Cytop as the gate dielectric, Al as the gate electrode and Au as the source and drain contacts; the output (upper) and transfer

(lower) curves were obtained when a ~40-50 nm thick pristine P5-1 film (annealed at 150 °C) was used as the channel, which shows typical ambipolar charge transport performance. (b) TGBC OTFT device structure similar to that in (a) except that the channel is a PSC:PEI blend film; the output (upper) and transfer (lower) curves were obtained when a ~40 nm thick P5-1:PEI (2% PEI) blend film (annealed at 150 °C) was used as the channel, which shows typical n-channel electron-only transport performance. Dimensions of all devices: channel length L = 30 μm; channel width W = 1 mm. 89

Figure 5.3. Dependence of hole and electron mobilities of P5-1~P5-4 in OTFT devices on PEI content in the PSC:PEI blends. The PSC or PSC:PEI blend films were annealed at 100, 150 or 200 °C. 93

Figure 5.4. XRD patterns of spin-coated thin films of P5-1 with different PEI contents (wt. % over P5-1) on bare SiO_2/Si substrates annealed at different temperatures measured in a reflection mode using Cu Kα1 radiation. 94

Figure 5.5. (a) Schematic of the TOF-SIMS measurement by sputtering a thin film of P5-1, PEI or P5-1:PEI (2% PEI) spin-coated on an Au (~20 nm)/n^{++}-Si substrate using argon cluster ions, Ar_{1000}^+, with ion beam energy of 5 keV and ion current of 1.8 nA. Positions on, above, and below the Au film's top surface are arbitrarily described be to 0 (horizontal dashed line), positive values, and negative values in units of nm, respectively. The secondary ion species, $C_2H_2N^-$, C^-, and Au^- were detected and analyzed. (b) TOF-SIMS depth profiles of the $C_2H_2N^-/C^-$ ratios of P5-1, PEI and P5-1:PEI (2% PEI) blend films spin-coated on Au/n^+-Si substrates as shown in (a). The polymer thin films were annealed at 150 °C for 15 min in nitrogen in a glove box prior to the measurement. Normalized Au^- signals (on the right Y axis) are also shown as depth references and were used to determine the positon of polymer/Au interface (the vertical dashed line at 0 nm). 95

Figure 5.6. AFM height images of P5-1:PEI blend films with different PEI contents annealed at various temperatures. The films were spin-coated on SiO_2/Si substrates. 97

Figure 5.7. UPS spectra of 150 °C-annealed pristine and 2% PEI doped P5-1, P5-2, P5-3, and P5-4 films deposited on Au (30 nm)/n^+-Si substrates: Left: the high energy region showing the Secondary Electron Cut-off (SEC); Right: the HMO region showing the difference between and the Fermi level (at 0 eV) and the HOMO level (curve onset), $\eta = E_F - E_{HOMO}$. After adding PEI, all polymers showed a shift in the Fermi level towards vacuum and an enlarged difference between the HOMO and Fermi level, indicating an n-doping effect of PEI on these polymers. 98

Figure 5.8. A dual-gate OTFT device containing a top-gate bottom-contact (TGBC) configuration and a BGBC configuration. TGBC configuration: (a) output and (b) transfer characteristics of hole enhancement mode; (c) output and (d) transfer characteristics of electron enhancement mode. BGBC configuration: (e) output and (f) transfer characteristics of hole enhancement mode; (g) output and (h) transfer

characteristics of electron enhancement mode. Inserted scheme shows the proposed hole trapping effect of the nitrogen atoms in PEI, which suppresses or eliminates hole transport observed in the TGBC configuration and other devices using the PSC:PEI blends in this study. The polymer semiconductor (PSC) is P5-1 (annealed at 150 °C) and the SiO_2 surface was modified with DDTS. 100

Figure 5.9. Output (top) and transfer (bottom) curves of a BGBC OTFT device with a pure P5-1 thin film annealed at 150 °C, which show a characteristic ambipolar charge transport performance. Device dimensions: channel length L = 30 μm; channel width W = 1 mm. The average electron/hole mobilities from 5 devices are 0.067/0.020 $cm^2V^{-1}s^{-1}$, respectively. 102

Figure 5.10. AFM height images (2 μm × 2 μm each) of thin films (~40-50 nm) of P5-3 blended with varied amounts of PEI (wt % over P5-3) spin-coated on bare SiO_2/Si substrates and annealed at 150 °C for 15 min. RMS: the root-mean square roughness. 104

Figure 5.11. UV-Vis-NIR absorption spectra of as-cast thin films of pure P5-1 and a P5-1:PEI (2% PEI) blend on quartz. 106

Figure 5.12. UV-Vis-NIR absorption spectra of as-cast thin films of pure P5-2 and a P5-2:PEI (2% PEI) blend on quartz. 107

Figure 5.13. UV-Vis-NIR absorption spectra of as cast thin films of pure P5-3 and a P5-3:PEI (2% PEI) blend on quartz. 107

Figure 5.14. UV-Vis-NIR absorption spectra of as-cast thin films of pure P5-4 and a P5-4:PEI (2% PEI) blend on quartz. 108

Figure 5.15. TOF-SIMS depth profiles of pristine P5-1 (black solid line), 2wt% PEI doped P5-1 (red dash line) and pure PEI (green dash dot line) on Au/Si substrate: a) $C_2H_2N^-$, mass-to-charge ratio (m/q) equal to 40, b) Au^-, m/q = 197, and c) C^-, m/q = 12......... 109

Figure 6.1. Architecture of complementary inverter (a) and ring oscillator built of three complementary inverters (b). 114

Figure 6.2. Chemical Structure of PDQT-24[160] and PIBDFTT.[161] 115

Figure 6.3. Voltage transfer characteristic (VTC) of the complementary inverter teste in air. 116

Figure 6.4. Voltage transfer characteristic of the complementary inverter encapsulated by PMMA. 117

List of Schemes

Scheme 2.1 The synthetic route to PDBPyBT: i) tert-C_4H_9OK/2-methyl-2-butanol/100 °C; ii) K_2CO_3/DMF/70 °C; iii) $Pd_2(dba)_3$/P(*o*-tolyl)$_3$/chlorobenzene/130 °C. Structures of two polymers analogous to PDBPyBT, PDBPBT[50] and PDQT[20, 25], are also shown........ 31

Scheme 3.1. Synthetic route to PDBPyTT via Stille coupling polymerization.[14-16] 51

List of Tables

Table 2.1. OTFT performance of PDBPyBT thin films in TGBC and BGBC devices......... 38

Table 3.1 Summary of device performance of OTFTs with PDBPyTT............................... 54

Table 4.1. OTFT performance of devices with pure Au source and drain electrodes and best unipolar n-channel devices with PEI-modified Au source and drain electrodes at the optimal PEI thicknesses. Each set of data were obtained from at least 5 devices. 73

Table 5.1. TGBC OTFT performance of devices with pristine PSC (PEI = 0 wt. %) or PSC:PEI blend films as channel semiconductors. Data were obtained from at least five devices for each condition. 91

Table 5.2. Field effect mobilities of dual-gated OTFT devices containing a TGBC configuration and a BGBC configuration as shown in Figure 5.2, where the polymer semiconductor (PSC) is P5-1 (annealed at 150 °C) and the SiO_2 surface was modified with dodecyltrichlorosilane (DDTS). Data were obtained from five devices. 99

List of Abbreviations

AFM	Atomic Force Microscopy
BGBC	Bottom Gate Bottom Contact
CV	Cyclic Voltammetry
D-A	Donor-Acceptor
DBPy	3,6-di(pyridin-2-yl)pyrrolo[3,4-*c*]pyrrole-1,4(2*H*, 5*H*)-dione
DDTS	Dodecyltrichlorosilane
DFT	Density Functional Theory
DPP	Diketopyrrolopyrrole
GND	Ground
GPC	Gel Permeation Chromatography
HOMO	Highest Occupied Molecular Orbital
L	Channel Length
LUMO	Lowest Unoccupied Molecular Orbital
M_n	Number-average molecular weight
M_w	Weight-average molecular weight
OFET	Organic Field Effect Transistor
OPV	Organic Photovoltaics
OTFT	Organic Thin Film Transistor
PDI	Polydispersity Index
PEI	Polyethylenimine
PMMA	Poly(methyl methacrylate)
RMS	Root Mean Square
TGBC	Top Gate Bottom Contact

TOF-SIMS	Time-of-Flight Secondary Ion Mass Spectrometry
UPS	Ultraviolet Photoelectron Spectroscopy
UV-Vis	Ultraviolet-Visible
V_{DD}	High Supply
V_{in}	Input Voltage
V_{out}	Output Voltage
VTC	Voltage Transfer Characteristic
W	Channel Width
WF	Work Function
XRD	X-ray Diffraction

Other abbreviations and symbols are defined in the text.

Chapter 1. Introduction

1.1 Overview

The first integrated circuit (IC) was developed by Jack Kilby at Texas Instruments in 1958,[1] which led to the revolution of electronics. A transistor is a semiconductor device used to control the flow of electric current between two terminals by applying and switching an input voltage on a third terminal. It is the fundamental element in the application of logic circuits since transistors can be used as electronic switches to provide “ON” or “OFF” signals.

Back in the 1920s, the field-effect transistor (FET) was first proposed by J.E. Lilienfeld.[2] Then the first point-contact transistor was achieved by John Bardeen and Walter Brattain at Bell Labs in 1947. They placed two gold contacts onto a germanium crystal producing a signal with output power greater than input. William Shockley developed the theory of the bipolar junction transistor and clearly discussed carrier injection into the semiconductor. His work greatly expanded the knowledge of semiconductors and transistors.[3] For their contributions to the field of semiconductors and their discovery of semiconductor transistors, William Shockley, John Bardeen and Walter Brattain were awarded the 1956 Nobel Prize in Physics.

1.2 Organic Thin-film Transistors (OTFTs)

In 1983, Ebisawa and co-workers reported the first organic field-effect transistor (OFET),[4] which was based on polyacetylene. OFETs are now commonly designed and fabricated as thin film devices known as organic thin-film transistors (OTFTs).

Figure 1.1 shows a bottom gate/bottom contact structure field-effect transistor, wherein the gate controls the current between the source and drain electrodes, similar to a tap that controls the water flow. The source electrode (S) is where the majority carriers enter the channel, the drain (D) is where the majority carriers leave the channel, and the gate (G) terminal controls the channel conductivity. By controlling the gate voltage, the current from source to drain can be adjusted.

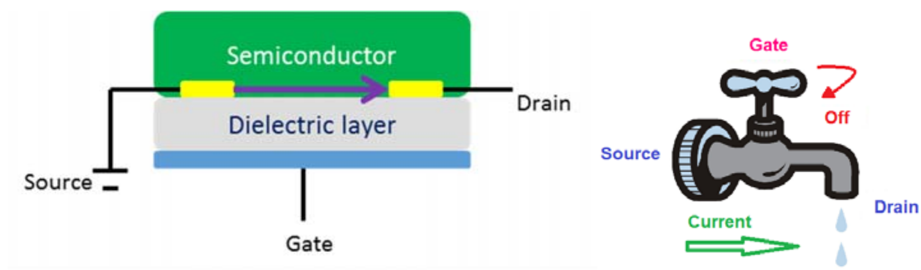

Figure 1.1 A field effect transistor with a structure of bottom gate/ bottom contact (left), whose operation is analogous to the control of water flow by a tap (right).

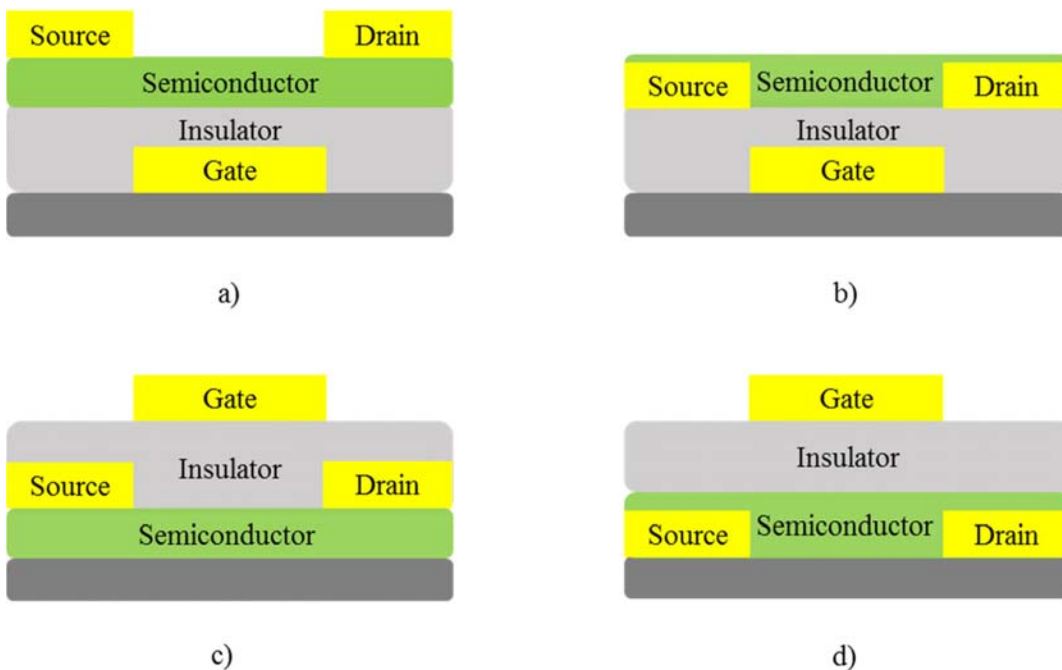

Figure 1.2 OTFT device designs: a) bottom gate/top contact (BGTC); b) bottom gate/bottom contact (BGBC); c) top gate/top contact (TGTC); d) top gate/bottom contact/ (TGBC).

Figure 1.2 shows four common device configurations used in OTFTs. The main components of the device are an organic semiconductor film, a dielectric layer, and three electrodes (source, drain and gate). The gate electrode contacting the dielectric layer controls the channel conductivity, while the other two electrodes source and drain directly contact the semiconductor layer for carrier transport.

The fabrication and characterization of an OTFT device using a polymer semiconductor **PDQT-26** (Figure 1.3c), [5] which consists of diketopyrrolopyrrole (DPP) and quarter-thiophene (QT), are described here as an example. **PDQT-26** was deposited by spin-coating a polymer solution on a SiO_2/Si substrate as the top active layer shown in Figure 1.3(a) in BGBC OTFTs with a channel width *W* and channel length *L*. When a bias is applied between the gate and the source, a conductive channel is formed and current flows between source and drain (holes as carriers for **PDQT-26** since it is a p-type semiconductor) as a drain voltage (V_D) is applied.

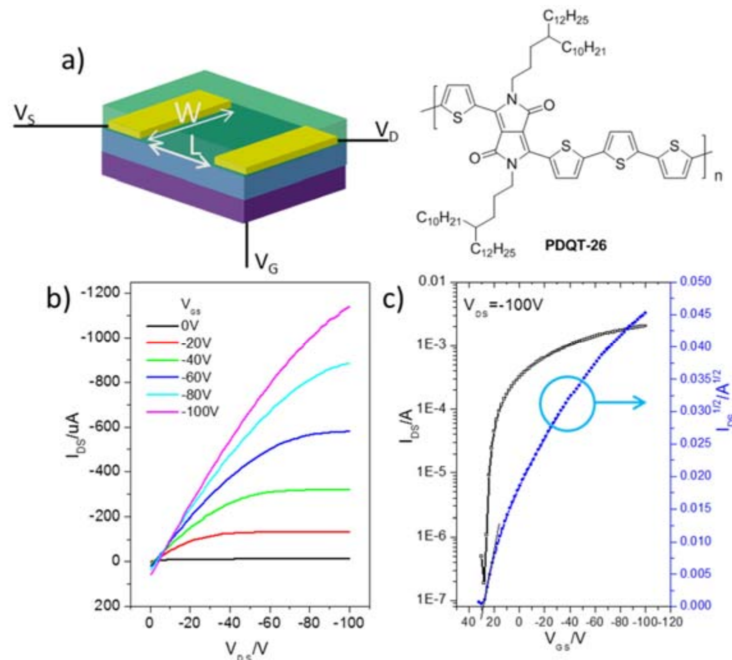

Figure 1.3. (a) The 3-D structure of a BGBC OTFT using **PDQT-26**. Typical output (b) and transfer (c) characteristics of hole accumulation regimes. OTFT was fabricated by employing BGBC (Au electrode) configuration on heavily doped n^{++}-silicon wafers with a 300 nm SiO_2 layer (capacitance 11 nF cm^{-2}) as the gate dielectric layer. The polymer film with a thickness of 40 nm was obtained by spin-coating a polymer solution on the substrate. Channel length L = 30 μm and channel width W = 1 mm. The saturation field effect mobility is 6.9 $cm^2V^{-1}s^{-1}$ at V_{DS} = -100 V.[5]

Figure 1.3b shows the output curves for different gate voltages, where ohmic (linear) behavior at low drain voltages and drain current saturation above the pinch-off point can be observed. The data can be fitted in both the linear (1) and saturation regions (2) as follows:[6]

$$I_{DS} = \mu C_i \frac{W}{L}((V_{GS} - V_{TH}) - \frac{V_{DS}}{2})V_{DS} \quad (1)$$

$$I_{DS} = \mu C_i \frac{W}{2L}(V_{GS} - V_{TH})^2 \quad (2)$$

where I_{DS} is the drain-source current, W and L are the channel width and length (Figure 1.3a), C_i is the gate insulator capacitance per area (F cm^{-2}), V_{GS} is the gate-source bias and V_{TH} is the threshold voltage. In the saturation regime, the field effect mobility μ can be calculated from the slope of the plot of $\sqrt{I_{DS}}$ versus V_{GS}. Figure 1.3c shows a logarithmic plot of I_{DS} versus V_{GS} and a plot of $\sqrt{I_{DS}}$ versus V_{GS} in the saturation region. The threshold voltage V_{TH} is extrapolated from the intersection of the slope (obtained above) and the x-axis. Another important measure of the ability of the device to switch off is the *ON/OFF current* ratio of the drain current while the device saturates for a given gate voltage to the drain current when no gate voltage is applied.

1.3 Integrated Circuits Based on Semiconducting Polymers

Solution processable polymer semiconductors have potential applications in radio-frequency identification (RFID) tags, flexible displays, electronic paper, and organic memory due to low cost, large area process, flexibility and good mechanical properties.[7-9] The fundamental element in many applications is an inverter, which is built of field-effect transistors to provide the 'NOT' logic function that implements logical negation. As shown in Figure 1.4, an inverter can be built using two different approaches: unipolar and complementary logic inverters.

Figure 1.4 a), b) and c) show three types of unipolar logic. When an input voltage (V_{in}) is applied, the transistor in a), the resistive load inverter,[10] is turned on and the output voltage (V_{out}) is close to the low supply voltage (ground, *GND*, a common return path for electric current). When the V_{in} is 0 V, the transistor will be turned off and the V_{out} is close to the high supply, V_{DD}. A leakage current flows from V_{DD} to *GND* through the load resistor and the channel when the logic is 'ON'. A resistor with a large resistance can be used to achieve a low leakage current, but a high V_{out} will be hard to achieve due to the large voltage drop across the resistor.

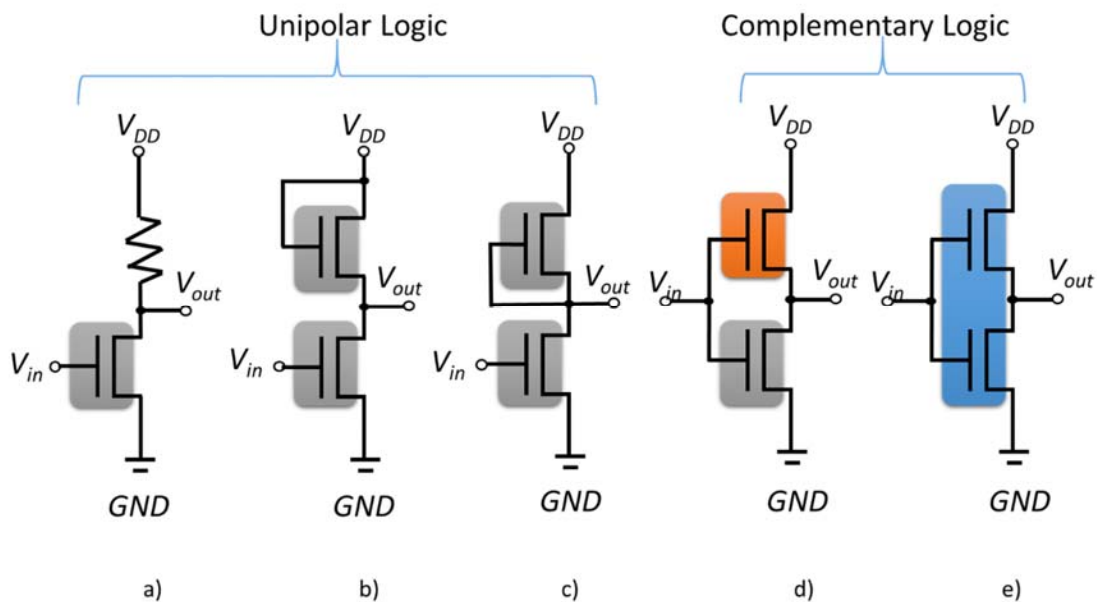

Figure 1.4 Architecture of the five different inverter types: a) resistive load inverter, b) diode type, c) V_{GS}0 type, complementary type d) based on two unipolar semiconductors and e) based on ambipolar semiconductor.[11]

If the load resistor in type a) is replaced by another transistor, it becomes a diode type inverter b).[12] The gate of the load transistor in b) is connected to V_{DD}. Thus, the load transistor is always on and the V_{out} will be close to V_{DD} when the V_{in} is 0 V. In order to pull the V_{out} close to low *GND* at a V_{in}, the load transistor is required to have a larger channel resistance than the drive transistor, which is realized by using a smaller channel width-to-length (W/L) ratio than that of the drive

transistor. One advantage of type b) inverter is the ease of fabrication since the load and drive transistors design can be used for inverters based on other semiconductor materials, while the load resistor in type a) may need a different material to achieve compatible resistance values and must be tuned for each transistor. In type c) inverter, the gate of the load transistor is connected to the output point of the inverter (source of load transistor). [12] This design requires a larger *W*/*L* ratio of the load transistor than that of the drive transistor.

In the case of complementary logic inverter, a p-type transistor and an n-type transistor are built in. When a V_{in} is applied, one of the two transistors will be 'ON', while the other one is 'OFF'. The V_{out} will be close to the supply voltage connected to the transistor in the 'ON' state. The type d) inverter consists of individual p-type and n-type transistors. The inverter current is always low whether the logic is 'ON' or 'OFF' because one of two transistors is in the 'OFF' state. Therefore, this inverter design can offer low power consumption, higher voltage gain and stronger robustness to noise than unipolar inverters. The type e) inverter is based on a single ambipolar semiconductor that can transport both holes and electrons, allowing the two transistors to behave as p-type and n-type transistors on demand. In comparison to type d), in which the p-type and n-type organic semiconductor regions must be deposited separately, the single semiconductor-based type e) inverter allows for the fabrication of complementary logic circuits using mass printing methods without the need for micro-patterning of the individual p-type and n-type transistors.[13, 14]

For application of inverters, the voltage gain, g, is the first criterion and is calculated using Eq. (3):

$$g = \text{abs}\left(\frac{dV_{out}}{dV_{in}}\right) \quad (3)$$

g reaches maximum at the point with the highest slope of V_{out} vs V_{in} as shown in Figure 1.5. g should be as high as possible.

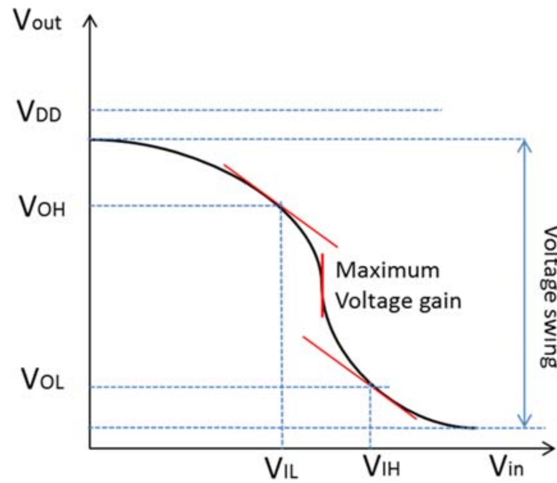

Figure 1.5. Voltage transfer characteristic (VTC) of an inverter.

Noise margin, which is the amount of noise that the circuit can withstand, is one of the most important characteristics of logic circuits. The noise margins at the high (NM_H) and low levels (NM_L) are calculated using Eq. (4) and (5):

$$NM_H = V_{OH} - V_{IH} \quad (4)$$

$$NM_L = V_{IL} - V_{OL} \quad (5)$$

where V_{IL} and V_{IH} are minimum and maximum input voltage, respectively; V_{OL} and V_{OH} are minimum and maximum output voltage. As shown in Figure 1.5, V_{IL}, V_{IH}, V_{OL} and V_{OH} occur when $\frac{dV_{out}}{dV_{in}} = -1$. The high noise margin (up to $V_{DD}/2$) leads to high noise immunity and noise robustness.

A ring oscillator, composed of an odd number of inverters, is a way to test the dynamic behavior of inverters operation in a logic circuit. The inverters are connected in a series and the output from the last one is fed back into the first one. The oscillation of the output between two voltage levels represents "ON" and "OFF", which is caused by the opposite signal of the last output to the first input.[15]

No physical device can switch instantaneously. The ring oscillation has a limited frequency which is an obstacle for practical applications such as RFID devices that need a frequency higher than 150 kHz.[16] In a logic circuit fabricated with FETs, each transistor requires a certain amount of operation time to charge the gates. Adding these inverter operation times gives the total circuit delay, which reduces the oscillation frequency. The propagation delay time (τ_p) of a single inverter is related to the circuit frequency (f_{osc}) given in Eq. (6):[17]

$$f_{osc} = 1/\ 2n\tau_p \quad (6)$$

where n is the number of inverters built in the logic, and τ_p is the delay time of the inverter.

τ_p can be expressed in Eq. (7):

$$\tau_p = (\tau_{pHL} + \tau_{pLH})/2 \approx 0.69CL(R_n+R_p)/2 \qquad (7)$$

where τ_{pHL} and τ_{pLH} are the delay times for high to low and low to high transition, CL is the gate input capacitance and R_n and R_p are the resistances of n- and p-type transistors operating in the saturation region. Two methods can be used to increase the frequency: 1) minimize the load capacitance and 2) use a high mobility semiconductor layer and/or increase the transistor W/L ratio to decrease the resistance of the transistors.

In 2012, Sirringhaus *et.al.* reported a very fast ambipolar logic based on a selenophene flanked diketopyrrolopyrrol (DPP) polymer, **PSeDPPBT**, which has well-balanced high hole and electron mobilities of 0.46 and 0.84 $cm^2V^{-1}s^{-1}$.[18] The switching voltage of the inverters is very close to $V_{DD}/2$, and the voltage gain is higher than 30. The noise margin is ~3.25 V at V_{DD} = 10 V (65% of $V_{DD}/2$) and ~5.75 V at V_{DD} = 20 V (58% of $V_{DD}/2$). As shown in Figure 1.6(b), a z-shape characteristic in the output voltage was observed due to the parasitic channel. This means neither transistor in an ambipolar semiconductor based complementary inverter can fully switch off. The leakage current increases the standby power consumption compared to the complementary logic

based on individual p-type and n-type transistors (the type d) inverter in Figure 1.4).[13] Therefore, type d) inverters are more preferred.

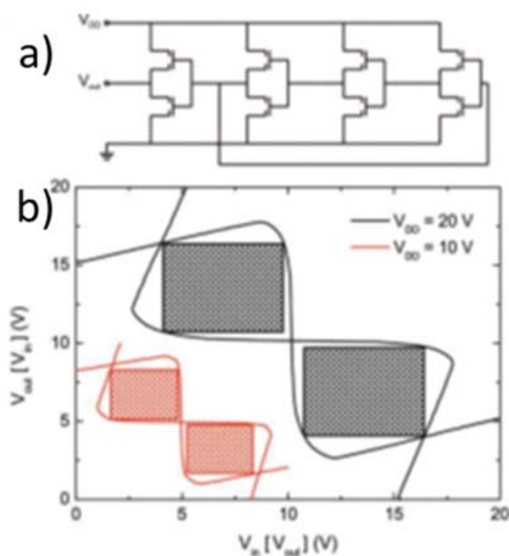

Figure 1.6 (a) Schematic representation of a three-stage ring oscillator consisting of complementary inverters based on ambipolar **PSeDPPBT**. (b) Input-output characteristics, worst-case noise margin extraction and gain of constituent inverters at positive drive voltages of 10 V and 20 V.[18] Copyright 2012, John Wiley & Sons, Inc.

The first all printed complementary inverter based on individual p-type and n-type OTFTs with high mobility semiconductors was reported by Facchetti and Noh in 2011.[19] n-Type polymer **P(NDI2OD-T2)** **(13)** (Figure 1.14) (Polyera ActivInk **N2200**) and a p-type dithiophene-based polymer, Polyera ActivInk **P2100**, were used as the semiconductor layers. **N2200** exhibited electron mobilities of 0.1-0.3 $cm^2V^{-1}s^{-1}$, while **P2100** gave a similar level of hole mobilities of 0.1-0.4 $cm^2V^{-1}s^{-1}$. These two polymers were inkjet-printed to form complementary inverters and ring oscillators. The inverters showed a voltage gain as high as ~ 32, which is much better than unipolar logic, which normally has a voltage gain lower than 10.[20]

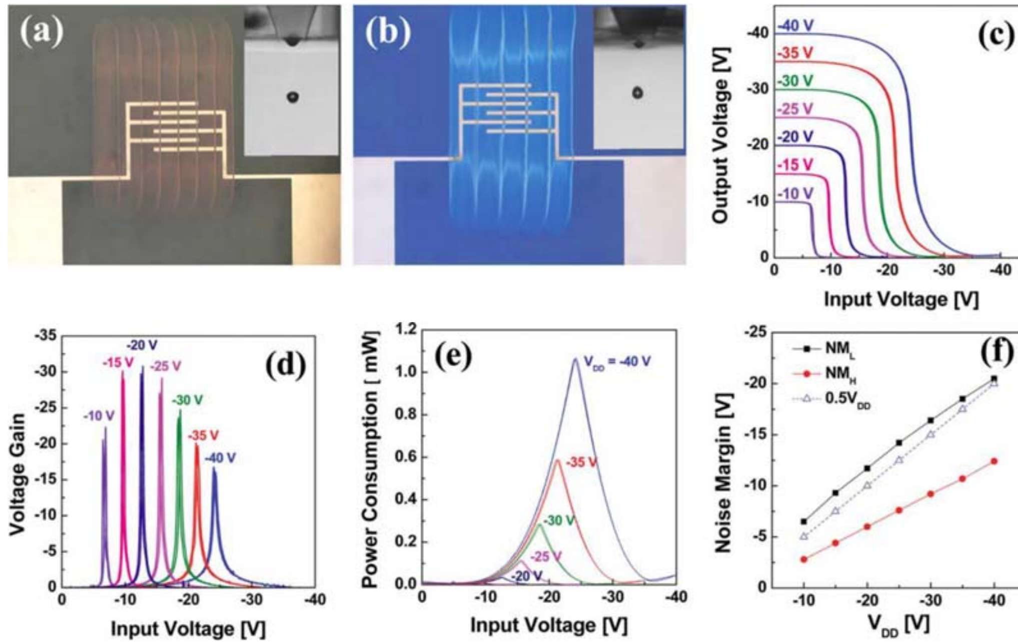

Figure 1.7. Optical image of inkjet-printed (a) **P2100** and (b) **N2200** TFTs and droplets (insets). Static inverter characteristics; (c) voltage transfer characteristics, (d) voltage gains, (e) corresponding power dissipation, and (f) noise margins of a complementary inverter at various V_{DD} [**P2100**:**N2200**, PMMA gate dielectric thickness 400 nm (2E solvent)].[19] Copyright 2011, John Wiley & Sons, Inc.

As shown in Figure 1.7(e), the power consumption of the inverter based on the **P2100**/**N2200** transistors was very low, particularly at low and high input voltages. The power consumption was less than ~1.1 mW when the inverter switched between low and high input voltages (one of the transistors build in completely switched off). In Figure 1.7(f), the noise margins for high and low logic levels were higher than 75% of $V_{DD}/2$, which was better than the ambipolar based inverters mentioned previously. Additionally, the inverters showed a fast average propagation delay time τ_p of 0.22 ms, corresponding to a ring oscillator with a frequency of 50 kHz. The authors also prepared devices using **N2200** and poly(3-hexyithiophene) (**P3HT**) that has lower hole mobilities of ~0.06-0.1 $cm^2V^{-1}s^{-1}$ than those of **P2100**. The frequency of ring oscillator was lower than 1 kHz at V_{DD} = -100 V, which was attributed to the poorer hole mobility of **P3HT**.

Therefore, complementary circuits that consist of unipolar p-type and n-type transistors are promising due to their low power consumption, high noise robustness, and high voltage gain. To broaden the application of polymer semiconductors in complementary logic, high charge carrier mobilities for both p-type and n-type unipolar polymer semiconductors are required.

1.4 Organic Semiconductors

Materials for the electronics application can be classified as conductors, semiconductors and insulators according their electrical conductivity. The electrical conductivity σ (units: S cm^{-1}) can be described using Eq. (8):

$$\sigma = e.n.\mu \qquad (8)$$

where e is the electric charge carried by a single proton or the negation of the electric charge carried by a single electron (a value of approximately 1.602×10^{-19} coulombs); n is the carrier concentration, the number of free carriers per unit volume in a semiconductor (units: cm^{-3}); and μ is the carrier mobility (units: $cm^2 V^{-1} s^{-1}$), characterizing the speed of the an individual carrier. Large n and μ are needed for high conductivity.

When two atoms are close enough to form overlapping atomic orbitals, these orbitals will split into two distinct energy levels following the Pauli Exclusion Principle as shown in Figure 1.8 (a). Two outermost shell electrons are shared between the two atoms and are allowed to fill the lower energy levels. When many atoms are joined together to form overlapping orbitals, the energy levels split and become continuous. The occupied energy levels form a valence band, and the unoccupied energy levels form the conduction band where the electrons are free to move as shown in Figure 1.8 (b). Between the top of the valence band and the bottom of the conduction band is an energy gap, E_g, where no electron can exist. The excitation probability of an electron overcoming the E_g is proportional to the Boltzmann factor, $\exp(-\frac{E_g}{k_B T})$. For a conductor, the conduction band and the

valence band overlap, which allow the valence band electrons to move freely within the conduction band. Normally, when the band gap is orders of magnitude larger than k_BT, the material will be an insulator since the valence band is fully occupied by electrons and the conduction band is empty. For a semiconductor, the band gap is narrow (<3 eV)[21] enough for an appreciable number of electrons in the valence band to jump the gap and reach the conduction band. The carrier concentration n_i in an intrinsic semiconductor can be given by[22]

$$n_i = A^{1/2}T^{3/2}\exp(-\frac{E_g}{2k_BT}) \qquad (9)$$

where A is a constant depending on the characteristics of the valence and conduction bands of the material, T is the absolute temperature, and k_B is the Boltzmann constant.

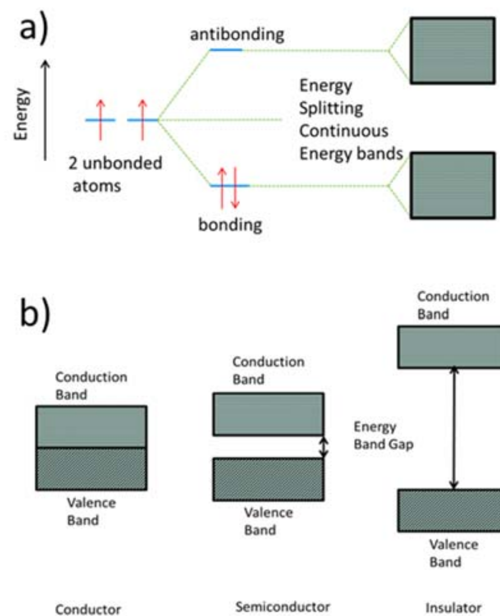

Figure 1.8. (a): atomic orbitals (left), formation of boding and antibonding (middle), energy level splitting (right); (b): energy bands in solid.

Organic semiconductors have been studied since the late 1940s[23] while conducting polymers were discovered and developed in the 1970s.[24] These organic materials can transport charge

similar to inorganic materials. Carbon is a Group IV atom, with four valence electrons, which can form four bonds with other atoms. However, orbitals of these valence electrons of carbon hybridizes in a number of forms, sp, sp^2, and sp^3, which can give double and triple bonds to form conjugated structures. Figure 1.9 a) and b) show the geometry of the sp^3 hybrid orbital structure and the sp^2 orbital structure. The sp^2 orbital is formed by hybridization of s, p_x and p_y orbitals along a plane separated from each other by 120 degrees, which can form σ bond formed by the in-plane overlap. As shown in Figure 1.9 c), ethylene has two-carbon bonds: one is a σ bond, the other is a π bond formed by the out-of-plane overlap of the remaining p_z orbitals.

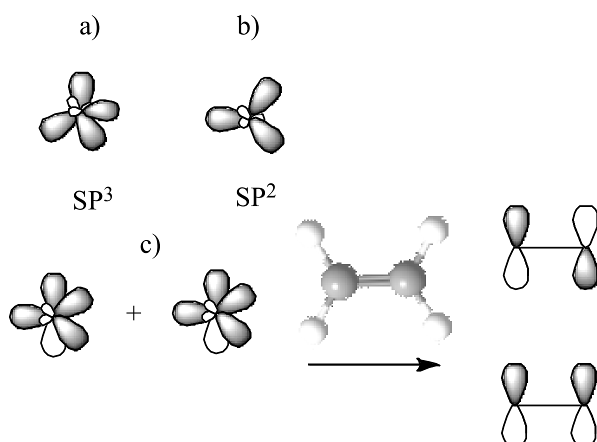

Figure 1.9. a) and b) are the geometry of the sp^3 and sp^2 orbital structures; c) shows the HOMO (highest occupied molecular orbital) and the LUMO (lowest occupied molecular orbital) with ethylene as the example.

In a molecule with alternating single and double bonds, the electrons of the overlapping π bonds can form delocalized clouds. For example, benzene has six π-molecular orbitals with three are bonding and three are anti-bonding orbitals as shown in Figure 1.10. The three orbitals below the energy of the isolated p_z orbital are bonding, each of which is occupied by two electrons with spin up and down, while the other three orbitals above are anti-bonding. The structure of benzene with

three π bonds can be written in two Lewis forms shown in Figure 1.10, illustrating two resonance structures. The resonance allows electrons to be delocalized within the ring.

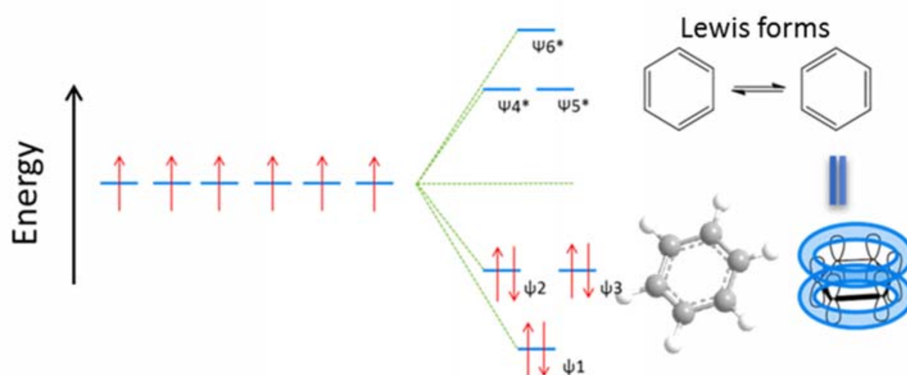

Figure 1.10 A schematic diagram showing the band splitting of benzene.

When many π-bonds are conjugated to form overlapping orbitals, these orbitals will split to form continuous energy levels as shown in Figure 1.11. The π electrons will fill the energy levels from lowest to highest. Thus, π and π* orbitals form the frontier orbitals of the molecules: HOMO (the highest occupied molecular orbital) which is filled with a pair of anti-parallel electrons and LUMO (the lowest occupied molecular orbital) which is empty. Roughly, the HOMO level of the organic semiconductor is equal to the top of the valence band of the inorganic semiconductor and the LUMO level is equal to the bottom of the conduction band. Generally, the greater the extent of π-bond conjugation, the smaller the HOMO-LUMO band gap becomes.

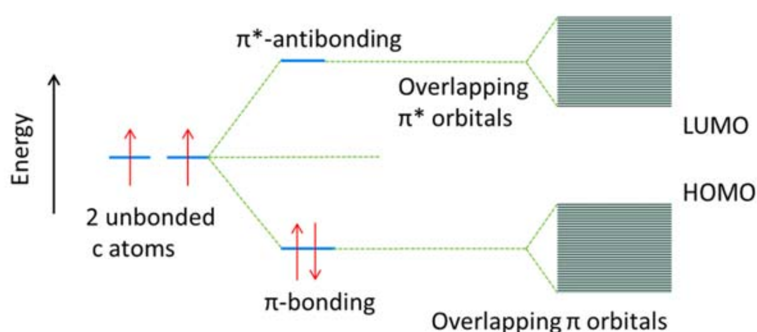

Figure 1.11 Carbon p_z atomic orbitals (left), formation of π-boding and π*-antibonding (middle), energy level splitting (right).

1.5 Polymer Semiconductors for OTFTs

Charge mobility is one of the most important parameters to evaluate the performance of a material in electronic applications. The early OTFTs consisting of polythiophene showed mobility of ~10^{-5} $cm^2V^{-1}s^{-1}$.[25] In the last few years, several new polymer semiconductors with mobilities above 1 $cm^2V^{-1}s^{-1}$ have been reported,[26-42] outperforming amorphous silicon (0.1~1 $cm^2V^{-1}s^{-1}$).[43] Most of these high mibilities[27-37, 40] were achieved with polymers having alternating electron donating (D) and accepting (A) building blocks in the backbone.[44] These D-A polymers also have larger conjugated units. The strong intermolecular static attraction between backbones due to the D-A interaction and large overlapping area gives a much closer π-π stacking distance, which dramatically facilitates the inter-chain charge hopping. Thus, the D-A strategy has been widely adopted for developing high mobility semiconducting polymers.

1.5.1 p-Type Polymer Semiconductors

Some high mobility polymer semiconductors are shown in Figure 1.12 and 错误!未找到引用源。. The majority of these high mobility polymers are p-type that transport holes. As previously mentioned, most of the high mobility polymers are D-A polymers with only two exceptions that have the D-D structures **(1)**[45] and **(2)**.[46]

The D-A polymer **CDT-BTZ (3)** developed by Müllen *et.al.*[47] had a mobility up to 0.11 $cm^2V^{-1}s^{-1}$. After optimization, the polymer showed a hole mobility above 3 $cm^2V^{-1}s^{-1}$ by increasing its number average molecular weight (M_n) to a 35 kDa.[39] Furthermore, the highly ordered single fibers of **CDT-BTZ (3)**, with M_n of 50 kDa, exhibited higher hole mobility up to 5.5 $cm^2V^{-1}s^{-1}$.[48] Another

D-A polymer **PCDTPT (4)** was reported by Bazan *et.al.* exhibited a hole mobility of up to 0.6 $cm^2V^{-1}s^{-1}$.[49] By utilizing the capillary action to control the polymer nanostructure, they were able to achieve a hole mobility as high as 52.7 $cm^2V^{-1}s^{-1}$.[50] This capillary action was also applied to **CDT-BTZ (3)** to yield an average hole mobility of 18.5 $cm^2V^{-1}s^{-1}$.[50]

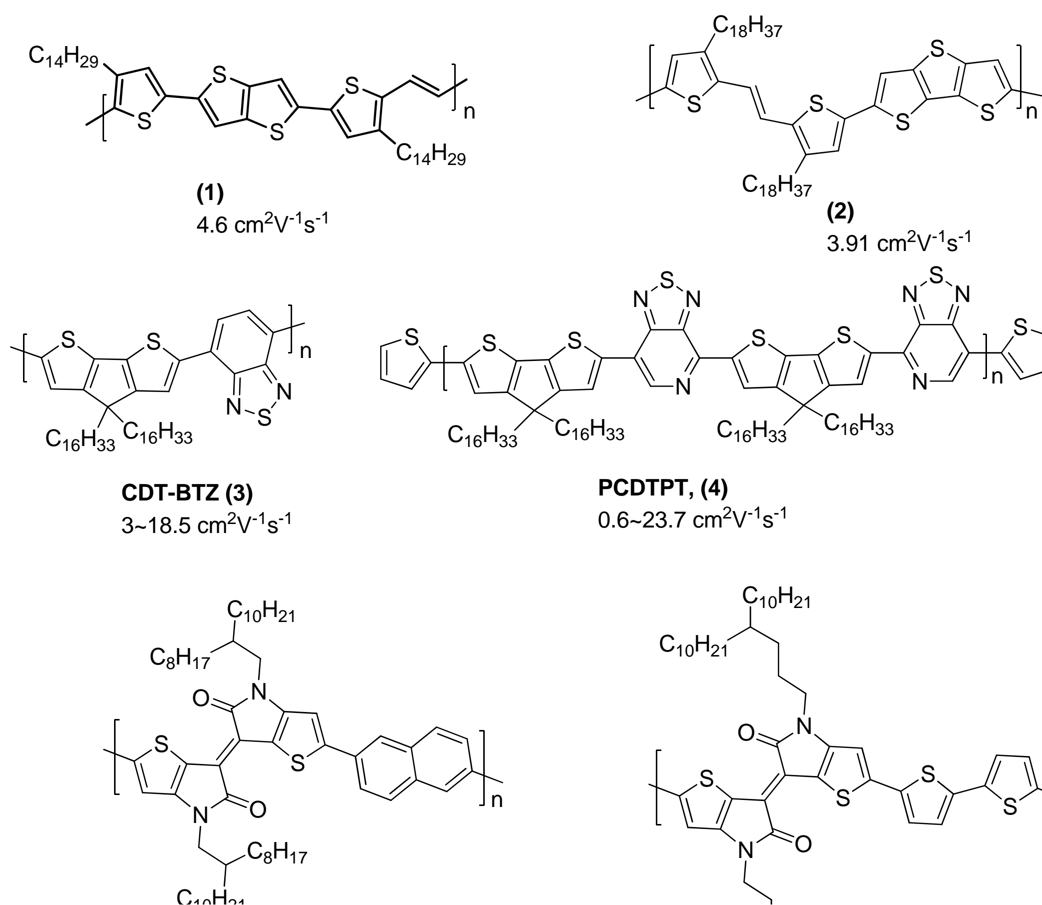

Figure 1.12 Representative p-type polymer semiconductors.[39, 45-52]

Pei *et.al.* reported a series of isoindigo (IID) and bithiohpene copolymers with different alkyl chain branching positions. **IIDDT-C3 (5)** with 3 carbons between the nitrogen atom and the branching position showed the highest hole mobility of 3.62 $cm^2V^{-1}s^{-1}$.[51] When the phenyl ring

was replaced by thiophene in IID, a new acceptor building block of thienoisoindigo (TIID) was developed. **PTIIG-Np (6)** was reported by Noh *et.al.* to have an ultrahigh hole mobility of 14.4 $cm^2V^{-1}s^{-1}$.[52]

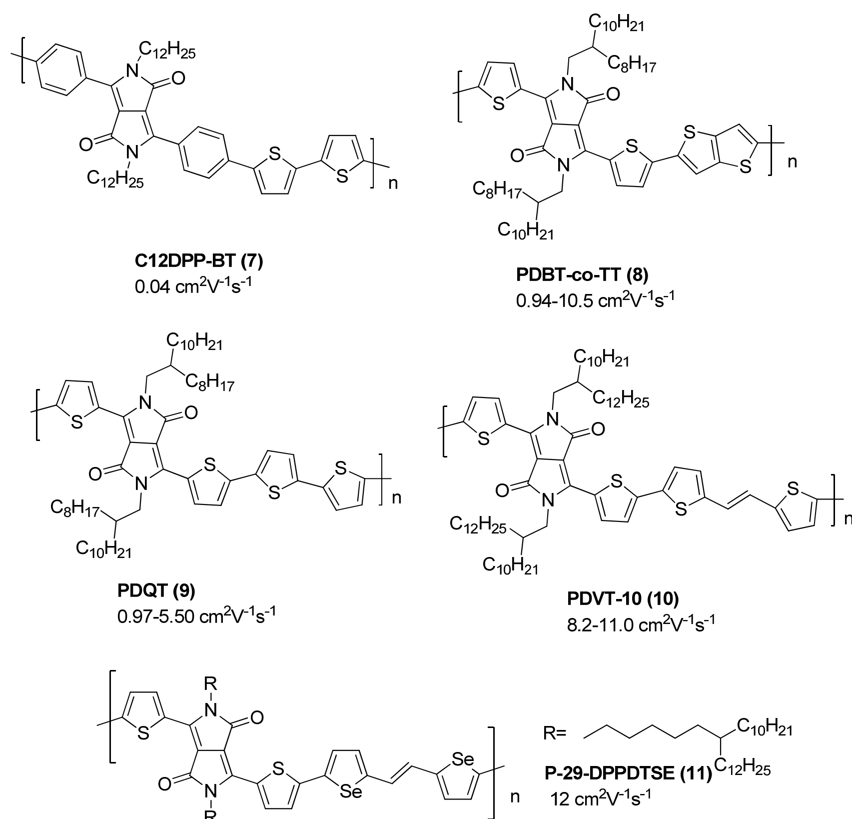

Figure 1.13 Representative DPP-based polymer semiconductors for OTFTs with high hole mobility.[27, 29-31, 33, 37, 53-56]

Polymers based on diketopyrrolopyrrole (DPP) display some of the highest mobilities (Figure 1.13), reaching a high hole mobility of 12 $cm^2V^{-1}s^{-1}$.[29] The first DPP polymer based on the diphenyl-DPP (DBP) unit, was reported as early as 1993[57] for photorefractive applications. Mobilities of DBP based polymers reported for OTFT applications were normally lower than 10^{-2} $cm^2V^{-1}s^{-1}$. This poor performance is due to the large twisting angle of ~ 20-40° between the phenyl ring and the DPP core.[58] The twisted backbone leads to poor packing between backbones and low ordering of the film, which in turn results in the poor charge transport. In 2010, our group reported

a **PDBT-co-TT(8)** copolymer,[33] with a hole mobility as high as 0.94 $cm^2V^{-1}s^{-1}$ in OTFTs with a bottom gate top contact (BGTC) device structure. When the polymer film was tested in a top gate structure with PMMA as a dielectric, the polymer showed a balanced ambipolar property with hole mobility as high as 1.62 $cm^2V^{-1}s^{-1}$ and electron mobility up to 1.86 $cm^2V^{-1}s^{-1}$ when annealed at 320 °C.[54] Liu *et.al.* optimized the polymerization condition to obtain a higher M_n of 110 kDa and achieved a much higher hole mobility of 10.5 $cm^2V^{-1}s^{-1}$.[30]

When bithiophene was introduced as the other co-monomer instead of thienothiophene to form a new polymer **PDQT(9)**, a hole mobility was initially up to 0.97 $cm^2V^{-1}s^{-1}$ [31] and was improved later to 5.50 $cm^2V^{-1}s^{-1}$. Interestingly, the highest performance was observed from a high M_n polymer with some oligomers, rather than from the pure high molecular weight polymer. It is believed that a certain amount of oligomers promote the formation of highly crystalline grain from high molecular weight polymer chains, which is called the "anti-plasticization effect".[37]

In 2013, (*E*)-2-(2-(thiophen-2-yl)vinyl)thiophene (TVT) units were added into thiophene-DPP polymer backbone with a longer side-chain instead of the bithiophene used by Liu *et.al.* to produce a high hole mobility of 8.2 $cm^2V^{-1}s^{-1}$ for **PDVT-10(10)** in BGBC OTFTs on a SiO_2 dielectric layer.[27] The polymer as the channel on a poly (vinyl alcohol) (PVA) dielectric in a TGBC OTFT gave a higher hole mobility of 11.0 $cm^2V^{-1}s^{-1}$.[55] The record hole mobility of 12 $cm^2V^{-1}s^{-1}$ based on DPP was achieved by **P-29-DPPDTSE(11)** (**错误!未找到引用源。**). The high mobility was attributed to excellent self-organizing properties from side-chain modification with an extended 6-carbon linear alkyl spacer that resulted in a π-π stacking distance as short as 3.58 Å.[29]

1.5.2 n-Type Polymer Semiconductors

As mentioned earlier, for complementary logic applications, p-type and n-type transistors with balanced hole and electron mobilities are required. While many high performance p-type polymer semiconductors have been reported, high performance n-type unipolar polymer semiconductors are rare. Several n-type polymer semiconductors with electron mobility higher than 1 $cm^2V^{-1}s^{-1}$ are listed in Figure 1.14.

While DPP-based D-A polymers comprise many high mobility p-type polymer semiconductors, the DPP-based polymer **N-CS2DPP-OD-TEG (12)** in Figure 1.14 also demonstrated a record high unipolar electron mobility of 3 $cm^2V^{-1}s^{-1}$. [59] However, this value is much lower in comparison to the highest hole mobility. The widely investigated **P(NDI2OD-T2) (13)** (Figure 1.14) developed by Facchetti *et.al.* [60] achieved electron mobility as high as 0.85 $cm^2V^{-1}s^{-1}$ in TGBC OTFTs.[60] In addition, the electron mobility can be improved to up to 1.5 $cm^2V^{-1}s^{-1}$ by controlling the extent of oriented domains by inducing pre-aggregates in the solution.[61] Another NDI based D-A polymer, **P(ThNDIThF4) (14)** exhibited a high electron mobility up to 1.3 $cm^2V^{-1}s^{-1}$ in TGBC OTFTs.[62] Pei *et.al.* reported a PPV-like acceptor based polymer, **BDPPV (15)**, which displayed unipolar electron mobility up to 1.1 $cm^2V^{-1}s^{-1}$.[63]

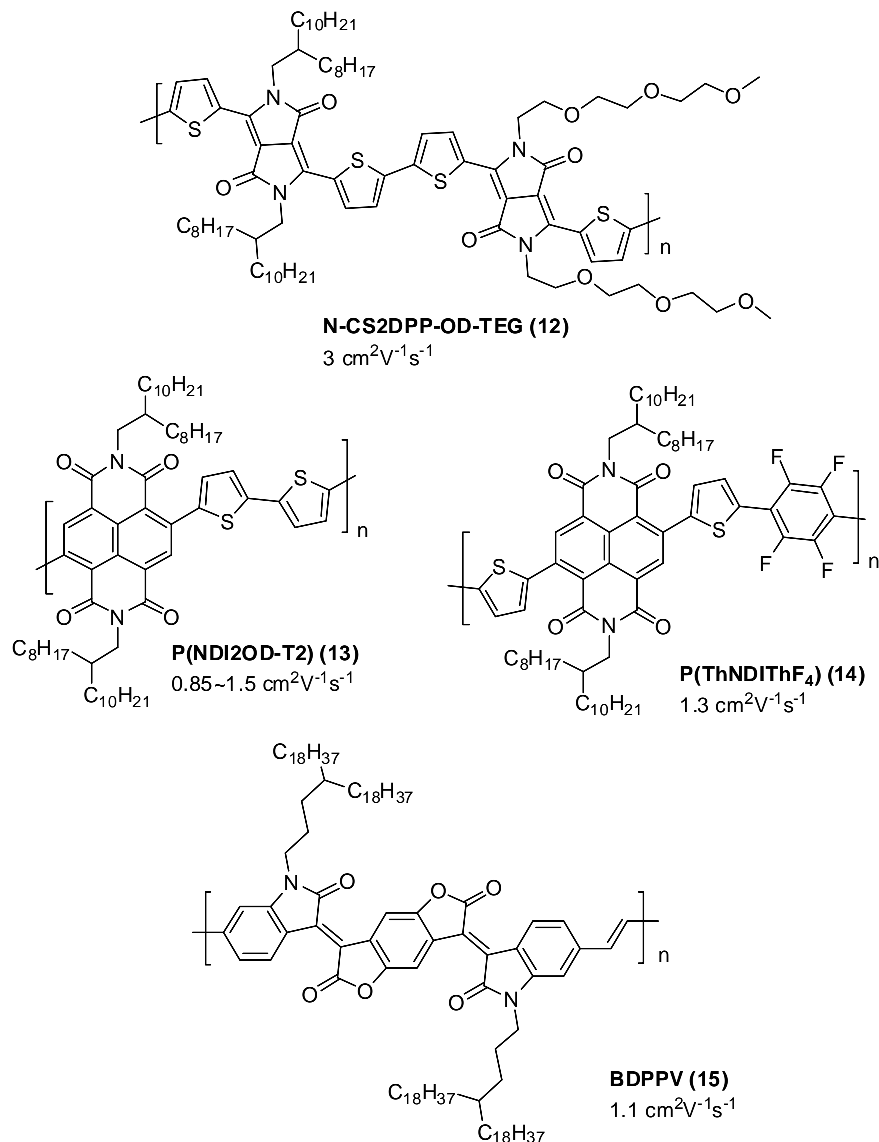

Figure 1.14 Representative n-type polymer semiconductors for OTFTs with high electron mobility.[59-63]

Although, the D-A strategy has been used to develop these high performance n-type semiconductor polymers, many D-A polymers have a high HOMO level and a low LUMO level[64] (Figure 1.15), which allow for both electron and hole injections and transport, making many D-A polymers ambipolar semiconductors.[35, 65-75] Even for **P(NDI2OD-T2) (13)**, ambipolar charge transport behavior was also observed in OTFTs.[76, 77]

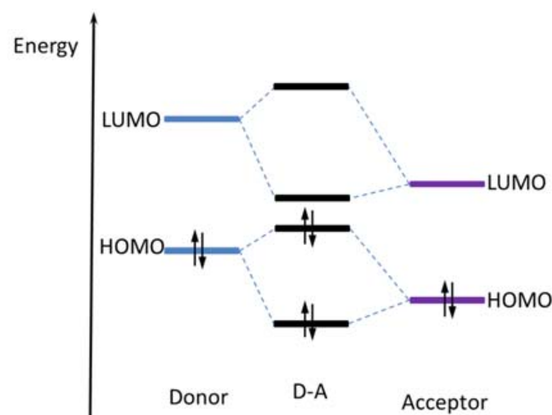

Figure 1.15. Alternating donor–acceptor units lower the effective band gap by orbital overlap.[64]

The D-A polymers shown in Figure 1.16 were reported to show ambipolar charge transport properties with electron mobilities greater than 1 $cm^2V^{-1}s^{-1}$. The highest electron mobility of 4.34 $cm^2V^{-1}s^{-1}$ was demonstrated by the DPP-based polymer **(19)** fabricated by a solution shearing process.[78] **DPPPhF4(16)**, which consists of thiophene-flanked DPP and electron-deficient fully fluorinated benzene (an electron deficient moiety) showed a high electron mobility of 2.36 $cm^2V^{-1}s^{-1}$ and hole mobility of 0.25 $cm^2V^{-1}s^{-1}$. [79]

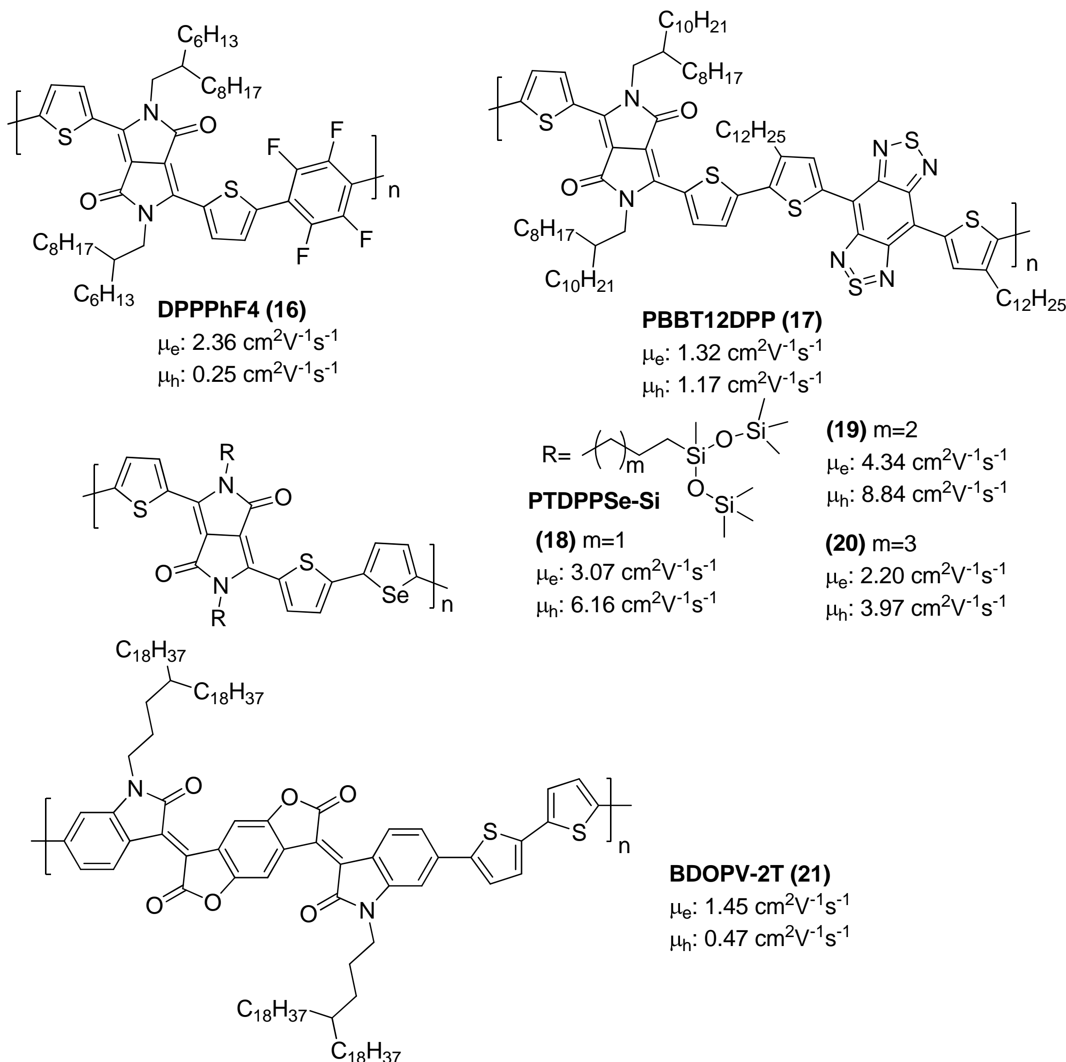

Figure 1.16 Representative ambipolar polymer semiconductors for OTFTs with high electron mobility (μ_e is electron mobility; μ_h is hole mobility).[40, 78-80]

These ambipolar polymer semiconductors are suitable for complementary inverters [11, 13, 54, 72] for large-area manufacturing. Unfortunately, as discussed earlier, complementary inverters based on ambipolar semiconductors have high power consumption due to the leakage current between V_{DD} and GND since the transistors do not completely switch off. In contrast, complementary inverters based on both p-type and n-type polymer semiconductor transistors consume much less power with negligibly low leakage current when they are in a stable logic state.

In order to achieve low OFF-state currents in ambipolar semiconductor based inverters, Facchetti *et.al.* selectively modified the electrode of inverters by using cesium salts to facilitate electron injection and block hole injection of one transistor in an inverter. This reduced the power consumption and achieved a good noise margin as high as ~75% of $V_{DD}/2$ even when hole transport was not suppressed completely.[81] Sirringhaus *et.al.* used organic thiol-modified Au electrodes to lower the work function to facilitate electron injection and increase the electron mobility in OTFTs.[82]

Besides the surface modification method, several other strategies to render ambipolar organic semiconductors unipolar were reported. For example, alteration of the molecular packing motif was found to be an effective method to change the charge carrier polarity. Zhang *et al.* reported three organic semiconductors differing only in their side chains.[83] Interestingly, two showed ambipolar, while the other one exhibited p-type unipolar transport behavior due to the difference in their molecular packing and film microstructures.[83] Similar phenomena was observed for a small molecule quinoidal oligothiophene, which showed p-type unipolar transport behavior with the as-prepared films in OTFTs, and showed n-type unipolar transport behavior while the devices annealed at 180ºC, which was attributed to the large difference in their molecular packing. [84] The molecular packing of quinoidal oligothiophene is also affected by the processing solvent. Unipolar n-type and p-type transport behavior were observed in the presence of the processing solvents, THF and chloroform, respectively. Additionally, the resulting OTFT devices that initially exhibited n-type or p-type behavior can be converted into an ambipolar device by treating the semiconductor layers with chloroform vapor. [85]

Another effective way to convert ambipolar semiconductors into unipolar semiconductors is by doping. Bao *et al.* reported a successful transition of **TIPS-pentacene** from p-type to n-type by doping with 2-(2-methoxyphenyl)-1,3-dimethyl-2,3-dihydro-1H-benzoimidazole (*o*-MeO-DMBI), which exhibited electron mobility up to 6.8 $cm^2V^{-1}s^{-1}$ compared to the undetectable electron

mobility value before doping. Furthermore, the hole mobility decreased from an average value of 0.21 $cm^2V^{-1}s^{-1}$ to an undetectable level.[86] Kim *et al*. reported that a typical ambipolar polymer semiconductor **P(NDI2DO-T2)** was converted to n-type unipolar by doping with cobaltocene ($CoCp_2$) or CsF. The **P(NDI2DO-T2)** film doped with 0.5wt% of $CoCp_2$ showed a dramatically increased electron mobility of 0.72 $cm^2V^{-1}s^{-1}$ up from 0.34 $cm^2V^{-1}s^{-1}$ for pristine **P(NDI2DO-T2)** film. The improved electron mobility was attributed to a shift of the Fermi level toward the LUMO level induced by n-type dopants, which increases the electron concentration but decreases the hole concentration in the semiconductor, thereby facilitating electron injection and inhibiting hole injection.[87]

1.6 Objective of This Work

A high-performance complementary logic circuit requires p-type and n-type transistors with high and comparable hole and electron mobilities. However, the electron mobilities of n-type polymer semiconductors are still several factors lower than the hole mobility of p-type polymers. Therefore, the objective of this work is to develop high mobility unipolar n-type polymer semiconductors. The following strategies are utilized to achieve this objective:

1) The D-A strategy has been utilized to develop high performance electron transport polymer semiconductors. Inspired by the high mobility of DPP acceptor based polymers, DPP is chosen as the basis for a novel strong electron accepting building block. The electron-deficient pyridine ring is used to replace the five-membered ring that flanks the DPP core. The resulting building block is highly coplanar and a strong electron deficient acceptor, which is suitable for making high electron mobility polymer semiconductors.

2) Since many high mobility D-A polymer semiconductors show ambipolar charge transport performance, conversion of ambipolar polymer semiconductors into unipolar n-type semiconductors is a strategy to achieve high performance n-channel OTFTs for complementary inverters. Polyethylenimine (PEI) was used to modify the Au electrodes to reduce the work function to 3.9 eV.[88] In this work we use PEI to modify source/drain electrodes to block hole injection in order to achieve unipolar n-type OTFTs using ambipolar polymer semiconductors.
3) We use PEI as an n-dopant to convent ambipolar polymer semiconductors to unipolar n-type polymer semiconductors.

The thesis is organized as follows:

1) In Chapter 2, a coplanar electron acceptor building block, 2-pyridinyl flanked DPP (**DBPy**), was designed and synthesized. A semiconducting polymer based on **DBPy** showed ambipolar charge transport performance with record high electron mobility of 6.3 $cm^2V^{-1}s^{-1}$.
2) In Chapter 3, a thieno[3,2-*b*]thiophene (TT) unit was chosen to copolymerize with **DBPy**. The resulting polymer still showed high ambipolar charge transport performance in OTFTs. The source and drain electrodes were modified with an ultra-thin layer of polyethyleneimine (PEI), which resulted in a high electron only mobility of 2.38 $cm^2V^{-1}s^{-1}$ in OTFTs.
3) In Chapter 4, the strategy of PEI modification in Chapter 3 was applied to several other ambipolar and p-type polymer semiconductors to realize n-channel OTFTs.
4) In Chapter 5, n-doping ambipolar and even p-type polymer semiconductors with PEI in was conducted to achieve high performance n-type unipolar polymer semiconductors in OTFTs.

5) Chapter 6 concluded the thesis work and demonstrated preliminary results on the fabrication of complementary inverters based on p-type polymers and PEI doped ambipolar polymers by inkjet-printing.

Chapter 2. High Electron Mobility Polymer Semiconductors Based on DBPy

This chapter is partially published in B. Sun, W. Hong, Z. Yan, H. Aziz, Y. Li, *Adv. Mater.* **2014**, *26*, 2636

Dr. Hong performed all cyclic voltammetry (CV) and UV-Vis measurements; Yan conducted the DFT simulations; and Sun carried out polymer synthesis and all other characterization.

2.1 Introduction

Organic thin film transistors (OTFTs) enabled by polymer semiconductors form the essential components of a variety of printed electronic applications such as radio-frequency identification (RFID) tags, flexible displays, medical sensors, memory devices, etc.[36, 38, 39, 89-99] While polymer semiconductors possess excellent processability and mechanical properties, their low charge carrier mobility has been the main barrier to many applications. Exploration of new building blocks for constructing high mobility polymer semiconductors remains a central topic for OTFT research. Recently, several classes of π-conjugated polymers showed highly efficient charge transport performance with mobilities close to or in excess of 1 $cm^2V^{-1}s^{-1}$ in OTFTs,[26-42] rivaling amorphous silicon typically exhibits a mobility range of 0.1~1 $cm^2V^{-1}s^{-1}$. The high mobility polymers reported are predominantly p-type semiconductors, where positive holes are the charge carriers. On the other hand, fewer electron transport n-type polymer semiconductors have been reported. In general, the magnitude of electron mobility is still several factors lower than the hole mobility of p-type polymers. The highest hole and electron mobility values reported are 12 $cm^2V^{-1}s^{-1}$ [29] and 3 $cm^2V^{-1}s^{-1}$, [59] respectively. This is mainly due to the unavailability of suitable electron accepting building blocks for polymers to reach a lowest unoccupied molecular orbital (LUMO) energy level deeper

than ~ -4 eV for simple injection and efficient transport of electrons.[60] High mobility n-type polymer semiconductors with matching electron mobility that matches the hole mobility of p-type polymer semiconductors are in demand for complementary metal-oxide-semiconductor (CMOS)-like logic circuits.[11, 59, 60, 63, 100] Recently discovered ambipolar polymer semiconductors, which can selectively transport electrons or holes under controlled biases, appear to be promising single-component semiconductors to enable CMOS-like circuitry design using much simpler fabrication processes.[11, 54, 72, 74] Some amibipolar polymer semiconductors also have unique application for organic light-emitting field effect transistors.[101-103]

2.2 Results and Discussion

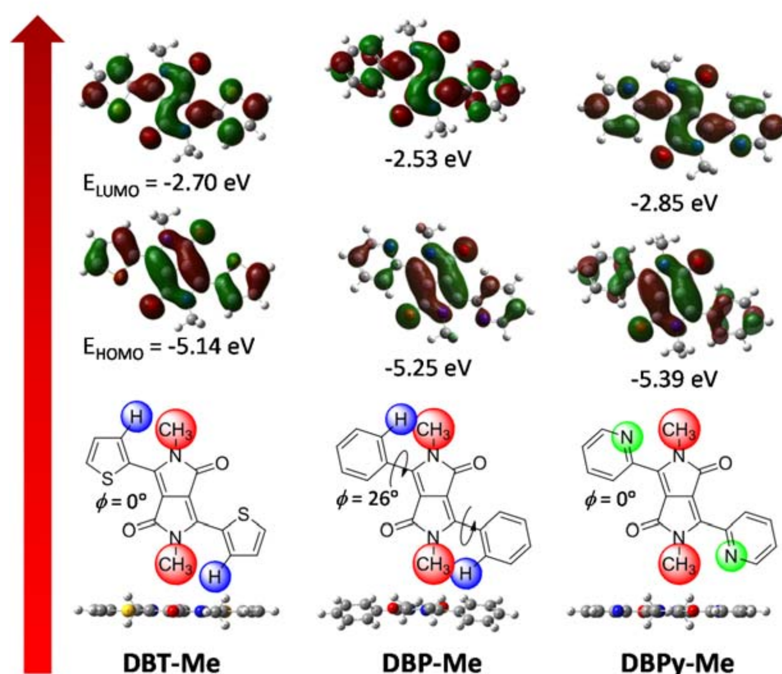

Figure 2.1. The optimized HUMO/LUMO electron distribution diagrams and geometry of 2,5-dimethyl-3,6-di(thiophen-2-yl)pyrrolo[3,4-*c*]pyrrole-1,4(2*H*,5*H*)-dione (**DBT-Me**), 2,5-dimethyl-3,6-diphenylpyrrolo[3,4-c]pyrrole-1,4(2*H*,5*H*)-dione (**DBP-Me**), and 2,5-dimethyl-3,6-di(pyridin-2-yl)pyrrolo[3,4-*c*]pyrrole-1,4(2*H*,5*H*)-dione (**DBPy-Me**) obtained by computer simulation with density functional theory (DFT) calculations.

In this study an electron acceptor moiety, diketopyrrolopyrrole (DPP), was chosen as the core of a novel strong electron accepting building block in order to achieve a LUMO level lying below -4 eV for more efficient electron injection and transport. In the past few years, DPP was found to be an excellent electron accepting moiety for a large number of polymer semiconductors for OTFTs, [26-37, 40] organic photovoltaics (OPVs)[34, 72, 104-107] and organic light-emitting diodes (OLEDs).[108, 109] All of the high mobility DPP polymers reported are comprised of a monomeric unit with a DPP core flanked with two five-membered ring-containing heteroaryls, namely, thiophene[31, 33] (**DBT**, Figure 2.1), furan (**DBF**), [32] selenophene, [35] or thieno[3,2-*b*]thiophene (**DBTT**). [26] The five-membered rings have minimal steric effects on the DPP core and thus render these building blocks highly coplanar. However, these five-membered rings have six π-electrons shared among five atoms, which gives these moieties an electron-rich nature of these moieties and offset the electron-withdrawing effect of the DPP core. Polymers based on five-membered ring-flanked DPP blocks generally exhibit a LUMO level higher than -4 eV.[26-37, 40] To further bring down the LUMO level, the incorporation of a more electron-deficient six-membered aromatic ring to be adjacent to the DPP core would be desirable. However, when the simplest six-membered aromatic ring (benzene) is used, the resulting DPP building block, **DBP** (Figure 2.1) has a large dihedral angle of ~20-40° between the phenyl ring and the DPP core once the nitrogen atoms of DPP are substituted with side chains. [58] The seriously twisted **DBP** unit shortens the effective conjugation path along the polymer backbone and lengthens the interchain π-π stacking distance, which would impede both intra- and intermolecular charge transport. Thus, **DBP**-based polymers[110-112] were reported to show mobility values that are several orders of magnitude lower compared with **DBT-**, **DBF-** or **DBTT-**based polymers.[34] Additionally, due to the band gap widening, the LUMO level of DBP-based polymers remains higher than -4 eV despite the fact that benzene is more electron deficient than thiophene and furan. To alleviate the steric hindrance of six-membered rings, 2-pyridinyl was deliberately chosen in this study as the adjacent substituent for the DPP core. Positioning the

sterically less demanding nitrogen atom at the ortho position of pyridine would help achieve an more coplanar 2-pyridinyl substituted DPP block (**DBPy**, Figure 2.1). Equally important is that pyridine is more electron-deficient than thiophene, furan and benzene, which would make **DBPy** a stronger electron acceptor. Thus, polymers based on **DBPy** are expected to possess a deeper LUMO energy level and may exhibit explicit electron transport characteristics in OTFTs. Here the first **DBPy** based polymer, which showed ambipolar charge transport performance with an unprecedentedly high electron mobility value of 6.30 $cm^2V^{-1}s^{-1}$, demonstrates that **DBPy** is a very promising new acceptor building block for highly efficient electron transporting polymer semiconductors.

Computer simulations was carried out on a **DBPy** model compound with methyl groups at the nitrogen atoms, **DBPy-Me** (Figure 2.1). The geometry of the energy-minimized **DBPy-Me** is completely coplanar with a dihedral angle (ϕ) between pyridine and DPP of 0°, which suggests that the 2-pyridinyl group can effectively avoid steric interaction with the DPP moiety. On the other hand, the model compound, **DBP-Me**, being flanked with two phenyl substituents, has a large dihedral angle of 26°. The simulation results also showed that the highest occupied molecular orbital (HOMO) and LUMO energy levels of **DBPy-Me** are -5.39 eV -2.85 eV, respectively. These levels are deeper than those of **DBT-Me** (E_{HOMO} = -5.14 eV; E_{LUMO} = -2.70 eV) and **DBP-Me** (E_{HOMO} = -5.25 eV; E_{LUMO} = -2.53 eV) (Figure 2.1), indicating that **DBPy** is a stronger electron-withdrawing building block.

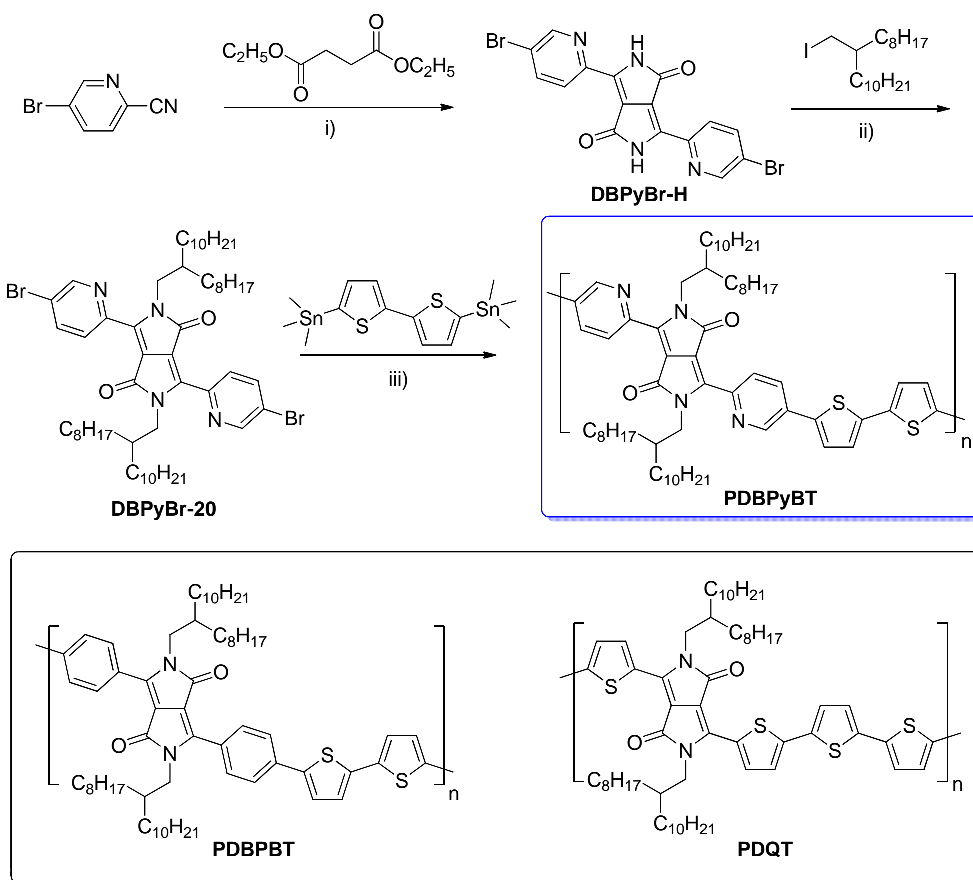

Scheme 2.1 The synthetic route to **PDBPyBT**: i) tert-C_4H_9OK/2-methyl-2-butanol/100 °C; ii) K_2CO_3/DMF/70 °C; iii) $Pd_2(dba)_3$/P(*o*-tolyl)$_3$/chlorobenzene/130 °C. Structures of two polymers analogous to **PDBPyBT**, **PDBPBT**[113] and **PDQT**[31, 37], are also shown.

A copolymer of **DBPy** and bithiophene (BT), **PDBPyBT**, was conveniently synthesized using a 3-step route shown in Scheme 2.1. **DBPy**Br-H bearing two functional bromo groups was synthesized in 53.5% yield via reaction of 5-bromopyridine-2-carbonitrile with diethyl succinate in the presence of tert-BuOK in 2-methyl-2-butanol. Two nitrogen atoms at the DPP core were subsequently substituted with 2-octyldodecyl using 2-octyldodecyl iodide in *N*,*N*-dimethylformamide (DMF) in the presence of potassium carbonate to produce the monomer **DBPy**Br-20 with 25.4% yield. The use of these long branched side chains was intended to solubilize the resulting polymer. **DBPy**Br-20 was then copolymerized with 5,5'-bis(trimethylstannyl)-2,2'-bithiophene via Stille coupling to produce the target polymer **PDBPyBT**

with 93.0% yield after Soxhlet purification. The weight (M_w) and number (M_n) average molecular weights of **PDBPyBT** are 93.6 kDa and 26.3 kDa, respectively, with a polydispersity index (PDI) of 3.56, determined using a high-temperature gel-permeation chromatography (HT-GPC) at a column temperature of 140 °C with 1,2,4-trichlorobenzene as the eluent and polystyrene as standards.

As shown in Figure 2.2, the maximum absorption wavelengths (λ_{max}) of **PDBPyBT** in solution (683 nm) and in thin film (695 nm) are significantly red-shifted in comparison with those (558 nm in solution and 570 nm in thin film) of its analogous DBP polymer, PDBPBT (structure shown in Scheme 2.1). [113] These results indicate that **PDBPyBT** has a more coplanar backbone structure in both solution and the solid state. However, the λ_{max} of **PDBPyBT** are blue-shifted by ~100 nm relative to those (784 nm in solution and 786 nm in thin film) of its analogous DBT polymer **PDQT** (Scheme 2.1). [37] This is most likely due to the weaker intrachain push-pull electron transfer between the pyridine and DPP units since pyridine is a much weaker donor than thiophene.

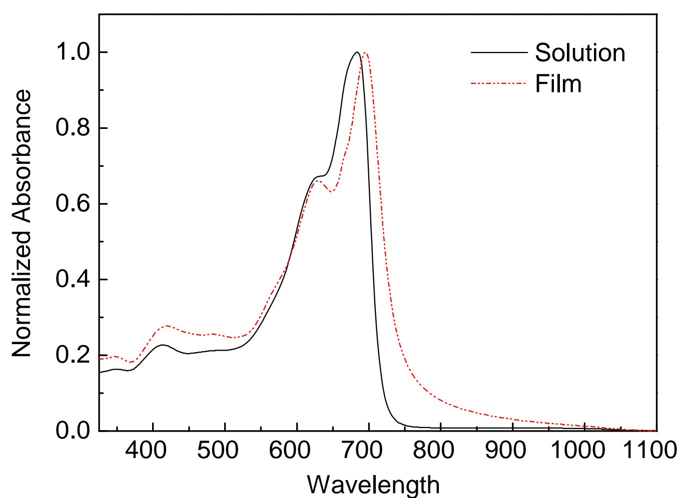

Figure 2.2. UV-vis absorption spectra of **PDBPyBT** solution (chloroform) and as-cast thin film on quartz.

Cyclic voltammetry (CV) technique was used to determine the frontier energy levels of **PDBPyBT**(Figure 2.3). A strong reversible oxidation peak was observed, suggesting the good oxidative stability of this polymer. The HOMO level was calculated to be -5.69 eV from the onset oxidation potential with ferrocene as a reference. The reductive process is also reversible, but the currents are much lower than in the oxidative process. The LUMO level of **PDBPyBT** was calculated to be -4.33 eV, which is markedly deeper than that of **PDQT** (-4.0 eV) [31, 37] and PDBPBT (-3.68 eV). [113] Such a low-lying LUMO would be beneficial for electron injection and transport in OTFTs. [60]

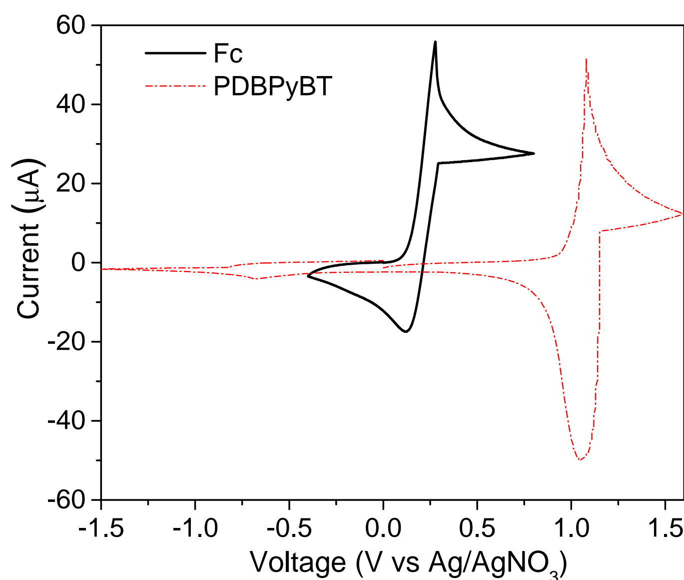

Figure 2.3 Cyclic voltammetry diagrams of **PDBPyBT** and the reference ferrocene (Fc) in acetonitrile at a sweep rate of 50 mV s^{-1}. The HOMO and LUMO energy levels of **PDBPyBT** were determined from the oxidative and reductive onset potentials to be -5.69 eV and -4.33 eV, respectively.

To investigate the chain packing of **PDBPyBT**, X-ray diffractometry (XRD) measurements in reflection mode was carried out in a reflective mode (Figure 2.4a) on polymer thin films spin coated on SiO_2/Si wafer substrates. For the as-spun polymer thin film, a strong primary diffraction peak at $2\theta = 4.36°$ was observed, which corresponds to a d-spacing of 0.203 nm. For the 150 °C-annealed

thin film, the primary peak intensified significantly, indicating much improved crystallinity. The position of the primary peak shifted slightly to 2θ = 4.32° (d = 0.204 nm). The thin film annealed at a higher temperature of 200 °C showed further enhanced crystallinity. Since the peak corresponding to the π-π stacking distance in the **PDBPyBT** thin films on SiO_2/Si substrates was not observed in the XRD patterns obtained with the reflective mode, this polymer presumably adopted a layered lamellar crystal structure with an edge-on chain orientation. [114, 115] This chain packing motif is beneficial for charge transport in an OTFT device, [114] since efficient intramolecular charge transport and intermolecular charge hopping along the π-π stacks are dominant, while the least efficient charge transport through the distantly separated lamellar layers is inhibited.

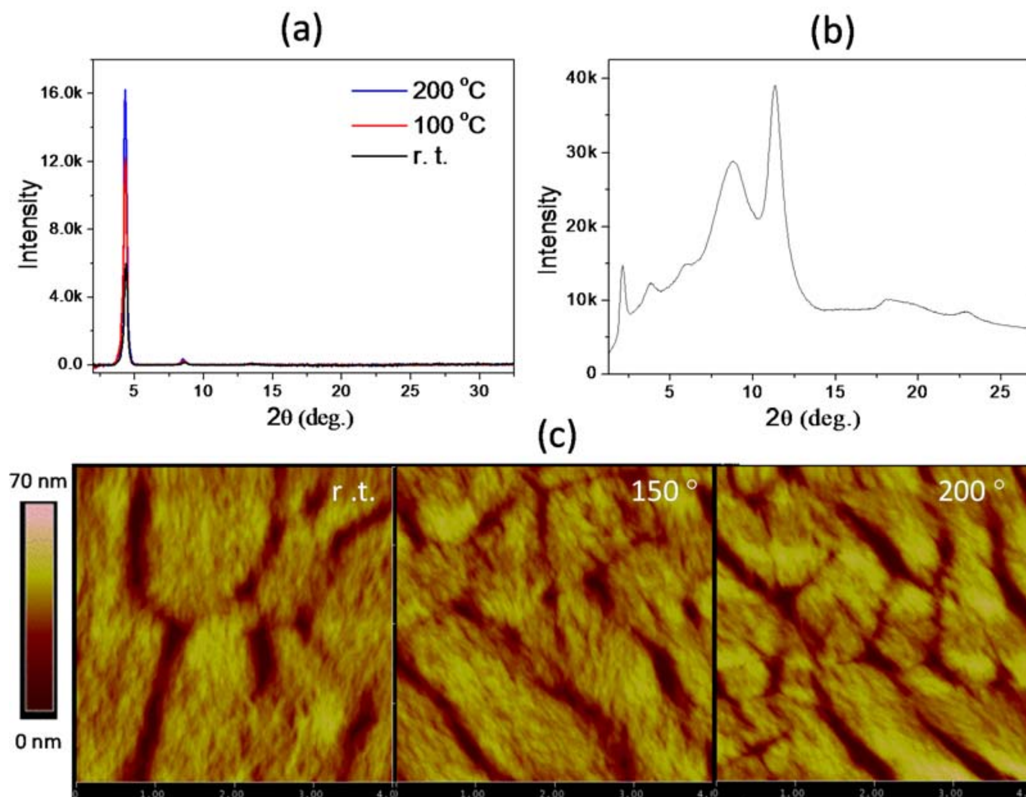

Figure 2.4. (a) XRD patterns of spin-coated **PDBPyBT** thin films on bare SiO_2/Si substrates annealed at different annealing temperatures measured in a reflection mode using Cu Kα1 radiation. (b) XRD pattern of a stack of non-annealed **PDBPyBT** thin films in a transmission mode using Mo Kα radiation. (c) AFM images (2 μm × 2 μm each) of **PDBPyBT** thin films on bare SiO_2/Si substrates annealed at different temperatures: the root-mean square (RMS) roughness is 8.2 nm, 8.3 nm, and 11.7 nm for the as-spun (r.t.),

150 °C-annealed, and 200 °C-annealed thin films, respectively. Annealing of the thin film samples for both XRD and AFM was conducted on a hot plate for 10 min in nitrogen.

To elucidate the molecular packing along the horizontal direction in a thin film, transmission XRD measurement was conducted on stacked polymer thin films. [116] As clearly seen in Figure 2.4b, a strong peak at $2\theta = 11.34°$ was observed, which corresponds to the π-π distance of 0.360 nm. The much shorter π-π distance of **PDBPyBT** than that of **PDQT** (~0.370-0.375 nm) [31, 37] would lead to more efficient hopping of charge carriers through the π-π stacks.

In addition to crystallinity, the attainment of uniform and well-interconnected thin film morphology has often been found to be crucial for facile charge hopping between crystalline domains. [34] To our surprise, the **PDBPyBT** thin films (~35 nm thick) on a SiO_2/Si substrate showed a very rough surface (the root-mean square roughness, RMS = 8.2 nm for the as-spun film) containing large domains of a few microns in size (Figure 2.4c), although this polymer is very soluble in the solvent used (chloroform) for spin coating. Large gaps of a few hundred nanometres between domains are clearly observed. The use of other solvents such as chlorobenzene, 1,2-dichlorobenzene, and tetrachloroethane could not improve the smoothness of the films. The poor thin film morphology was considered due to the rapid crystallization of this polymer upon evaporation of the solvent, which caused the films to crack. Annealing the polymer thin films at 150 °C and 200 °C increased the roughness of the thin films and resulted in smaller domains and more cracks. It should be noted that the thin film samples for XRD and AFM measurements were prepared by spin coating a polymer solution on bare SiO_2/Si substrates. The polymer thin films showed very poor adhesion to the SiO_2 surface that was modified using an organosilane agent such as dodecyltrichlorosilane (DDTS). Thus might also have been caused by the rapid crystallization of this polymer from solution.

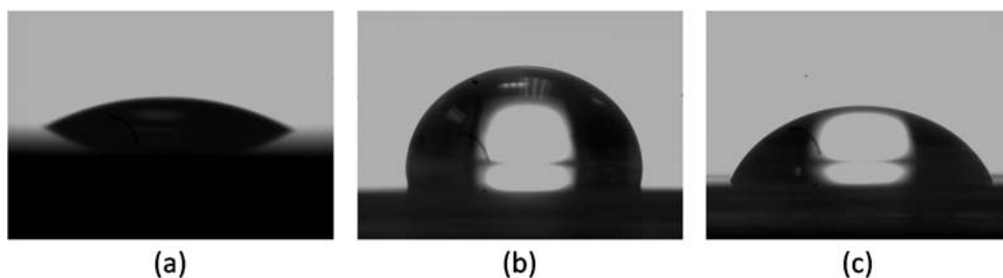

Figure 2.5 Photographs of water droplets on the surfaces of a bare SiO_2/Si substrate (a), DDTS-modified SiO_2/Si substrate, and gold film (c) by axisymmetric droplet shape analysis at 20 °C. The contact angles are (a) 28°, (b) 104°, and (c) 76°, indicating the wettability order of (a) > (c) > (b).

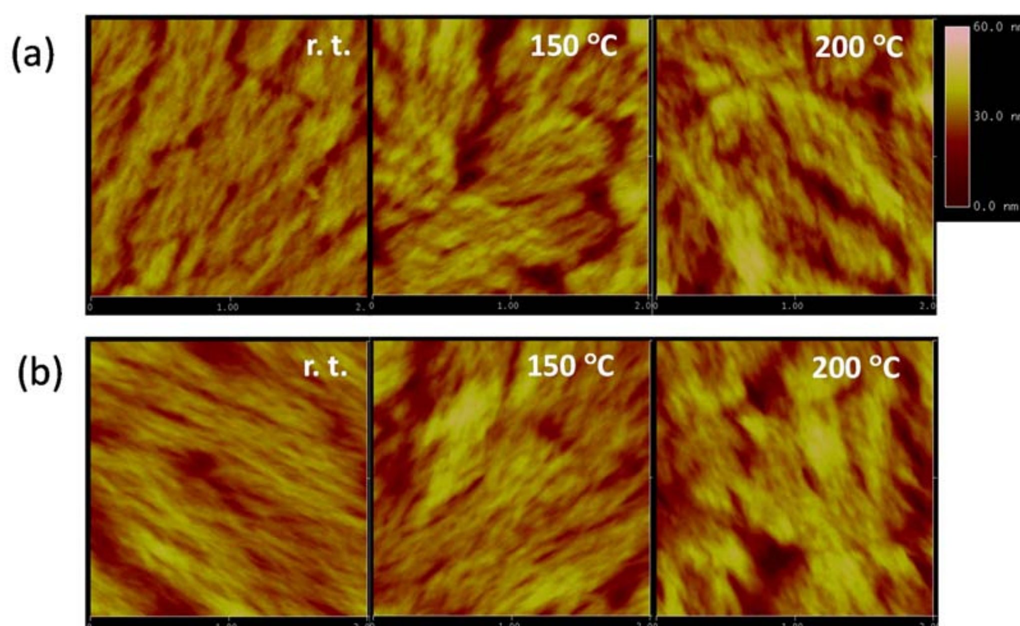

Figure 2.6. AFM images (2 μm × 2 μm each) of **PDBPyBT** thin films between gold source/drain contacts on (a) DDTS-modified bare SiO_2/Si substrates annealed at different temperatures: the root-mean square (RMS) roughness is 4.2 nm, 6.7 nm, and 6.7 nm for the as-spun (r.t.), 150 °C-annealed, and 200 °C-annealed thin films, respectively; (b) bare SiO_2/Si substrates annealed at different temperatures: the root-mean square (RMS) roughness is 5.0 nm, 6.2 nm, and 8.2 nm for the as-spun (r.t.), 150 °C-annealed, and 200 °C-annealed thin films, respectively.

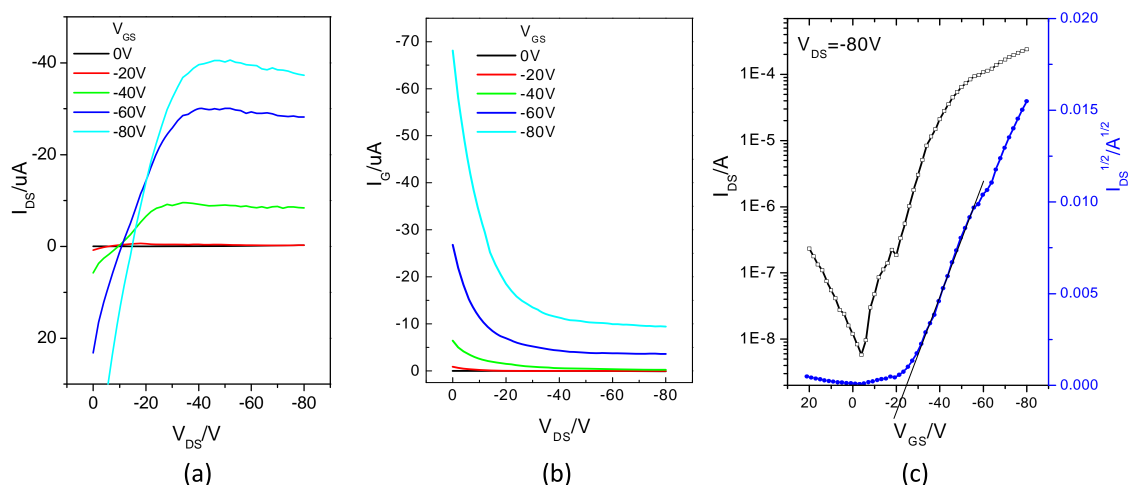

Figure 2.7. (a) Output, (b) leakage current through gate, and (c) transfer curves of a BGBC OTFT device using a **PDBPyBT** thin film annealed at 200 °C. Hole mobility: 0.46 $cm^2V^{-1}s^{-1}$.

PDBPyBT was tested in bottom-gate, bottom-contact (BGBC) OTFT devices using heavily n-doped SiO_2/Si wafer substrates, where the thermally grown SiO_2 layer (~200 nm) was used as the dielectric and Si as the gate electrode. After depositing gold source and drain contacts, the SiO_2 surface was modified with DDTS to minimize surface charge trapping. The patterned gold source-drain pairs (channel length L = 30 μm; channel width W = 1 mm) somewhat helped the adhesion of the polymer thin film to the substrate during the spin-coating process due to the better wettability of the gold film than the DDTS modified SiO_2/Si surface (Figure 2.5). The obtained polymer thin film (~35 nm) was annealed at 100, 150 or 200 °C. It was found that the **PDBPyBT** films on the DDTS modified SiO_2/Si surface with Au source/drain contacts improved slightly with less cracks (Figure 2.6). The annealed polymer thin films were then covered with a ~500 nm-thick PMMA encapsulation layer by spin coating a PMMA solution and drying at 80 °C. Unexpectedly all devices exhibited only p-channel hole transport behavior and no electron transport was observed although **PDBPyBT** has a rather low LUMO level. The 100 °C-annealed **PDBPyBT** films exhibited a hole mobility of up to 0.088 $cm^2V^{-1}s^{-1}$. The devices with 150 °C-annealed polymer films showed much

improved mobility of up to 0.25 $cm^2V^{-1}s^{-1}$. At a higher annealing temperature of 200 °C, the mobility increased further to 0.46 $cm^2V^{-1}s^{-1}$ (Figure 2.7). The output and transfer curves are very noisy and many nonworking devices were obtained. This is probably due to the cracking of polymer thin films observed in the AFM images and the poor contact of the polymer films with the DDTS-modified SiO_2 dielectric layer, both of which are originated from the spontaneous crystallization of this polymer from solution during spin coating.

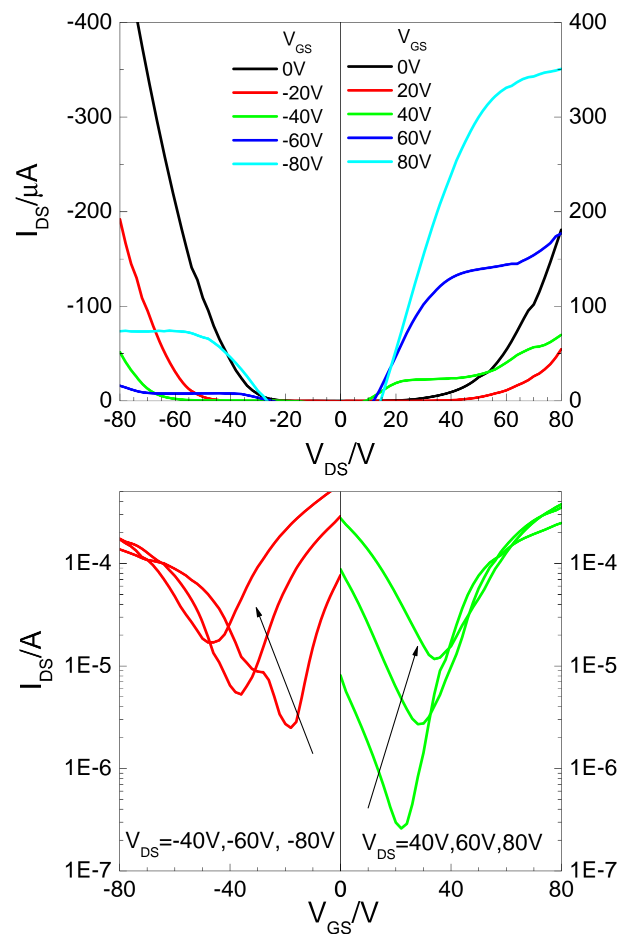

Figure 2.8. Output (top) and transfer (bottom) curves of a typical top-gate, bottom-contact (TGBC) OTFT device with a **PDBPyBT** thin film annealed at 100 °C. Device dimensions: channel length $L = 30$ μm; channel width $W = 1$ mm.

Table 2.1. OTFT performance of **PDBPyBT** thin films in TGBC and BGBC devices.

$T_{annl.}$ [a)] °C	TGBC				BGBC		
	μ_e, [b)] cm^{2}V^{-1}s^{-1}		μ_h, [c)] cm^{2}V^{-1}s^{-1}		μ_h, [d)] cm^{2}V^{-1}s^{-1}		I_{on}/I_{off} [e)]
	$\mu_{e\ max}$ [f)]	$\mu_{e\ ave}$ (STD [g)])	$\mu_{h\ max}$	$\mu_{h\ ave}$	$\mu_{h\ max}$	$\mu_{h\ ave}$	
100	6.30	4.54 (±1.27)	2.78	2.20 (±0.37)	0.088	0.072 (±0.014)	~10^3
150	3.91	3.50 (±0.40)	2.25	1.90 (±0.29)	0.25	0.23 (±0.022)	~10^4
200	3.32	2.30 (±0.62)	1.80	1.25 (±0.39)	0.46	0.39 (±0.046)	~10^4

Annealing temperature; [b)] Electron mobility measured at V_{DS} = 60 V; [c)] Hole mobility measured at V_{DS} = -60 V; [d)] Hole mobility measured at V_{DS} = -80 V; [e)] Current on to off ratio; [f)] The maximum mobility of the OTFT devices; [g)] The standard deviation.

To improve the interfacial properties between the dielectric and the **PDBPyBT** layer, a top-gate, bottom-contact (TGBC) device configuration was adopted. The bare SiO_2/Si wafer (without DDTS modification) patterned with gold source and drain contacts was used as the substrate in order to improve the adhesion of the polymer thin film (the bare SiO_2/Si substrate surface has much better wettability than the DDTS-modified SiO_2/Si substrate surface as shown in Figure 2.5). **PDBPyBT** thin films (~35 nm) were spin coated on the substrates and annealed at a certain temperature. **PDBPyBT** thin films on the bare SiO_2/Si substrates showed similar morphologies to those of the thin films deposited on the DDTS-modified substrates (Figure 2.6). Then a Cytop layer (~570 nm) was deposited by spin coating and dried at 100 °C as the top gate dielectric. Finally, a ~70 nm-thick aluminum layer was thermally deposited as the top gate electrode. The TGBC devices showed smoother output and transfer curves (Figure 2.8) compared to the BGBC devices. Interestingly all devices exhibited ambipolar charge transport performance. Very high average mobility values of

4.54 $cm^2V^{-1}s^{-1}$ for electrons and 2.20 $cm^2V^{-1}s^{-1}$ for holes were obtained for the 100 °C-annealed **PDBPyBT** films (Table 2.1). The best device showed electron and hole mobility values of 6.30 $cm^2V^{-1}s^{-1}$ and 2.78 $cm^2V^{-1}s^{-1}$, respectively. These are the highest mobility values reported for ambipolar polymer OTFTs so far. Especially the observed electron mobility of 6.30 $cm^2V^{-1}s^{-1}$ is the record high value achieved for polymer semiconductor OTFTs. The highly efficient charge transport performance observed for **PDBPyBT** is believed to be due to the high backbone coplanarity, very high crystallinity and close π-π stacking distance of this polymer. On the other hand, the low-lying LUMO level helped to achieve electron transport due to the reduced electron injection barrier from the gold contact and the stabilized charge carrier species. Compared to the BGBC devices, the dramatically improved performance for the TGBC devices is attributed primarily to the improved interface between the polymer semiconductor layer and the dielectric. Based on the poor adhesion of **PDBPyBT** films to the DDTS-modified SiO_2/Si surface, the contact between **PDBPyBT** and the hard SiO_2 interface is probably poor. On the other hand, Cytop is an amorphous polymer, which can fill the cracks and grain boundaries of the underlying **PDBPyBT** film to form a good interfacial contact. The observation of electron transport for the TGBC devices is also considered due to the use of Cytop as the dielectric layer. It was reported that passivation of the SiO_2/Si surface is crucial for charge transport, particularly for the electron transport, since the Si-OH groups are detrimental electron trapping sites.[80, 117, 118] In the BGBC devices, residual Si-OH may exist, which would suppress the electron transport,[80] while no electron traps exist in the dielectric material Cytop (a fluorinated polymer, which structure is shown in Figure 2.9) in the TGBC devices. Cytop is frequently used as the dielectric layer in top-gate OTFTs for ambipolar and n-type polymers for efficient electron transport.[59, 63, 80, 119] When the annealing temperature increased to 150 °C and 200 °C, the average electron/hole mobility values dropped to 3.50 $cm^2V^{-1}s^{-1}$/1.90 $cm^2V^{-1}s^{-1}$ and 2.30 $cm^2V^{-1}s^{-1}$/1.80 $cm^2V^{-1}s^{-1}$, respectively, which is most likely caused by the formation of more cracks in the polymer thin films with increasing temperature.

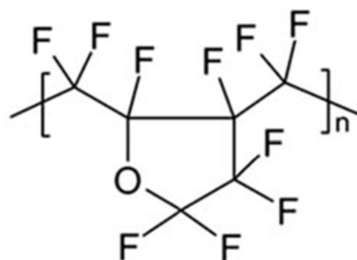

Figure 2.9. The chemical structure of Cytop.

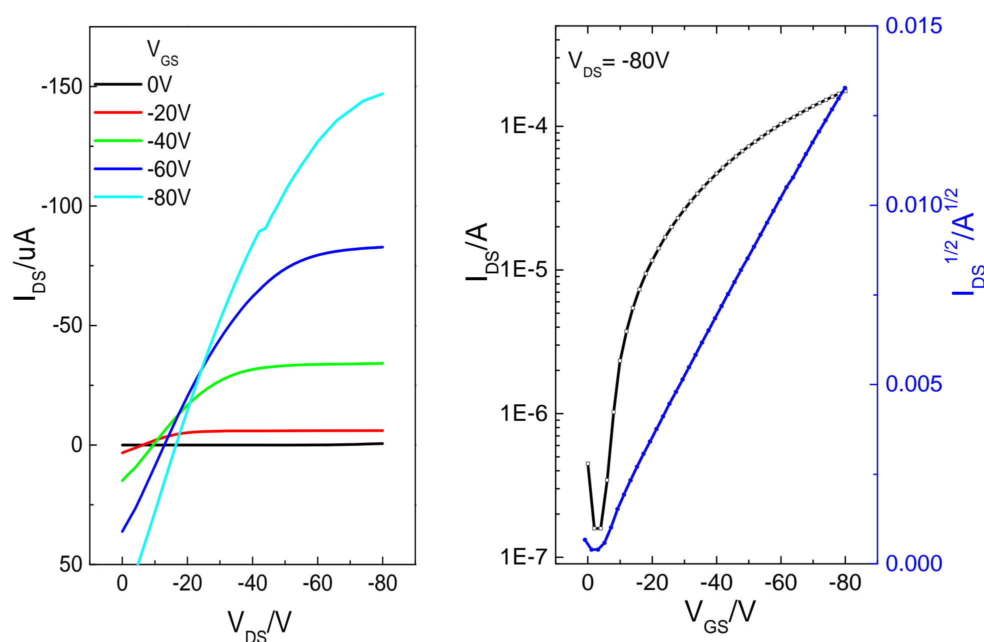

Figure 2.10. Output (left) and transfer (right) curves of a top-gate, bottom-contact (TGBC) OTFT device using a **PDQT** (structure shown in Scheme 2.1 in the main text) thin film annealed at 100 °C. Hole mobility: 1.01 $cm^2V^{-1}s^{-1}$.

As a comparison, **PDQT** in TGBC devices was evaluated. **PDQT** showed only p-type semiconductor performance with lower hole mobility of 0.55-1.01 $cm^2V^{-1}s^{-1}$ (Figure 2.10), 0.51-0.63 $cm^2V^{-1}s^{-1}$, and 0.32-0.52 $cm^2V^{-1}s^{-1}$ in 100 °C, 150 °C, and 200 °C-annealed thin films, respectively. On the other hand, in the BGBC devices, **PDQT** showed higher hole mobility up to 0.97-5.50 $cm^2V^{-1}s^{-1}$.[31, 37] These results suggest that the mobility of **PDBPyBT** is much higher than

that of **PDQT** in TGBC devices and that the performance of **PDBPyBT** may be further enhanced in the BGBC devices upon optimization of side chain and molecular weight[31, 36-39, 89-99] to improve the thin film quality. Although the charge transport performance of the analogous DBP polymer, PDBPBT (Scheme 2.1), has not previously been reported or studied in this study, a comparison of two counterpart copolymers of DBP and DBT with vinylene, PDBPV and PDBTV, were investigated previously in OTFTs.[110] It was found that the PDBPV exhibited p-channel characteristics in OTFTs with extremely low hole mobility of (4.9×10^{-7} $cm^2V^{-1}s^{-1}$) related tp that of PDBTV (0.17 $cm^2V^{-1}s^{-1}$). Based on our results, the new building block **DBPy** through substitution of phenyl in DBP or thienyl in DBT with pyridyl could greatly enhance the charge transport performance, particularly electron transport, due to the higher molecular ordering, shorter π-π distance and low-lying LUMO energy level.

2.3 Conclusion

In conclusion, a new electron accepting building block, **DBPy**, which consists of a DPP core flanked with two 2-pyridinyl substituents was reported. The 2-pyridinyl substituents could effectively reduce steric interaction with the DPP core, resulting in a highly coplanar structure, while the relatively electron-deficient nature of pyridine helps to reduce the LUMO energy level. A donor-acceptor copolymer of **DBPy** and bithiophene, **PDBPyBT**, was synthesized, which showed high crystallinity and a very short π-π stacking distance of 0.36 nm. High ambipolar charge transport performance with a record high electron mobility value of 6.30 $cm^2V^{-1}s^{-1}$ was achieved in OTFT devices at a mild annealing temperature of 100 °C. Our results demonstrate that **DBPy** is a promising new building block for polymer semiconductors for OTFTs and other applications. Other donors will be tested for copolymerization with **DBPy** to achieve high mobility polymer semiconductors.

2.4 Experimental

2.4.1 Materials and Instrumentation

Cytop (a perfluorinated amorphous resin solution) was purchased from AGC Chemicals. All other materials were purchased from commercial sources and used without further purification. Synthesis and properties of **PDQT** (M_n = 40 kDa; PDI = 3.22) were reported previously. [37] UV-Vis spectra were recorded on a Thermo Scientific GENESYS™ 10 Spectrophotometer. NMR data were collected on a Bruker DPX 300 MHz spectrometer and the chemical shifts were reported relative to tetramethylsilane (TMS, δ = 0ppm). Reflective XRD diagrams of polymer thin films (~30-40 nm) spin coated on bare SiO_2/Si substrates were obtained on a Bruker D8 Advance powder diffractometer using standard Bragg-Brentano geometry with Cu Kα1 radiation (λ = 1.5406 Å). Transmission XRD measurements were carried out on a stack of polymer thin films [116] using Bruker Smart Apex2 CCD with Mo Kα radiation (λ = 0.71073 Å). Atomic force microscopic (AFM) images were obtained on polymer thin films (~30-40 nm) spin coated on bare SiO_2/Si substrates with a Dimension 3100 Scanning Probe Microscope. Cyclic voltammetry (CV) measurements of polymer thin films were conducted on a Digi-Ivy DY2111 Potentiostat using an Ag/AgCl reference electrode, a Pt wire counter electrode, and a Pt foil working electrode in 0.1 M tetrabutylammonium hexafluorophosphate in dry acetonitrile at a scan rate of 50 mVs^{-1}. Ferrocene, which has a highest occupied molecular orbital (HOMO) of -4.8 eV,[120] was used as a reference. A Malvern 350 high-temperature gel-permeation chromatography system was used to measure the molecular weights of the polymer using 1,2,4-trichlorobenzene as an eluent with polystyrene as standards at column temperature of 140 °C.

Geometry optimization of 2,5-dimethyl-3,6-di(thiophen-2-yl)pyrrolo[3,4-*c*]pyrrole-1,4(2*H*,5*H*)-dione (DBT-Me), 2,5-dimethyl-3,6-diphenylpyrrolo[3,4-*c*]pyrrole-1,4(2*H*,5*H*)-dione (DBP-Me), and 2,5-dimethyl-3,6-di(pyridin-2-yl)pyrrolo[3,4-*c*]pyrrole-1,4(2*H*,5*H*)-dione (**DBPy**-Me) were

performed with density functional theory (DFT) calculation using the B3LYP hybrid functional [121] with the 6-31G basis set on the Shared Hierarchical Academic Research Computer Network (SHARCNET) of Canada. Molecular orbital shapes and energies in the main text were obtained by conducting calculations for the optimized structures. Orbital pictures were prepared with GaussView 5.0 software [122] and all calculations were performed with Gaussian 09W package. (Æ. Frisch, *Gaussian 09W Reference*, Gaussian, Inc., Wallingford, CT, 2009)

2.4.2 Synthesis

*3,6-Di(5-bromopyridin-2-yl)pyrrolo[3,4-c]pyrrole-1,4(2H,5H)-dione (**DBPy**Br-H)*

5-bromopyridine-2-carbonitrile (6.19 g, 34 mmol) was added to a solution of potassium tert-butoxide (4.14 g, 37 mmol) in 2-methyl-2-butanol (70mL) at room temperature and the mixture was then heated to 110 °C. Diethyl succinate (2.61 g, 15 mmol) in 2-methyl-2-butanol (30 mL) was added drop-wise over 1 hr. The reaction mixture was stirred for 20 hr at 100 °C before cooling down to room temperature. 100 mL of water were added to the mixture and the solid was filtered off, washed with methanol and water, and dried at 100 °C in vacuum oven to give the titular product (3.58 g, 53.5%). The product is insoluble in common NMR solvents and was used in the next step without further purification.

*Synthesis of 3,6-di(5-bromopyridin-2-yl)-2,5-bis(2-octyldodecyl)pyrrolo[3,4-c]pyrrole-1,4(2H,5H)-dione (**DBPy**Br-20)*

DBPyBr-H (1.2 g, 2.7 mmol), potassium carbonate (1.0 g, 7.2 mmol), and 2-octyldodecyl iodide (3.6 g, 8.8 mmol) were stirred in DMF (30 mL) for 18 hr at 70 °C under argon. After cooling down to room temperature, the mixture was poured into 50 ml of water and extracted with ethyl acetate. The combined organic phase was dried over anhydrous Na_2SO_4 and filtered. After removing solvent in vacuo, the obtained crude product was purified by column chromatography on silica gel using

toluene as the eluent to give the pure target product. Yield: 690 mg (25.4%). ^{1}H NMR (Figure 2.11) (300 MHz, $CDCl_3$) δ 8.93 (d, J = 8.5 Hz, 2H), 8.74 (d, J = 2.1 Hz, 2H), 8.01 (dd, J = 8.6, 2.3 Hz, 2H), 4.28 (d, J = 7.3 Hz, 4H), 1.61 (m, 2H), 1.24 (m, 64H), 0.93-0.81 (m, 12H). ^{13}C NMR (Figure 2.12) (75 MHz, $CDCl_3$) δ 162.36, 149.98, 145.95, 144.84, 139.57, 128.34, 122.45, 111.31, 76.47, 46.18, 38.10, 31.79, 31.33, 29.89, 29.55, 29.47, 29.22, 26.26, 22.56, 14.00.

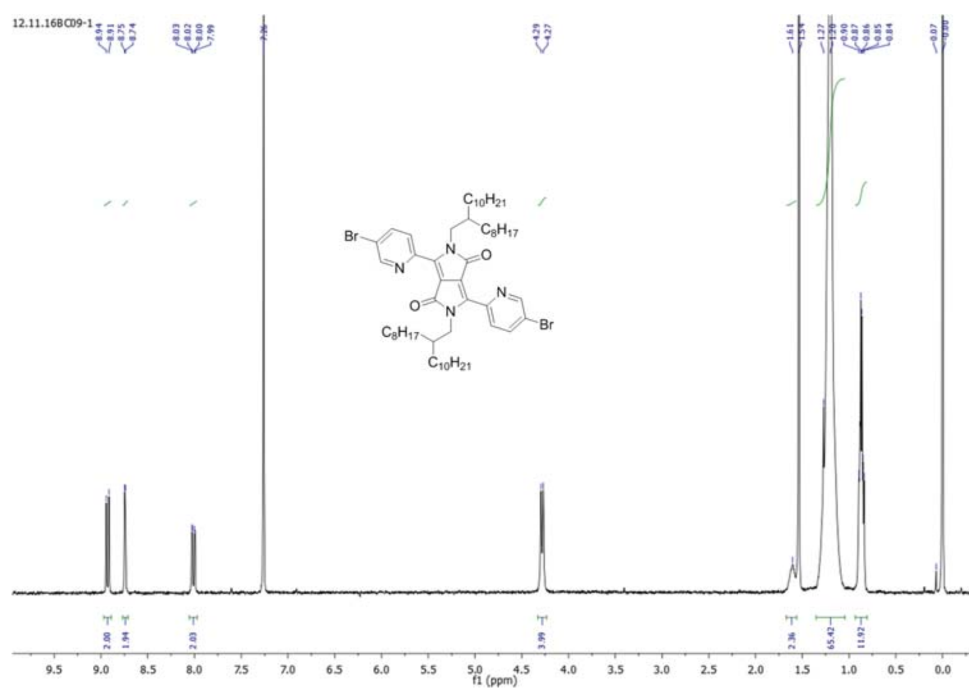

Figure 2.11. The 300 MHz ^{1}H NMR spectra of **DBPy**Br-20.

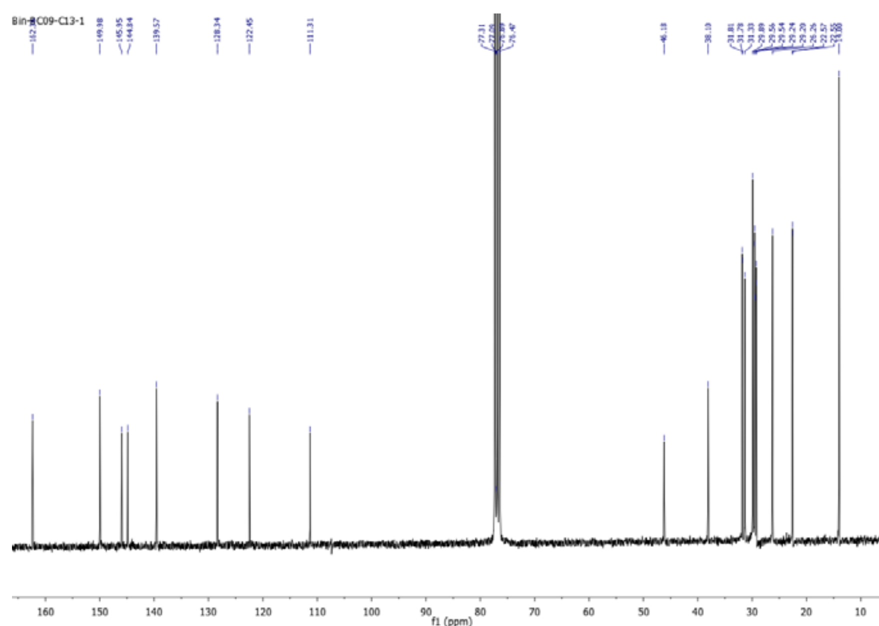

Figure 2.12. The 75 MHz ^{13}C NMR spectrum of **DBPyBr-20**.

*Synthesis of poly(2,5-bis(2-octyldodecyl)-3,6-di(pyridin-2-yl)-pyrrolo[3,4-c]pyrrole-1,4(2H,5H)-dione-alt-2,2'-bithiophen) copolymer (**PDBPyBT**)*

To a 50 mL dry flask was added **DBPy**Br-20 (0.2021 g, 0.2 mmol), 5,5'-bis(trimethylstannyl)bithiophene (0.0988 g, 0.2 mmol) and tri(*o*-tolyl)phosphine (5.6 mg, 9 mol %, 0.018 mmol). After degassing and filling with argon for 3 times, tris(dibenzylideneacetone)-dipalladium (4.0mg, 0.0044 mmol) and anhydrous chlorobenzene (20 ml) was added under argon. The mixture was stirred for 72 h at 130 ºC, cooled down to room temperature and poured into 100mL of methanol. The precipitated product was collected by filtration and subjected to consecutive Soxhlet extraction with acetone, hexane and chloroform. The final chloroform fraction was dried to obtain the target polymer. Yield: 189 mg (93.0%). GPC: M_n = 26.3 kDa; PDI = 3.56. λ_{max}: 683 nm (in chloroform); 695 nm (in thin film).

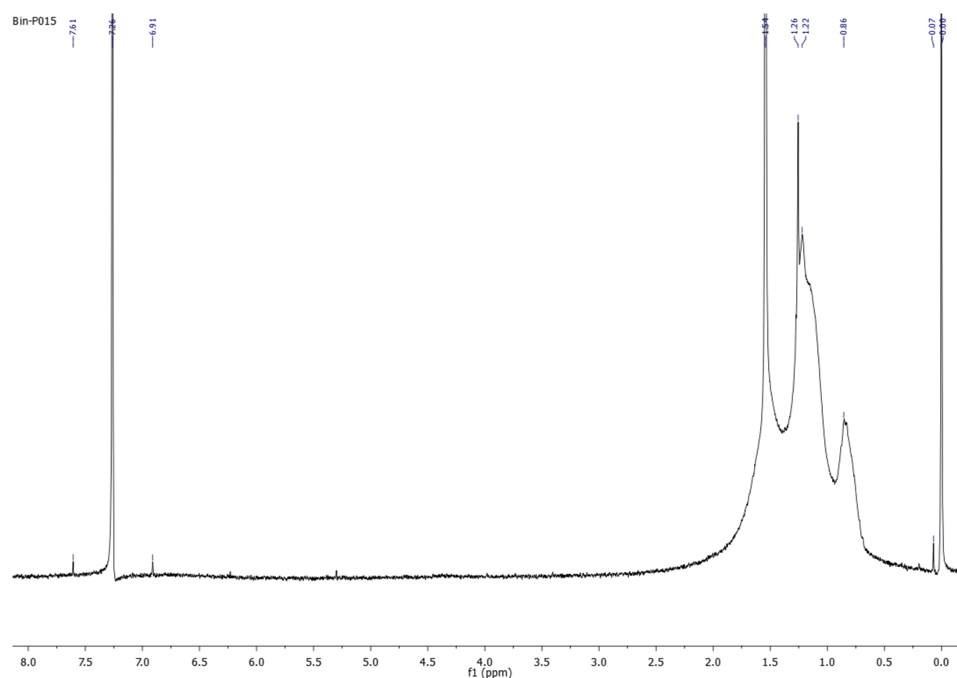

Figure 2.13. The 300 MHz ^{1}H NMR spectrum of **PDBPyBT**.

2.4.3 Fabrication and Characterization of OTFT Devices

2.4.3.1 BGBC OTFT Devices

Heavily n-doped Si wafer with a 200 nm-thick thermally grown SiO_2 top layer was used as the substrate. The silicon operates as the gate electrode and SiO_2 as the gate dielectric. The gate dielectric layer has a capacitance of ∼17 nF cm^{-2}. Gold source and drain patterns were deposited by thermal evaporation on the SiO_2 layer using a conventional lithography technique. The patterned substrate was cleaned with O_2 plasma, acetone and isopropanol sequentially. The substrate was modified with dodecyltrichlorosilane (DDTS) in toluene (10 mg mL^{-1}) at 60 °C for 20 min, followed by washing with toluene and drying under a nitrogen flow. A polymer semiconductor film (~35 nm) was deposited on the substrate by spin-coating a 10 mg mL^{-1} polymer solution in chloroform at 3000 rpm for 90 s. After annealing on a hotplate in a glove box at 100, 150 or 200 °C for 10 min, the devices were encapsulated with a 500 nm-thick poly(methyl methacrylate)

(PMMA) layer by spin-coating a PMMA solution in butyl acetate (8 wt %) at 3000 rpm for 60 s, and dried at 80 °C for 30 min on a hot plate under nitrogen. The devices were characterized in air in the absence of light using an Agilent 4155C Semiconductor Parameter Analyzer. The carrier mobility was calculated from the slope of the $(I_{DS})^{1/2}$ versus V_{GS} plot according to the equation, $I_{DS} = \mu C_i W/2L (V_{GS}-V_{TH})^2$, in the saturated regime, where μ is the carrier mobility in saturation regime, I_{DS} is the drain current, L and W are the channel length (30 μm) and channel width (1000 μm), C_i is the gate dielectric layer capacitance per unit area, V_{GS} and V_{TH} are the gate voltage and threshold voltage, respectively.

2.4.3.2 TGBC OTFT Devices

A Si wafer with a 300 nm-thick SiO_2 top layer with thermally evaporated gold source and drain electrodes was used as the substrate for the TGBC devices. The SiO_2 layer was not modified with DDTS. The polymer semiconductor film was deposited by spin-coating a polymer solution in chloroform (10 mg mL^{-1}), followed by annealing on a hotplate in nitrogen for 10 min. Then a Cytop layer (~570 nm with Ci = 3.2 nF cm^{-2}) was deposited as the gate dielectric on the polymer semiconductor layer by spin-coating a Cytop solution at 2000 rpm, flowed by drying on a hotplate at 100 °C for 30 min. Finally, a 70 nm-thick Al layer was deposited as the gate electrode by thermal evaporation. Characterization of the devices was conducted similarly as described for the bottom-gate, bottom-contact OTFT devices.

Output and transfer characteristics of OTFTs in Chapter 2 are included in the Appendix.

Chapter 3. Conversion of PDBPyTT Ambipolar Polymer into Unipolar n-Type and p-type Semiconductors in Organic Thin Film Transistors

Part of this chapter is published in B. Sun, W. Hong, H. Aziz, Y. Li, *Polym. Chem.* **2015**, *6*, 938

Dr. Hong conducted all CV and UV-Vis measurements; Sun carried out the polymer synthesis and all other characterizations.

3.1 Introduction

Using the promising **DBPy** acceptor discovered in Chapter 2, it was copolymerized with a thieno[3,2-*b*]thiophene (TT) donor unit, which is a well-known building block for high performance p-type polymers.[30, 33, 123, 124] In fact it is better than bithiophene in some cases, due to the large overlap area for intermolecular charge carrier hopping. The resulting polymer, **PDBPyTT**, showed typical ambipolar transport performance, which is suitable for complementary logic. However, complementary logic based on ambipolar semiconductors typically show a substantial OFF-state current, which will result in high standby power consumption and serious losses in device performance.[125] The exhibition of ambipolar charge transport for many D-A polymers is mainly due to the presence of both the electron donor unit, which raises the HOMO level, and the electron acceptor unit, which lowers the LUMO level. The consequently narrowed band gap reduces the injection barriers for both electrons and holes when the source electrode in an OTFT has a Fermi level lying around the middle of the band gap of the polymer. When the LUMO level is adequately low (≤ -4 eV)[79, 126] for stable electron transport, the polymer may exhibit ambipolar transport performance.

It would be feasible to realize electron-only charge transport, i.e. unipolar n-type performance, for an ambipolar polymer, if the contact electrode with a sufficiently high Fermi level close to or

higher than the LUMO of the polymer semiconductor is used to enhance electron injection and suppress hole injection. In contrast, a contact electrode with a low Fermi level would be able to selectively inject holes rather than electrons to the semiconductor and yield unipolar p-type semiconductor behavior. Surface modification of the source and drain contacts with MoO_3,[127-129] Cs salts,[81] organic thiols,[82] and polyethylenimines[88] has been used to facilitate either electron or hole injection for small molecule or polymer semiconductors in OTFTs. However, conversion of an ambipolar organic semiconductor to a unipolar n-type or p-type semiconductor using the electrode modification strategy has not been demonstrated prior to this work. **PDBPyTT** was synthesized to demonstrate the feasibility that an ambipolar polymer semiconductor being readily converted to either a unipolar n-type semiconductor or a unipolar p-type semiconductor in OTFTs, by tuning the Fermi level of the source and drain contacts through simple surface modification.

3.2 Results and Discussion

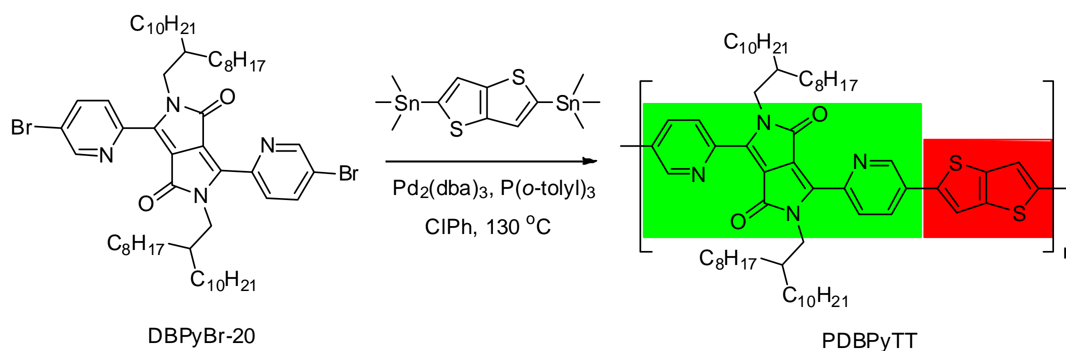

Scheme 3.1. Synthetic route to **PDBPyTT** via Stille coupling polymerization.[130-132]

The new D-A polymer **PDBPyTT** (Scheme 3.1) is composed of a building block **DBPy**[133, 134] containing a DPP core flanked by two 2-pyridinyl units. The use of the more electron deficient pyridinyl, rather than the electron rich thienyl that is employed in other high mobility DPP polymers,enables a lower LUMO energy level to facilitate electron injection and transport. A thieno[3,2-*b*]thiophene (TT) unit, which is a well-known building block for high performance p-

type polymers,[30, 33, 123, 124] is selected as an electron donor to achieve high hole mobility. **PDBPyTT** containing long branched 2-octyldodecyl side chains was conveniently synthesized via Stille coupling polymerization of the dibromo **DBPy** co-monomer (**DBPy**Br-20)[134] with 2,5-bis(trimethylstannyl)-thieno[3,2-*b*]thiophene according to the route depicted in Scheme 2.1. The number average molecular weight (M_n) and the polydispersity index (PDI) of **PDBPyTT** are 24,500 and 3.00, respectively, as determined by high-temperature gel-permeation chromatography (HT-GPC) using 1,2,4-trichlorobenzne as an eluent and polystyrene as standards.

The HOMO level of **PDBPyTT** was obtained using cyclic voltammetry to be -5.7 eV with ferrocene as a reference (E_{HOMO} of ferrocene = -4.8 eV),[120] while the LUMO level was calculated to be -4.0 eV from the HOMO and the optical band gap (ca. 1.7 eV). These HOMO and LUMO levels of **PDBPyTT** are favored for our purpose since they would enable stable hole ($E_{HOMO} < -5$ eV)[135] and electron ($E_{LUMO} \leq -4$ eV)[79, 126] transport. When Au is used as the source and drain electrodes in an OTFT with **PDBPyTT** as the channel semiconductor, the barrier to both electron and hole injection from Au (with a work function of 4.7-5.1 eV)[136, 137] are quite small (Figure 3.1). Therefore, **PDBPyTT** should exhibit ambipolar charge transport behavior in an OTFT device when Au is used as the source and drain electrodes.

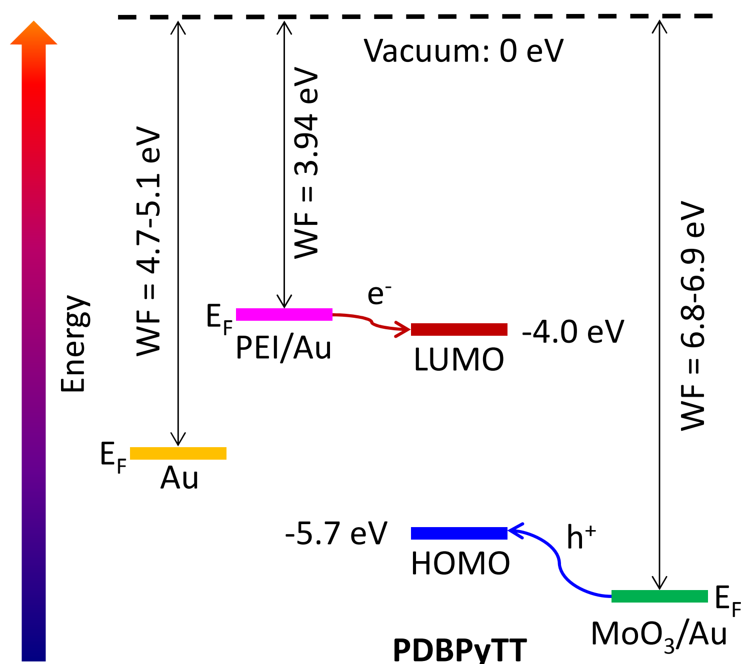

Figure 3.1. Energy diagrams of **PDBPyTT**, Au, PEI-modified Au, and MoO_3-modified Au, where WF and E_F are work function and Fermi energy level, respectively. WF values of Au, PEI/Au (PEI modified Au), and MoO_3 are taken from the literature.

Charge transport performance of **PDBPyTT** was evaluated in top-gate bottom-contact OTFT devices consisting of silicon wafer with a 300 nm-thick insulating SiO_2 layer as the substrate. Au source and drain pairs were deposited on top of the SiO_2 layer using a conventional photolithography technique. A solution of **PDBPyTT** in chloroform was spin-coated on the substrate and the resulting polymer thin film (~50 nm) was annealed at a certain temperature in a glove box filled with nitrogen. A Cytop solution was then spin-coated on top of the **PDBPyTT** layer, followed by baking at 100 °C for 30 min to form a ~570 nm-thick dielectric layer. Finally a ~70 nm-thick Al layer was thermally evaporated on top of the Cytop layer to complete device fabrication. The devices were characterized in air using an Agilent I-V Semiconductor Parameter Analyzer. As expected, all devices showed typical ambipolar charge transport performance (Table 3.1). Devices with the 100 °C-annealed **PDBPyTT** films exhibited electron mobility of up to 1.74

$cm^2V^{-1}s^{-1}$ and hole mobility of up to 0.35 $cm^2V^{-1}s^{-1}$. For the 150 °C-annealed polymer thin films, the maximum electron and hole mobilities significantly improved to 3.31 $cm^2V^{-1}s^{-1}$ and 2.04 $cm^2V^{-1}s^{-1}$, respectively. When the annealing temperature was increased to 200 °C, the maximum electron mobility slightly improved to 3.36 $cm^2V^{-1}s^{-1}$, while the maximum hole mobility dropped to 1.26 $cm^2V^{-1}s^{-1}$. Figure 3.2 shows the output and transfer curves of a typical OTFT device with a **PDBPyTT** film annealed at 150 °C. Based on these device data, it seems that **PDBPyTT** has similar hole transport performance to, but poorer electron transport capability than **PDBPyBT** in Chapter 2. The less efficient charge transport property of **PDBPyTT** is probably due to its less ordered molecular organization as discussed later. **PDBPyTT** was also tested in a bottom-gate bottom-contact (BGBC) device configuration. However, hole-only transport with much lower mobilities (~10^{-2} $cm^2V^{-1}s^{-1}$) was obtained, most likely due to the poor interfacial property between the polymer film and the dielectric layer. Similar phenomenon was observed for **PDBPyBT**,

Table 3.1 Summary of device performance of OTFTs with **PDBPyTT**.

$T_{annl.}$ [a)] °C	Electrode Modification	$\mu_{e,}$ [b)] $cm^2V^{-1}s^{-1}$		$\mu_{h,}$ [c)] $cm^2V^{-1}s^{-1}$		I_{on}/I_{off} [g)]
		$\mu_{e,max}$ [d)]	$\mu_{e,ave}$ [e)] (STD[f)])	$\mu_{h\ max}$ [d)]	$\mu_{h,ave}$ [e)] (STD[f)])	
100	None	1.74	1.43 (0.35)	0.35	0.28 (0.094)	-
150	None	3.31	2.65 (0.50)	2.04	1.51 (0.40)	-
200	None	3.36	3.11 (0.31)	1.26	1.22 (0.049)	-
150	PEI (4.7 nm)	2.14	1.77 (0.33)	-	-	~10^3-10^4
150	PEI (4.3 nm)	1.77	1.39 (0.35)	-	-	~10^2-10^3

150	PEI (3.9 nm)	2.16	1.72 (0.40)	-	-	~10^2-10^3
150	PEI (3.8 nm)	1.61	1.30 (0.27)	-	-	~10^2-10^3
150	PEI (2.9 nm)	2.38	1.85 (0.57)	-	-	~10^3
150	PEI (2.2 nm)	1.82	1.49 (0.36)	0.068	0.05 (0.016)	-
150	PEI (1.5 nm)	1.66	1.42 (0.23)	0.20	0.072 (0.076)	-
150	MoO_3(4.0 nm)	-	-	2.89	2.40 (0.47)	~10^4-10^6
150	MoO_3(3.0 nm)	0.13	0.048 (0.070)	1.75	1.56 (0.26)	~10^4-10^5
150	MoO_3(2.6 nm)	0.11	0.054 (0.044)	2.14	1.54 (0.46)	~10^4-10^5
150	MoO_3(2.2 nm)	0.20	0.093 (0.073)	1.07	0.79 (0.23)	~10^4
150	MoO_3(2.0 nm)	0.28	0.11 (0.11)	1.16	0.77 (0.39)	~10^3
150	MoO_3(1.8 nm)	0.19	0.094 (0.064)	0.63	0.49 (0.14)	~10^3
150	MoO_3(1.4 nm)	1.67	1.03 (0.68)	2.53	1.56 (0.97)	-
150	MoO_3(1.2 nm)	4.55	2.11 (1.63)	2.38	1.26 (0.74)	-

a) Annealing temperature; [b)] Electron mobility measured at V_{DS} = 80 V; [c)] Hole mobility measured at V_{DS} = -80 V; [d)] The maximum mobility of the FET devices; [e)] The average mobility obtained from at least five devices; [f)] The standard deviation; [g)] Current on to off ratio.

Next, we attained the unipolar electron transport performance in this polymer by increasing the Fermi level of the contact electrodes. Since thermal annealing at 150 °C afforded well-balanced and high electron and hole mobilities (Table 3.1), we chose this annealing temperature for the subsequent investigations. A previous study demonstrated that even polymer semiconductors that are conventionally considered to be p-type such as regioregular poly(3-hexylthiophene) (P3HT) could show pronounced electron transport behavior once a low work function metal Ca was used

as the source and drain contacts.[138] However, low work function metals are generally highly reactive to the moisture and oxygen in air and are not suitable for the fabrication and application of OTFT devices. Recently, a "universal" approach to reducing the work function of conductors was reported by Zhou *et al*.[88] They used air-stable commercially available branched polyethylenimine (PEI) and ethoxylated polyethylenimine (PEIE) to modify the conductor surface. The work function of many conductor materials can be reduced significantly with an ultrathin PEI or PEIE layer (1-10 nm) due to the molecular dipole moments of the amine groups in these insulating polymers and the charge transfer interaction between the amine groups and the conductor surface. For instance, the work function of the surface-modified Au thin films with PEI and PEIE was reduced to 3.94 eV and 3.90 eV, respectively. The mobility of an n-type polymer semiconductor, **P(NDI2OD-T2) (13)** (Figure 1.14) was improved from 0.04 $cm^2V^{-1}s^{-1}$ to 0.1 $cm^2V^{-1}s^{-1}$ after the Au contacts were modified with PEIE, owing to the lower electron injection barrier.[88] This recent finding inspired us to explore the possibility of using this approach to reduce the work function (or increase the Fermi level) of the source and drain electrodes not only to promote electron injection, but also to suppress the hole transport characteristics of our ambipolar polymer **PDBPyTT** in OTFTs. A similar device configuration (Figure 3.2b) as that used for the ambipolar OTFTs (Figure 3.2a) except that a PEI layer on top of the source and drain electrodes (as well as the exposed SiO_2 surface in the channel region) was added. The raised Fermi level of the PEI-modified Au electrodes (-3.94 eV) would reduce the electron injection barrier, but cause a large hole injection barrier (E_F (Electrode) – E_{HOMO} (**PDBPyTT**) = ~1.76 eV) from the electrode to **PDBPyTT** (Figure 3.1). The PEI layer was deposited by spin-coating a PEI solution on the SiO_2/Si substrate pre-patterned with Au source and drain pairs, followed by baking at 100 °C for 10 min, before depositing the **PDBPyTT** layer. The concentration of PEI was varied to investigate the effect of the PEI layer thickness on the device performance. As clearly seen in Figure 3.3, the average hole mobility dropped precipitously from 1.51 $cm^2V^{-1}s^{-1}$ for the devices without a PEI layer to 0.072 $cm^2V^{-1}s^{-1}$ for the devices with a 1.5 nm-thick PEI layer. When the PEI layer thickness increased to 2.9 nm,

the ability to transport hole completely vanished and the devices exhibited unipolar n-channel performance. The average electron mobility is in the range between 1.30 $cm^2V^{-1}s^{-1}$ and 1.89 $cm^2V^{-1}s^{-1}$ for all unipolar n-type OTFT devices with a PEI layer thickness ranging from 2.9 nm to 4.0 nm (Table 3.1). The highest electron mobility of 2.38 $cm^2V^{-1}s^{-1}$ was achieved for an n-channel device with a 2.9 nm-thick PEI layer. This electron mobility is among the best values for n-type polymer OTFTs reported so far. [59, 60, 63, 80, 91, 100]

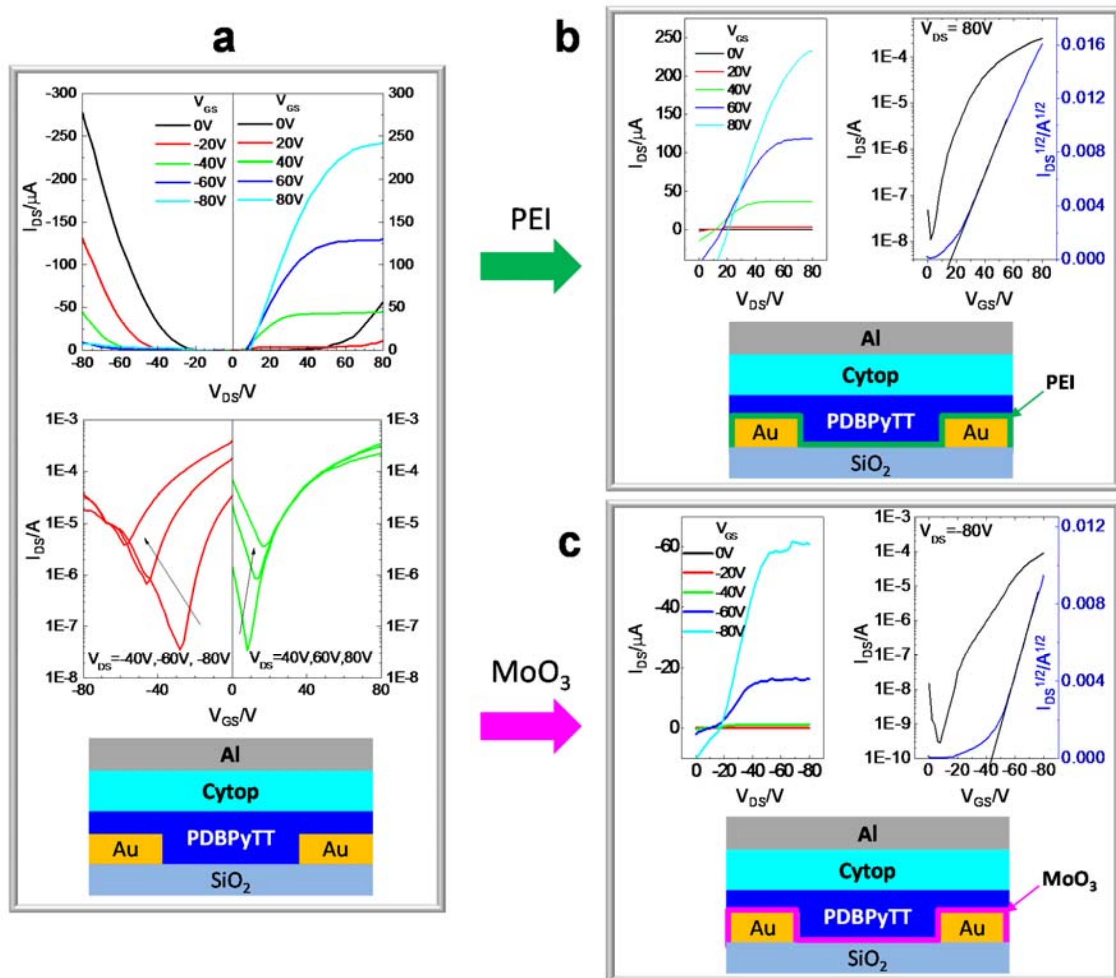

Figure 3.2. a) Output (top) and transfer (middle) curves of a typical ambipolar OTFT device (bottom) under hole and electron enhancement modes; b) Output (top, left) and transfer (top, right) curves of a typical OTFT device (bottom) with a PEI interlayer between the Au contacts and the **PDBPyTT** layer; c) Output (top, left) and transfer (top, right) curves of a typical OTFT device with a MoO_3 interlayer between the Au contacts and

the **PDBPyTT** layer. The **PDBPyTT** thin films (~50 nm) in these devices were annealed at 150 °C for 15 min in nitrogen.

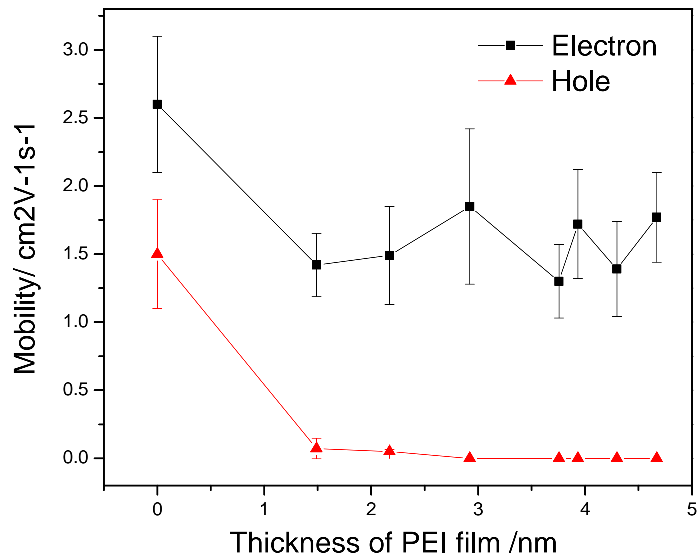

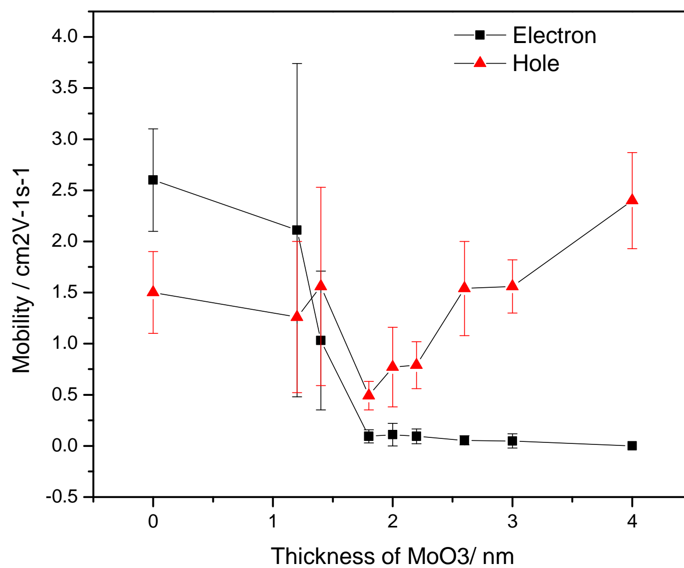

Figure 3.3. The dependences of electron and hole mobilities on the thickness of the PEI layer (top) and the MoO_3 layer (bottom). Mobility values were obtained from at least 5 OTFT devices for each data point.

Recently, metal oxides have been investigated extensively to act as a thin interlayer between the electrode and the semiconductor to align the energy levels for efficient hole or electron injection in organic light emitting diodes (OLEDs), organic photovoltaics (OPVs), and OTFTs. [127-129, 139, 140] In this study, MoO_3 was chosen as the surface modification layer to facilitate hole injection from the electrode to the semiconductor **PDBPyTT**, while building up a high electron injection barrier (E_{LUMO} (**PDBPyTT**) – E_F (MoO_3) = ~ 2.8~2.9 eV), since MoO_3 has a high work function of ~ 6.8~6.9 eV (Figure 3.1).[140-142] MoO_3 was used to modify the source and drain electrodes in OTFTs with p-type organic semiconductors such as pentacene to reduce the contact resistance for improved device performance.[127-129] During a parallel study on polymer solar cells, MoO_3 was used as an interlayer between a blend layer containing a DPP-based polymer donor and a PCBM (phenyl-C_{61}-butyric acid methyl ester) acceptor and an ITO electrode to successfully realize the hole-only charge transport characteristic of a diode device.[53] In this study, a thin MoO_3 layer was thermally evaporated on top of the SiO_2/Si substrate having the Au source and drain patterns. The **PDBPyTT**, Cytop, and Al layers were then sequentially deposited as described above to complete the device fabrication (Figure 3.2c). As shown in Figure 3.3 (and Table 3.1), the average electron mobility of the devices dropped rapidly from 2.65 $cm^2V^{-1}s^{-1}$ to 0.1 $cm^2V^{-1}s^{-1}$ as the MoO_3 layer thickness increased from 0 nm to 1.8 nm. When the MoO_3 layer thickness reached 4 nm, electron transport characteristic was no longer observed. The average hole mobility decreased with an increase in the MoO_3 layer thickness from 0 nm to 1.8 nm. Interestingly, the hole mobility increased steadily as the MoO_3 layer thickness further increased from ~2 nm to 4 nm. The highest hole mobility for the unipolar p-type OTFTs is 2.89 $cm^2V^{-1}s^{-1}$ achieved by a device with a 4 nm-thick MoO_3 layer.

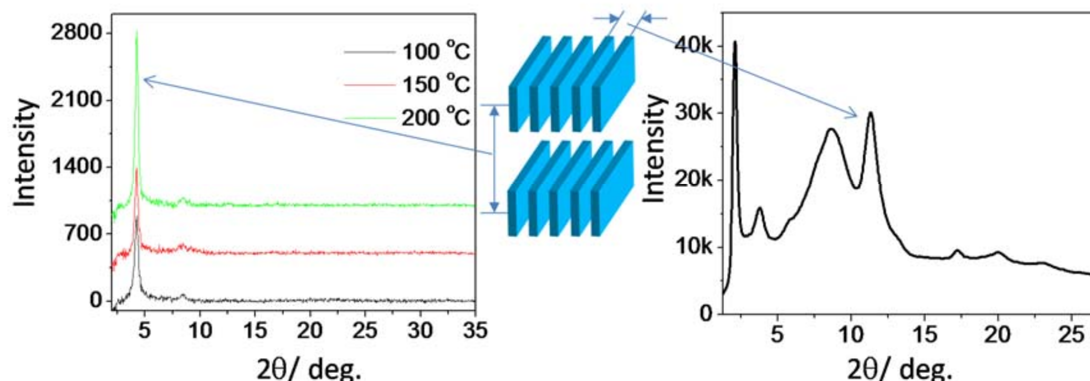

Figure 3.4. Left: The reflection XRD diagrams of **PDBPyTT** thin films (~50 nm thick) spin-coated on SiO_2/Si substrates and annealed at difference temperatures. Right: The transmission XRD diagram of a stack of **PDBPyTT** thin films sandwiched between two Mylar substrates. The inserted graph in the middle represents the lamellar crystal structure with edge-on chain orientation in the polymer films.

To gain insight into the high charge transport performance observed for this new D-A polymer **PDBPyTT**, X-ray diffractometry (XRD) was utilized to examine the polymer chain packing, since the crystal structure has a huge impact on the charge transport performance of polymers.[34] The **PDBPyTT** thin films spin-coated on the SiO_2/Si substrates clearly showed a primary peak at 2θ = 4.23°, which corresponds to a d-spacing of 2.09 nm. A small peak at 2θ = 8.34° is also observed, which is assigned to the secondary reflection peak (Figure 3.4). These XRD results indicate that the polymer chains in the thin films adopt a layer-by-layer lamellar packing motif,[115] which has been observed for most crystalline conjugated polymers.[34, 143] No reflection peak is observed at ~20°, which represents the typical π-π stacking distance of ~0.3-0.4 nm. Therefore, the polymer chains in the thin films likely adopted an edge-on packing pattern (Figure 3.4), which is considered to be most favored for the charge transport in an OTFT device. [114]

To elucidate the π-π stacking distance between polymer main chains, polymer thin films were measured using a transmission XRD mode. As revealed in the diffractogram in Figure 3.4 (right),

a strong peak at 2θ = 11.34° is observed, which is corresponding to the π-π distance of 0.36 nm. Such a close π-π distance would facilitate the charge hopping through the stacks.

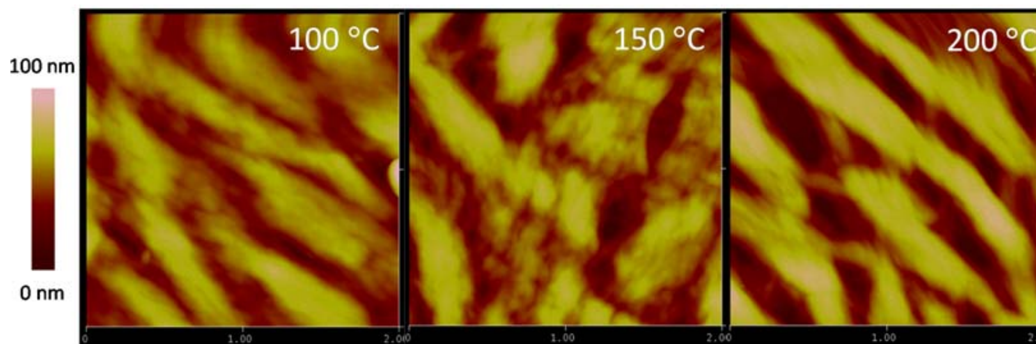

Figure 3.5. AFM images (2 μm × 2 μm each) of **PDBPyTT** thin films (~50 nm) on SiO_2/Si substrates annealed at different temperatures. Root-mean-square (RMS) roughness: 11.8 nm (100 °C), 14.3 nm (150 °C), and 19.1 nm (200 °C).

The thin film morphology of **PDBPyTT** was examined using atomic form microscopy (AFM). For thin film sample annealed at 100 °C, large ~1 μm × 200 nm-domains were clearly observed. Each domain was composed of many small spherical grains (Figure 3.5). The film has a large root-mean-square (RMS) roughness of 11.8 nm. When the annealing temperature was increased to 150 °C and then 200 °C, the films became even rougher, i.e. the RMS roughness is 14.3 nm for the 150 °C-annealed film and 19.1 nm for the 200 °C-annealed film. The very large crystalline domains present in the polymer thin films may contribute to the very high mobility observed for this polymer. However, the large boundaries (or trenches) between domains would be detrimental for charge transport. Optimization of the thin film processing conditions and the side chain design may lead to improved film uniformity and thus further enhanced charge transport performance of this polymer.

3.3 Conclusion

In summary, a new donor-acceptor polymer semiconductor **PDBPyTT** comprising an acceptor **DBPy** unit and a donor thieno[3,2-*b*]thiophene unit, is reported showing ambipolar charge transport performance with high electron and hole mobilities of 3.36 $cm^2V^{-1}s^{-1}$ and 2.65 $cm^2V^{-1}s^{-1}$, respectively, in OTFT devices with gold source and drain electrodes. By simply modifying the source and drain electrodes with a thin layer of PEI or MoO_3, unipolar n-type and p-type charge transport characteristics with high electron and hole mobilities of 2.38 $cm^2V^{-1}s^{-1}$and 2.89 $cm^2V^{-1}s^{-1}$ were successfully realized for this ambipolar polymer. This is the first polymer that exhibits high mobilities exceeding 2 $cm^2V^{-1}s^{-1}$ in n-type, p-type and ambipolar OTFTs. The method of changing the type of charge carriers of ambipolar polymer in OTFTs reported in this study will be applied to other ambipolar polymers to achieve a universal strategy for approaching unipolar polymer semiconductors.

3.4 Experimental Section

3.4.1 Materials and Instrumentation

All other materials were purchased from commercial sources and used as is. 3,6-Di(5-bromopyridin-2-yl)-2,5-bis(2-octyldodecyl)pyrrolo[3,4-*c*]pyrrole-1,4(2*H*,5*H*)-dione (**DBPy**Br-20) was synthesized in Chapter 2. UV/Vis spectra were collected on a Thermo Scientific GENESYS™ 10 Spectrophotometer. Reflective XRD spectra were performed on a Bruker D8 Advance powder diffractometer using standard Bragg-Brentano geometry with Cu Kα1 radiation (λ = 1.5406 Å). The polymer thin films (~50 nm thick) were prepared by spin-coating a polymer solution in chloroform on bare SiO_2/Si substrates and annealed at different temperatures. Transmission XRD measurements were carried out on polymer flakes between two Mylar substrates using Bruker

Smart Apex2 CCD with Mo Kα radiation (λ = 0.71073 Å). The atomic force microscopic (AFM) images were obtained on polymer thin films spin-coated on bare SiO_2/Si substrates with a Dimension 3100 Scanning Probe Microscope. Cyclic voltammetry (CV) measurements of polymer thin films were conducted on a Digi-Ivy DY2111 Potentiostat using a Pt counter electrode, a Pt working electrode and an Ag/AgCl reference electrode in a 0.1 M tetrabutylammonium hexafluorophosphate solution in dry acetonitrile at a scan rate of 50 mVs^{-1}. Ferrocene was used as a reference. A Malvern 350 high-temperature gel-permeation chromatography system was used to determine the molecular weight of the polymer using 1,2,4-trichlorobenzene as an eluent with polystyrene as standards at a column temperature of 140 °C. ^1H NMR data was collected on a Bruker DPX 300 MHz spectrometer using tetramethylsilane (TMS, δ = 0ppm) as a reference. The thickness of **PDBPyTT** and Cytop films were measured using a Dektak 8 Stylus profilometer. The thickness of PEI thin films was measured using a WVASE32 Spectroscopic Ellipsometer by considering a single-layer model (without surface roughness) and Cauchy model fitting.

3.4.2 Synthesis

*Synthesis of poly(2,5-bis(2-octyldodecyl)-3,6-di(pyridin-2-yl)-pyrrolo[3,4-c]pyrrole-1,4(2H,5H)-dione-alt- 2,5-thieno[3,2-b]thiophene) copolymer (**PDBPyTT**).*

To a 50 mL flask were added 3,6-di(5-bromopyridin-2-yl)-2,5-bis(2-octyldodecyl)pyrrolo[3,4-*c*]pyrrole-1,4(2*H*,5*H*)-dione[134] (0.2018 g, 0.2 mmol), 2,5-bis(trimethylstannyl)thieno[3,2-*b*]thiophene (0.0932 g, 0.2 mmol) and tri(*o*-tolyl)phosphine (5.3 mg, 0.018 mmol). After degassing and filling with argon 3 times, tris(dibenzylideneacetone)-dipalladium ($Pd_2(dba)_3$) (4.0 mg, 0.0044 mmol) and anhydrous chlorobenzene (20 ml) were added. The mixture was stirred at 130 ºC for 72 h, cooled down to room temperature, and poured into methanol (100 mL). The precipitated product was filtered and subjected to Soxhlet extraction sequentially with acetone, hexane and chloroform. The final polymer product was formed after extraction from chloroform the last time. Yield: 123

mg (62.4%). GPC: M_n = 24.5 kDa, PDI = 3.00; UV/Vis: λ_{max} 684 nm (in chloroform), 690 nm (in thin film).

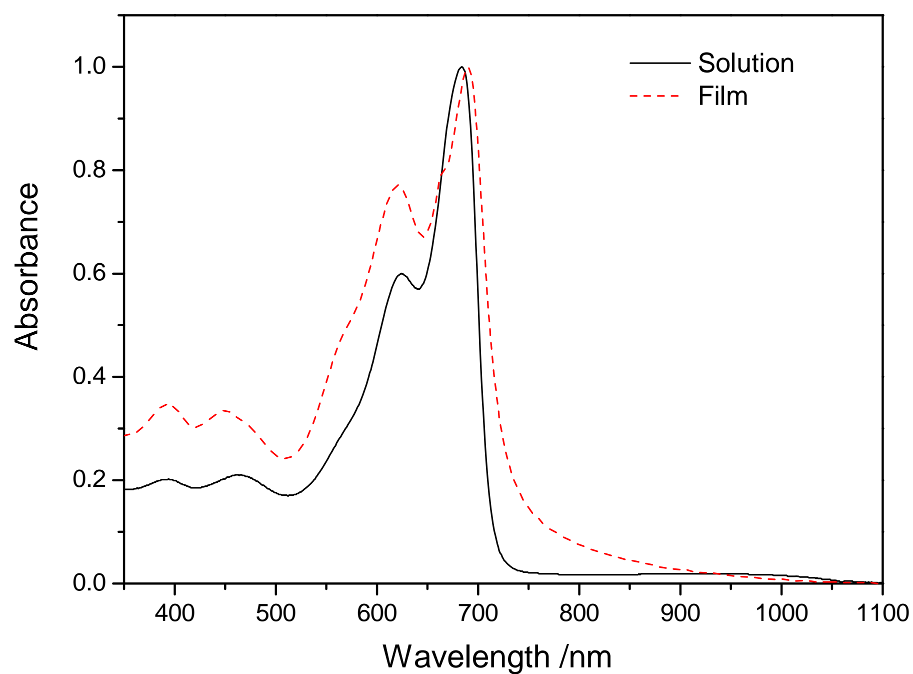

Figure 3.6. UV-vis absorption spectra of **PDBPyTT** solution (chloroform) and as-cast thin film on quartz.

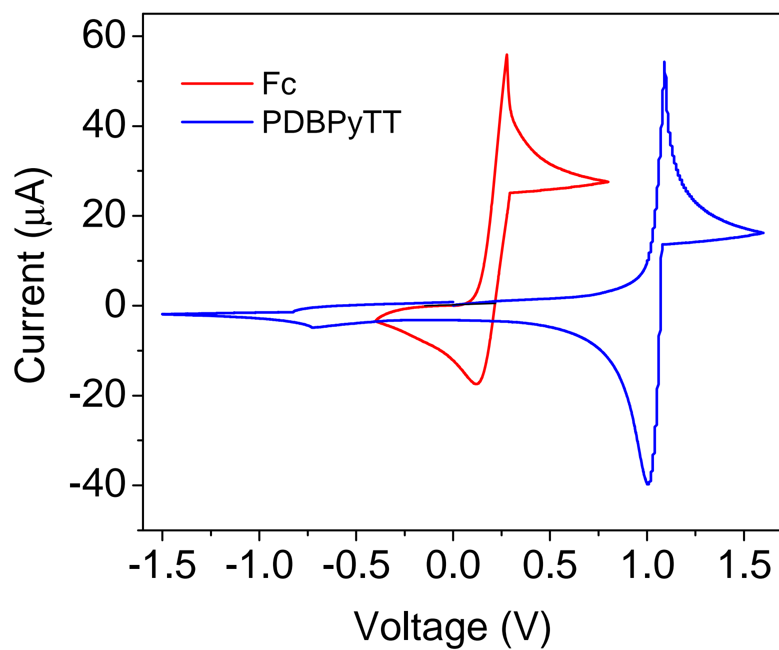

Figure 3.7. Cyclic voltammetry (CV) curves of **PDBPyTT** and ferrocene (Fc) (as a reference) in 0.1 M tetrabutylammonium hexafluorophosphate in anhydrous acetonitrile at a scan rate of 50 mVs^{-1}.

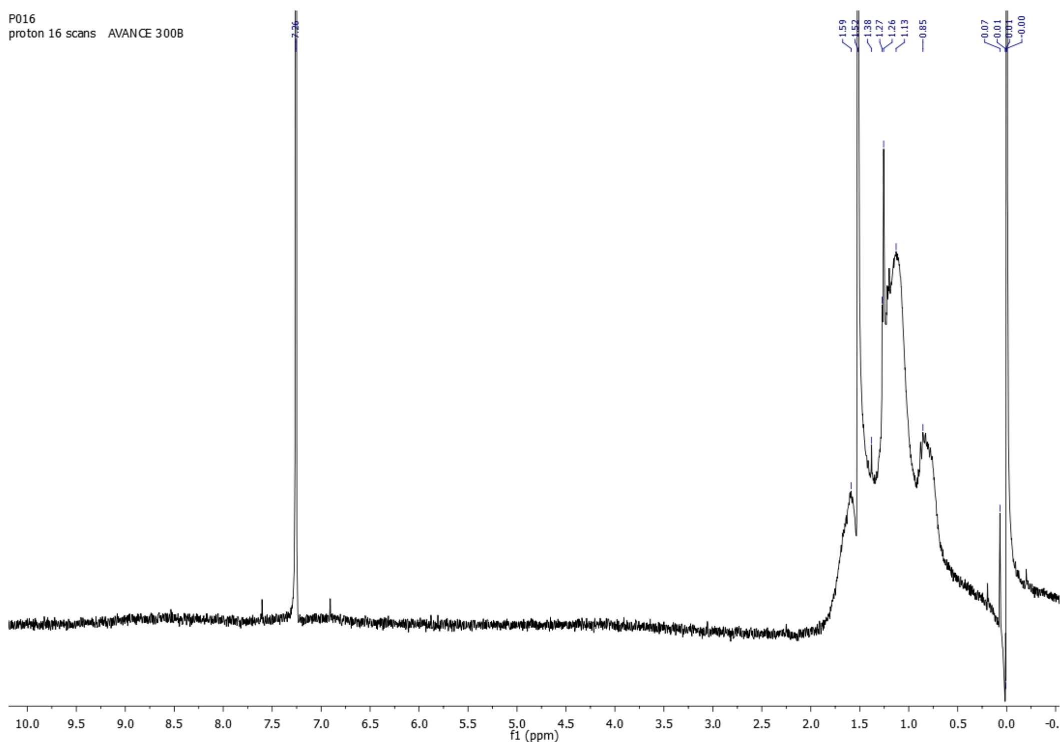

Figure 3.8 The 300 MHz ^{1}H NMR spectrum of **PDBPyTT**.

3.4.3 Device Fabrication

SiO_2/Si wafer patterned with thermally evaporated Au source and drain electrodes with a channel length (L) of 30 μm and a channel width (W) of 1 mm was used as the substrate for the top-gate bottom-contact OTFT devices. The patterned substrate was cleaned with air plasma and then rinsed with acetone and isopropanol.

OTFTs without electrode modification. A **PDBPyTT** solution in chloroform (10 mg mL^{-1}) was spin-coated on a cleaned substrate with patterned source and drain pairs at 2000 rpm for 60 s. The substrate with the deposited polymer film (~50 nm) was annealed on a hotplate in nitrogen for 10 min. A Cytop layer (~570 nm with Ci = 3.2 nF cm^{-2}) as the gate dielectric was deposited on the polymer semiconductor layer by spin-coating a Cytop solution at 2000 rpm for 60 s, followed by annealing on a hotplate at 100, 150, and 200 °C for 10 min in nitrogen. Finally, a 70 nm of Al layer as the gate electrode was deposited by thermal evaporation.

OTFTs modified with PEI. A PEI (branched polyethylenimine with an average M_w of ~25 kDa, Sigma Aldrich) solution diluted with isopropanol was spin-coated on a cleaned substrate with patterned source and drain pairs at 5000 rpm for 60 s. After baking on a hotplate at 100 °C for 10 min, a **PDBPyTT** solution in chloroform (10 mg mL^{-1}) was spin-coated and the substrate was annealed at 150 °C for 10 min. The Cytop dielectric layer and the Al top gate layer were then deposited as described above.

OTFTs modified with MoO_3. A MoO_3 thin film was thermally deposited at a rate of 0.2 Å s^{-1} on the cleaned substrate with patterned source and drain pairs. Then the **PDBPyTT** film was deposited

by spin-coating a polymer solution, followed by annealing at 150 °C for 10 min. The Cytop dielectric layer and the Al top gate layer were then deposited as described above.

The OTFT devices were characterized in air in the absence of light using an Agilent 4155C Semiconductor Parameter Analyzer. The carrier mobility was calculated from the slope of the $(I_{DS})^{1/2}$ versus V_{GS} plot according to the equation, $I_{DS} = \mu C_i \, W/2L \, (V_{GS}-V_{TH})^2$, in the saturated regime.

Output and transfer characteristics of OTFTs evaluated in Chapter 3 are included in the Appendix.

Chapter 4. n-Type Unipolar Conversion from Ambipolar and p-Type Polymer Semiconductors by PEI-modification of Au Electrodes

This work is published in B. Sun, W. Hong, E. Thibau, H. Aziz, Z.-H. Lu, Y. Li, *Org. Electron.* **2014**, *15*, 3787

Dr. Hong synthesized polymer **P4-2~P4-6**; Thibau conducted UPS measurement; and Sun carried out all other characterizations.

4.1 Introduction

In Chapter 3, the conversion of ambipolar polymer, **PDBPyTT**, to unipolar n-type polymer semiconductor was achieved. Here an ultrathin layer (~ 2-5 nm) of polyethyleneimine (PEI) modification of source and drain electrodes is a general approach to converting ambipolar polymers and can even convert p-type semiconductors into unipolar n-type semiconductors in OTFTs is demonstrated. This universal method will serve as a guide for the design of novel high performance n-type polymer semiconductors and expand the polymer semiconductors application in complementary logic.

4.2 Results and Discussion

A thin layer (~10 nm) of air-stable polyethyleneimine (PEI) on the conductor surface used to achieve a low work function has been reported for efficient electron injection in organic electronics including organic photovoltaics, thin film transistors and light-emitting diodes.[88] Ultraviolet photoelectron spectroscopy (UPS) measurements were carried out on gold (Au) thin films with a

thin layer of PEI and confirmed that their work function decreased sharply from ~5.1 eV to ~3.2 eV as the PEI layer thickness increases from 0 nm to ~5 nm and remained almost unchanged with a thickness up to ~9 nm in Figure 4.1. By using the PEI-modified Au as source and drain contacts, it should be possible to increase the energy barrier to a level that is sufficient to block hole injection, and realize electron-only charge transport behavior of ambipolar polymers in OTFT devices.

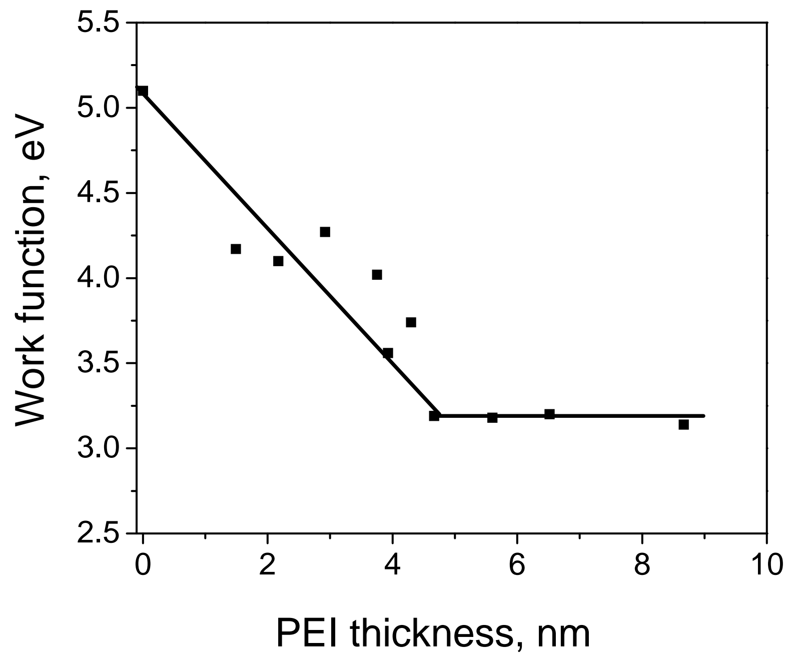

Figure 4.1. Effect of PEI thickness on the work function of gold (Au) modified by a layer of PEI.

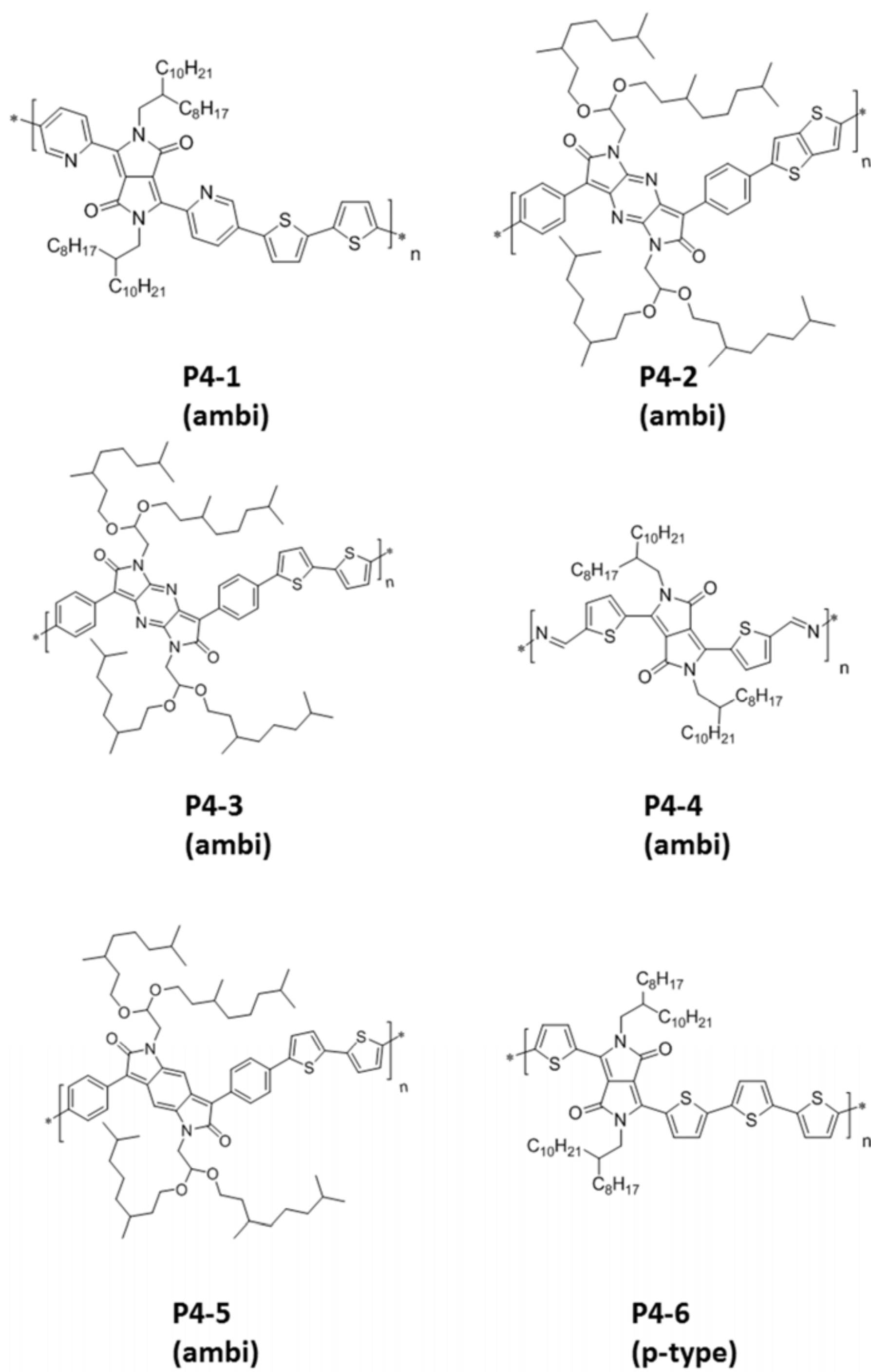

Figure 4.2. Structures of polymer semiconductors studied in this work.

In this study, a number of ambipolar D-A polymers were chosen, which were developed previously in our group, based on strong electron acceptors, diketopyrrolopyrrole (DPP) (**P4-1** and **P4-4**),[119, 134] dipyrrolo[2,3-*b*:2',3'-*e*]pyrazine-2,6(1*H*,5*H*)-dione (PzDP) (**P4-2** and **P4-3**),[66] and pyrrolo[2,3-*f*]indole-2,6(1*H*,5*H*)-dione (BDP') (**P4-5**)[144] (Figure 4.2). All of these polymers have relatively low LUMO levels ranging from -4.0 eV to -4.3 eV (Figure 4.3), which are sufficient for stable electron transport. They also have rather low-lying HOMO levels ranging from -5.5 eV to -5.7 eV. If the PEI-modified Au (e.g., with a ~5 nm PEI layer) is used as the electrode, there would be no energy barrier for electron injection from the electrode to the semiconductor layer. On the other hand, hole injection barrier, $\Delta E = E_F$ (electrode) – E_{HOMO} (semiconductor), would increase dramatically from 0.4-0.6 eV for pure Au to 2.3-2.5 eV for the PEI-modified Au. A known unipolar p-type DPP-based D-A polymer, **P4-6**,[31, 37], which has a low LUMO level of -4.0 eV and a relatively high HOMO level of -5.2 eV was also selected.[37] The energy barrier for hole injection can be increased to 2.0 eV if a PEI layer of ≥ 5 nm is used to modify the source and drain contacts. A study on the behavior of this polymer would provide information on whether such a barrier is adequate to block hole injection and whether electron transport can be induced to transform this p-type polymer into an n-type semiconductor by using PEI-modified Au electrodes.

These polymers were tested as the active layer in top gate/bottom contact (TGBC) OTFT devices (Figure 4.3). The Au source and drain pairs patterned on a SiO_2/Si wafer substrate were first modified with a layer of PEI by spin-coating a PEI solution in isopropanol and dried at 100 °C. Next, a polymer semiconductor solution was spin-coated on the substrate, followed by thermal annealing at 150 °C. Then, a Cytop (a fluoropolymer product of Asahi Glass Co.) solution was spin-coated and dried at 100 °C before an Al layer was thermally evaporated as the top gate electrode. For comparison, devices with pure Au contacts (without PEI modification) were also fabricated.

Figure 4.3. The top gate, bottom contact (TGBC) OTFT device configuration and the HOMO and LUMO energy levels of ambipolar semiconductors and the Fermi levels of pure Au and PEI-modified Au.

Table 4.1. OTFT performance of devices with pure Au source and drain electrodes and best unipolar n-channel devices with PEI-modified Au source and drain electrodes at the optimal PEI thicknesses. Each set of data were obtained from at least 5 devices.

Polymer	Pure Au S/D				PE-modified Au S/D			
	μ_e, cm^{2}V^{-1}s$^{-1, a)}$		μ_h, cm^{2}V^{-1}s$^{-1, b)}$		PEI thickness, nm	μ_e, cm^{2}V^{-1}s^{-1}		I_{on}/I_{off} c)
	Max.	Ave (STD)[d]	Max.	Ave (STD)		Max.	Ave. (STD)	
P4-1	5.45	4.16 (1.01	2.60	2.28 (0.29)	2.2	1.42	1.03 (0.26)	~10^3
P4-2	0.13	0.10 (0.029)	0.039	0.029 (0.010)	2.9	0.18	0.083 (0.044)	~10^4
P4-3	0.063	0.051 (0.0082)	0.098	0.055 (0.029)	1.5	0.11	0.078 (0.022)	~10^4
P4-4	0.40	0.38 (0.02)	0.29	0.29 (0.0057)	2.9	0.53	0.46 (0.0044)	~10^4
P4-5	0.0027	0.0024 (0.00025)	0.048	0.044 (0.0042)	4.7	0.0018	0.0014 (0.00028)	~10^3
P4-6	-	-	0.63	0.56 (0.048)	4.7	0.036	0.027 (0.0059)	~10^3

[a] Electron mobility measured at V_{DS} = 80 V; [b] Hole mobility measured at V_{DS} = -80 V; [c] Current on to off ratio. [d] Standard deviation.

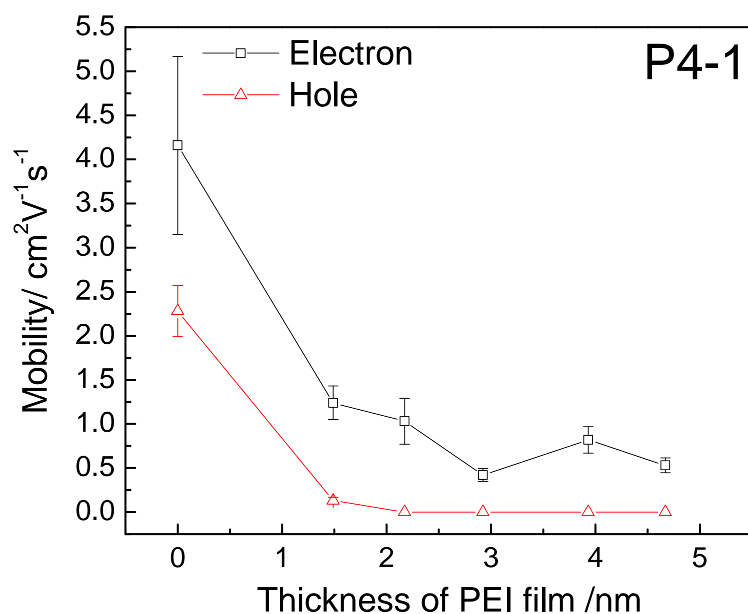

Figure 4.4 Mobility changes of **P4-1** with increasing PEI layer thickness on the surface of Au source and drain electrodes in OTFT devices.

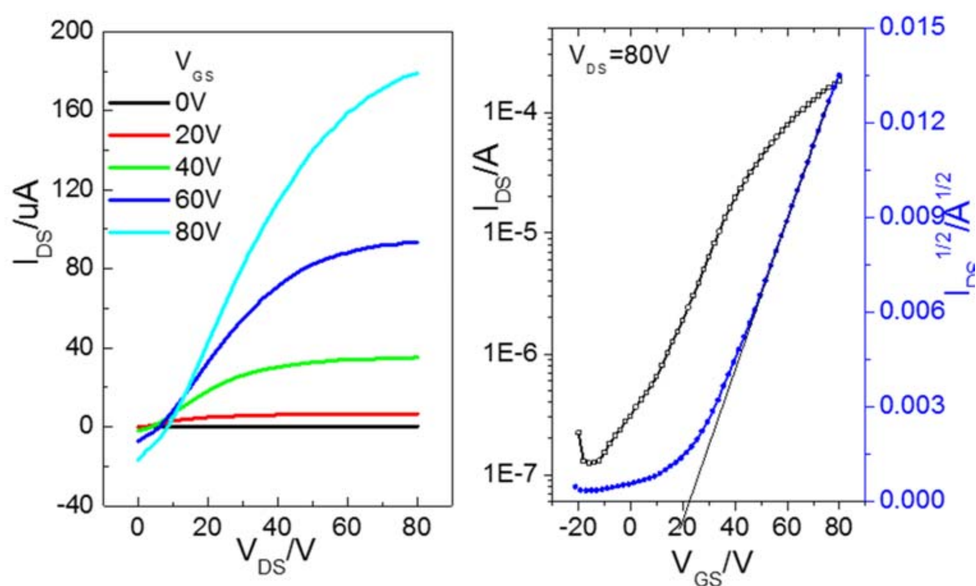

Figure 4.5 Output (left) and transfer (right) curves of representative unipolar n-channel OTFT devices of **P4-1** with PEI (3.9nm; μ_e = 1.03 cm^{2}V^{-1}s^{-1}) modified source and drain electrodes.

The first polymer, **P4-1**, showed ambipolar performance with high electron mobility of 4.16 $cm^2V^{-1}s^{-1}$ and hole mobility of 2.28 $cm^2V^{-1}s^{-1}$ (average values) in TGBC device without electrode modification (Table 4.1), indicating that electron transport is more favoured over hole transport due to the polymer containing more electron accepting moieties (DPP and pyridine) than the electron-donating unit (bithiophene) ones. With merely a ~3 nm-thick PEI layer on the Au source and drain electrodes, hole transport can be completely suppressed and unipolar electron transport behavior was observed (Figure 4.4). The best performance was achieved at a PEI thickness of ~4 nm, achieving electron mobility up to 1.03 $cm^2V^{-1}s^{-1}$. However, the electron mobility values are lower than those obtained for the ambipolar devices when no PEI was used. Reason for this electron mobility drop will be discussed later.

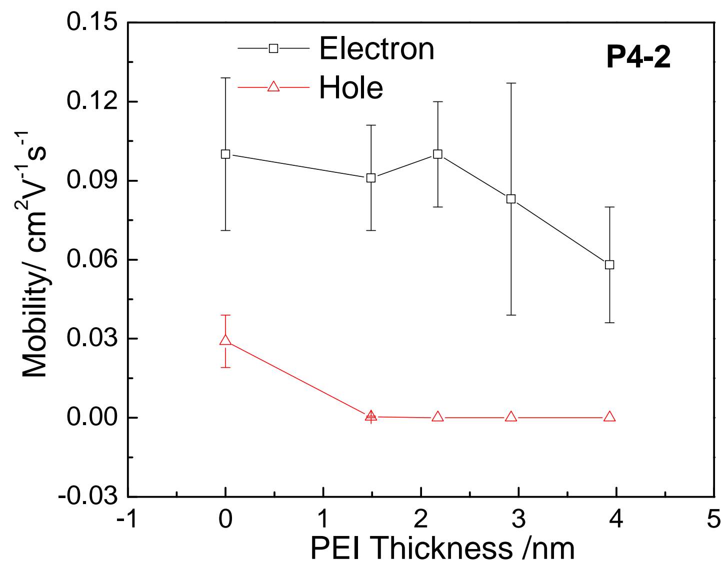

Figure 4.6 Mobility changes of **P4-2** with increasing PEI layer thickness on the surface of Au source and drain electrodes in OTFT devices.

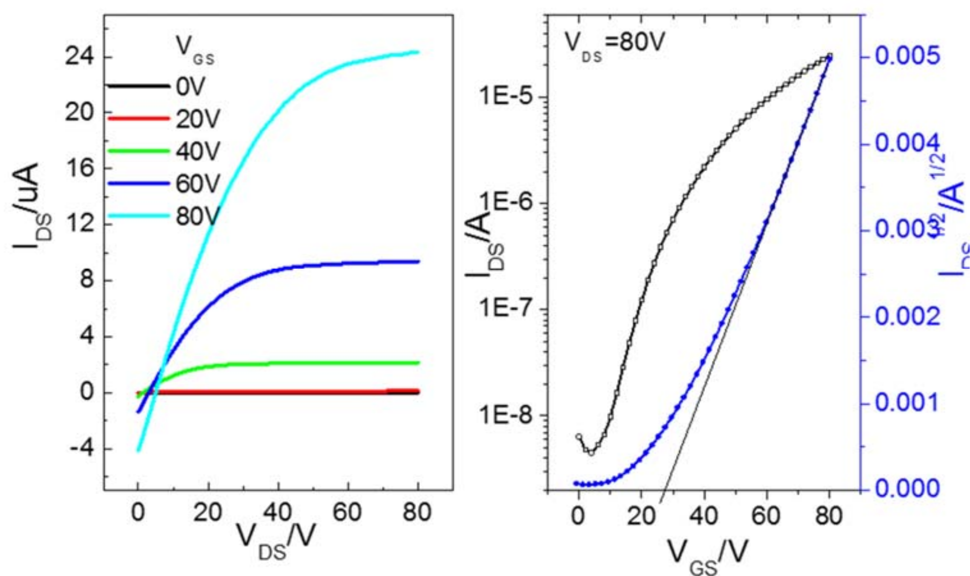

Figure 4.7 Output (left) and transfer (right) curves of representative unipolar n-channel OTFT devices of **P4-2** with PEI (2.9nm; μ_e = 0.18 cm^{2}V^{-1}s^{-1}) modified source and drain electrodes.

P4-2, which showed electron/hole mobilities up to 0.13 cm^{2}V^{-1}s^{-1}/0.039 cm^{2}V^{-1}s^{-1}in devices with pure Au contacts, is an electron-transport dominating ambipolar polymer. Complete suppression of hole transport was observed at a PEI thickness of ~2 nm. The best electron mobility of 0.18 cm^{2}V^{-1}s^{-1} (Table 4.1) was achieved at a PEI thickness of ~3 nm, which is higher than the electron mobility of the devices without PEI modification. Another **PzDP**-based polymer, **P4-3**, showed comparable electron/hole mobilities up to 0.063 cm^{2}V^{-1}s^{-1}/0.098 cm^{2}V^{-1}s^{-1}in devices with pure Au contacts. This polymer also showed unipolar n-type semiconductor performance at a PEI thickness of ~2 nm, where high electron mobility of 0.11 cm^{2}V^{-1}s^{-1} was achieved. This mobility value is a 75% increase compared with the electron mobility of the devices without PEI.

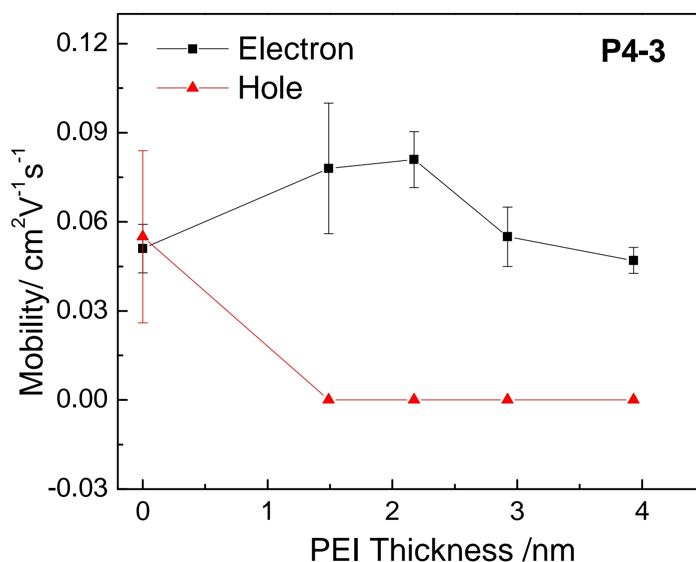

Figure 4.8 Mobility changes of **P4-3** with increasing PEI layer thickness on the surface of Au source and drain electrodes in OTFT devices.

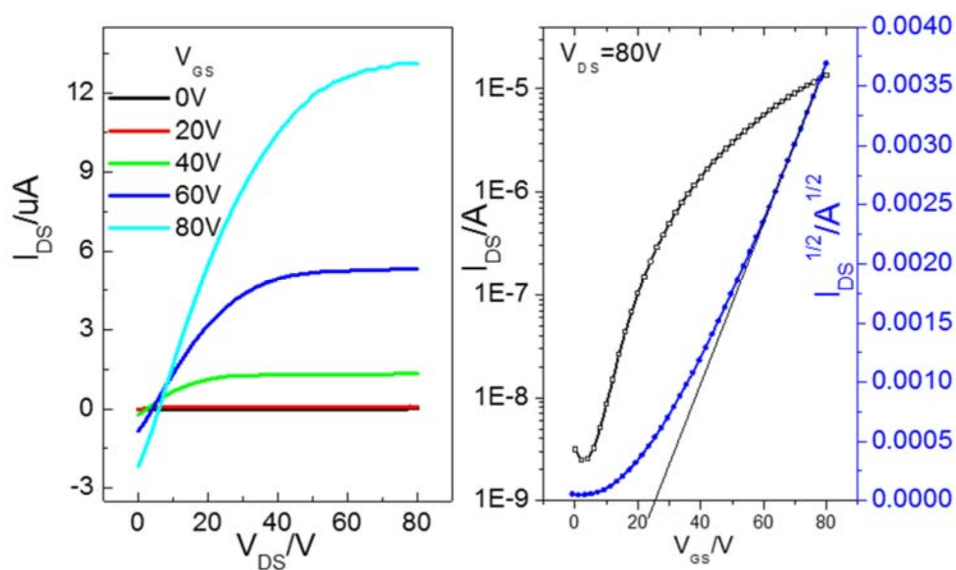

Figure 4.9 Output (left) and transfer (right) curves of representative unipolar n-channel OTFT devices of **P4-3** with PEI (2.2nm; μ_e = 0.091 $cm^2V^{-1}s^{-1}$) modified source and drain electrodes.

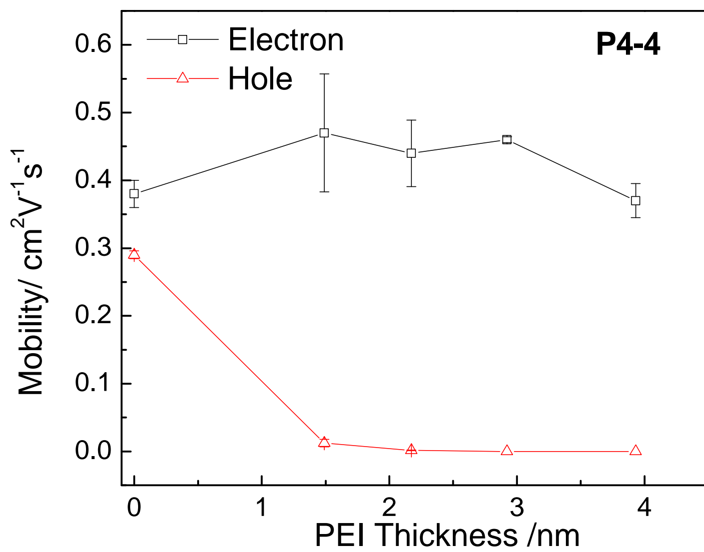

Figure 4.10 Mobility changes of **P4-4** with increasing PEI layer thickness on the surface of Au source and drain electrodes in OTFT devices.

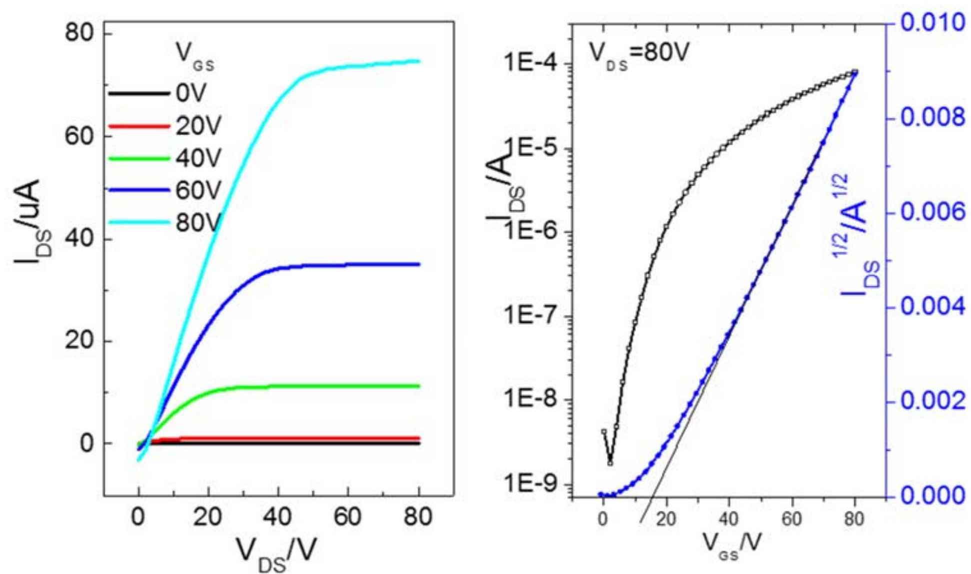

Figure 4.11 Output (left) and transfer (right) curves of representative unipolar n-channel OTFT devices of **P4-4** with PEI (3.9nm; μ_e = 0.41 $cm^2V^{-1}s^{-1}$) modified source and drain electrodes.

P4-4 showed well-balanced electron and hole mobilites up to 0.40 $cm^2V^{-1}s^{-1}$ and 0.29 $cm^2V^{-1}s^{-1}$, respectively, in the devices with pure Au electrodes. After modifying the Au with ~3 nm PEI, unipolar electron mobility as high as 0.53 $cm^2V^{-1}s^{-1}$ was achieved, which is significantly improved in comparison to the electron mobility of the devices with pure Au.

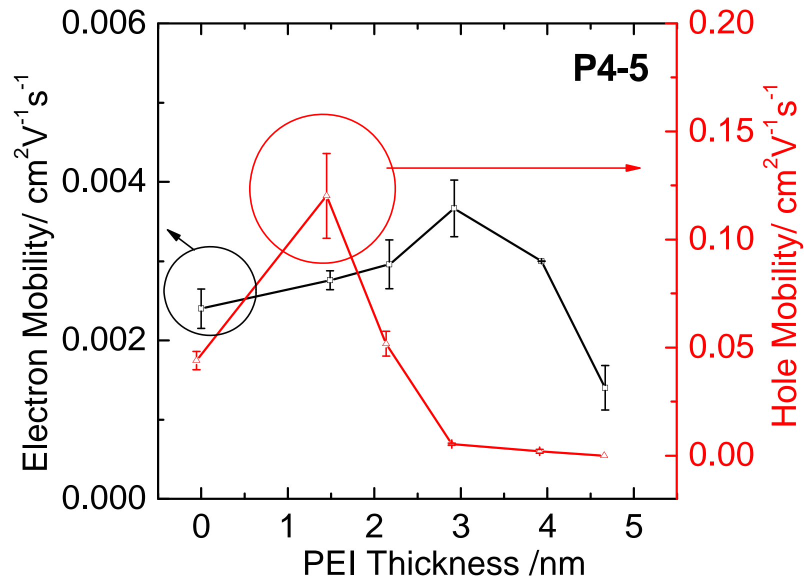

Figure 4.12 Mobility changes of **P4-5** with increasing PEI layer thickness on the surface of Au source and drain electrodes in OTFT devices.

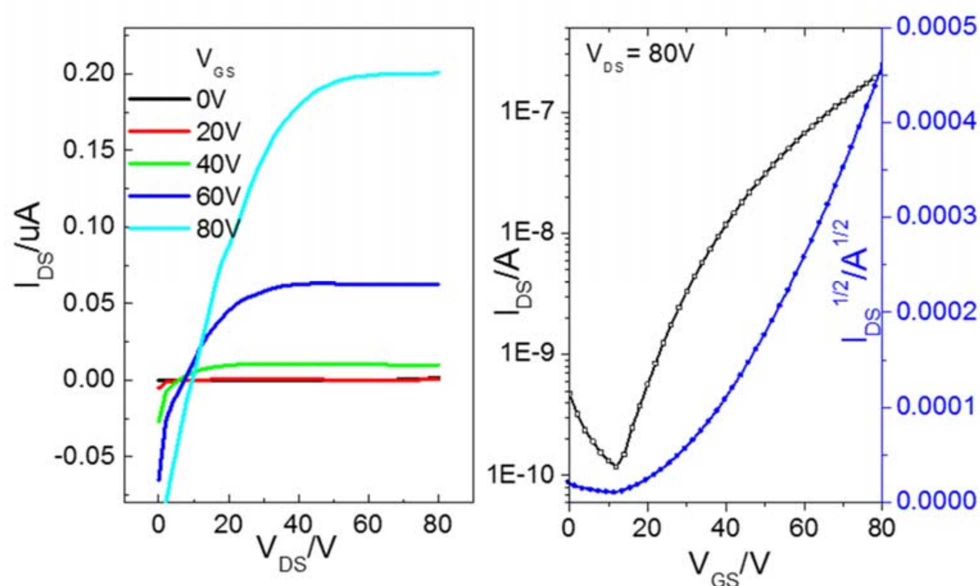

Figure 4.13 Output (left) and transfer (right) curves of representative unipolar n-channel OTFT devices of **P4-5** with PEI (4.7nm; μ_e = 0.0018 cm^{2}V^{-1}s^{-1}) modified source and drain electrodes.

P4-5 is a hole-transport dominating ambipolar polymer with electron mobility up to 0.0027 cm^{2}V^{-1}s^{-1} and one order of magnitude higher hole mobility up to 0.048 cm^{2}V^{-1}s^{-1} in devices without PEI. Interestingly, when the Au contacts were modified with a 1.5 nm-thick PEI layer, the hole mobility increased ~2.5 times along with a slight increase in the electron mobility. Complete hole transport suppression was not achieved until the PEI thickness reached ~5 nm. The best unipolar electron mobility is 0.0018 cm^{2}V^{-1}s^{-1}, which is lower than the electron mobility achieved for the non-modified devices. This is most likely due to the higher contact resistance caused by the thicker insulating PEI layer. **P4-3** and **P4-5** have very similar structure, differing only in their central core, the acceptors: pyrazine for **P4-3** and benzene for **P4-5**. They have almost the same HOMO levels: -5.59 eV (**P4-3**) vs. -5.62 eV (**P4-5**). The higher PEI thickness required for **P4-5** to achieve unipolar electron transport is considered due to its much lower crystallinity (or more amorphous) [144] compared with **P4-3**,[66] which might facilitate the diffusion of **P4-5** polymer chains into the PEI

layer, thus reducing the effective PEI thickness. This may also explain the initial surge in the hole mobility of this polymer at the PEI thickness of 1.5 nm.

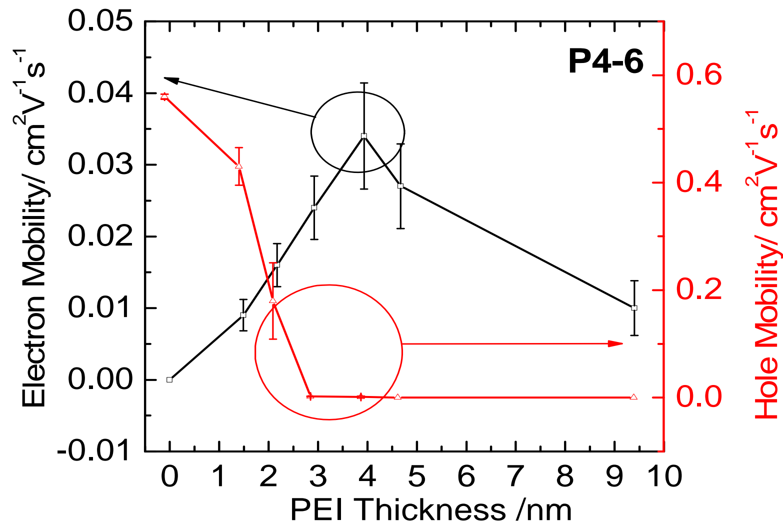

Figure 4.14 Mobility changes of **P4-6** with increasing PEI layer thickness on the surface of Au source and drain electrodes in OTFT devices.

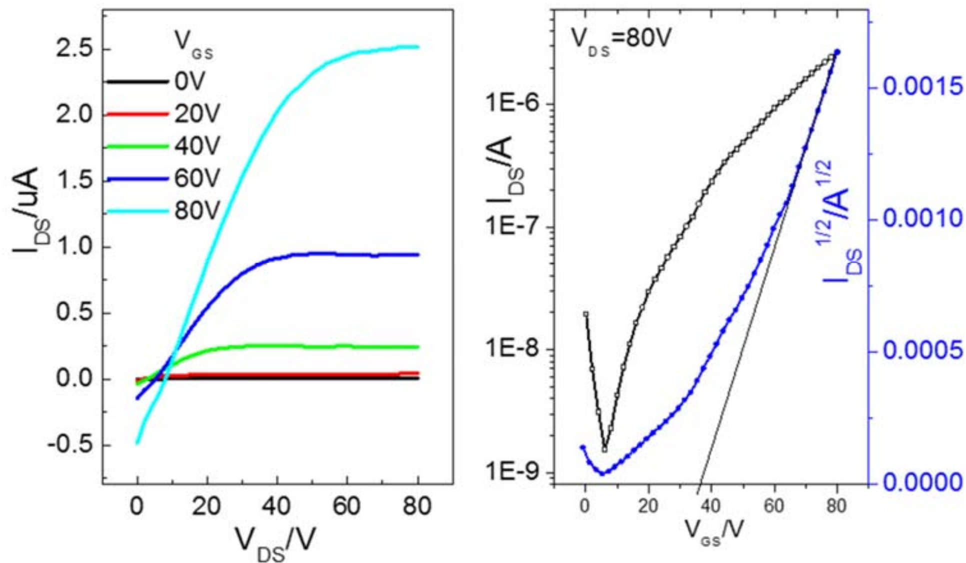

Figure 4.15 Output (left) and transfer (right) curves of representative unipolar n-channel OTFT devices of **P4-6** with PEI (4.7nm; μ_e = 0.036 cm^{2}V^{-1}s^{-1}) modified source and drain electrodes.

For the unipolar p-type polymer **P4-6**, the hole mobility decreased and electron transport appeared with increasing PEI thickness. Unipolar n-type semiconductor behavior was observed at a PEI thickness of ~4 nm and highest electron mobility of 0.036 $cm^2V^{-1}s^{-1}$ was achieved at this PEI thickness.

Based on our observations, it seems that a PEI layer thickness of ~ 5nm is sufficient to build up a high hole injection barrier to suppress the hole transport of the chosen polymers, which have HOMO energy levels of ≤ ~-5.2 eV. For polymers **P4-2** to **P4-6**, enhanced electron transport compared with the devices without PEI modification was observed in the PEI thickness range of ~2-4 nm, which is possibly due to the improved metal-polymer semiconductor interfacial contact in the presence of an ultrathin layer of PEI. The reason for the drop in electron mobility observed for **P4-1** in the devices with PEI-modified electrodes is still unclear. It might be due to the poor interfacial contact between this polymer and the PEI layer because severe contact resistance was observed for the **P4-1**-based devices (see the S-shaped output curves near the origin in Figure 4.5). One possible reason is the extremely high crystallinity of this polymer, which was found to result in very poor contact of **P4-1** with the substrate. [134]Another reason might be due to the lone electron pair of the pyridine unit, which may have a repulsive interaction with the PEI layer that has the electron-rich NH_2 groups on the surface, leading to poor interfacial contact of **P4-1** and PEI. It was found that a PEI layer thickness greater than ~4 nm resulted in decreased electron mobility most likely due to the increased contact resistance caused by the excessively thick insulating PEI layer.

4.3 Conclusion

In this study, modification of the gold source and drain contacts with an ultrathin (~2-5 nm) polyethyleneimine (PEI) layer is demonstrated as an effective general approach to convert

ambipolar polymers and even a p-type semiconductor with sufficiently low LUMO energy levels into unipolar n-type semiconductors in organic thin film transistors. It should be noted that other conductor materials such as Ag can be used to replace Au since the work function reduction by PEI is achievable for many other underlying conductor materials. This simple technique will greatly broaden the scope of available polymer semiconductors for various applications including CMOS-like circuits where n-channel OTFTs are required by simply modifying the source and drain electrodes by PEI.

4.4 Experimental

4.4.1 Materials and Methods.

PEI (branched polyethylenimine with an average M_w of ~25 kDa) was purchased from Sigma Aldrich. Cytop (a fluoropolymer of Asahi Glass Co., Ltd.) was purchased from Bellex International Corporation. All other chemicals were obtained from commercial sources and used as received. Synthesis and properties of ambipolar polymers, **PDBPyBT**(**P4-1**, M_n = 26.3 kDa, PDI = 3.56),[134] **PPzDPDP-TT** (**P4-2**, M_n = 28.6 kDa, PDI = 2.56),[66] **PPzDPDP-BT** (**P4-3**, M_n = 27.5 kDa, PDI = 2.84),[66] **PDBTAZ** (**P4-4**, M_n = 102 kDa, PDI = 4.30),[119] and **PBDPDP24a-BT** (**P4-5**, M_n=22.8 kDa, PDI = 2.89),[144] and a p-type polymer, **PDQT** (**P4-6**, M_n = 40 kDa, PDI = 3.22)[37] used in this study were reported previously. The thickness of PEI thin films was determined by using a WVASE32 Spectroscopic Ellipsometer by considering a single-layer model (without surface roughness) and Cauchy model fitting.

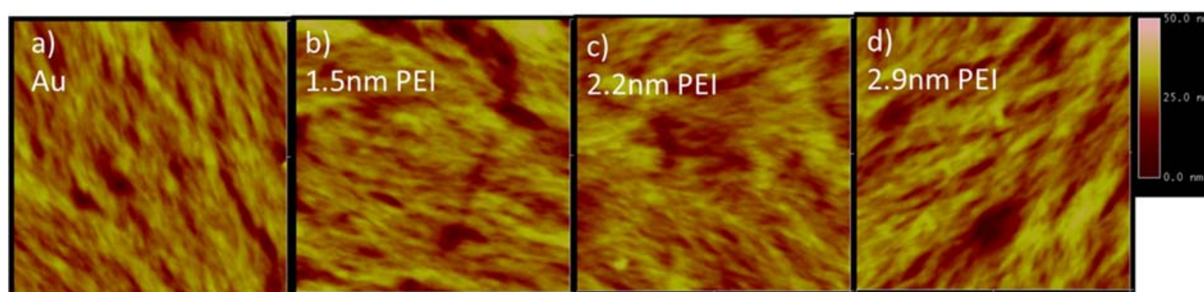

Figure 4.16. The AFM height images (2 μm × 2 μm each) of **P4-1** thin films (~50 nm) on pure Au electrode (a) and modified Au electrodes (b-d) with different PEI thicknesses.

4.4.2 Work Function Measurement.

A PEI film was deposited on a 40 nm of Au film on n-heavily doped Si wafer (3 nm of Cr as adhesion layer) by spin coating the PEI solution in isopropanol, and then the substrate was dried on a hotplate at 100 °C for 10 min. UPS were collected on a Physical Electronics 5500 Multi-Technique system under ultra-high vacuum (pressure: ~1 × 10^{-9} torr). The work function was measured at a take-off angle of 88 °, while the sample was held at a negative bias of -15 V relative to the spectrometer during UPS measurements. The work function (ϕ) was calculated from the equation: $\phi = 21.22 - SEC$, where SEC is the Secondary Electron Cut-off, giving by the intersection of the extrapolation of the linear portion of the initial peak with the x-axis. The energy of the incident UV light is 21.22 eV (He Iα radiation), and an electrical bias of -15 is t applied during measurement.

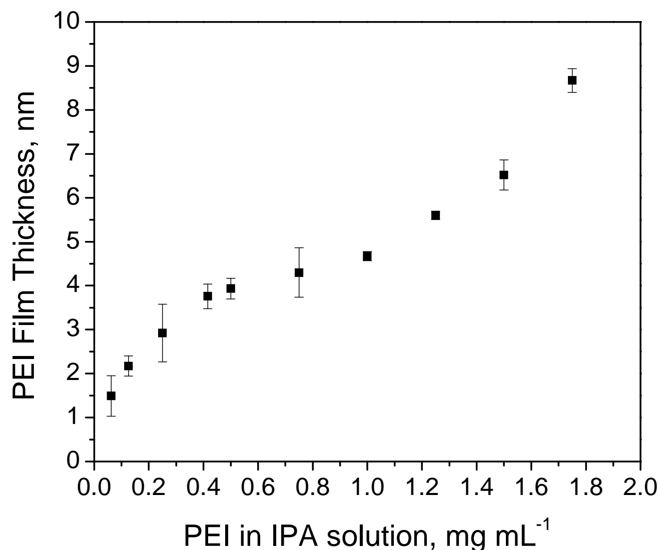

Figure 4.17. The PEI thicknesses at different PEI concentrations in isopropanol (IPA). The PEI thin films were spin coated on SiO_2/Si wafer substrates at 5000 rpm. Each data point was obtained from at least 3 samples.

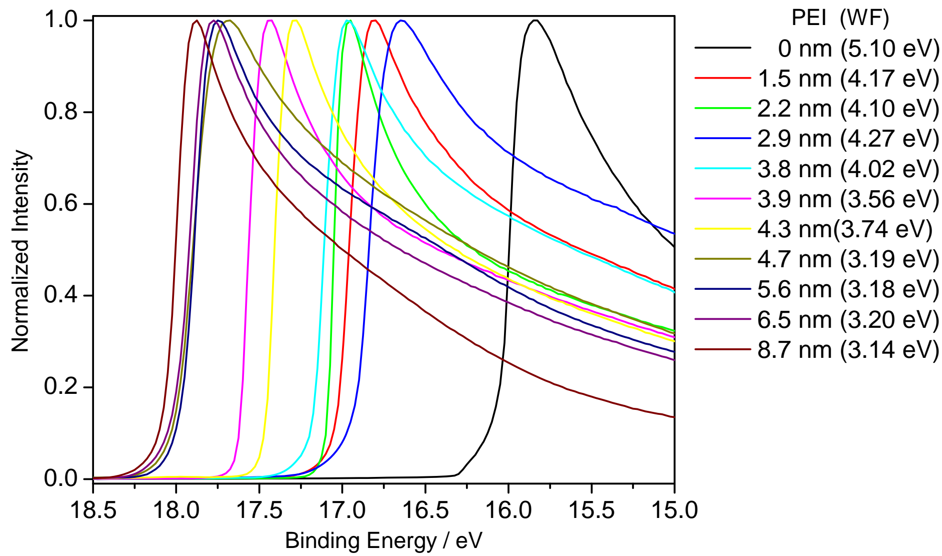

Figure 4.18. UPS spectra of pure Au film and PEI-modified Au films with various PEI thicknesses. Work function (WF) values obtained from the UPS spectra were used to make the graph in Figure 4.1.

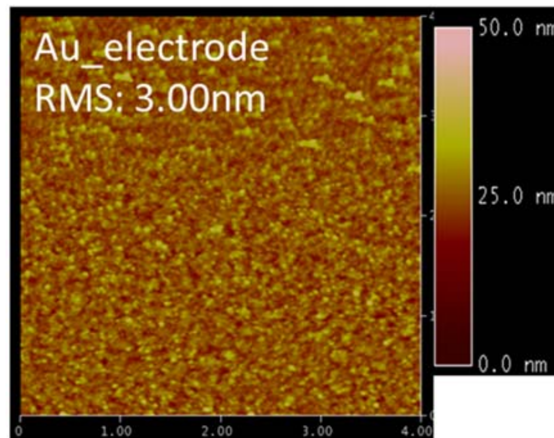

Figure 4.19 The AFM height image of the 40 nm-thick Au electrode film (3 nm of Cr as adhesion layer, thermally deposited at 0.01 nm s^{-1}) thermally evaporated on the SiO_2/Si wafer substrate with a deposition rate of 0.03 nm s^{-1} at a pressure of 5×10^{-6} bar using Intel Vac thermal deposition instrument.

4.4.3 OTFT Device Fabrication.

Top-gate bottom-contact OTFT devices were fabricated and measured following the same procedure shown in Chapter 2.

Output and transfer characteristics of OTFTs fabricated in Chapter 4 are included in the Appendix.

Chapter 5. Polyethylenimine (PEI) as an Effective Dopant for n-Type Unipolarization from Ambipolar and p-type Polymer Semiconductors

This work is published in B. Sun, W. Hong, E. S. Thibau, H. Aziz, Z. H. Lu, Y. Li, *ACS Appl Mater Interfaces* **2015**, *7*, 18662.

Dr. Hong synthesized polymers **P5-1**, **P5-2**, and **P5-4**; Thibau performed UPS measurements; and Sun conducted all other characterizations.

5.1 Introduction

Ambipolar organic semiconductors can be converted into unipolar materials by changing their packing motif by side chain design,[83] thermal annealing[84] and choice of processing solvent.[85] Surface modification of the source and drain contacts with barium or cerium salts, [81, 82] organic thiols and polyethylenimine [88] has been used as a strategy to reduce the work function (or raise the Fermi energy) of the electrodes and facilitate electron injection of small molecules or polymer semiconductors in OTFTs. In Chapter 4, ambipolar and p-type OTFTs based on several D-A polymers were converted into unipolar n-type OTFTs [145, 146] by depositing a thin layer (~2-5 nm) of polyethylenimine (PEI, Figure 5.1) on the Au source/drain contacts. The work function of the PEI-modified Au could be dramatically reduced from 5.1 eV to as low as 3.2 eV. [88, 145] Such a low work function should yield a large energy barrier for hole injection and facilitate electron injection. Another effective way to suppress hole transport and promote electron transport of small molecule or polymer semiconductors is n-type doping with cobaltocenes, [87, 147] small molecule amine compounds [86, 148-150] or CsF.[87],[151] In this study, PEI is also demonstrated to be a very effective polymeric dopant to convert ambipolar and even p-type D-A polymer semiconductors (PSCs) into

high-performance unipolar n-type polymers in OTFTs. PEI and these PSCs are readily miscible in a common solvent to form homogenous and stable solutions, which can be spin-coated into smooth blend films with uniformly distributed PEI at the nanoscale.

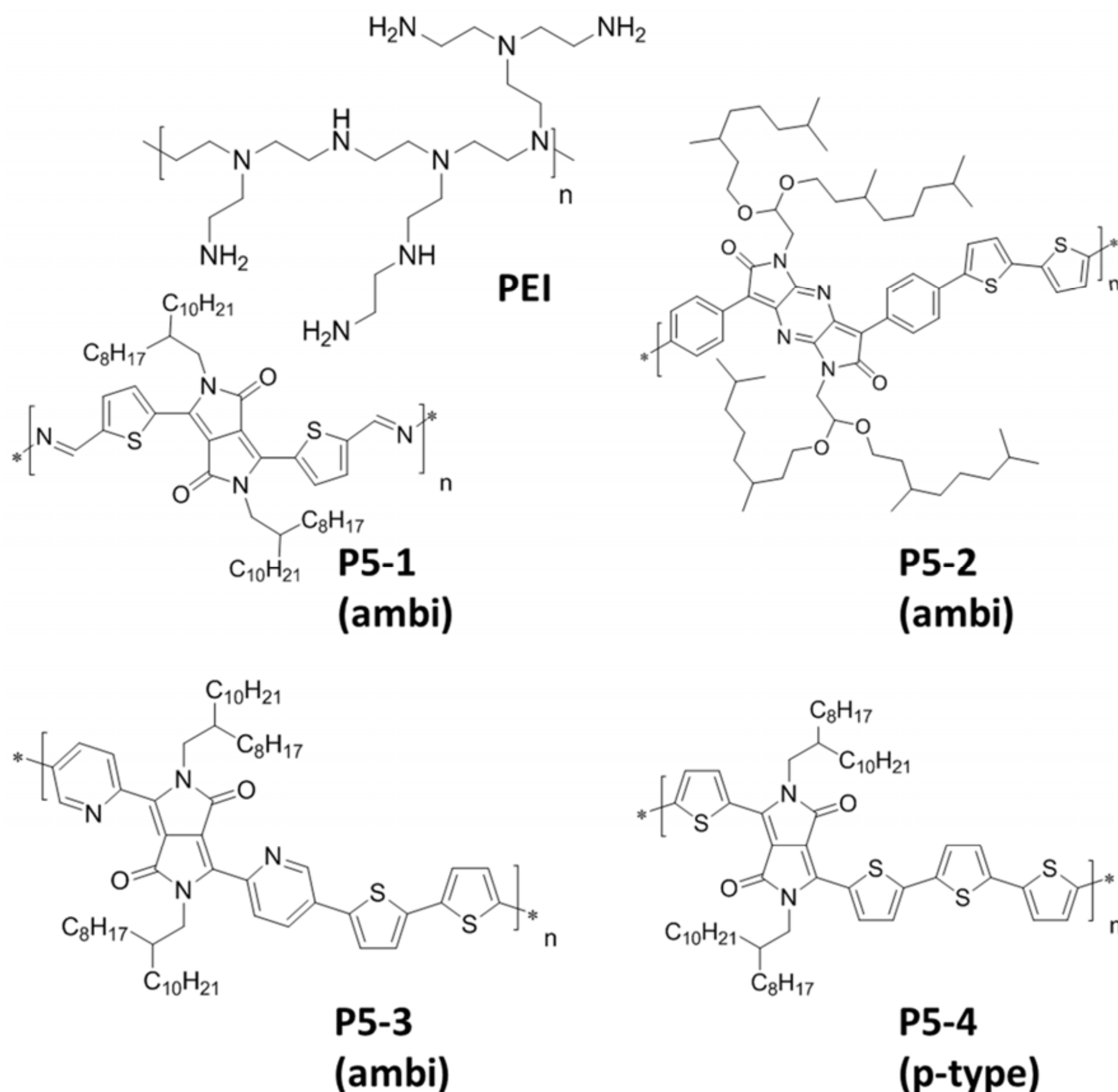

Figure 5.1. Chemical structures of PEI (branched polyethylenimine) and polymer semiconductors **PDBTAZ (P5-1)**[119] (E_{HOMO}/E_{LUMO} = -5.67 eV/-4.24 eV), **PPzDPDP-BT (P5-2)**[134] (E_{HOMO}/E_{LUMO} = -5.59 eV/-4.17 eV), **PDBPyBT (P5-3)**[66] (E_{HOMO}/E_{LUMO} = -5.69 eV/-4.33 eV), and **PDQT (P5-4)**[31, 37] (E_{HOMO}/E_{LUMO} = -5.24 eV/-4.04 eV) used in this study. **P5-1**, **P5-2**, and **P5-3** were previously reported to show typical ambipolar (ambi) charge transport performance, while **P5-4** showed typical p-type hole-only transport performance when gold was used as source/drain contacts in an OTFT device.

5.2 Results and discussion

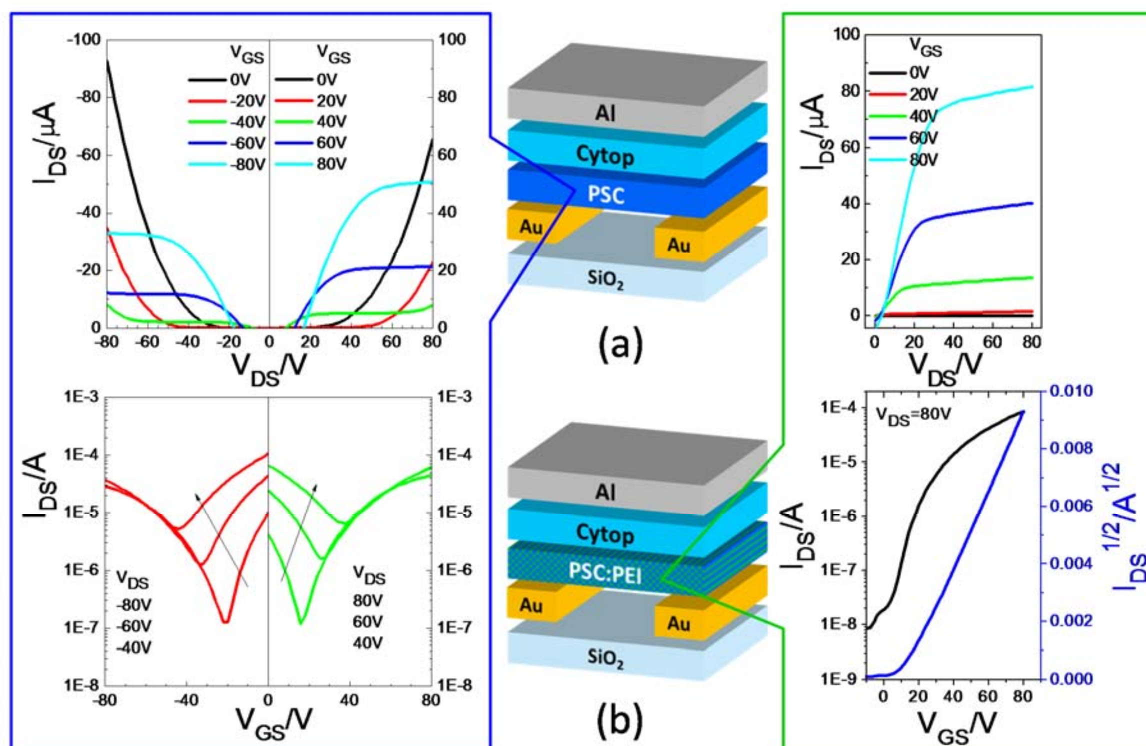

Figure 5.2. (a) Top-gate bottom-contact (TGBC) OTFT device structure with a pristine polymer semiconductor (PSC) as the channel, Cytop as the gate dielectric, Al as the gate electrode and Au as the source and drain contacts; the output (upper) and transfer (lower) curves were obtained when a ~40-50 nm thick pristine **P5-1** film (annealed at 150 °C) was used as the channel, which shows typical ambipolar charge transport performance. (b) TGBC OTFT device structure similar to that in (a) except that the channel is a PSC:PEI blend film; the output (upper) and transfer (lower) curves were obtained when a ~40 nm thick **P5-1**:PEI (2% PEI) blend film (annealed at 150 °C) was used as the channel, which shows typical n-channel electron-only transport performance. Dimensions of all devices: channel length L = 30 μm; channel width W = 1 mm.

The chemical structures of four D-A polymers **P5-1~P5-4** used in this study are shown in Figure 5.1. These polymers have deep LUMO levels of $\sim\leq -4$eV (shown in Figure 5.1 caption), which are desirable for stable electron transport.[60, 126] To evaluate the charge transport performance of these polymers, the following top-gate bottom-contact (TGBC) OTFT configuration was adopted: Au as the source and drain contacts, Cytop as the gate dielectric and Al as the top gate electrode

(Figure 5.2). A Si wafer with a 300 nm-thick thermally grown SiO_2 was used as the supporting substrate.

Pristine **P5-1** showed typical ambipolar charge transport behavior with balanced electron and hole mobilities at different annealing temperatures (Figure 5.2a, Figure 5.3 and Table 5.1). The best average electron and hole mobilities ($\bar{\mu}_e$ and $\bar{\mu}_h$) are 0.41 $cm^2V^{-1}s^{-1}$ and 0.33 $cm^2V^{-1}s^{-1}$, respectively, achieved for the films annealed at 200 °C. Then PEI and **P5-1** were dissolved in chlorobenzene to form a solution containing 0.5 % of PEI (wt% relative to the amount of the polymer semiconductor), which was then deposited as a blend film by spin-coating. TGBC OTFTs with these **P5-1**:PEI blend films exhibited similar $\bar{\mu}_e$ but significantly lower $\bar{\mu}_h$ (down to ~10^{-3} $cm^2V^{-1}s^{-1}$) compared with pristine **P5-1** at all annealing temperatures. When the PEI content was increased to 1%, films annealed at 200 °C showed very weak hole transport characteristics, while those annealed at 100 °C and 150° exhibited electron-only charge transport with slightly improved electron mobility values. When 2% PEI was added, hole transport was completely suppressed in all devices, while the electron mobility was further enhanced in most of the cases. The largest electron mobility of 0.88 $cm^2V^{-1}s^{-1}$ was achieved in a unipolar n-channel device with a 200 °C-annealed film, which is much higher than the best electron mobility of the ambipolar devices with a pristine **P5-1** film (0.47 $cm^2V^{-1}s^{-1}$, Table 5.1) and the n-channel devices with PEI-modified Au contacts (0.53 $cm^2V^{-1}s^{-1}$).[145, 146] With a further increase in the PEI content to 4%, 10% and 20%, the electron mobility decreased gradually, but moderate values up to 0.18 $cm^2V^{-1}s^{-1}$ were still retained even when 20% PEI was added. It should be mentioned that **P5-1** (and **P5-2~P5-4**) and PEI could be dissolved at any blend ratio in a common solvent such as chlorobenzene, chloroform or a mixture of chloroform and 1,2-dichlorobenzene (DCB) to form a homogeneous solution. (The solution could be easily filtered through a 0.2 µm syringe filer.)

Table 5.1. TGBC OTFT performance of devices with pristine PSC (PEI = 0 wt. %) or PSC:PEI blend films as channel semiconductors. Data were obtained from at least five devices for each condition.

Polymer	PEI [wt. %]	$T_{Ann.}$ [a] [°C]	$\mu_{e,max}$ [b] [$cm^2V^{-1}s^{-1}$]	$\mu_{e,ave}$ (std [c]) [$cm^2V^{-1}s^{-1}$]	$\mu_{h,max}$ [d] [$cm^2V^{-1}s^{-1}$]	$\mu_{h,ave}$ (std) [$cm^2V^{-1}s^{-1}$]	V_{th} [e] [V]	I_{on}/I_{off} [f]
P5-1	0	100	0.088	0.071 (0.016)	0.060	0.052 (0.011)		
		150	0.40	0.38 (0.016)	0.29	0.29 (0.0058)		
		200	0.47	0.41 (0.054)	0.41	0.33 (0.052)		
	0.5	100	0.097	0.073 (0.020)	0.007	~2.7 × 10^{-3}		
		150	0.55	0.37 (0.11)	0.005	~1.7 × 10^{-3}		
		200	0.37	0.31 (0.032)	0.002	~8.6 × 10^{-4}		
	1	100	0.16	0.12 (0.023)		None	2	~10^2-10^3
		150	0.64	0.41 (0.15)		None	20	~10^3
		200	0.56	0.44 (0.093)		~1 × 10^{-3}	28	~10^2-10^3
	2	100	0.34	0.18 (0.084)		None	9	~10^4-10^5
		150	0.38	0.27 (0.076)		None	12	~10^3-10^4
		200	0.88	0.61 (0.20)		None	21	~10^3-10^4
	4	100	0.063	0.050 (0.0094)		None	-5	~10^3-10^4
		150	0.39	0.32 (0.085)		None	12	~10^3-10^4

		200	0.30	0.27 (0.034)		None	22	~10^3-10^4
	10	100	0.068	0.053 (0.0089)		None	0	~10^1-10^2
		150	0.21	0.16 (0.029)		None	8	~10^2-10^3
		200	0.21	0.17 (0.028)		None	20	~10^3-10^4
	20	150	0.15	0.12 (0.022)		None	8	~10^2
		200	0.18	0.17 (0.011)		None	21	~10^3-10^4
P5-2	0	150	0.063	0.051 (0.0082)	0.098	0.056 (0.0029)		
	1	150	0.071	0.064 (0.0047)		~1×10^{-5}	24	~10^3
	2	150	0.084	0.072 (0.0097)		None	22	~10^3
	4	150	0.060	0.056 (0.033)		None	23	~10^3
P5-3	0	150	3.13	2.74 (0.28)	1.93	1.72 (0.17)		
	1	150	0.73	0.50 (0.15)	0.05	0.020 (0.024)		
	2	150	0.95	0.88 (0.058)		None	4	~10^2-10^3
P5-4	0	150	None	None	0.58	0.54 (0.034)	-12	~10^3
	2	150	0.027	0.024 (0.0021)	2.7×10^{-5}	~1.3×10^{-5}	37	~10^2

	4	150	0.011	0.010 (8.2 × 10^{-4})	9.4 × 10^{-4}	~3.9 × 10^{-4}	31	~10^2
	10	150	0.010	0.0074 (0.0017)		None	39	~10^2-10^3

a) Annealing temperature; b) Electron mobility measured at V_{DS} = 80 V; c) Standard deviation; d) Hole mobility measured at V_{DS} = -80 V; e) Threshold voltage; f) Current on-to-off ratio.

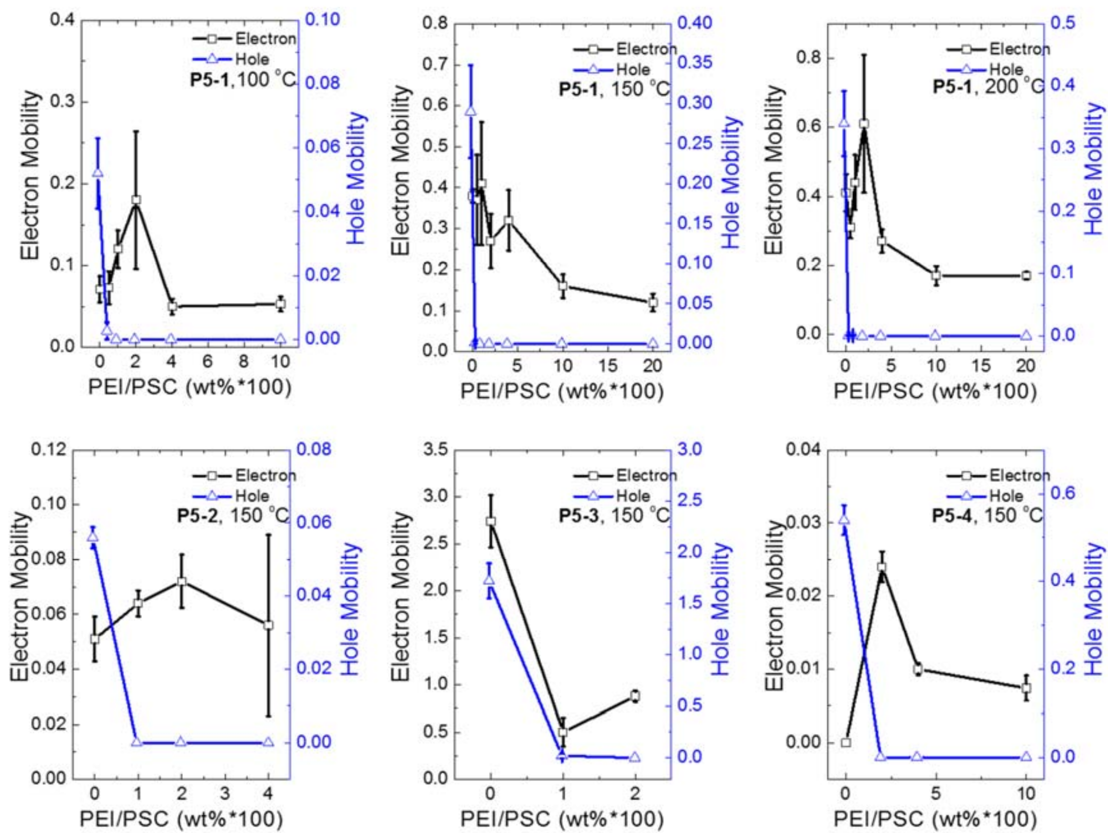

Figure 5.3. Dependence of hole and electron mobilities of **P5-1~P5-4** in OTFT devices on PEI content in the PSC:PEI blends. The PSC or PSC:PEI blend films were annealed at 100, 150 or 200 °C.

XRD patterns of the **P5-1**:PEI blend thin films with 1% PEI showed no or only a slight decrease in crystallinity in comparison to the pristine **P5-1** film at various annealing temperatures (Figure 5.4). When 2% PEI was added, the crystallinity of the blend film started to decrease. At 10% PEI,

the crystallinity of the 100 °C-annealed film became very poor, indicating that the ordering of **P5-1** polymer chains was impeded by the PEI molecules. At higher temperatures, however, the films became quite crystalline.

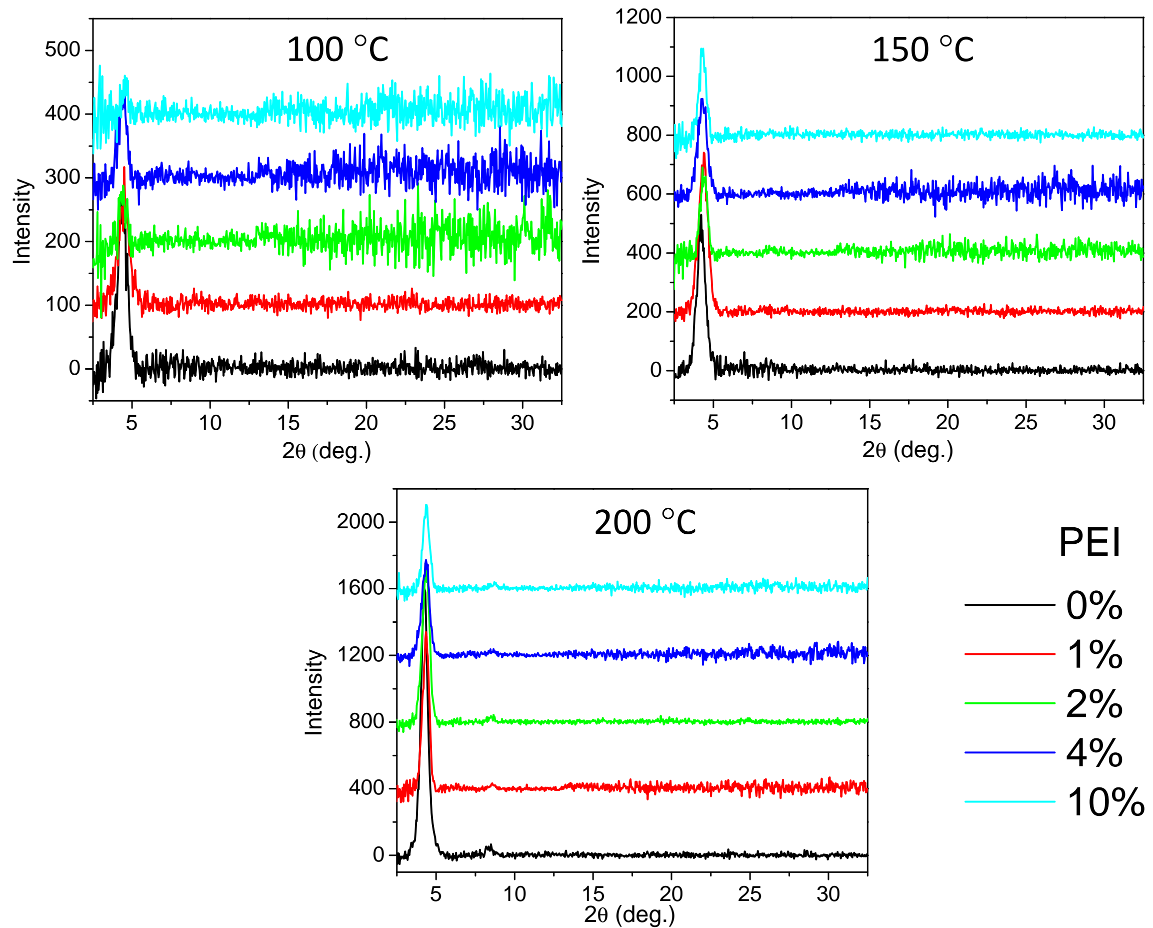

Figure 5.4. XRD patterns of spin-coated thin films of **P5-1** with different PEI contents (wt. % over **P5-1**) on bare SiO_2/Si substrates annealed at different temperatures measured in a reflection mode using Cu Kα1 radiation.

Time-of-flight secondary ion mass spectrometry (TOF-SIMS) is a powerful technique to determine the chemical composition of a surface within a depth of 1 to 2 nm. TOF-SIMS was utilized to shed light on the vertical distribution of PEI in the **P5-1**:PEI blend thin films, since accumulation of PEI on the substrate in the TGBC devices (Figure 5.2) would reduce the work function of Au source and drain contacts to influence the charge injection (a detailed discussion

will be made later). For comparison, three polymer thin films, PEI, **P5-1**, and **P5-1**:PEI (2% PEI) were deposited on Au coated n^{++}- Si substrates and annealed at 150 °C for 15 min in nitrogen prior to the TOF-SIMS measurement (Figure 5.5a). Argon gas cluster ions (Ar_{1000}^{+}) were used as the primary ions to sputter the polymer films.

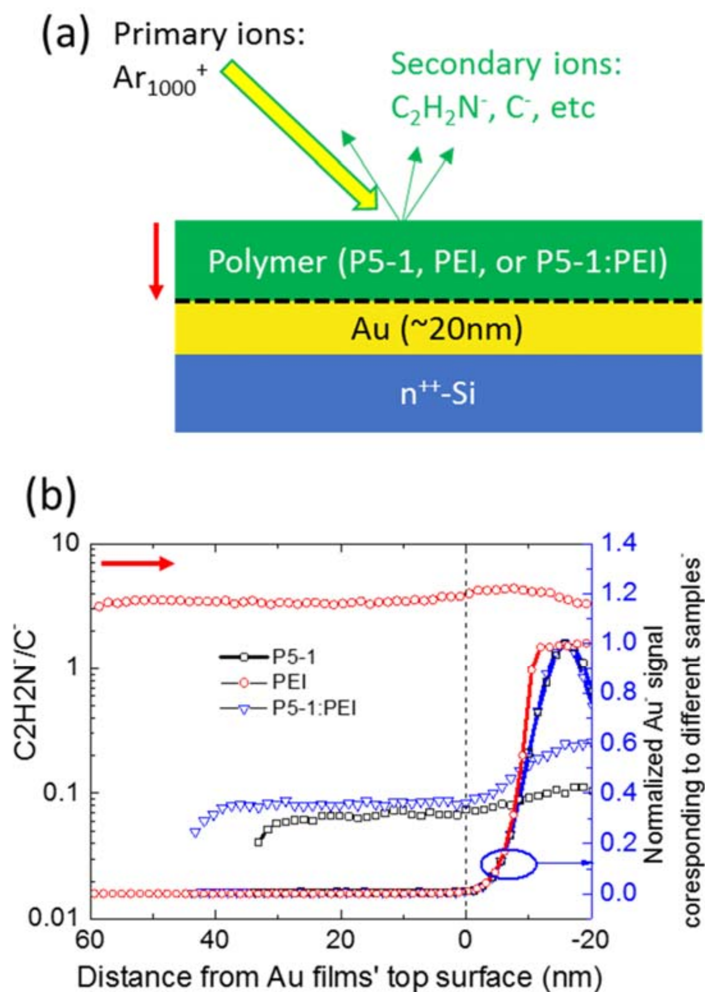

Figure 5.5. (a) Schematic of the TOF-SIMS measurement by sputtering a thin film of **P5-1**, PEI or **P5-1**:PEI (2% PEI) spin-coated on an Au (~20 nm)/n^{++}-Si substrate using argon cluster ions, Ar_{1000}^{+}, with ion beam energy of 5 keV and ion current of 1.8 nA. Positions on, above, and below the Au film's top surface are arbitrarily described be to 0 (horizontal dashed line), positive values, and negative values in units of nm, respectively. The secondary ion species, $C_2H_2N^-$, C^-, and Au^- were detected and analyzed. (b) TOF-SIMS depth profiles of the $C_2H_2N^-/C^-$ ratios of **P5-1**, PEI and **P5-1**:PEI (2% PEI) blend films spin-coated on Au/n^+-Si substrates as shown in (a). The polymer thin films were annealed at 150 °C for 15 min in nitrogen in a glove box prior to the measurement. Normalized Au^- signals (on the right Y axis) are also shown as depth references and were used to determine the positon of polymer/Au interface (the vertical dashed line at 0 nm).

Among many secondary ion species detected for the PEI film, $C_2H_2N^-$ was chosen for analysis because of its suitable signal intensity and appropriate mass for differentiating it from other ion species. For the pristine **P5-1** film, $C_2H_2N^-$ ions were also observed because this polymer contains C, H, and N atoms. Nonetheless, since $C_2H_2N^-$ signals for **P5-1** were about two orders of magnitude weaker than those of PEI, analysis of this ion species can still serve our purpose to study the vertical distribution of PEI in the **P5-1**:PEI film. Because the intensity of ion signals is significantly influenced by the experimental conditions, a comparison of the absolute $C_2H_2N^-$ ion counts between different polymer samples is inappropriate. Therefore the C^- ion species generated from each sample were used as an internal reference and used the $C_2H_2N^-/C^-$ ratio (the left Y-axis in Figure 5.5b to plot the depth profiles. In addition, to determine the position of the polymer/Au interface (the top surface of the Au film), Au^- ions were also analyzed. The vertical dashed line shown in Figure 5.5b represents the position where the Au- ions start to increase, indicating that the primary ion beam had etched away the polymer film and reached the Au film's top surface. It can be clearly seen that the $C_2H_2N^-/C^-$ ratio remained almost constant at distances ranging from 0 nm to ~40 nm away from the Au surface. Additionally, the $C_2H_2N^-/C^-$ ratio for the **P5-1**:PEI film is slightly higher than that of **P5-1** film throughout. These results suggest that PEI was rather evenly distributed along the vertical direction in the **P5-1**:PEI blend film. Lower $C_2H_2N^-/C^-$ ratios were obtained in the first few nm on the surface of both **P5-1** and **P5-1**:PEI films, which is considered to be due to the lower concentration of liberated secondary ion species that might act as a source of ionizing agents, causing the initial fluctuation of the ion signals.[152, 153] Another anomaly is that the $C_2H_2N^-/C^-$ ratios for **P5-1** and **P5-1**:PEI films increased dramatically once the Au layer was sputtered, while only slight increases in the actual $C_2H_2N^-$ ion counts within this range were observed (Figure 5.15). This could be explained by the stronger absorption of the "knock-off" $C_2H_2N^-$ ions over the C^- ions by the Au film.

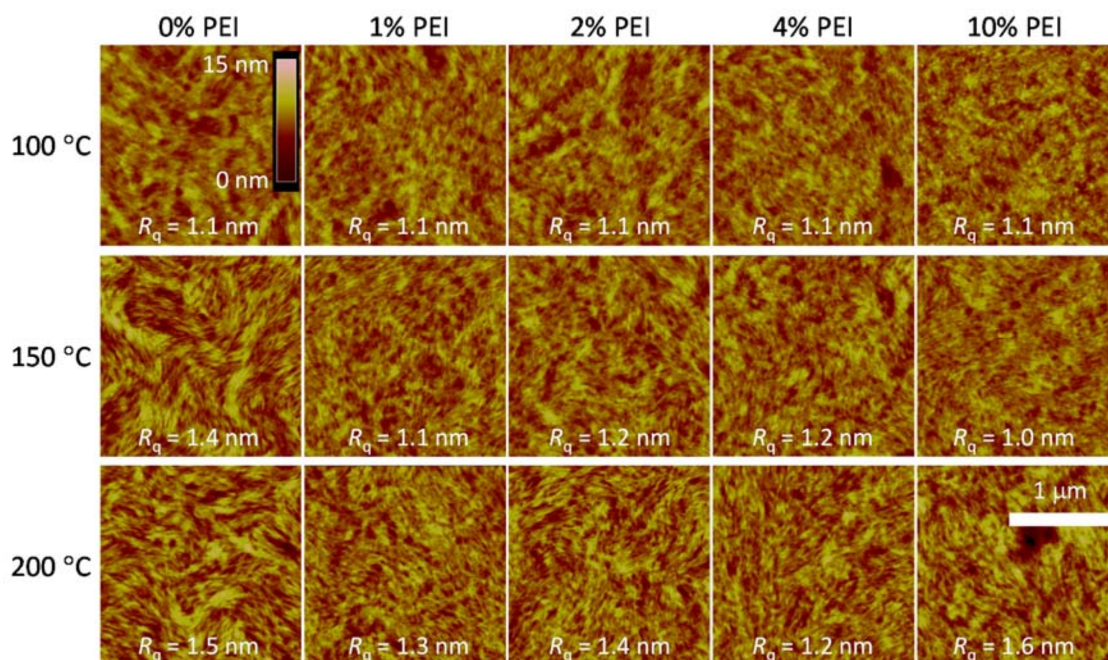

Figure 5.6. AFM height images of **P5-1**:PEI blend films with different PEI contents annealed at various temperatures. The films were spin-coated on SiO_2/Si substrates.

AFM images (Figure 5.6) showed that all the **P5-1**:PEI blend films containing up to 10% PEI and annealed at high temperatures up to 200 °C are very smooth and uniform (with the root mean square roughness (R_q) values < 2 nm). At each annealing temperature, a transition from nanofibrils composed of adjoining grains characteristic of pristine **P5-1** to the more distinct grains in the **P5-1**:PEI blend films was evident, which likely resulted from the separation of the polymer semiconductor grains by the amorphous PEI phase. With an increased amount of PEI, the excess PEI molecules present at the **P5-1** grain boundaries would be expected to disrupt the charge transport pathways and decrease the charge carrier mobility, in agreement with the trend observed in Figure 5.3. In general, the grains became more defined with increasing annealing temperature at each PEI concentration, which is consistent with the dependence of the thin film crystallinity and mobility on the annealing temperature.

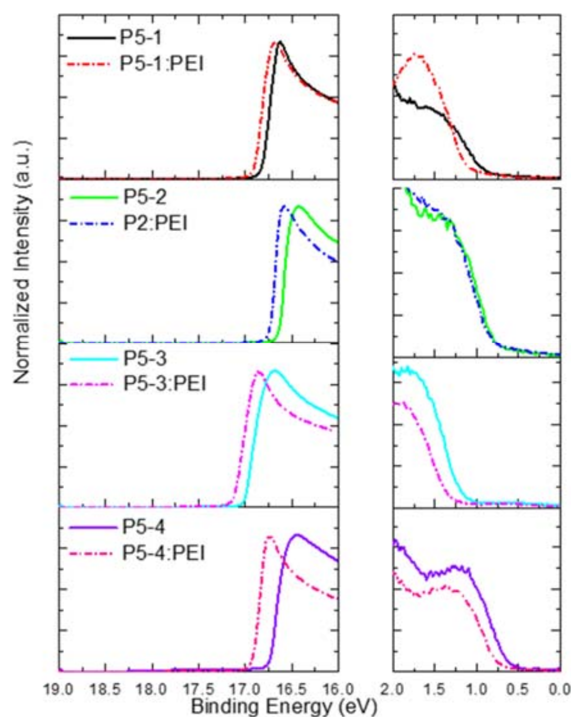

Figure 5.7. UPS spectra of 150 °C-annealed pristine and 2% PEI doped **P5-1**, **P5-2**, **P5-3**, and **P5-4** films deposited on Au (30 nm)/n+-Si substrates: Left: the high energy region showing the Secondary Electron Cut-off (SEC); Right: the HMO region showing the difference between and the Fermi level (at 0 eV) and the HOMO level (curve onset), $\eta = E_F - E_{HOMO}$. After adding PEI, all polymers showed a shift in the Fermi level towards vacuum and an enlarged difference between the HOMO and Fermi level, indicating an n-doping effect of PEI on these polymers.

The suppression of hole transport observed in **P5-1** by PEI can be explained by a shift in the Fermi level toward the LUMO due to the electron-donating nitrogen atoms in PEI, similar to the mechanism proposed for the ambipolar-to-n-type conversion of another D-A polymer, **P(NDI2OD-T2) (13)**, in the presence of an n-type dopant $CoCp_2$ or CsF. [87, 151] The raised Fermi level of the **P5-1**:PEI blend would increase the electron concentration but reduce the hole concentration. The increased electron concentration would inhibit hole injection[87, 151] and trap injected holes, [86] thereby suppressing hole transport.

Table 5.2. Field effect mobilities of dual-gated OTFT devices containing a TGBC configuration and a BGBC configuration as shown in Figure 5.2, where the polymer semiconductor (PSC) is **P5-1** (annealed at 150 °C) and the SiO_2 surface was modified with dodecyltrichlorosilane (DDTS). Data were obtained from five devices.

BGBC configuration				TGBC configuration			
Electron enhancement mode		Hole enhancement mode		Electron enhancement mode		Hole enhancement mode	
$\mu_{e,max}$ a) [$cm^2V^{-1}s^{-1}$]	$\mu_{e,ave}$ (std b)) [$cm^2V^{-1}s^{-1}$]	$\mu_{h,max}$ c) [$cm^2V^{-1}s^{-1}$]	$\mu_{h,ave}$ (std b)) [$cm^2V^{-1}s^{-1}$]	$\mu_{e,max}$ a) [$cm^2V^{-1}s^{-1}$]	$\mu_{e,ave}$ (std b)) [$cm^2V^{-1}s^{-1}$]	$\mu_{h,max}$ c) [$cm^2V^{-1}s^{-1}$]	$\mu_{h,ave}$ (std b)) [$cm^2V^{-1}s^{-1}$]
0.028	0.023 (0.0067)	0.0053	0.0037 (0.0011)	0.12	0.096 (0.019)	None	None

a) Electron mobility measured at V_{DS} = 80 V; b) Standard deviation; c) Hole mobility measured at V_{DS} = -80 V

Ultraviolet photoelectron spectroscopy (UPS) measurements were conducted on pristine and PEI-doped (2% PEI) **P5-1** films to determine the Fermi level (E_F) and HOMO level changes (Figure 5.7). The UPS results confirmed that the **P5-1** showed an increase in the Fermi level from -4.38 eV to -4.28 eV upon doping with PEI (Table 5.2). It was also observed that the difference η between HOMO and E_F increased from 0.91 eV to 1.12 eV by PEI doping, similar to the trend observed for the n-doping of pentacene.[154] Since the band gap of the PEI-doped **P5-1** did not change upon PEI doping, E_F shifted towards the LUMO level, which is similar to the observation reported for n-type doping with $CoCp_2$ or CsF. [87, 151] The increase in the Fermi level can be ascribed to the filling of electron traps in the polymer semiconductor by the n-type dopant, which can lead to an increase in electron mobility. [87, 155, 156] At a low PEI content (≤ 2%), an increase in electron mobility is indeed observed for the **P5-1**:PEI blends. When the PEI content is greater than 2%, a decrease in electron mobility is observed, which could be attributed to disruptions of the molecular ordering[87] and

charge transport pathways by the excess insulating PEI present at the grain boundaries as discussed above.

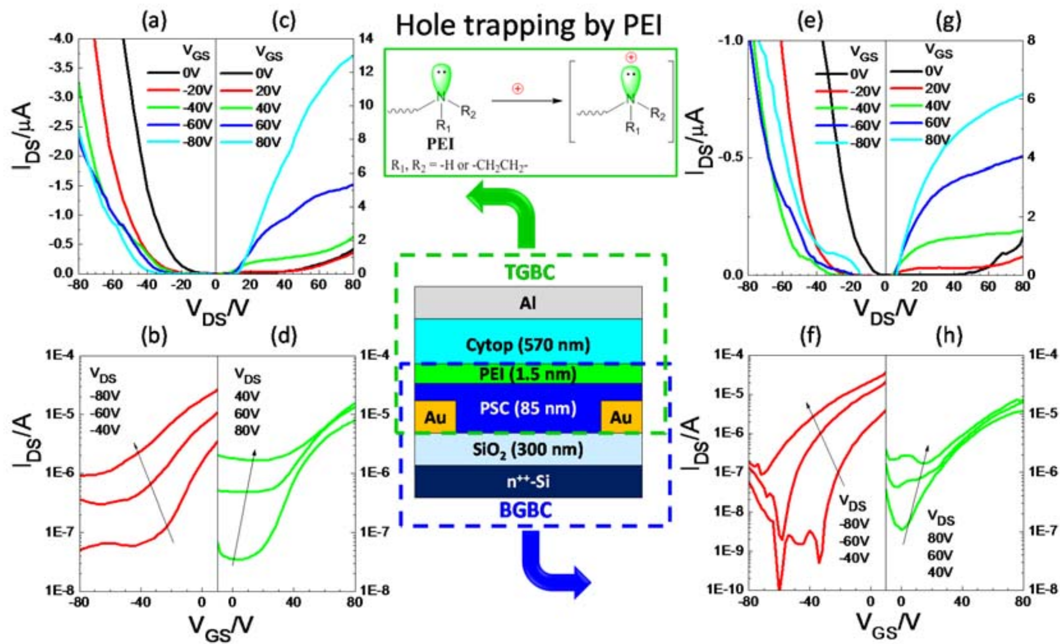

Figure 5.8. A dual-gate OTFT device containing a top-gate bottom-contact (TGBC) configuration and a BGBC configuration. TGBC configuration: (a) output and (b) transfer characteristics of hole enhancement mode; (c) output and (d) transfer characteristics of electron enhancement mode. BGBC configuration: (e) output and (f) transfer characteristics of hole enhancement mode; (g) output and (h) transfer characteristics of electron enhancement mode. Inserted scheme shows the proposed hole trapping effect of the nitrogen atoms in PEI, which suppresses or eliminates hole transport observed in the TGBC configuration and other devices using the PSC:PEI blends in this study. The polymer semiconductor (PSC) is **P5-1** (annealed at 150 °C) and the SiO_2 surface was modified with DDTS.

Another possible contribution to the suppression of hole transport is the work function reduction of the contact electrodes by PEI present in the polymer blend. As observed in our previous studies, a sufficiently reduced work function could block hole injection and suppress the hole transport behavior of ambipolar and p-type polymers.[145, 146]

To determine whether PEI promotes hole-trapping, a dual-gate OTFT device was designed using **P5-1** as the semiconductor on a DDTS-modified SiO_2/Si substrate, and Cytop and SiO_2 as the dielectrics for the TGBC and BGBC configurations, respectively. A thin layer of PEI (~1.5 nm)

was inserted between the thick polymer semiconductor layer (**P5-1:** ~85 nm) and the top dielectric Cytop layer (Figure 5.8). The active layer for the TGBC configuration is the top portion of the **P5-1** layer adjacent to the PEI layer, while the active layer in the BGBC configuration is the bottom portion of the **P5-1** layer adjacent to the SiO_2 layer. The purpose of using a rather thick **P5-1** layer is to prevent the Au source and drain contacts from contacting PEI. In this way, the hole blocking effect due to the work function reduction of Au by PEI can be avoided. Based on the charge transport behavior of these two configurations, we can gain further insight into the hole transport suppression mechanism, i.e., if PEI can trap holes, the TGBC configuration should show weakened or no hole transport performance, while the BGBC configuration should still transport holes.

In the hole enhancement mode of the TGBC configuration (Figure 5.8a and b), the I-V curves show that I_{DS} does not increase when holes accumulate in the top portion of the **P5-1** as $|V_{GS}|$ increases. The inability to transport holes is caused either by the lack of hole injection from the source or trapping of holes in the top portion of the **P5-1** layer, which is the active channel of this configuration. By examining the output curve at V_{GS} = 0 V in the electron enhancement mode (Figure 5.8 c), I_{DS} increases notably with V_{DS} when V_{DS} is > 30 V, which confirms that holes were injected from the drain (due to the positive drain-source bias) and transported to the source across the **P5-1** layer under the V_{DS} bias. This observation infers that the hole transport suppression observed in the hole enhancement mode at V_{GS}> 0 V and V_{DS}> 0 V (Figure 5.8 a and b) was caused by trapping of the holes induced by the negative gate bias in the **P5-1**and PEI interface and not due to a lack of injected holes. In the electron enhancement mode (Figure 5.8 c and d), the TGBC configuration showed typical electron transport performance with an electron mobility up to 0.12 $cm^2V^{-1}s^{-1}$ (Table 5.1). The above data obtained from the TGBC configuration strongly indicate that the top portion of the **P5-1** layer adjacent to the PEI layer is capable of transporting electrons but not holes. It should be noted that a rather high off-current in the electron enhancement mode (Figure 5.8 d) was observed due to hole conduction along the thick ambipolar **P5-1** layer in the portion far away from the hole-trapping PEI layer.

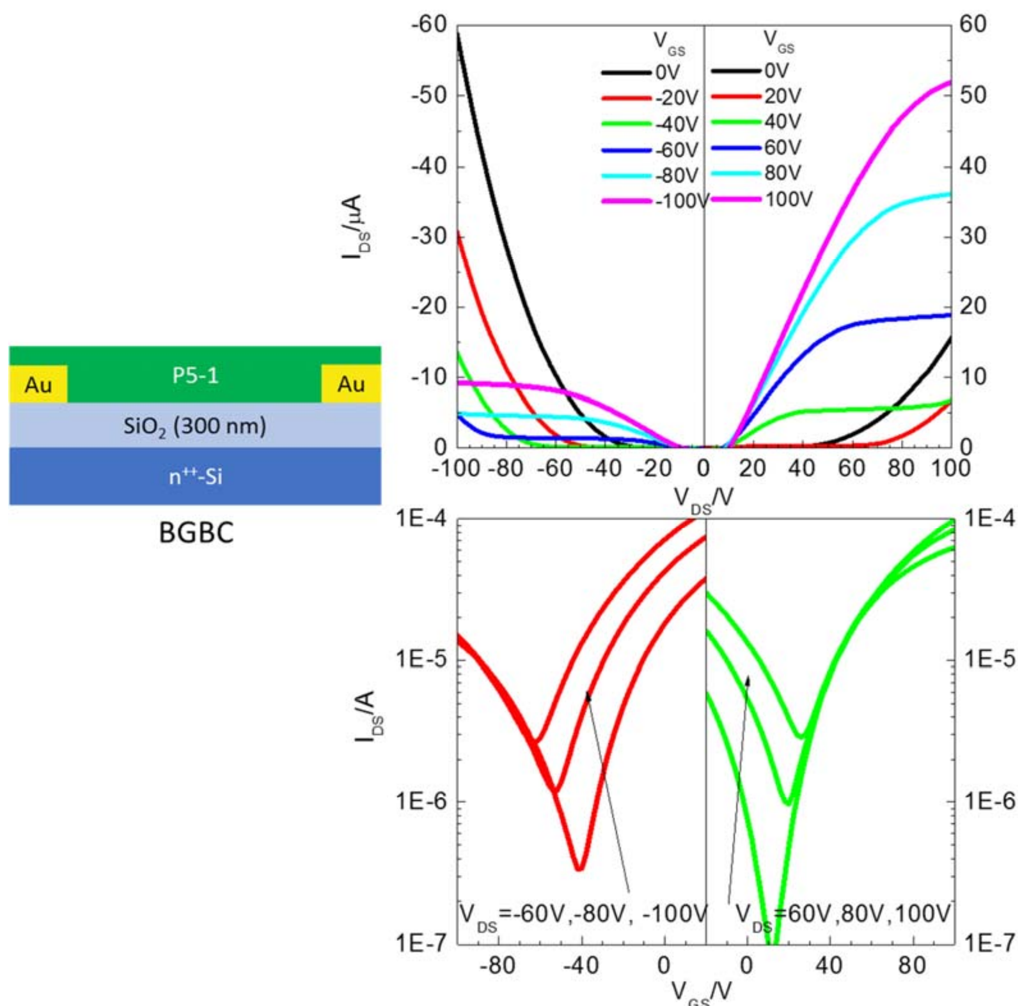

Figure 5.9. Output (top) and transfer (bottom) curves of a BGBC OTFT device with a pure **P5-1** thin film annealed at 150 °C, which show a characteristic ambipolar charge transport performance. Device dimensions: channel length L = 30 μm; channel width W = 1 mm. The average electron/hole mobilities from 5 devices are 0.067/0.020 $cm^2V^{-1}s^{-1}$, respectively.

On the other hand, the BGBC configuration in this dual-gate device showed obvious evidence of hole transport in the hole enhancement mode (Figure 5.8e and f), confirming that holes *were injected* from the source and transported to the drain through the bottom portion of **P5-1** layer

adjacent to the SiO_2 interface. The device also exhibited electron transport in the electron enhancement mode (V_{GS} > 0 V, V_{DS} > 0 V). $\bar{\mu}_e$ and $\bar{\mu}_h$ of the BGBC configuration with the dual-gate structure are 0.023 $cm^2V^{-1}s^{-1}$ and 0.0037 $cm^2V^{-1}s^{-1}$, respectively, which are similar to those (0.067 $cm^2V^{-1}s^{-1}$ and 0.020 $cm^2V^{-1}s^{-1}cm^2V^{-1}s^{-1}$) of the BGBC devices with pristine **P5-1** films built on DDTS-modified SiO_2/Si substrates (Figure 5.9 and Table 5.2). The much lower mobilities of BGBC devices on SiO_2/Si substrates than those ($\bar{\mu}_e$ = 0.38 $cm^2V^{-1}s^{-1}$ and $\bar{\mu}_h$ = 0.29 $cm^2V^{-1}s^{-1}$) of the **P5-1**-based TGBC devices shown in Figure 5.2a might be due to their different dielectric materials and/or the different PSC/dielectric interfacial properties.

Since the TGBC and BGBC configurations in the above dual-gate device exhibited unipolar n-channel and ambipolar device performances, respectively, it can be concluded that PEI promotes hole trapping, which is at least partially attributed to the suppression of hole transport observed in the **P5-1**:PEI blends (and other PSC blends discussed below), although the work function reduction of Au by PEI present in the PSC:PEI blends might also play a role.

UPS measurements confirmed that polymer semiconductors **P5-2**, **P5-3**, and **P5-4** also showed a shift of the Fermi level towards the vacuum and an increase in the difference between the Fermi level and the HOMO level upon PEI doping (Figure 5.7 and Table 5.2), indicating that hole suppression of these polymers in OTFTs would also be possible through PEI doping.

The same device structures (Figure 5.2 a and b) were utilized to evaluate **P5-2** and **P5-3**, which are ambipolar polymers, at an annealing temperature of 150 °C. Both polymers also showed complete suppression of hole transport when the PEI content is greater than 2% (Figure 5.3). The best electron mobility of 0.084 $cm^2V^{-1}s^{-1}$ was achieved in a **P5-2**:PEI blend containing 2% PEI, which is superior to the highest value of 0.063 $cm^2V^{-1}s^{-1}$ in the ambipolar devices based on pristine **P5-2** (Table 5.1). This improvement is probably due to the electron trap-filling effect of PEI discussed previously for the **P5-1**:PEI blend. For **P5-3**, the best unipolar n-channel device was also obtained in a **P5-3**:PEI blend containing 2% PEI that exhibited an electron mobility of 0.95 $cm^2V^{-1}s^{-1}$. However, this electron mobility is lower than that (up to 3.13 $cm^2V^{-1}s^{-1}$) of the ambipolar

devices with pristine **P5-3**. This drop in electron mobility in the **P5-3**:PEI blends might be caused by the poor morphology of the blend films (Figure 5.9). For the **P5-3**:PEI blend film containing 2% PEI, in particular, many large gaps between grain aggregates formed, which would disrupt the charge hopping between polymer semiconductor grain aggregates.

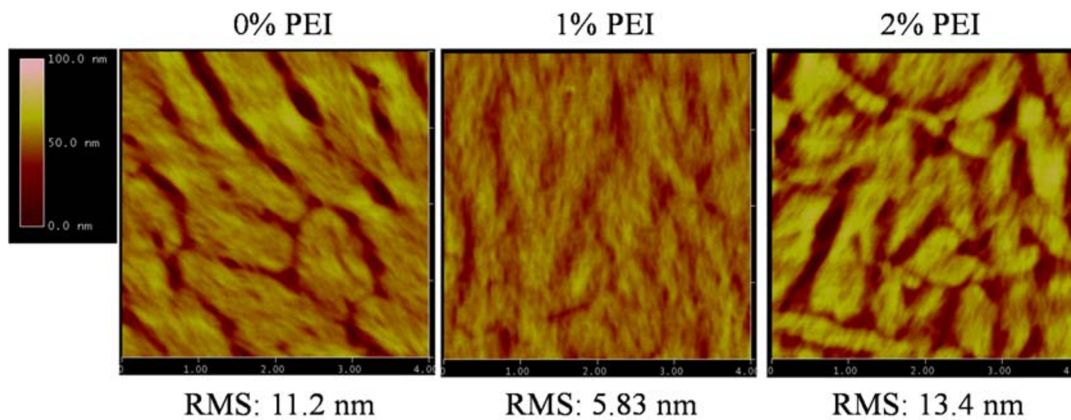

Figure 5.10. AFM height images (2 μm × 2 μm each) of thin films (~40-50 nm) of **P5-3** blended with varied amounts of PEI (wt % over **P5-3**) spin-coated on bare SiO_2/Si substrates and annealed at 150 °C for 15 min. RMS: the root-mean square roughness.

Pristine **P5-4** showed typical p-type semiconductor behavior with hole mobility up to 0.58 $cm^2V^{-1}s^{-1}$ when Au is used as the source/drain contacts (Table 5.1). When 2 % PEI was blended in **P5-4**, $\bar{\mu}_h$ dropped precipitously to 1.3 × 10^{-5} $cm^2V^{-1}s^{-1}$. On the contrary, electron transport behavior with $\bar{\mu}_e$ of 0.024 $cm^2V^{-1}s^{-1}$ was observed. Hole transport was completely suppressed at a higher PEI content of 10 %, but $\bar{\mu}_e$ decreased to 0.0074 $cm^2V^{-1}s^{-1}$ most likely due to the larger separation of **P5-4** grains by the increased amount of electrically insulating PEI. Since **P5-4** showed no electron mobility in its pristine form, the observation of electron transport behavior in the presence of PEI is most likely due to the filling of electron traps by PEI, a similar mechanism proposed to explain the electron transport performance of a poly(2-methoxy-5-2-ethylhexyloxy-1,4-phenylenevinylene

(MEH-PPV):decamethylcobaltocene (DMC, an n-type dopant) blend,[147] where the deep electron traps[157] in the polymer semiconductor could be filled by DMC.

5.3 Conclusion

In this study, a simple approach to converting ambipolar and p-type D-A polymer semiconductors into unipolar n-type polymers is demonstrated by adding a small amount of polyethylenimine (PEI) as an n-type dopant to obtain uniform dopant distribution and smooth thin films (with up to 10 % PEI and an annealing temperature of 200°C). The electron-rich nitrogen atoms in PEI are thought to fill the electron traps, raise the Fermi level and trap sites for holes, resulting in unipolar n-channel OTFT performance with improved electron mobility. The method presented here will be very useful in achieving high performance electron transport organic semiconductors for CMOS logic and other applications such as organic solar cells and thermoelectric devices using readily available ambipolar and even p-type organic semiconductors.

5.4 Experimental Section

5.4.1 Materials and Methods

PEI (branched polyethylenimine with an M_w of ~25 kDa by light scattering and an M_n of 10 kDa by GPC) was purchased from Sigma Aldrich. Cytop (a fluoropolymer of Asahi Glass Co., Ltd.) was purchased from Bellex International Corporation. All other chemicals were obtained from commercial sources and used without further purification. Ambipolar polymers, **PDBTAZ** (**P5-1**)[119] (M_n = 102 kDa, PDI (polydispersity index) = 4.30), **PPzDPDP-BT** (**P5-2**)[134] (M_n = 27.5 kDa, PDI = 2.84), **PDBPyBT** (**P5-3**)[66] (M_n = 26.3 kDa, PDI = 3.56), and a p-type polymer, **PDQT** (**P5-4**)[37] (M_n = 40 kDa, PDI = 3.22), used in this study were synthesized and reported previously.

Ultraviolet–visible-near infrared (UV-Vis-NIR) spectroscopy measurements of polymer thin films spin-coated on quartz were performed on a Perkin Elmer Lambda 1050 UV/Vis/NIR spectrophotometer. The X-ray diffractometry (XRD) measurements of the polymer thin films spin-coated on SiO_2/Si substrates were carried out on a Bruker D8 Advance diffractometer with Cu Kα1 radiation (λ = 1.5406 Å) in Bragg geometry. Atomic force microscopy (AFM) images of polymer thin films spin-coated on SiO_2/Si substrates were obtained by a Dimension 3100 Scanning Probe Microscope.

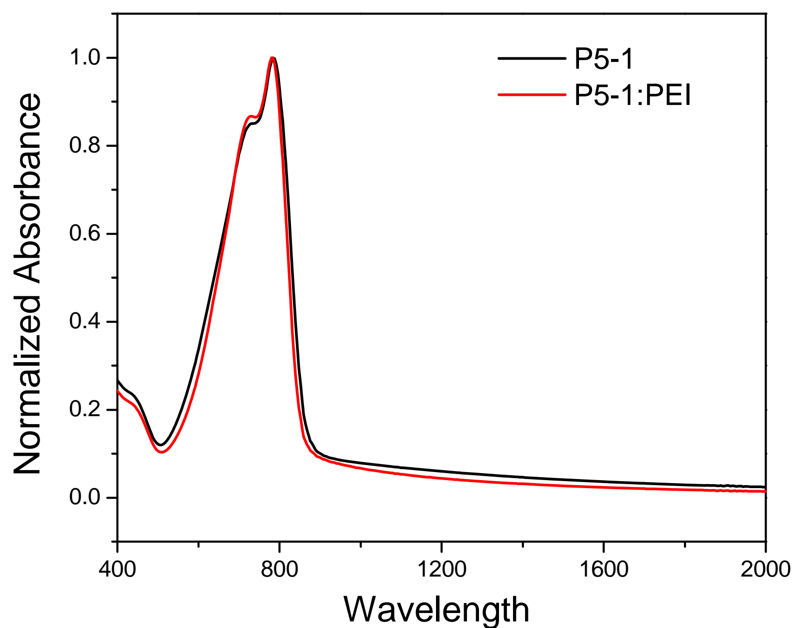

Figure 5.11. UV-Vis-NIR absorption spectra of as-cast thin films of pure **P5-1** and a **P5-1**:PEI (2% PEI) blend on quartz.

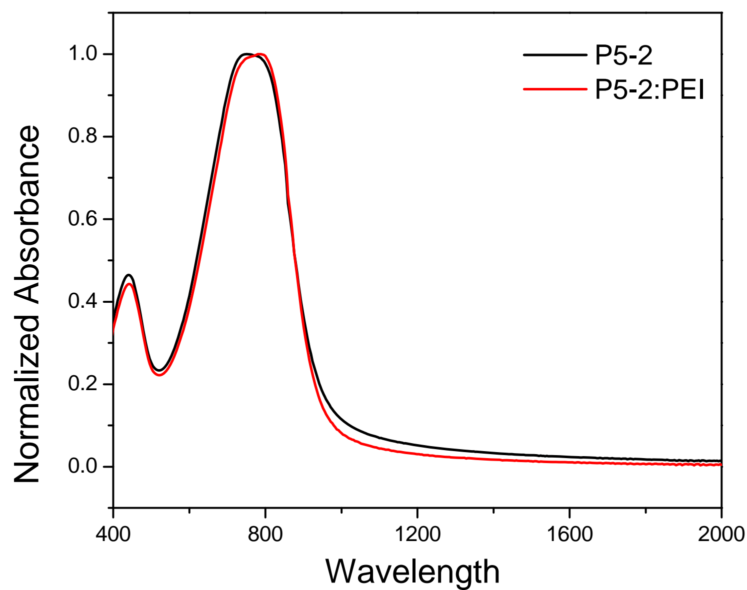

Figure 5.12. UV-Vis-NIR absorption spectra of as-cast thin films of pure **P5-2** and a **P5-2**:PEI (2% PEI) blend on quartz.

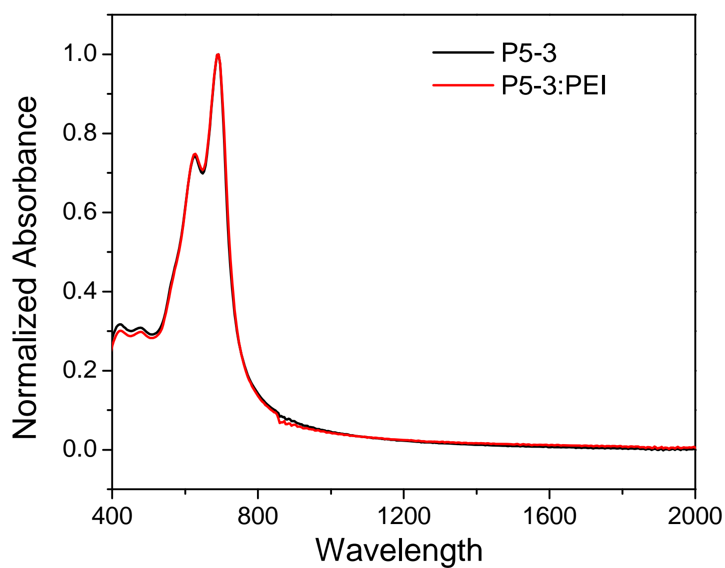

Figure 5.13. UV-Vis-NIR absorption spectra of as cast thin films of pure **P5-3** and a **P5-3**:PEI (2% PEI) blend on quartz.

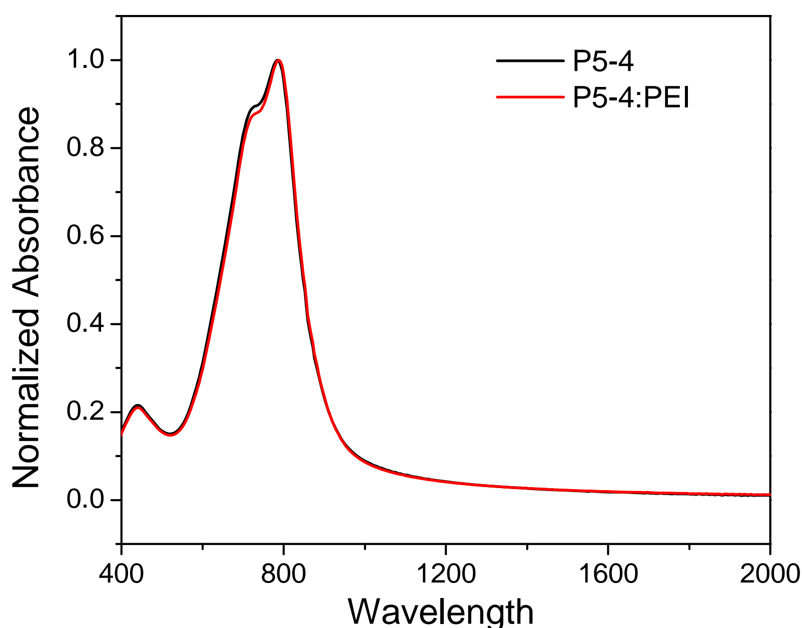

Figure 5.14. UV-Vis-NIR absorption spectra of as-cast thin films of pure **P5-4** and a **P5-4**:PEI (2% PEI) blend on quartz.

5.4.2 Time-of-flight Secondary Ion Mass Spectrometry (TOF-SIMS) Measurement:

A one-side polished, 500 μm-thick heavily n-doped Si(100) (n^{++}-Si) substrate with a resistivity of 0.1-0.01 ohm-cm was cleaned by RCA 1 (H_2O_2-NH_4OH-H_2O) and then rinsed in buffered HF for 1min to remove any SiO_2 present on its surface. A 20 nm Au layer (with 3 nm of Cr as a bottom adhesion layer) was thermally deposited on the polished side of the Si substrate. A polymer film was then deposited on the substrate by spin-coating a polymer solution and then drying on a hot plate at 150°C for 15 min. TOF-SIMS depth profiles of the polymer film were obtained using an ION-TOF 5 system (IONTOF GmbH) in the spectrometry mode (non-interlaced) with a reflection time-of-flight analyzer operated in the negative polarity mode with a Bi^{3+} analysis ion source (30 kV), cycle time of 200 μs, and sampling area of 150 × 150 μm^2. [158] The sample was sputtered with Ar cluster ions (Ar_{1000}^+) at ion beam energy of 5 keV over an area of 400 × 400 μm^2. The TOF-SIMS spectra were mass-calibrated on carbon fragments (C_x). The species with mass-to-charge

ratio (m/q) equal to 40 (corresponding to $C_2H_2N^-$), 12 (corresponding to C^-) and 197 (corresponding to Au^-) were used for detailed analysis.

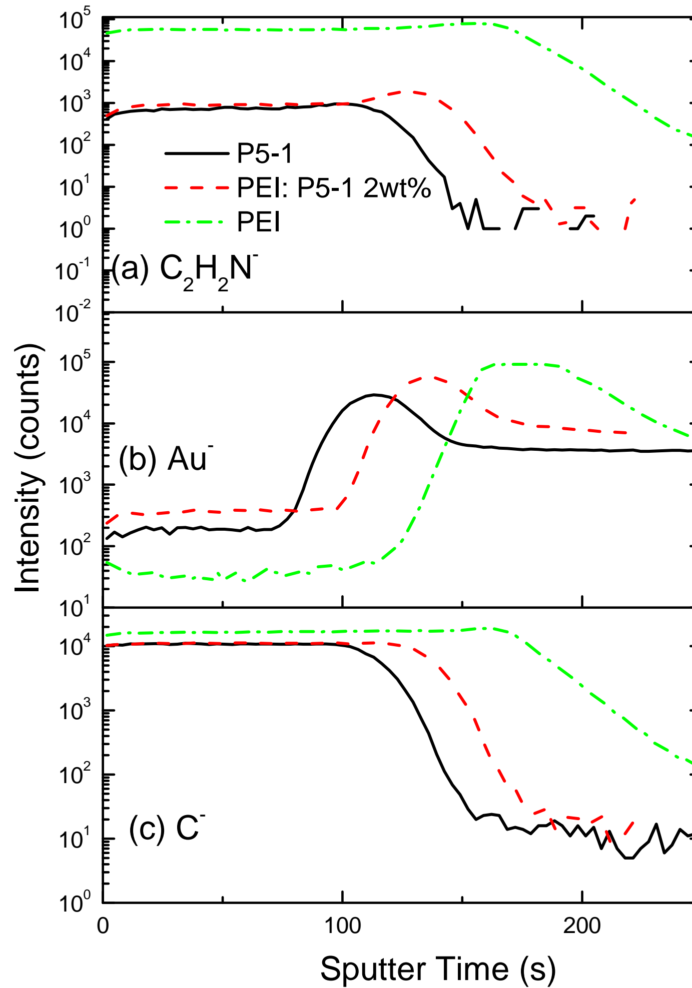

Figure 5.15. TOF-SIMS depth profiles of pristine **P5-1** (black solid line), 2wt% PEI doped **P5-1** (red dash line) and pure PEI (green dash dot line) on Au/Si substrate: a) $C_2H_2N^-$, mass-to-charge ratio (m/q) equal to 40, b) Au^-, m/q = 197, and c) C^-, m/q = 12.

5.4.3 OTFT Device Fabrication: OTFT devices were fabricated on n^{++}-Si wafer substrate with a 300 nm-thick thermally grown SiO_2 layer. Au source and drain electrodes (40 nm thick) with a Cr adhesion layer (3 nm) were thermally deposited on the substrate using a conventional

photolithography method. The substrate with source and drain pairs was cleaned sequentially with air plasma, acetone and isopropanol before being dried under a nitrogen flow.

Top-gate bottom-contact (TGBC) devices with structure (a) (Figure 5.2a)**:** A polymer semiconductor (PSC) solution in chlorobenzene (5 mg mL^{-1} for **P5-1**), chloroform (10 mg mL^{-1} for **P5-3**) or a mixture (9/1, v/v) of chloroform and 1,2-dichlorobenzene (DCB) (5 mg mL^{-1} for **P5-2** and **P5-4**) was spin-coated on the cleaned substrate to form a film with thickness of ~40-50 nm and then annealed at 100, 150 or 200 °C for 15 min in nitrogen. Then Cytop (~570 nm with C_i = 3.2 nF cm^{-2}) as the gate dielectric layer was deposited on the PSC by spin-coating, followed by drying on a hotplate at 100 °C for 1 h. Finally, an Al layer with a thickness of 70 nm was thermally deposited as the gate electrode. The device performance was characterized in air in the absence of light using an Agilent 4155C Analyzer. The carrier mobility was calculated from the slope of the $(I_{DS})^{1/2}$ versus V_{GS} plot in the saturation regime according to the equation: $I_{DS} = \mu C_i W/(2L) (V_{GS}-V_{TH})^2$, where L (30 μm) and W (1 mm) are the channel length and width, respectively.

TGBC devices with structure (b) (Figure 5.2b): The devices were fabricated and characterized following the similar procedure described for devices with structure (a) except that a PSC:PEI mixture solution was used to make the PSC:PEI blend layer. A mixture of PSC:PEI in a certain ratio was dissolved in chlorobenzene (for **P5-1**), chloroform (for **P5-3**) or a mixture (9/1, v/v) of chloroform and DCB (for **P5-2** and **P5-4**) by stirring at 45 °C for 1 h before cooling to room temperature.

Dual-gate devices (Figure 5.8): The devices were fabricated and characterized following the similar procedures described for devices with structure (a) except that a PEI layer (~1.5 nm) was deposited on top of the PSC (**P5-1**) layer by spin-coating a PEI solution (0.062 mg mL^{-1}) in IPA. The thickness of the PSC layer was ~85nm. These dual-gate devices contain TGBC and bottom-gate bottom-contact (BGBC) configurations.

BGBC devices (Figure 5.9): A solution of **P-1** in chlorobenzene (5 mg mL^{-1}) was spin-coated on the cleaned substrate to form a polymer film with a thickness of ~40-50 nm, followed by annealing at 150 °C for 15 min in nitrogen.

Output and transfer characteristics of OTFTs discussed in Chapter 5 are included in the Appendix.

Ultraviolet photoelectron spectroscopy (UPS) measurement: A polymer semiconductor (with or without 2 wt% PEI) solution in chloroform (1 mg mL^{-1}) was spin-coated on a 30 nm Au film coated on n^{++}-Si substrate to form a film, followed by annealing at 150 °C for 15 min in nitrogen. UPS measurements were performed in a PHI5500 Multi-Technique described in Chapter 4. [154]

Chapter 6. Chapter 6. Conclusion and Outlook

This thesis successfully demonstrated two general approaches to achieving high mobility n-type unipolar polymer semiconductors from ambipolar and p-type polymer semiconductors, broadening the applications of polymer semiconductors in low power consuming complementary circuits.

In Chapter 2, a copolymer semiconductor **PDBPyBT** was designed and synthesized achieving high ambipolar charge transport performance in OTFT devices with a record electron mobility value of up to 6.30 $cm^2V^{-1}s^{-1}$ at a mild annealing temperature of 100 ºC. The polymer is based on a new acceptor building block, a DPP core flanked with two 2-pyridinyl substituents (**DBPy**), which has a completely planar molecular structure and a low-lying LUMO energy level from the relatively electron deficient flanked pyridine ring. The resulting high electron mobility was attributed to the low LUMO energy level, high crystallinity and short π-π stacking distance of 0.36 nm. The high ambipolar charge transport performance demonstrates that **DBPy** is a highly promising building block for polymer semiconductors for OTFTs, integrated circuits and other applications.

For the promising **DBPy** acceptor obtained in Chapter 2, a thieno[3,2-*b*]thiophene (TT) unit, a well-known building block for high performance p-type polymers,[30, 33, 123, 124] was chosen as an electron donor to achieve a high mobility polymer. The polymer **PDBPyTT** also showed ambipolar performance with high electron and hole mobilities of 3.36 $cm^2V^{-1}s^{-1}$ and 2.65 $cm^2V^{-1}s^{-1}$, respectively, in TGBC OTFT devices with Au source and drain electrodes. In comparison to **PDBPyBT** in Chapter 2, **PDBPyTT** has the same π-π stacking distance of 0.36 nm, but the XRD data showed that **PDBPyTT** polymer chains in thin films are less ordered, resulting in lower charge transport performance. We found that when the source and drain electrodes were modified with a thin layer of polyethyleneimine (PEI), the hole transport characteristic of this polymer disappeared and a unipolar n-channel performance with a high electron mobility of 2.38 $cm^2V^{-1}s^{-1}$ was realized.

Electrode modification with PEI is a promising new approach to convert ambipolar polymers into unipolar n-type polymers.

As an effective way to convert **PDBPyBT**-based ambipolar OTFTs into n-type OTFTs in Chapter 3, the strategy of PEI modification of Au electrodes was applied to several other ambipolar and p-type polymer semiconductors with low-lying LUMO energy levels (≤-4eV) to successfully realize the n-type polarity conversion in Chapter 4. After modifying the Au source and drain electrodes by an ultrathin layer (2~5 nm) of PEI, the work function of gold is dramatically reduced to as low as 3.2 eV to suppress the injection of holes and facilitate the electron-only charge transport in OTFTs. This general approach broadens the application of ambipolar and even p-type polymers for fabricating n-channel OTFTs.

In Chapter 5, we developed a novel, simple strategy to convert several ambipolar and p-type polymer semiconductors into high performance n-type unipolar polymer semiconductors in OTFTs by doping with PEI. The electron rich nitrogen atoms in PEI are thought to fill the electron traps to increase the Fermi level of the polymer semiconductor, resulting in n-type unipolar OTFTs with improved electron mobility. The PEI dopants (with up to 10%) remained uniformly distribute with the polymer semiconductors even when annealed at high temperature up to 200ºC, which is more advantageous than small molecule or inorganic n-dopants.

Since n-type unipolar OTFTs have been obtained by modifying the source/drain electrodes or doping ambipolar polymer semiconductors by PEI, complementary logic circuit (Figure 6.1) can be demonstrated by choosing appropriate p-type polymer semiconductors. Solution-processed film deposition, including spin-coating, drop-casting, doctor blading, printing, etc. is suitable for large area, low cost, flexible and low temperature applications. Printing provides an especially unique ability to deposit multiple materials and pattern devices in one step.

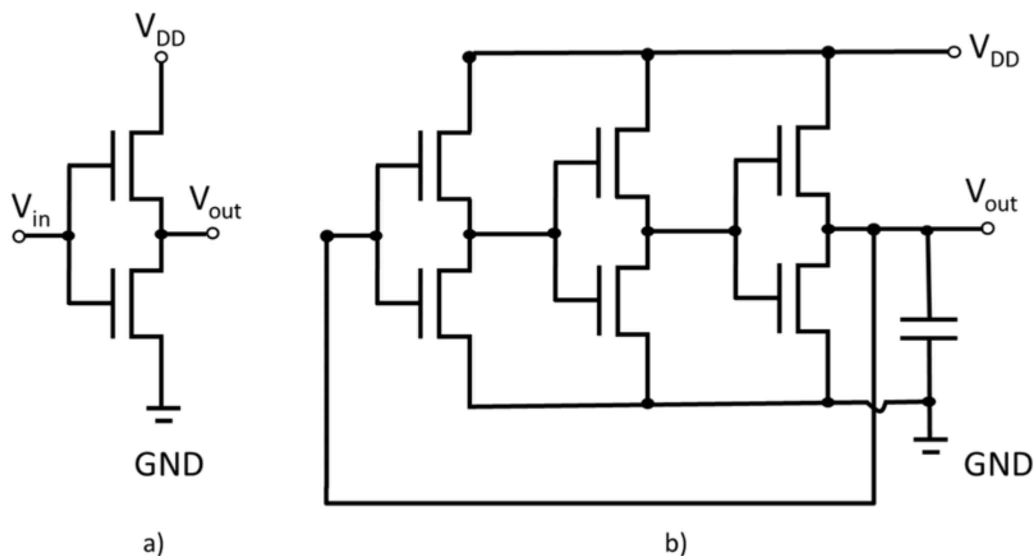

Figure 6.1. Architecture of complementary inverter (a) and ring oscillator built of three complementary inverters (b).

Inkjet printing is one of the effective ways to pattern the devices (print different film patterns on same substrate) and realize low-cost organic electronics.[159] Therefore, inkjet printing to deposit both p-type and n-type OTFT patterns on one substrate was explored at the end of this work. The best n-type polymer semiconductor for complementary logic circuit is **PDBPyBT** with PEI dopant (Chapter 5). Therefore, the PEI-doped **PDBPyBT** was used as an n-type semiconductor and the pristine **PDQT-24**[160] was used as a p-type semiconductor to fabricate inverters comprised of n- and p-type TGBC OTFTs by inkjet printing. First, the PEI-doped **PDBPyBT** and **PDQT-24** inks were inkjet printed on the target n- and p-channels that were pre-patterned Au source and drain pairs on a SiO_2/Si substrate. Then, a Cytop solution was spin coated on the entire substrate to form the gate dielectric layer. Finally, an Al layer was thermally deposited on top of the Cytop layer as the gate electrode to complete the OTFTs and the inverters. While the n-channel OTFTs operated well, the p-channel OTFTs showed very poor performance. The failure of the p-channel OTFTs was considered due to the hole transport suppression of **PDQT-24** by the PEI contaminant. When the Cytop solution was spin coated, PEI in the PEI-doped **PDBPyBT** was probably partially

dissolved by the solvent in the Cytop solution and transferred to the **PDQT-24** channels. To prevent the p-type OTFTs from PEI contamination, a BGBC OTFT configuration is more desirable. However, **PDBPyBT** performs poorly in BGBC devices due to its poor contact with the dielectric layer (Chapter 2). Therefore, an ambipolar polymer semiconductor **PIBDFTT** (Figure 6.2)[161] with average electron and hole mobilities of 0.24 and 0.17 $cm^2V^{-1}s^{-1}$, which was recently synthesized in our lab, was chosen to replace **PDBPyBT**.

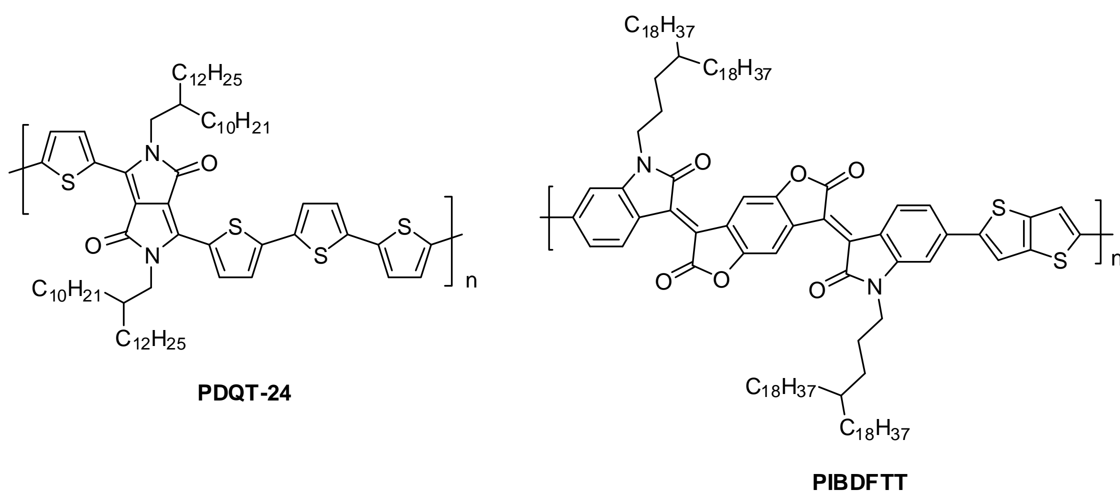

Figure 6.2. Chemical Structure of **PDQT-24**[160] and **PIBDFTT**.[161]

Solutions of **PDQT-24** and 2% PEI doped **PIBDFTT** in dichlorobenzene were printed on a DDTS modified SiO_2/Si substrate with pre-patterned Au source/drain pairs by Ceradrop's L-Series Inkjet printer to form p-type and n-type BGBC OTFTs and inverters. (**PDQT-24** and **PIBDFTT** polymers were synthesized by Dr. Wei Hong and Yinghui He, respectively, and the printing process and programming were performed by Melissa Chow in Dr. William Wong's group.) The OTFTs and inverters were tested in air.

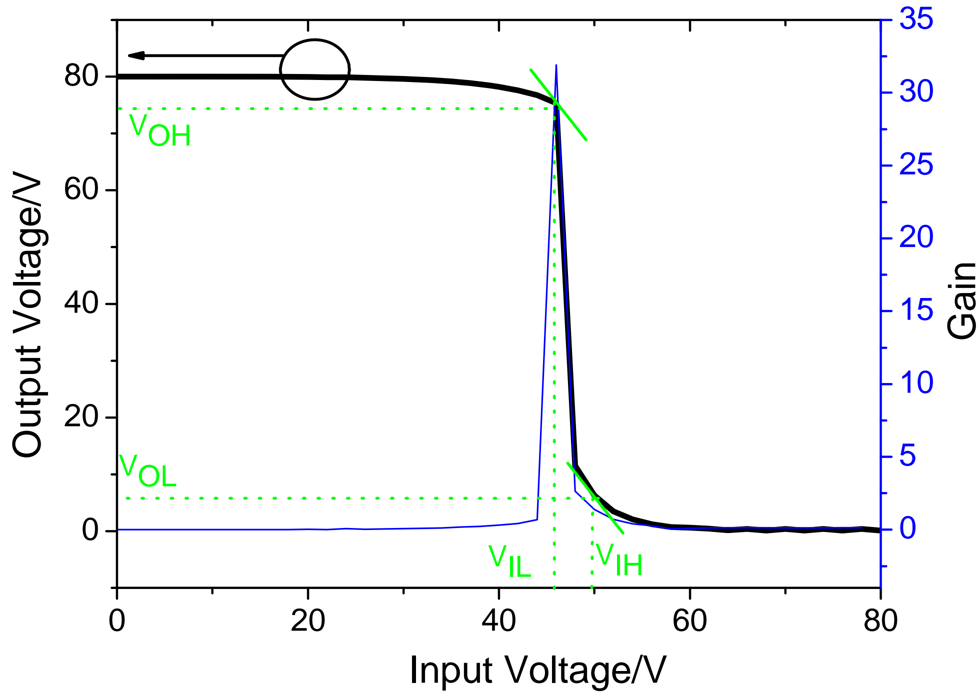

Figure 6.3. Voltage transfer characteristic (VTC) of the complementary inverter teste in air.

The voltage transfer characteristic (VTC) with a supply voltage (V_{DD}) of 80 V is shown in Figure 6.3. Clear inverter action with full swing close to the supply voltage (V_{out} = 80 V when V_{in} = 0 V, and V_{out} = 0 V when V_{in} = 80 V) is observed. The voltage gain defined as abs ($\frac{dV_{out}}{dV_{in}}$) was ~32, which is higher than many of the reported polymer-based inverters.[11, 162] The relatively high operation voltage stems from the high threshold voltages of the OTFTs, which can be improved by increasing the gate dielectric capacitance. The inverter characteristic is highly symmetric with a switching voltage at 47.1 V close to half of the supply voltage (80 V). The noise margins at the high (NM_H) and low levels (NM_L) are calculated as follows:

$$NM_H = V_{OH} - V_{IH} \quad (4)$$

$$NM_L = V_{IL} - V_{OL} \quad (5)$$

where V_{IL} and V_{IH} are the minimum and maximum input voltages, respectively, and V_{OL} and V_{OH} are the minimum and maximum output voltages, respectively (Figure 6.3). V_{IL}, V_{IH}, V_{OL} and V_{OH} were obtained when the slope of V_{out} vs V_{in} is -1 ($dV_{out}/dV_{in} = -1$). The NM_H and NM_L shown in Figure 6.2 were 25.4 and 39.7 V, respectively, giving a large allowance for robust logic operation (> 20% of V_{DD}). [163] Tests on individual p-type and n-type OTFT devices in inverters in air showed hole and electron mobilities of 0.05 and 0.005 $cm^2V^{-1}s^{-1}$, lower than those tested in N_2 glove box, which were 0.5 and 0.1 $cm^2V^{-1}s^{-1}$ for **PDQT-24** and **PIBDFTT**, respectively.

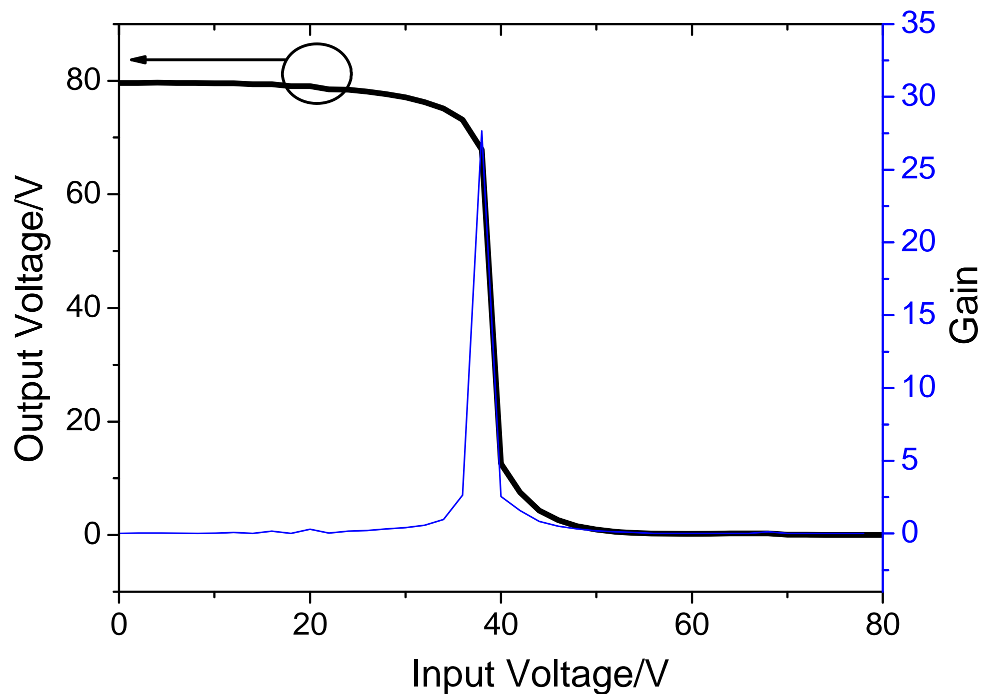

Figure 6.4. Voltage transfer characteristic of the complementary inverter encapsulated by PMMA.

The low hole and electron mobilities in the previous inverter may be due to air instability of the semiconductors. Additionally, air may also shift the threshold voltage (V_{TH}) of OTFTs,[164] which will move the switching voltage of the inverter.[11] So we protected the devices from the ambient environment by encapsulation with PMMA film to shift the switching voltage towards the half of

V_{DD} and thus to get more balanced noise margin. As expected, the resulting inverter characteristic of the inverter in Figure 6.4 showed clear inverter action with the full swing close to the supply voltage. The switching voltage at 39.0 V is roughly equal to half of the supply voltage (80 V) and the more balanced NM_H and NM_L at 31.2 and 28.5 V, respectively, were obtained, which are slightly improved over the inverter tested in air. Furthermore, switching speed is very important in integrated circuit applications, which can be improved by increasing charge carrier mobility.[11] The hole and electron mobilities of p-type and n-type OTFTs in the encapsulated inverter were 0.5 and 0.05 $cm^2V^{-1}s^{-1}$, respectively, which are one order of magnitude higher than the one tested in air. The switching speed can be evaluated in the ring oscillators, which is proposed as part of the future work.

In conclusion, the contributions of this work are as follows

1. A novel **DBPy** acceptor building block was developed and used to obtain two new semiconducting polymers. The polymers showed high ambipolar charge transport performance and one even set a record for electron mobility.
2. A universal approach to realizing n-type unipolar semiconducting polymers by converting ambipolar and p-type polymer semiconductors with a simple modification of the source and drain electrodes with PEI was developed. This method provides much more choices of polymer semiconductors to fabricate n-channel OTFTs that can be used for complementary logic circuits and other applications.
3. A very simple and convenient way to convert ambipolar and p-type polymer semiconductors to unipolar n-type semiconductors was developed, which uses PEI as an n-dopant. The new approach can make use a variety of high performance ambipolar polymers and p-type polymers to fabricate complementary logic circuits using printing techniques.

The future work after this thesis is proposed as follows:

1. Optimize the printing conditions including solvent and concentration of polymer solutions to obtain optimal viscosity of the solution, film thickness, film uniformity, and the size of the printed droplets and features.[162]
2. To solve the issue of contamination of the p-type polymer by PEI during the fabrication of inverters with TGBC OTFTs, the following methods are considered.
    a) Using high molecular weight PEI can be used to decrease its solubility in the solvent used for the dielectric;
    b) Inkjet printing the dielectric layer on the p- and n-channel regions, respectively;
    c) Modifying the PEI molecules by other groups to decrease the solubility of PEI in the dielectric solvent.
3. After solving the PEI contamination issue, polymers doped with PEI in Chapter 5 can be used for n-type TGBC OTFTs, achieving high performance inverters. Subsequently, different materials will be utilized as the dielectric, including PMMA, Cytop, etc. and dielectric thicknesses will be optimized for low voltage operation.
4. In order to test the dynamic behavior and especially to obtain information about the switching frequency of a logic circuit, a ring oscillator (Figure 6.1 (b)), which is a simple circuit composed of an odd number of inverters, is usually used. Ring oscillator devices with high oscillation frequency will be designed and printed using the n-type polymers developed in this work and high performance p-type semiconductors such as **PDQT-24** to bring the technology closer to potential application.

References

[1] J. S. Kilby, *IEEE Trans. Electron Devices* **1976**, *23*, 648.
[2] *J. E. Lilienfeld, US Pat. US1745175*.
[3] W. F. Brinkman, D. E. Haggan, W. W. Troutman, *IEEE J Solid-State Circuits* **1997**, *32*, 1858.
[4] F. Ebisawa, T. Kurokawa, S. Nara, *J. Appl. Phys.* **1983**, *54*, 3255.
[5] S. Chen, B. Sun, W. Hong, H. Aziz, Y. Meng, Y. Li, *J. Mater. Chem. C* **2014**, *2*, 2183.
[6] D. Braga, G. Horowitz, *Adv. Mater.* **2009**, *21*, 1473.
[7] M. O. Ahmed, C. Wang, P. Keg, W. Pisula, Y.-M. Lam, B. S. Ong, S.-C. Ng, Z.-K. Chen, S. G. Mhaisalkar, *J. Mater. Chem.* **2009**, *19*, 3449.
[8] H. H. Fong, V. A. Pozdin, A. Amassian, G. G. Malliaras, D.-M. Smilgies, M. He, S. Gasper, F. Zhang, M. Sorensen, *J. Am. Chem. Soc.* **2008**, *130*, 13202.
[9] M. L. Tang, A. D. Reichardt, N. Miyaki, R. M. Stoltenberg, Z. Bao, *J. Am. Chem. Soc.* **2008**, *130*, 6064.
[10] H. Sirringhaus, T. Kawase, R. H. Friend, T. Shimoda, M. Inbasekaran, W. Wu, E. P. Woo, *Science* **2000**, *290*, 2123.
[11] K. J. Baeg, M. Caironi, Y. Y. Noh, *Adv. Mater.* **2013**, *25*, 4210.
[12] M. Hambsch, K. Reuter, H. Kempa, A. C. Hübler, *Org. Electron.* **2012**, *13*, 1989.
[13] Z. Chen, H. Lemke, S. Albert-Seifried, M. Caironi, M. M. Nielsen, M. Heeney, W. Zhang, I. McCulloch, H. Sirringhaus, *Adv. Mater.* **2010**, *22*, 2371.
[14] T. D. Anthopoulos, D. M. de Leeuw, E. Cantatore, S. Setayesh, E. J. Meijer, C. Tanase, J. C. Hummelen, P. W. M. Blom, *Appl. Phys. Lett.* **2004**, *85*, 4205.
[15] A. R. Brown, A. Pomp, C. M. Hart, D. M. de Leeuw, *Science* **1995**, *270*, 972.
[16] D. S. Sen, Prosenjit; Das, Anand M. , *RFID For Energy and Utility Industries*, PennWell, 2009.
[17] R. J. Baker, in *Chapter 1*, (Eds: S. K. Tewksbury, J. E. Brewer), John Wiley & Sons, Hoboken, NJ 2010, 6.
[18] A. J. Kronemeijer, E. Gili, M. Shahid, J. Rivnay, A. Salleo, M. Heeney, H. Sirringhaus, *Adv. Mater.* **2012**, *24*, 1558.
[19] K.-J. Baeg, D. Khim, D.-Y. Kim, S.-W. Jung, J. B. Koo, I.-K. You, H. Yan, A. Facchetti, Y.-Y. Noh, *J. Polym. Sci. Part B: Polym. Phys.* **2011**, *49*, 62.
[20] J. Smith, R. Hamilton, M. Heeney, D. M. de Leeuw, E. Cantatore, J. E. Anthony, I. McCulloch, D. D. C. Bradley, T. D. Anthopoulos, *Appl. Phys. Lett.* **2008**, *93*, 253301.
[21] R. K. Singh, A. Dixit, *Basic Electronics Engineering & Devices*, Laxmi Publications Pvt Limited, 2007.
[22] K. Misiakos, D. Tsamakis, *J. Appl. Phys.* **1993**, *74*, 3293.
[23] M. Pope, C. E. Swenberg, *Electronic Processes in Organic Crystals and Polymers*, Oxford University Press, Oxford 1999.
[24] H. Shirakawa, E. J. Louis, A. G. MacDiarmid, C. K. Chiang, A. J. Heeger, *J. Chem. Soc., Chem. Commun.* **1977**, 578.
[25] A. Tsumura, H. Koezuka, T. Ando, *Appl. Phys. Lett.* **1986**, *49*, 1210.
[26] H. Bronstein, Z. Chen, R. S. Ashraf, W. Zhang, J. Du, J. R. Durrant, P. Shakya Tuladhar, K. Song, S. E. Watkins, Y. Geerts, M. M. Wienk, R. A. J. Janssen, T. Anthopoulos, H. Sirringhaus, M. Heeney, I. McCulloch, *J. Am. Chem. Soc.* **2011**, *133*, 3272.
[27] H. J. Chen, Y. L. Guo, G. Yu, Y. Zhao, J. Zhang, D. Gao, H. T. Liu, Y. Q. Liu, *Adv. Mater.* **2012**, *24*, 4618.
[28] J. S. Ha, K. H. Kim, D. H. Choi, *J. Am. Chem. Soc.* **2011**, *133*, 10364.

[29] I. Kang, H. J. Yun, D. S. Chung, S. K. Kwon, Y. H. Kim, *J. Am. Chem. Soc.* **2013**, *135*, 14896.
[30] J. Li, Y. Zhao, H. S. Tan, Y. Guo, C.-A. Di, G. Yu, Y. Liu, M. Lin, S. H. Lim, Y. Zhou, H. Su, B. S. Ong, *Sci. Rep.* **2012**, *2*, 754.
[31] Y. Li, P. Sonar, S. P. Singh, M. S. Soh, M. van Meurs, J. Tan, *J. Am. Chem. Soc.* **2011**, *133*, 2198.
[32] Y. Li, P. Sonar, S. P. Singh, W. Zeng, M. S. Soh, *J. Mater. Chem.* **2011**, *21*, 10829.
[33] Y. Li, S. P. Singh, P. Sonar, *Adv. Mater.* **2010**, *22*, 4862.
[34] Y. Li, P. Sonar, L. Murphy, W. Hong, *Energy. Environ. Sci.* **2013**, *6*, 1684.
[35] M. Shahid, T. McCarthy Ward, J. Labram, S. Rossbauer, E. B. Domingo, S. E. Watkins, N. Stingelin, T. D. Anthopoulos, M. Heeney, *Chem. Sci.* **2012**, *3*, 181.
[36] P. Sonar, S. P. Singh, Y. Li, Z. E. Ooi, T. j. Ha, I. Wong, M. S. Soh, A. Dodabalapur, *Energy. Environ. Sci.* **2011**, *4*, 2288.
[37] B. Sun, W. Hong, H. Aziz, N. M. Abukhdeir, Y. Li, *J. Mater. Chem. C* **2013**, *1*, 4423.
[38] H. N. Tsao, D. Cho, J. W. Andreasen, A. Rouhanipour, D. W. Breiby, W. Pisula, K. Müllen, *Adv. Mater.* **2009**, *21*, 209.
[39] H. N. Tsao, D. M. Cho, I. Park, M. R. Hansen, A. Mavrinskiy, D. Y. Yoon, R. Graf, W. Pisula, H. W. Spiess, K. Müllen, *J. Am. Chem. Soc.* **2011**, *133*, 2605.
[40] J. D. Yuen, J. Fan, J. Seifter, B. Lim, R. Hufschmid, A. J. Heeger, F. Wudl, *J. Am. Chem. Soc.* **2011**, *133*, 20799.
[41] T. Lei, Y. Cao, Y. Fan, C. J. Liu, S. C. Yuan, J. Pei, *J. Am. Chem. Soc.* **2011**, *133*, 6099.
[42] T. Lei, J.-H. Dou, Z.-J. Ma, C.-H. Yao, C.-J. Liu, J.-Y. Wang, J. Pei, *J. Am. Chem. Soc.* **2012**, *134*, 20025.
[43] A. J. Snell, W. E. Spear, P. G. Le Comber, K. Mackenzie, *Appl. Phys. A.* **1981**, *26*, 83.
[44] E. E. Havinga, W. ten Hoeve, H. Wynberg, *Polym. Bull.* **1992**, *29*, 119.
[45] Z. Fei, P. Pattanasattayavong, Y. Han, B. C. Schroeder, F. Yan, R. J. Kline, T. D. Anthopoulos, M. Heeney, *J. Am. Chem. Soc.* **2014**, *136*, 15154.
[46] S.-Y. Jang, I.-B. Kim, J. Kim, D. Khim, E. Jung, B. Kang, B. Lim, Y.-A. Kim, Y. H. Jang, K. Cho, D.-Y. Kim, *Chem. Mater.* **2014**, *26*, 6907.
[47] M. Zhang, H. N. Tsao, W. Pisula, C. Yang, A. K. Mishra, K. Müllen, *J. Am. Chem. Soc.* **2007**, *129*, 3472.
[48] S. Wang, M. Kappl, I. Liebewirth, M. Müller, K. Kirchhoff, W. Pisula, K. Müllen, *Adv. Mater.* **2012**, *24*, 417.
[49] L. Ying, B. B. Y. Hsu, H. Zhan, G. C. Welch, P. Zalar, L. A. Perez, E. J. Kramer, T.-Q. Nguyen, A. J. Heeger, W.-Y. Wong, G. C. Bazan, *J. Am. Chem. Soc.* **2011**, *133*, 18538.
[50] C. Luo, A. K. K. Kyaw, L. A. Perez, S. Patel, M. Wang, B. Grimm, G. C. Bazan, E. J. Kramer, A. J. Heeger, *Nano Lett.* **2014**, *14*, 2764.
[51] T. Lei, J. H. Dou, J. Pei, *Adv. Mater.* **2012**, *24*, 6457.
[52] G. Kim, S. J. Kang, G. K. Dutta, Y. K. Han, T. J. Shin, Y. Y. Noh, C. Yang, *J. Am. Chem. Soc.* **2014**, *136*, 9477.
[53] W. Li, T. Lee, S. J. Oh, C. R. Kagan, *ACS Appl. Mater. Interfaces* **2011**, *3*, 3874.
[54] Z. Chen, M. J. Lee, R. S. Ashraf, Y. Gu, S. Albert-Seifried, M. M. Nielsen, B. Schroeder, T. D. Anthopoulos, M. Heeney, I. McCulloch, H. Sirringhaus, *Adv. Mater.* **2012**, *24*, 647.
[55] X. Liu, Y. Guo, Y. Ma, H. Chen, Z. Mao, H. Wang, G. Yu, Y. Liu, *Adv. Mater.* **2014**, *26*, 3631.
[56] H. J. Yun, G. B. Lee, D. S. Chung, Y. H. Kim, S. K. Kwon, *Adv. Mater.* **2014**, *26*, 6612.
[57] W. K. Chan, Y. Chen, Z. Peng, L. Yu, *J. Am. Chem. Soc.* **1993**, *115*, 11735.
[58] C. Kim, J. H. Liu, J. S. Lin, A. B. Tamayo, B. Walker, G. Wu, T. Q. Nguyen, *Chem. Mater.* **2012**, *24*, 1699.
[59] C. Kanimozhi, N. Yaacobi-Gross, K. W. Chou, A. Amassian, T. D. Anthopoulos, S. Patil, *J. Am. Chem. Soc.* **2012**, *134*, 16532.

[60] H. Yan, Z. Chen, Y. Zheng, C. Newman, J. R. Quinn, F. Dotz, M. Kastler, A. Facchetti, *Nature* **2009**, *457*, 679.
[61] A. Luzio, L. Criante, V. D'Innocenzo, M. Caironi, *Sci. Rep.* **2013**, *3*, 3425.
[62] A. Luzio, D. Fazzi, F. Nübling, R. Matsidik, A. Straub, H. Komber, E. Giussani, S. E. Watkins, M. Barbatti, W. Thiel, E. Gann, L. Thomsen, C. R. McNeill, M. Caironi, M. Sommer, *Chem. Mater.* **2014**, *26*, 6233.
[63] T. Lei, J. H. Dou, X. Y. Cao, J. Y. Wang, J. Pei, *J. Am. Chem. Soc.* **2013**, *135*, 12168.
[64] E. Bundgaard, F. C. Krebs, *Sol. Energy Mater. Sol. Cells* **2007**, *91*, 954.
[65] P. Sonar, T. R. B. Foong, A. Dodabalapur, *Phys. Chem. Chem. Phys.* **2014**, *16*, 4275.
[66] W. Hong, B. Sun, J. Yuen, Y. N. Li, S. F. Lu, C. Huang, A. Facchetti, *Chem. Commun.* **2013**, *49*, 484.
[67] Y. Zhang, C. Kim, J. Lin, N. Thuc-Quyen, *Adv. Funct. Mater.* **2012**, *22*, 97.
[68] K. Tandy, G. K. Dutta, Y. Zhang, N. Venkatramaiah, M. Aljada, P. L. Burn, P. Meredith, E. B. Namdas, S. Patil, *Org. Electron.* **2012**, *13*, 1981.
[69] P. Sonar, T. R. B. Foong, S. P. Singh, Y. Li, A. Dodabalapur, *Chem. Commun.* **2012**, *48*, 8383.
[70] X. Zhao, X. Zhan, *Chem. Soc. Rev.* **2011**, *40*, 3728.
[71] S. P. S. Prashant Sonar , Yuning Li , * Mui Siang Soh ,and Ananth Dodabalapur *, *Adv. Mater.* **2010**, *22*, 5409.
[72] J. C. Bijleveld, A. P. Zoombelt, S. G. J. Mathijssen, M. M. Wienk, M. Turbiez, D. M. de Leeuw, R. A. J. Janssen, *J. Am. Chem. Soc.* **2009**, *131*, 16616.
[73] L. Bürgi, M. Turbiez, R. Pfeiffer, F. Bienewald, H.-J. Kirner, C. Winnewisser, *Adv. Mater.* **2008**, *20*, 2217.
[74] T. D. Anthopoulos, C. Tanase, S. Setayesh, E. J. Meijer, J. C. Hummelen, P. W. M. Blom, D. M. de Leeuw, *Adv. Mater.* **2004**, *16*, 2174.
[75] G. Guillaud, M. Al Sadoun, M. Maitrot, J. Simon, M. Bouvet, *Chem. Phys. Lett.* **1990**, *167*, 503.
[76] G. C. Schmidt, D. Hoft, K. Haase, A. C. Hubler, E. Karpov, R. Tkachov, M. Stamm, A. Kiriy, F. Haidu, D. R. T. Zahn, H. Yan, A. Facchetti, *J. Mater. Chem. C* **2014**, *2*, 5149.
[77] K.-J. Baeg, D. Khim, S.-W. Jung, M. Kang, I.-K. You, D.-Y. Kim, A. Facchetti, Y.-Y. Noh, *Adv. Mater.* **2012**, *24*, 5433.
[78] J. Lee, A. R. Han, H. Yu, T. J. Shin, C. Yang, J. H. Oh, *J. Am. Chem. Soc.* **2013**, *135*, 9540.
[79] J. H. Park, E. H. Jung, J. W. Jung, W. H. Jo, *Adv. Mater.* **2013**, *25*, 2583.
[80] T. Lei, J. H. Dou, X. Y. Cao, J. Y. Wang, J. Pei, *Adv. Mater.* **2013**, *25*, 6589.
[81] K. J. Baeg, J. Kim, D. Khim, M. Caironi, D. Y. Kim, I. K. You, J. R. Quinn, A. Facchetti, Y. Y. Noh, *ACS Appl Mater Interfaces* **2011**, *3*, 3205.
[82] X. Y. Cheng, Y. Y. Noh, J. P. Wang, M. Tello, J. Frisch, R. P. Blum, A. Vollmer, J. P. Rabe, N. Koch, H. Sirringhaus, *Adv. Funct. Mater.* **2009**, *19*, 2407.
[83] H. Xu, Y.-C. Zhou, X.-Y. Zhou, K. Liu, L.-Y. Cao, Y. Ai, Z.-P. Fan, H.-L. Zhang, *Adv. Funct. Mater.* **2014**, *24*, 2907.
[84] J. C. Ribierre, S. Watanabe, M. Matsumoto, T. Muto, T. Aoyama, *Appl. Phys. Lett.* **2010**, *96*, 083303.
[85] J. C. Ribierre, S. Watanabe, M. Matsumoto, T. Muto, A. Nakao, T. Aoyama, *Adv. Mater.* **2010**, *22*, 4044.
[86] B. D. Naab, S. Himmelberger, Y. Diao, K. Vandewal, P. Wei, B. Lussem, A. Salleo, Z. Bao, *Adv. Mater.* **2013**, *25*, 4663.
[87] C. Liu, J. Jang, Y. Xu, H. J. Kim, D. Khim, W. T. Park, Y. Y. Noh, J. J. Kim, *Adv. Funct. Mater.* **2015**, *25*, 758.
[88] Y. Zhou, C. Fuentes-Hernandez, J. Shim, J. Meyer, A. J. Giordano, H. Li, P. Winget, T. Papadopoulos, H. Cheun, J. Kim, M. Fenoll, A. Dindar, W. Haske, E. Najafabadi, T. M. Khan, H.

Sojoudi, S. Barlow, S. Graham, J.-L. Brédas, S. R. Marder, A. Kahn, B. Kippelen, *Science* **2012**, *336*, 327.
[89] P. Lin, F. Yan, *Adv. Mater.* **2012**, *24*, 34.
[90] M. Singh, H. M. Haverinen, P. Dhagat, G. E. Jabbour, *Adv. Mater.* **2010**, *22*, 673.
[91] Y. Wen, Y. Liu, *Adv. Mater.* **2010**, *22*, 1331.
[92] A. C. Arias, J. D. MacKenzie, I. McCulloch, J. Rivnay, A. Salleo, *Chem. Rev.* **2010**, *110*, 3.
[93] C. Wang, H. Dong, W. Hu, Y. Liu, D. Zhu, *Chem. Rev.* **2011**, *112*, 2208.
[94] Y. Wen, Y. Liu, Y. Guo, G. Yu, W. Hu, *Chem. Rev.* **2011**, *111*, 3358.
[95] H. Klauk, *Chem. Soc. Rev.* **2010**, *39*, 2643.
[96] B. S. Ong, Y. Wu, Y. Li, P. Liu, H. Pan, *Chem. Eur. J.* **2008**, *14*, 4766.
[97] A. Facchetti, *Chem. Mater.* **2010**, *23*, 733.
[98] M. E. Roberts, A. N. Sokolov, Z. Bao, *J. Mater. Chem.* **2009**, *19*, 3351.
[99] C. Reese, M. Roberts, M.-m. Ling, Z. Bao, *Mater. Today* **2004**, *7*, 20.
[100] H. Li, F. S. Kim, G. Ren, S. A. Jenekhe, *J. Am. Chem. Soc.* **2013**, *135*, 14920.
[101] M. C. Gwinner, D. Kabra, M. Roberts, T. J. K. Brenner, B. H. Wallikewitz, C. R. McNeill, R. H. Friend, H. Sirringhaus, *Adv. Mater.* **2012**, *24*, 2728.
[102] M. Ahles, A. Hepp, R. Schmechel, H. von Seggern, *Appl. Phys. Lett.* **2004**, *84*, 428.
[103] J. Zaumseil, R. H. Friend, H. Sirringhaus, *Nat. Mater.* **2006**, *5*, 69.
[104] J. C. Bijleveld, V. S. Gevaerts, D. Di Nuzzo, M. Turbiez, S. G. J. Mathijssen, D. M. de Leeuw, M. M. Wienk, R. A. J. Janssen, *Adv. Mater.* **2010**, *22*, E242.
[105] F. Liu, Y. Gu, C. Wang, W. Zhao, D. Chen, A. L. Briseno, T. P. Russell, *Adv. Mater.* **2012**, *24*, 3947.
[106] J. W. Jung, F. Liu, T. P. Russell, W. H. Jo, *Energy. Environ. Sci.* **2012**, *5*, 6857.
[107] W. Li, W. S. C. Roelofs, M. M. Wienk, R. A. J. Janssen, *J. Am. Chem. Soc.* **2012**, *134*, 13787.
[108] B. Tieke, A. R. Rabindranath, K. Zhang, Y. Zhu, *Beilstein J. Org. Chem.* **2010**, *6*, 830.
[109] D. Cao, Q. Liu, W. Zeng, S. Han, J. Peng, S. Liu, *J. Polym. Sci., Part A: Polym. Chem.* **2006**, *44*, 2395.
[110] P. T. Wu, F. S. Kim, S. A. Jenekhe, *Chem. Mater.* **2011**, *23*, 4618.
[111] C. Kanimozhi, P. Balraju, G. D. Sharma, S. Patil, *J. Phys. Chem. B* **2010**, *114*, 3095.
[112] L. Chen, D. Deng, Y. Nan, M. Shi, P. K. L. Chan, H. Chen, *J. Phys. Chem. C* **2011**, *115*, 11282.
[113] Y. Zhu, I. Heim, B. Tieke, *Macromol. Chem. Phys.* **2006**, *207*, 2206.
[114] H. Sirringhaus, P. J. Brown, R. H. Friend, M. M. Nielsen, K. Bechgaard, B. M. W. Langeveld-Voss, A. J. H. Spiering, R. A. J. Janssen, E. W. Meijer, P. Herwig, D. M. de Leeuw, *Nature* **1999**, *401*, 685.
[115] T.-A. Chen, X. Wu, R. D. Rieke, *J. Am. Chem. Soc.* **1995**, *117*, 233.
[116] H. L. Pan, Y. N. Li, Y. L. Wu, P. Liu, B. S. Ong, S. P. Zhu, G. Xu, *J. Am. Chem. Soc.* **2007**, *129*, 4112.
[117] M.-H. Yoon, C. Kim, A. Facchetti, T. J. Marks, *J. Am. Chem. Soc.* **2006**, *128*, 12851.
[118] R. P. Ortiz, A. Facchetti, T. J. Marks, *Chem. Rev.* **2009**, *110*, 205.
[119] W. Hong, B. Sun, H. Aziz, W. T. Park, Y. Y. Noh, Y. N. Li, *Chem. Commun.* **2012**, *48*, 8413.
[120] B. W. D'Andrade, S. Datta, S. R. Forrest, P. Djurovich, E. Polikarpov, M. E. Thompson, *Org. Electron.* **2005**, *6*, 11.
[121] C. Lee, W. Yang, R. G. Parr, *Phys. Rev. B* **1988**, *37*, 785.
[122] H. P. H. Æ. Frisch, R. D. Dennington II, T. A. Keith, J. Millam, A. B. Nielsen, A. J. Holder, J. Hiscocks, , *GaussView 5 Reference*, Gaussian, Inc., Wallingford, CT 2009.

[123] I. McCulloch, M. Heeney, C. Bailey, K. Genevicius, I. MacDonald, M. Shkunov, D. Sparrowe, S. Tierney, R. Wagner, W. Zhang, M. L. Chabinyc, R. J. Kline, M. D. McGehee, M. F. Toney, *Nat. Mater.* **2006**, *5*, 328.
[124] Y. Li, Y. Wu, P. Liu, M. Birau, H. Pan, B. S. Ong, *Adv. Mater.* **2006**, *18*, 3029.
[125] M. Bronner, A. Opitz, W. Brütting, *Phys. Status Solidi A* **2008**, *205*, 549.
[126] B. A. Jones, A. Facchetti, M. R. Wasielewski, T. J. Marks, *J. Am. Chem. Soc.* **2007**, *129*, 15259.
[127] C. W. Chu, S. H. Li, C. W. Chen, V. Shrotriya, Y. Yang, *Appl. Phys. Lett.* **2005**, *87*.
[128] D. Kumaki, T. Umeda, S. Tokito, *Appl. Phys. Lett.* **2008**, *92*.
[129] X. Yu, J. Yu, J. Zhou, Y. Jiang, *Synth. Met.* **2012**, *162*, 936.
[130] C. Cheng, C. Yu, Y. Guo, H. Chen, Y. Fang, G. Yu, Y. Liu, *Chem. Commun.* **2013**, *49*, 1998.
[131] X. M. Hong, H. E. Katz, A. J. Lovinger, B.-C. Wang, K. Raghavachari, *Chem. Mater.* **2001**, *13*, 4686.
[132] H. Kong, S. Cho, D. H. Lee, N. S. Cho, M. J. Park, I. H. Jung, J. H. Park, C. E. Park, H. K. Shim, *Journal of Polymer Science Part a-Polymer Chemistry* **2011**, *49*, 2886.
[133] J. W. Jung, F. Liu, T. P. Russell, W. H. Jo, *Chem. Commun.* **2013**, *49*, 8495.
[134] B. Sun, W. Hong, Z. Yan, H. Aziz, Y. Li, *Adv. Mater.* **2014**, *26*, 2636.
[135] B. S. Ong, Y. Wu, P. Liu, S. Gardner, *J. Am. Chem. Soc.* **2004**, *126*, 3378.
[136] S. Braun, W. R. Salaneck, M. Fahlman, *Adv. Mater.* **2009**, *21*, 1450.
[137] A. Wan, J. Hwang, F. Amy, A. Kahn, *Org. Electron.* **2005**, *6*, 47.
[138] L. L. Chua, J. Zaumseil, J. F. Chang, E. C. W. Ou, P. K. H. Ho, H. Sirringhaus, R. H. Friend, *Nature* **2005**, *434*, 194.
[139] M. T. Greiner, M. G. Helander, W.-M. Tang, Z.-B. Wang, J. Qiu, Z.-H. Lu, *Nat. Mater.* **2012**, *11*, 76.
[140] Z.-H. L. Mark T Greiner, *NPG Asia Materials* **2013**, *5*, e55.
[141] M. Kröger, S. Hamwi, J. Meyer, T. Riedl, W. Kowalsky, A. Kahn, *Appl. Phys. Lett.* **2009**, *95*, 123301.
[142] M. T. Greiner, L. Chai, M. G. Helander, W. M. Tang, Z. H. Lu, *Adv. Funct. Mater.* **2012**, *22*, 4557.
[143] C. Guo, W. Hong, H. Aziz, Y. Li, *Rev. Adv. Sci. Eng.* **2012**, *1*, 200.
[144] W. Hong, C. Guo, Y. Li, Y. Zheng, C. Huang, S. Lu, A. Facchetti, *J. Mater. Chem.* **2012**, *22*, 22282.
[145] B. Sun, W. Hong, E. Thibau, H. Aziz, Z.-H. Lu, Y. Li, *Org. Electron.* **2014**, *15*, 3787.
[146] B. Sun, W. Hong, H. Aziz, Y. Li, *Polym. Chem.* **2015**, *6*, 938.
[147] Y. Zhang, B. de Boer, P. W. M. Blom, *Phys. Rev. B* **2010**, *81*, 085201.
[148] P. Wei, J. H. Oh, G. Dong, Z. Bao, *J. Am. Chem. Soc.* **2010**, *132*, 8852.
[149] B. D. Naab, S. Zhang, K. Vandewal, A. Salleo, S. Barlow, S. R. Marder, Z. Bao, *Adv. Mater.* **2014**, *26*, 4268.
[150] B. D. Naab, S. Guo, S. Olthof, E. G. B. Evans, P. Wei, G. L. Millhauser, A. Kahn, S. Barlow, S. R. Marder, Z. Bao, *J. Am. Chem. Soc.* **2013**, *135*, 15018.
[151] D. Khim, K.-J. Baeg, M. Caironi, C. Liu, Y. Xu, D.-Y. Kim, Y.-Y. Noh, *Adv. Funct. Mater.* **2014**, *24*, 6252.
[152] C. M. Mahoney, *Mass Spectrom. Rev.* **2010**, *29*, 247.
[153] A. Wucher, *Appl. Surf. Sci.* **2006**, *252*, 6482.
[154] B. Lüssem, M. L. Tietze, H. Kleemann, C. Hoßbach, J. W. Bartha, A. Zakhidov, K. Leo, *Nat Commun* **2013**, *4*, 2775.
[155] L. Ma, W. H. Lee, Y. D. Park, J. S. Kim, H. S. Lee, K. Cho, *Appl. Phys. Lett.* **2008**, *92*, 063310.
[156] S. Olthof, S. Mehraeen, S. K. Mohapatra, S. Barlow, V. Coropceanu, J.-L. Brédas, S. R. Marder, A. Kahn, *Phys. Rev. Lett.* **2012**, *109*, 176601.

[157] H. T. Nicolai, M. Kuik, G. A. H. Wetzelaer, B. de Boer, C. Campbell, C. Risko, J. L. Brédas, P. W. M. Blom, *Nat. Mater.* **2012**, *11*, 882.
[158] J. P. Thomas, K. T. Leung, *Adv. Funct. Mater.* **2014**, *24*, 4978.
[159] S. R. Forrest, *Nature* **2004**, *428*, 911.
[160] W. Hong, S. Chen, B. Sun, M. A. Arnould, Y. Meng, Y. Li, *Chem. Sci.* **2015**, *6*, 3225.
[161] X. Zhou, N. Ai, Z. H. Guo, F. D. Zhuang, Y. S. Jiang, J. Y. Wang, J. Pei, *Chem. Mater.* **2015**, *27*, 1815.
[162] P. S. K. Amegadze, Y.-Y. Noh, *J. Inf. Disp.* **2014**, *15*, 213.
[163] D. Bode, C. Rolin, S. Schols, M. Debucquoy, S. Steudel, G. H. Gelinck, J. Genoe, P. Heremans, *IEEE Trans. Electron Devices* **2010**, *57*, 201.
[164] D. Kumaki, T. Umeda, S. Tokito, *Appl. Phys. Lett.* **2008**, *92*, 093309.

Appendix:

Part 1. Output and transfer characteristics of OTFT devices in Chapter 3

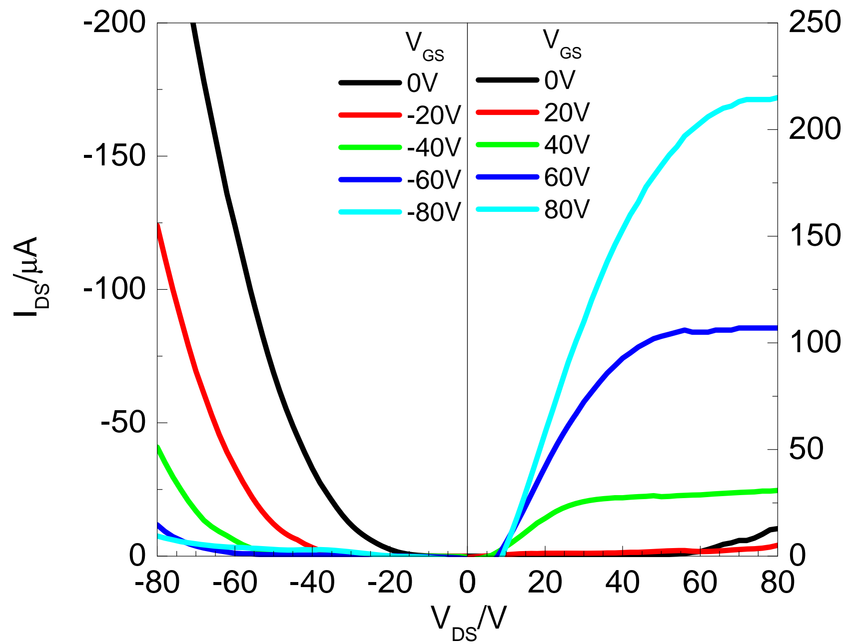

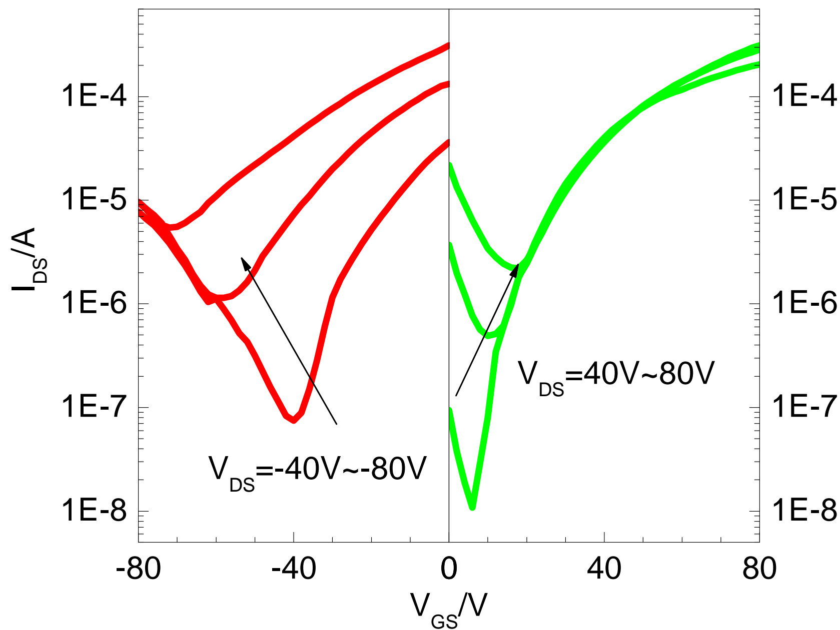

Figure S1. Output (top) and transfer (bottom) characteristics of an ambipolar OTFT device based on **PDBPyBT** annealed at 100ºC for 10min.

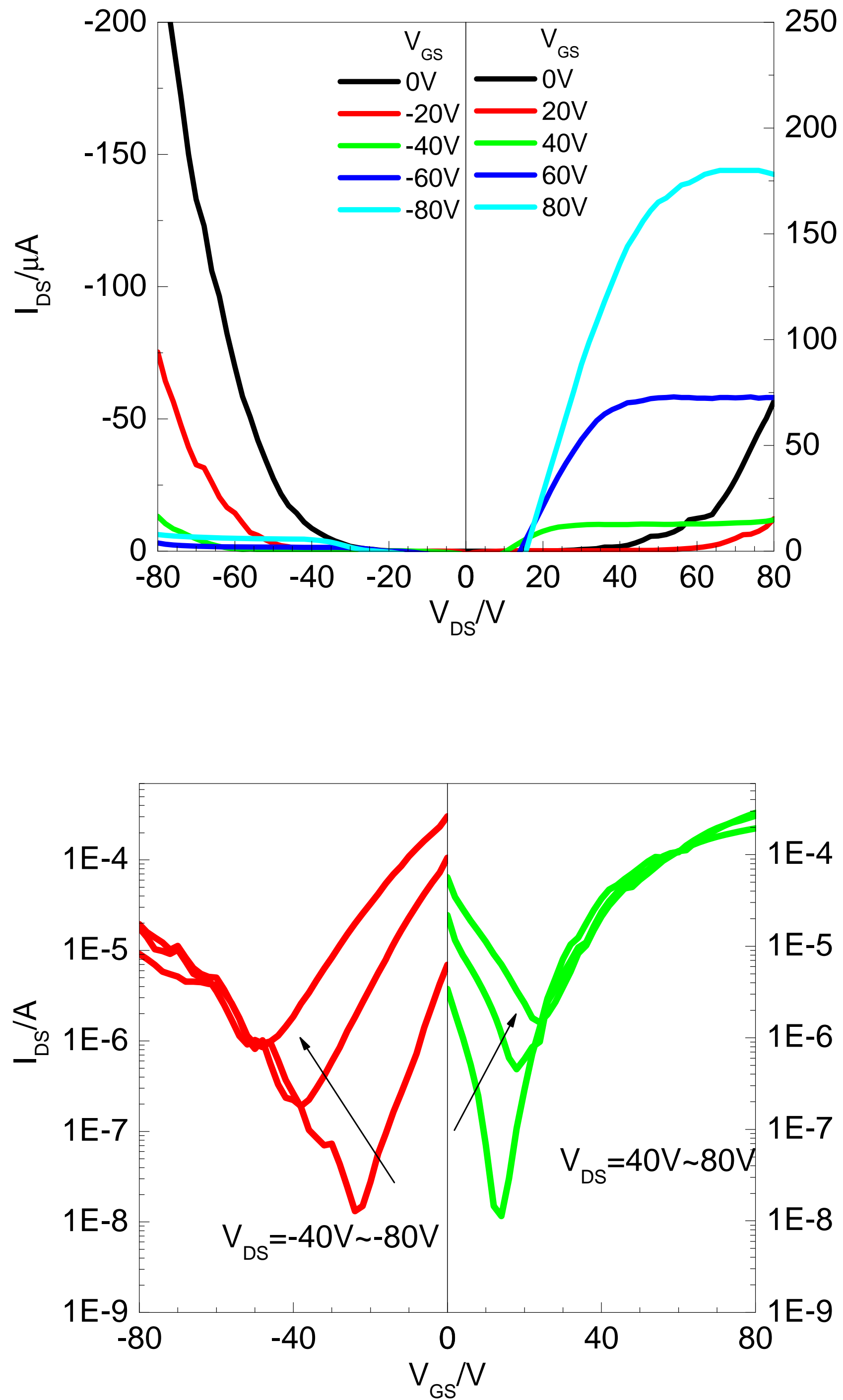

Figure S2. Output (top) and transfer (bottom) characteristics of an ambipolar OTFT device based on **PDBPyBT** annealed at 200ºC for 10min.

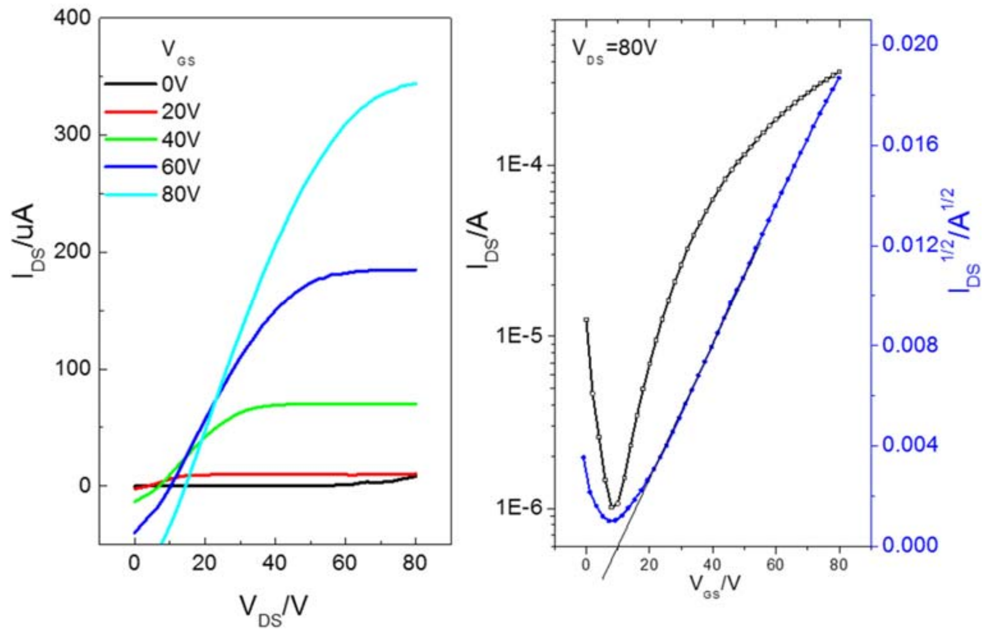

Figure S3. Output (left) and transfer (right) curves of OTFT device with about 1.5 nm of PEI interlayer between the Au contacts and the **PDBPyBT** layer annealed at 150ºC.

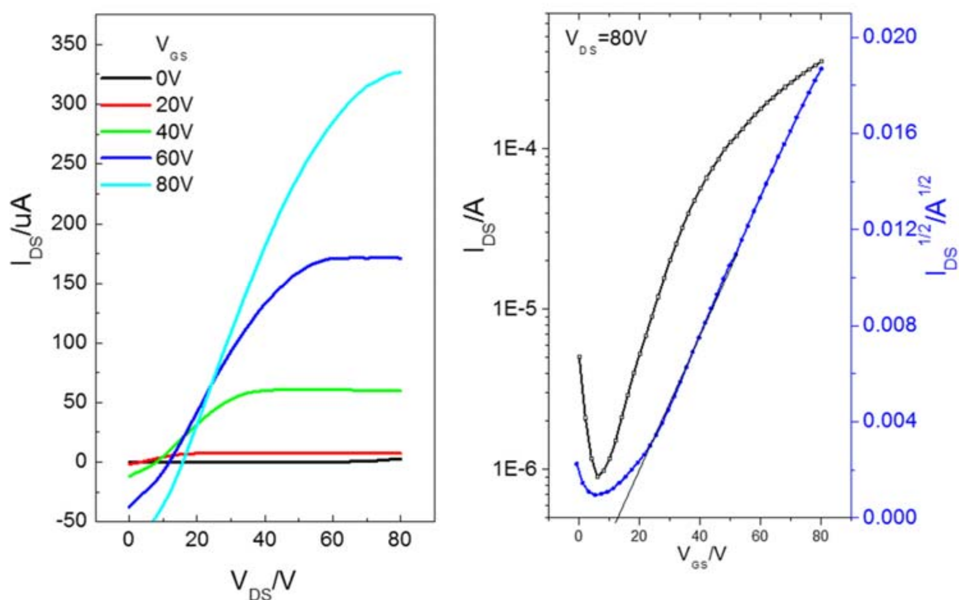

Figure S4. Output (left) and transfer (right) curves of OTFT device with about 2.2 nm of PEI interlayer between the Au contacts and the **PDBPyBT** layer annealed at 150ºC

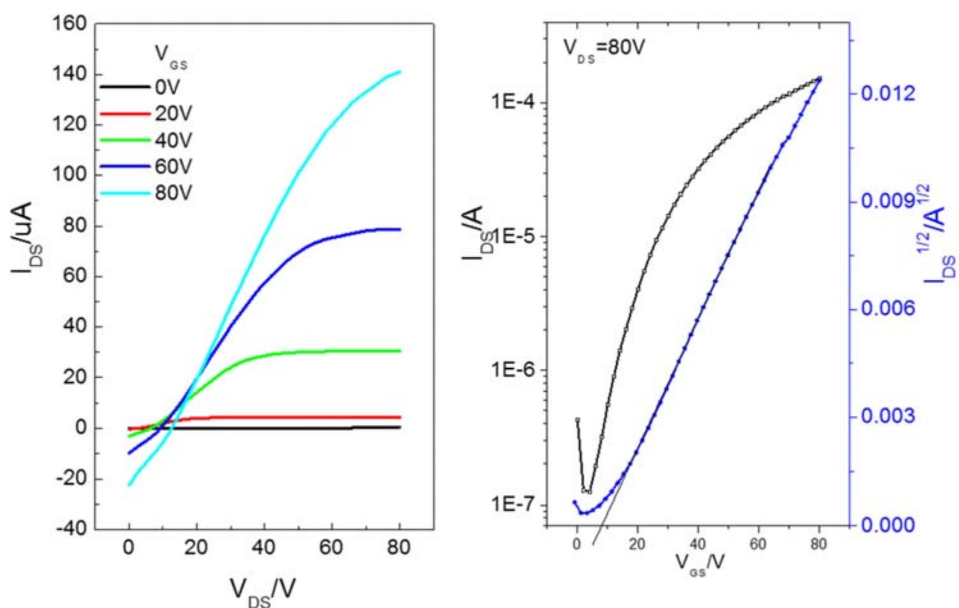

Figure S5. Output (left) and transfer (right) curves of OTFT device with about 2.9 nm of PEI interlayer between the Au contacts and the **PDBPyBT** layer annealed at 150ºC

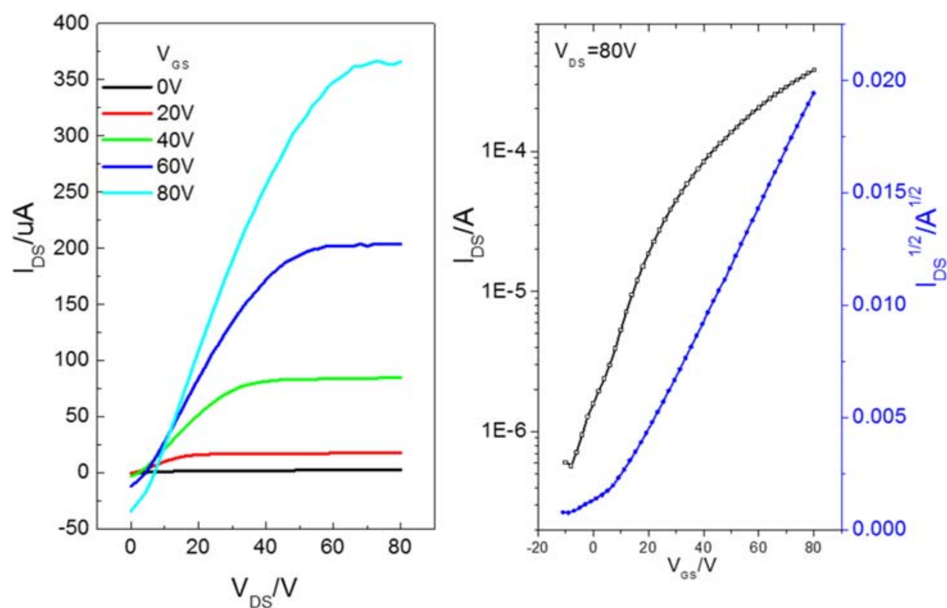

Figure S6. Output (left) and transfer (right) curves of OTFT device with about 3.8 nm of PEI interlayer between the Au contacts and the **PDBPyBT** layer annealed at 150ºC

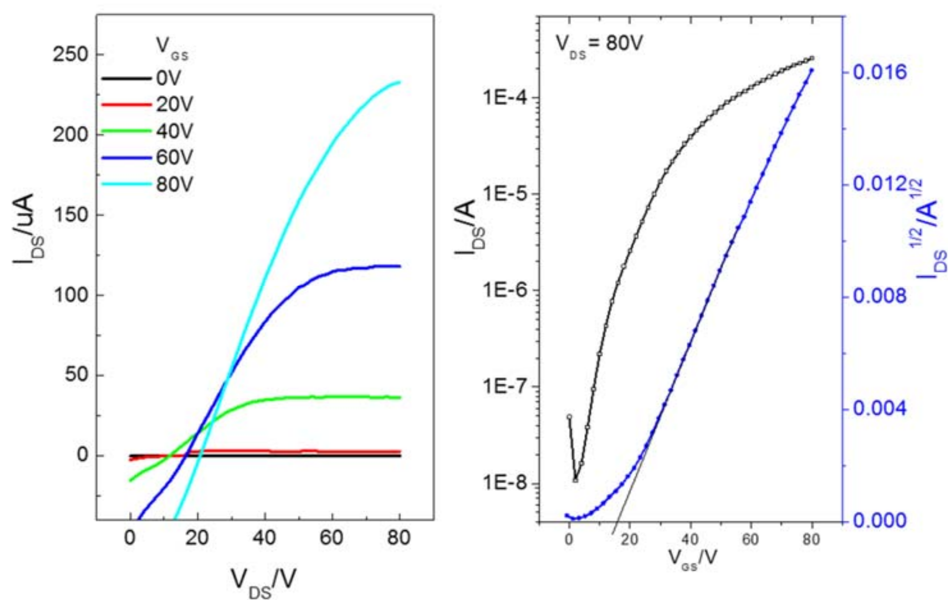

Figure S7. Output (left) and transfer (right) curves of OTFT device with about 3.9 nm of PEI interlayer between the Au contacts and the **PDBPyBT** layer annealed at 150ºC

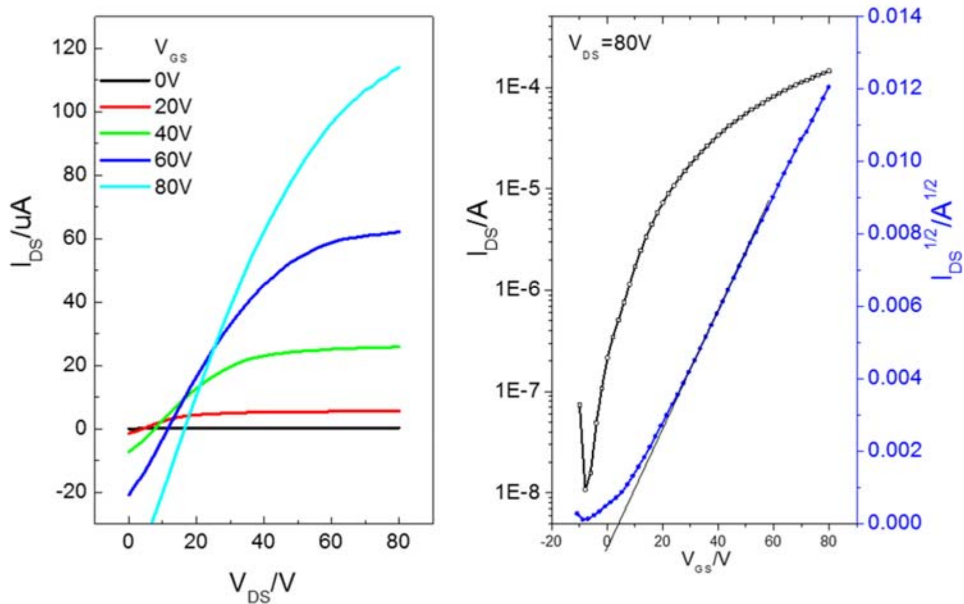

Figure S8. Output (left) and transfer (right) curves of OTFT device with about 4.3 nm of PEI interlayer between the Au contacts and the **PDBPyBT** layer annealed at 150ºC

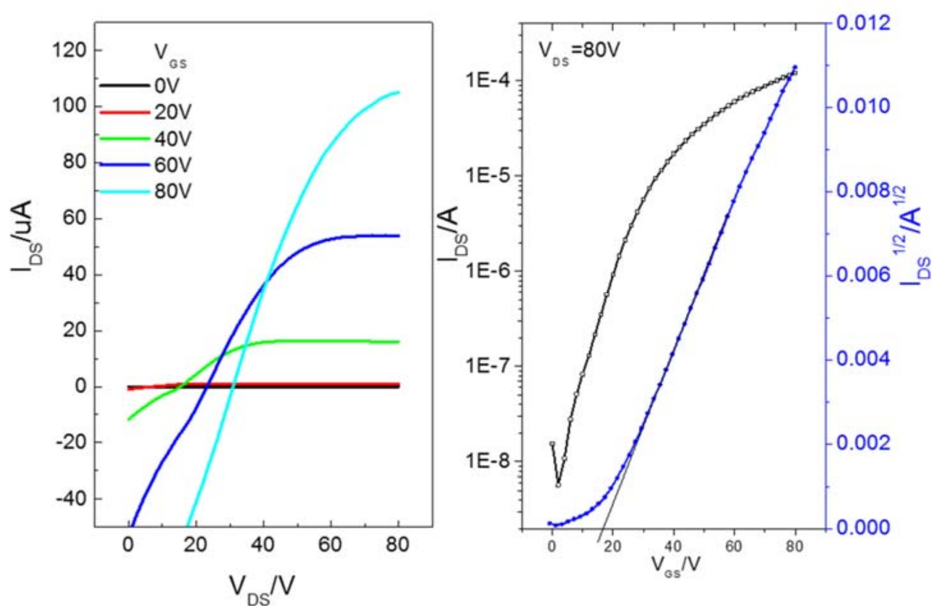

Figure S9. Output (left) and transfer (right) curves of OTFT device with about 4.7 nm of PEI interlayer between the Au contacts and the **PDBPyBT** layer annealed at 150ºC

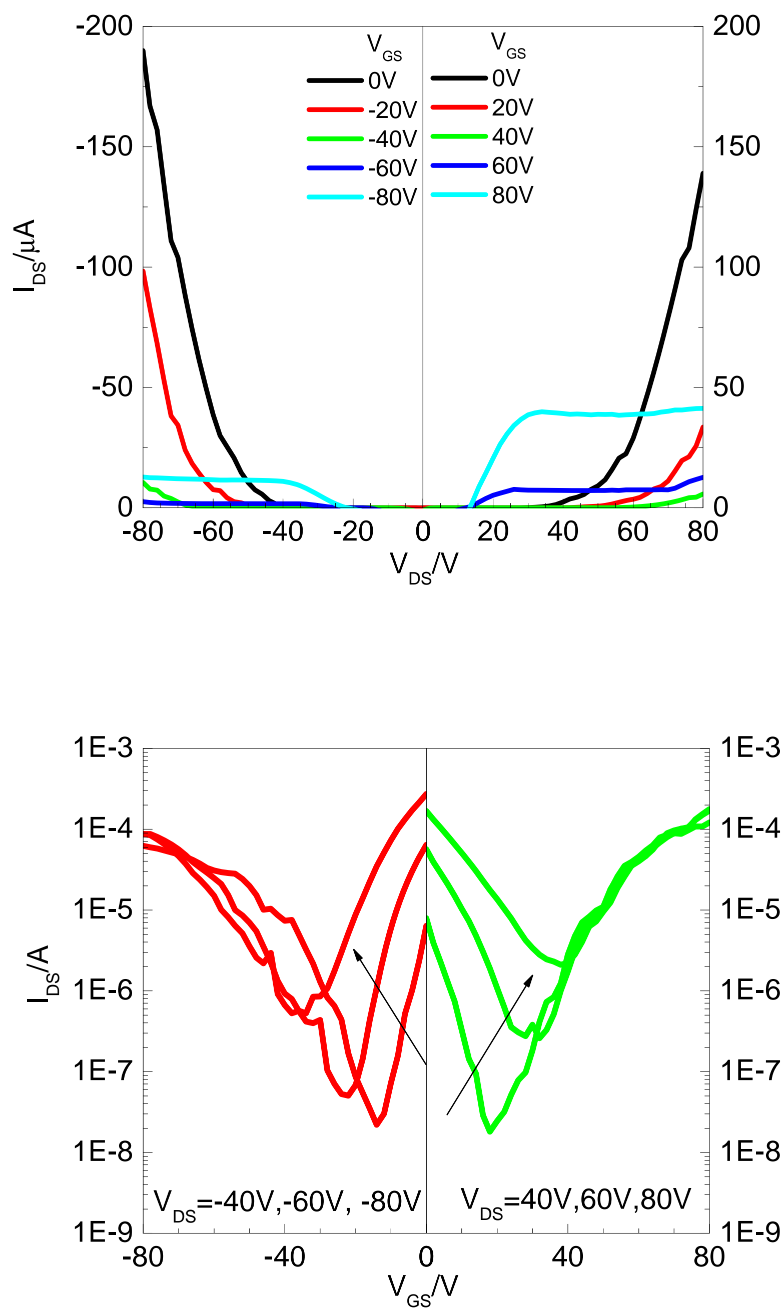

Figure S10. Output (top) and transfer (bottom) curves of OTFT device with about 1.2 nm of MoO_3 interlayer between the Au contacts and the **PDBPyBT** layer annealed at 150ºC

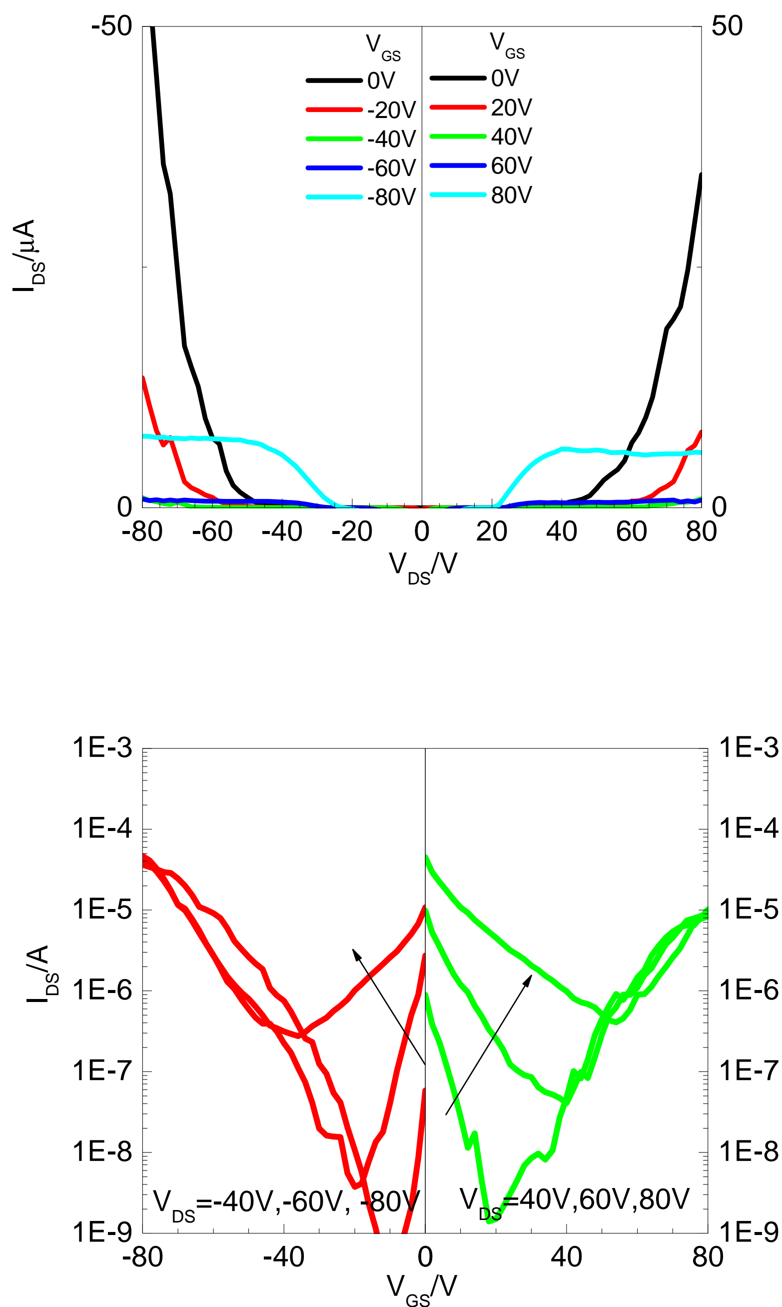

Figure S11. Output (top) and transfer (bottom) curves of OTFT device with about 1.4 nm of MoO_3 interlayer between the Au contacts and the **PDBPyBT** layer annealed at 150ºC

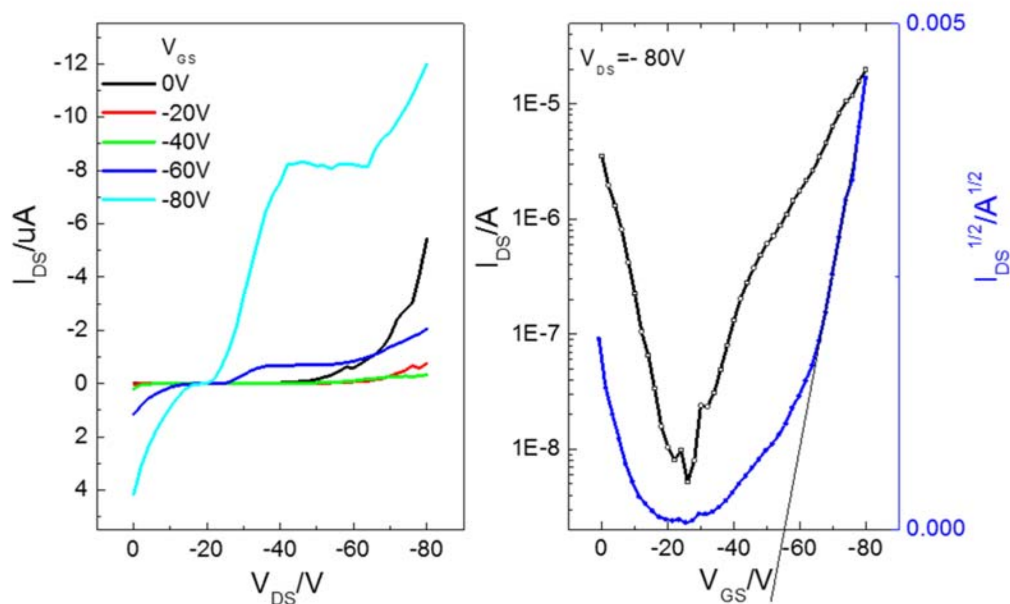

FigureS12. Output (left) and transfer (right) curves of OTFT device with about 1.8 nm of MoO_3 interlayer between the Au contacts and the **PDBPyBT** layer annealed at 150ºC

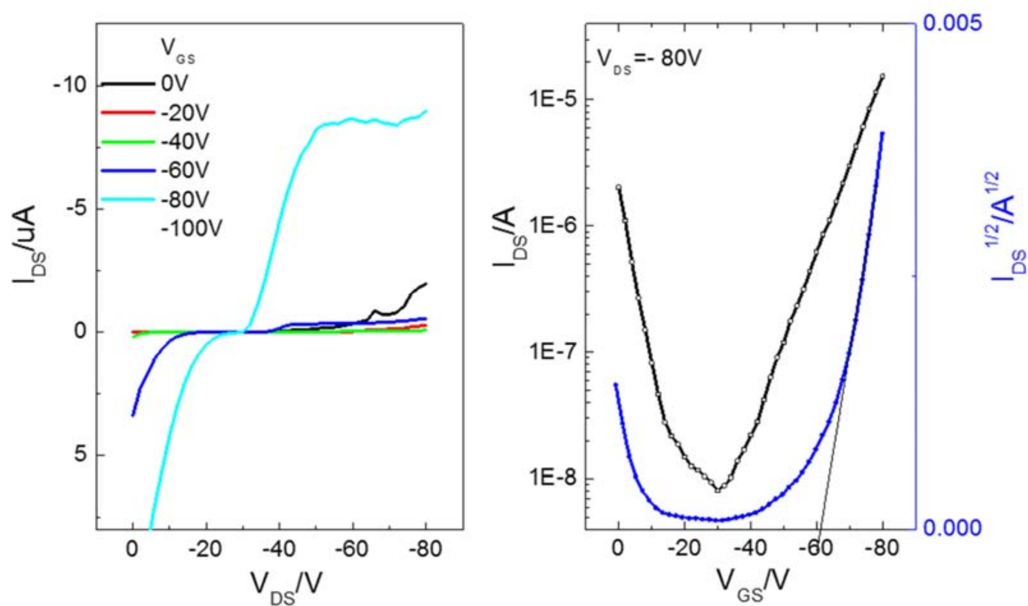

Figure S13. Output (left) and transfer (right) curves of OTFT device with about 2.0 nm of MoO_3 interlayer between the Au contacts and the **PDBPyBT** layer annealed at 150ºC

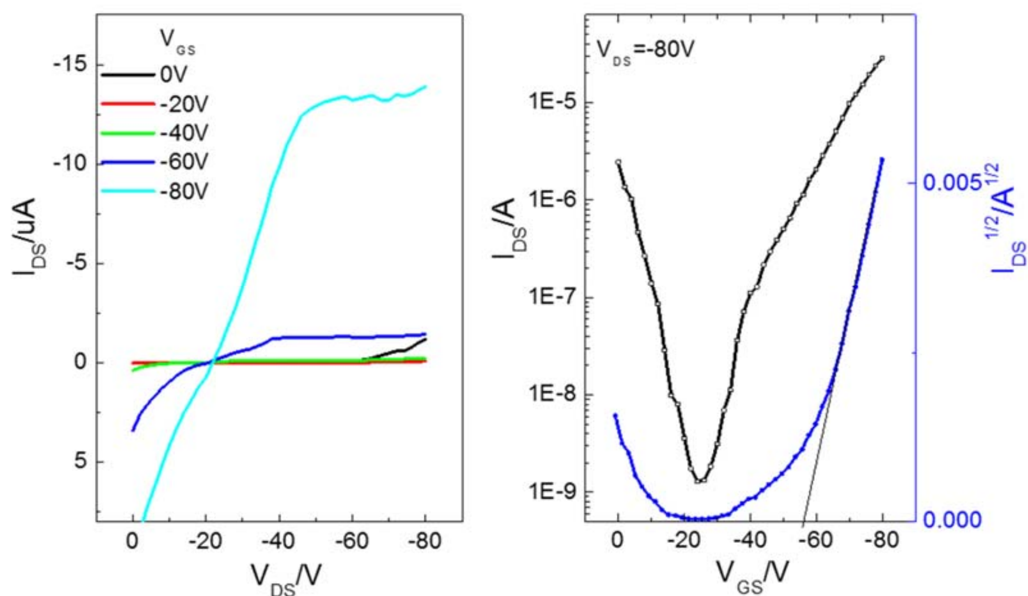

Figure S14. Output (left) and transfer (right) curves of OTFT device with about 2.2 nm of MoO_3 interlayer between the Au contacts and the **PDBPyBT** layer annealed at 150ºC

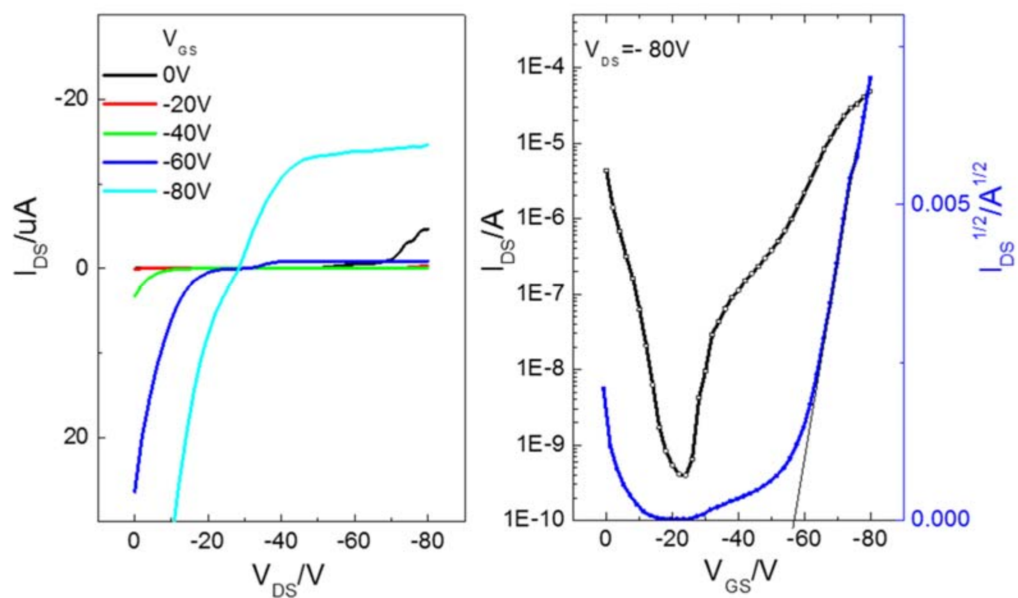

Figure S15. Output (left) and transfer (right) curves of OTFT device with about 2.6 nm of MoO_3 interlayer between the Au contacts and the **PDBPyBT** layer annealed at 150ºC

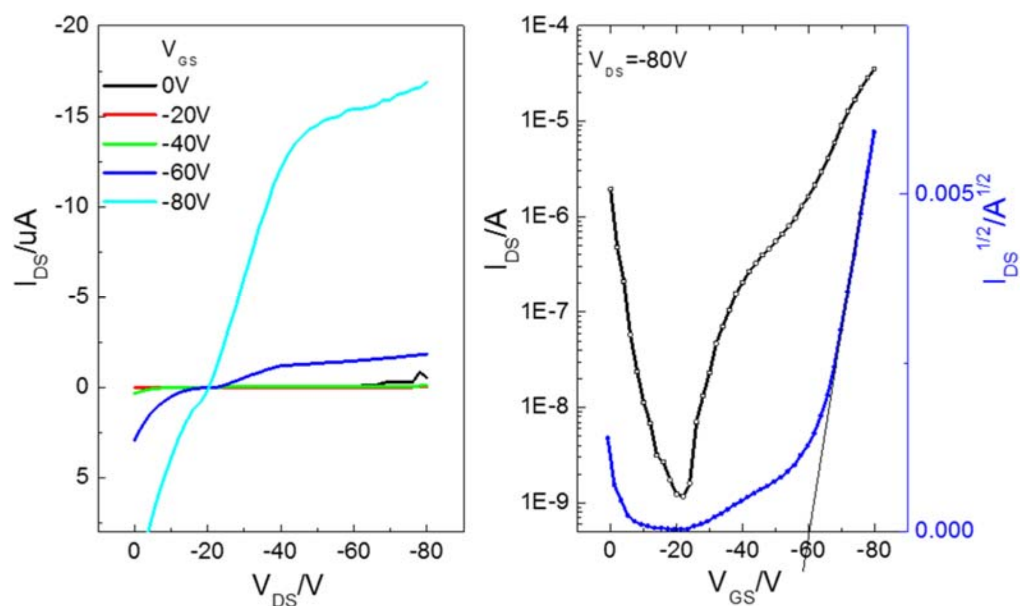

Figure S16. Output (left) and transfer (right) curves of OTFT device with about 3.0 nm of MoO_3 interlayer between the Au contacts and the **PDBPyBT** layer annealed at 150ºC

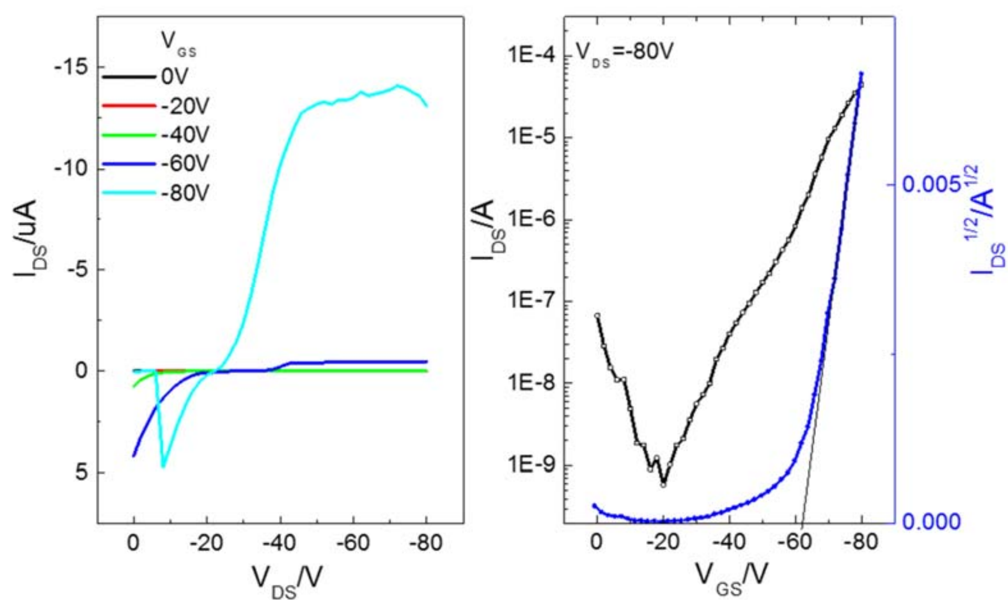

Figure S17. Output (left) and transfer (right) curves of OTFT device with about 4.0 nm of MoO_3 interlayer between the Au contacts and the **PDBPyBT** layer annealed at 150ºC

Part 2. Output and transfer characteristics of OTFT devices in Chapter 4

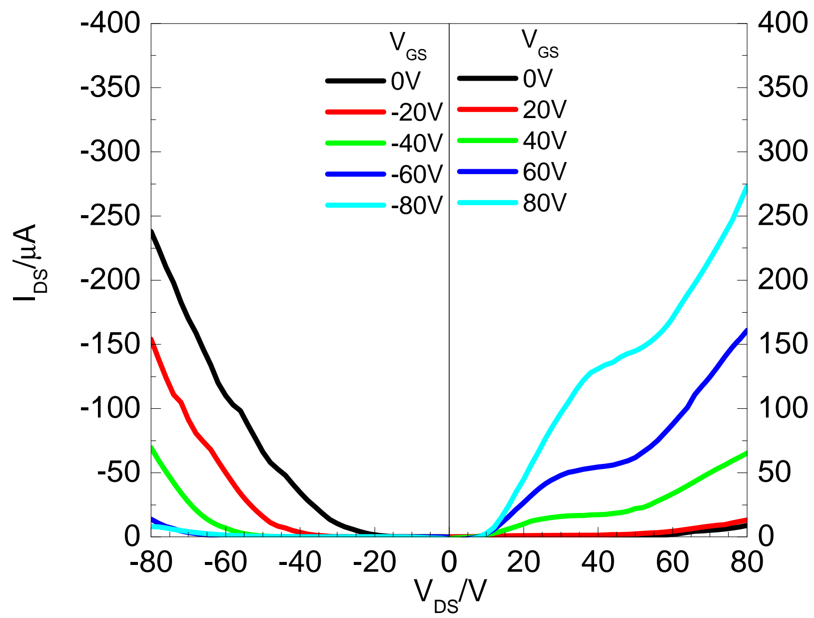

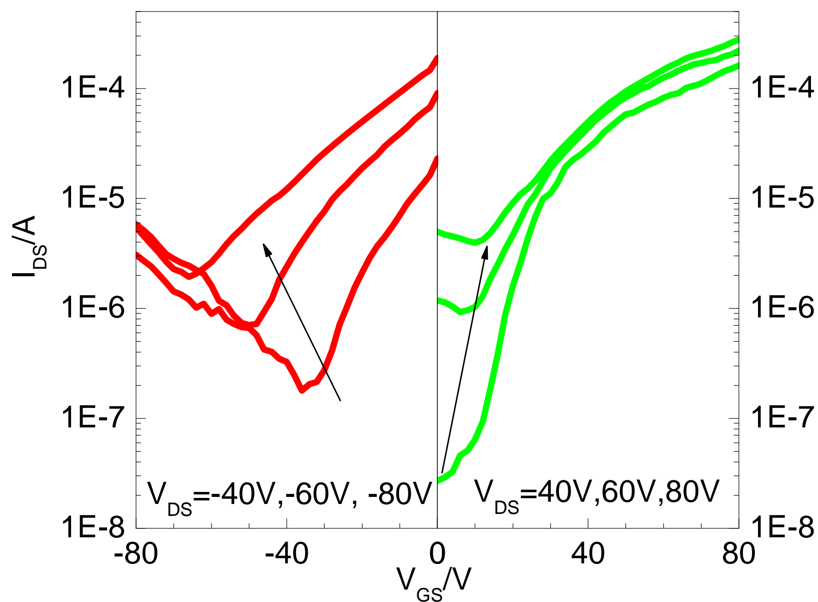

Figure S18. Output (left) and transfer (right) curves of ambipolar OTFT devices of **P4-1** with PEI (1.5nm) modified source and drain electrodes.

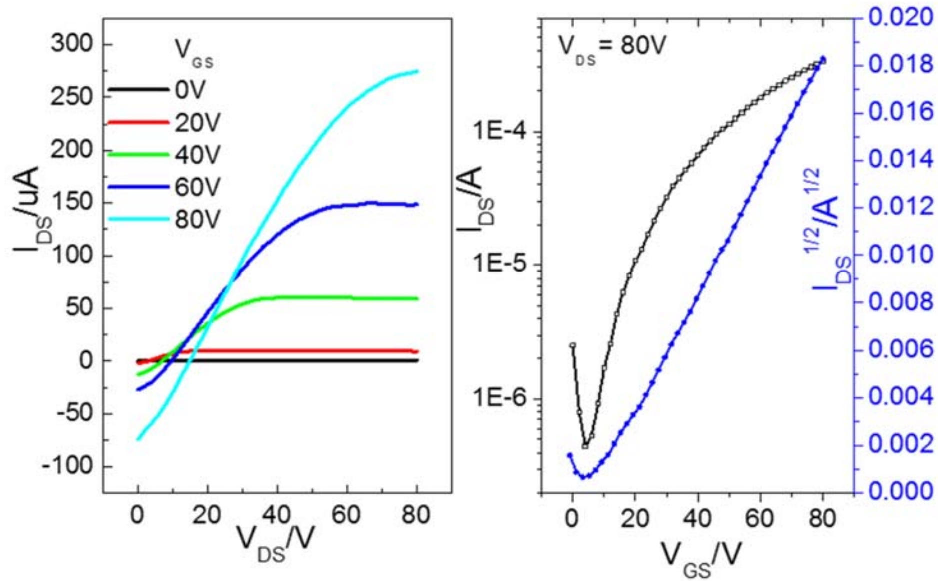

Figure S19. Output (left) and transfer (right) curves of representative unipolar n-channel OTFT devices of **P4-1** with PEI (2.2 nm) modified source and drain electrodes.

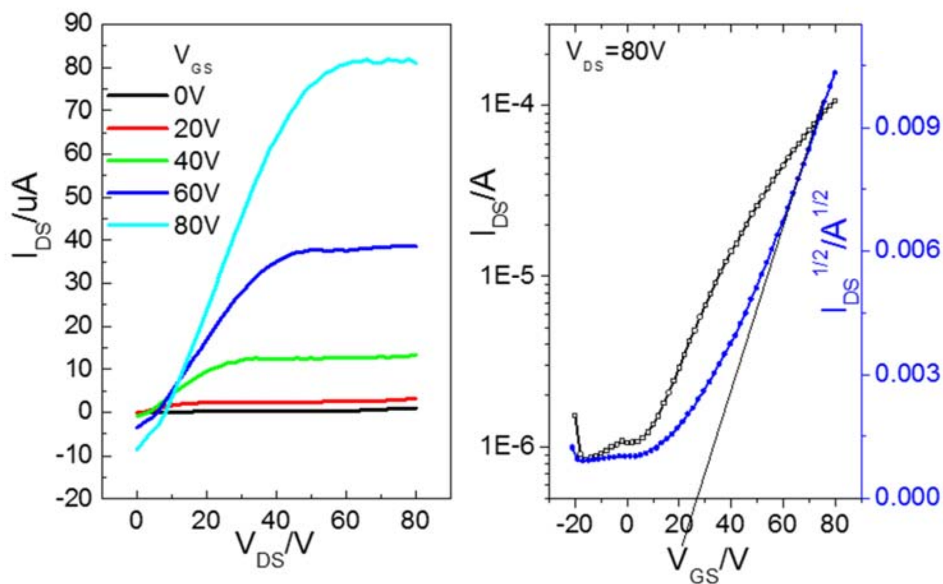

Figure S20. Output (left) and transfer (right) curves of representative unipolar n-channel OTFT devices of **P4-1** with PEI (2.9 nm) modified source and drain electrodes.

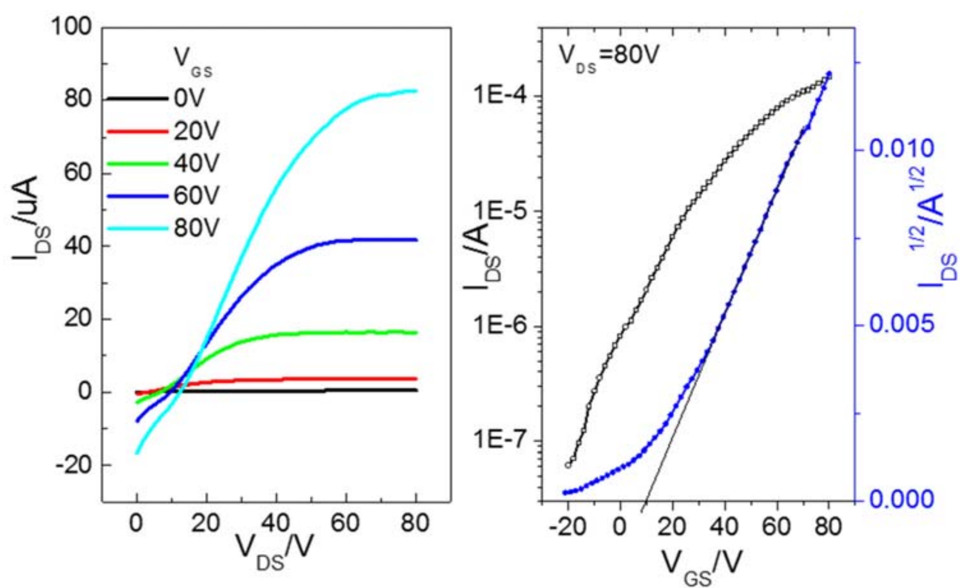

Figure S21. Output (left) and transfer (right) curves of representative unipolar n-channel OTFT devices of **P4-1** with PEI (4.7 nm) modified source and drain electrodes.

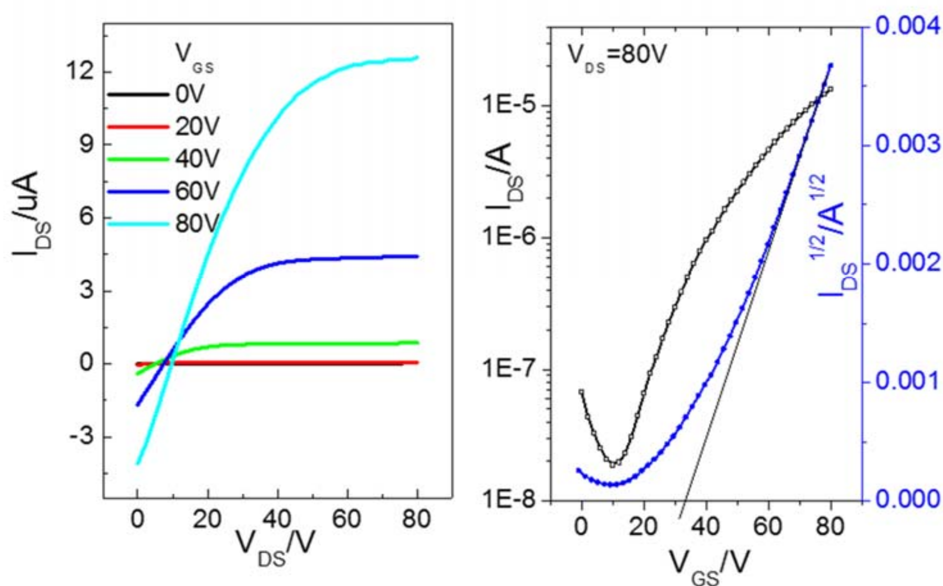

Figure S22. Output (left) and transfer (right) curves of representative unipolar n-channel OTFT devices of **P4-2** with PEI (1.5 nm) modified source and drain electrodes.

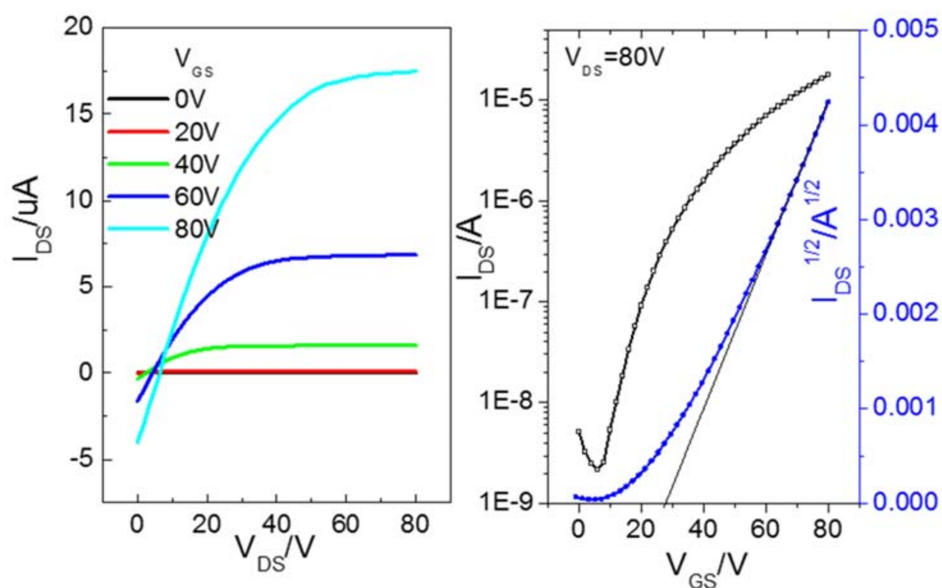

Figure S23. Output (left) and transfer (right) curves of representative unipolar n-channel OTFT devices of **P4-2** with PEI (2.2 nm) modified source and drain electrodes.

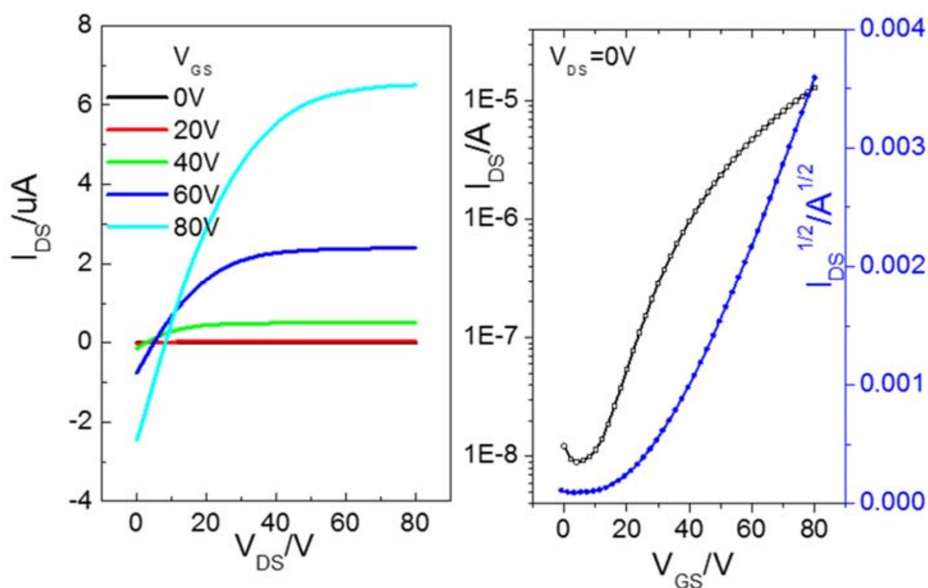

Figure S24. Output (left) and transfer (right) curves of representative unipolar n-channel OTFT devices of **P4-2** with PEI (3.9 nm) modified source and drain electrodes.

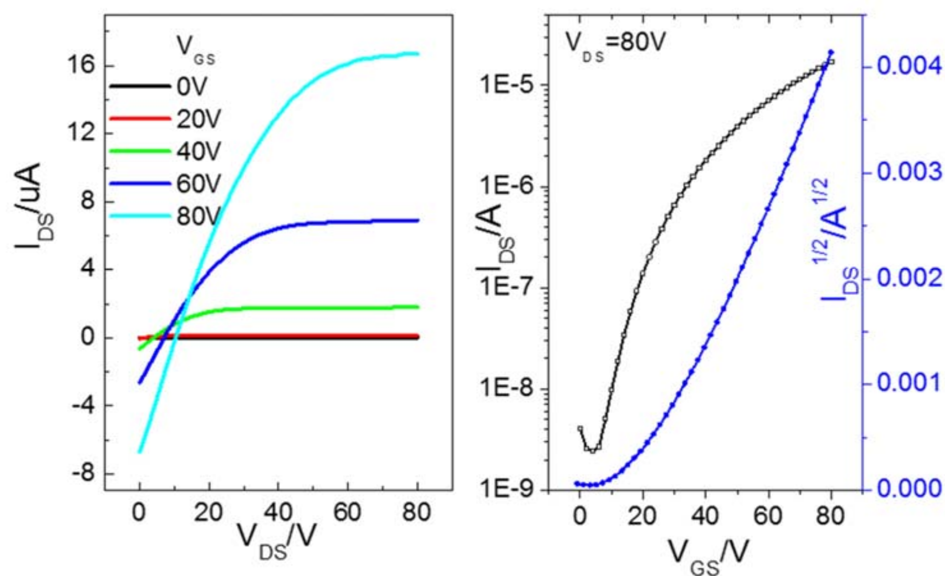

Figure S25. Output (left) and transfer (right) curves of representative unipolar n-channel OTFT devices of **P4-3** with PEI (1.5 nm) modified source and drain electrodes.

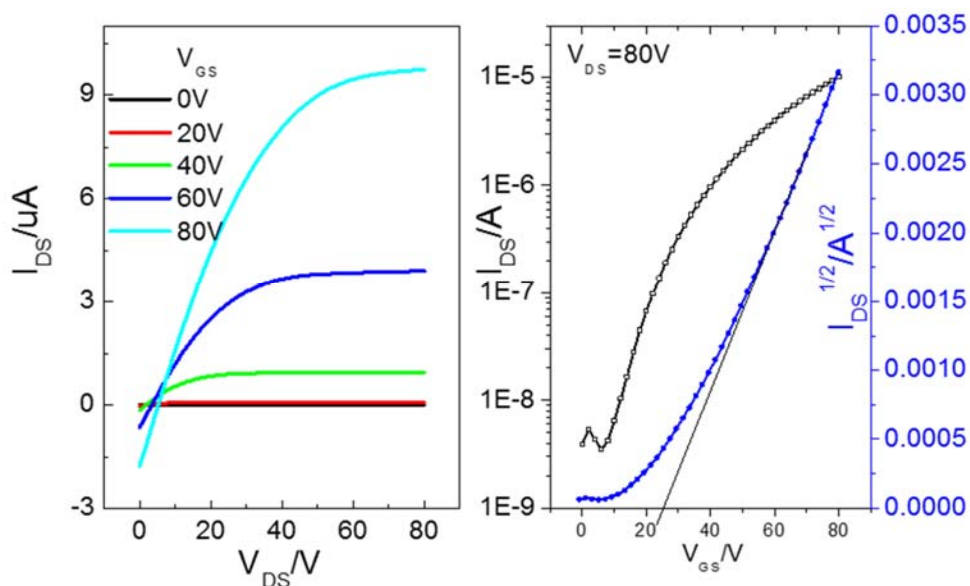

Figure S26. Output (left) and transfer (right) curves of representative unipolar n-channel OTFT devices of **P4-3** with PEI (2.9 nm) modified source and drain electrodes.

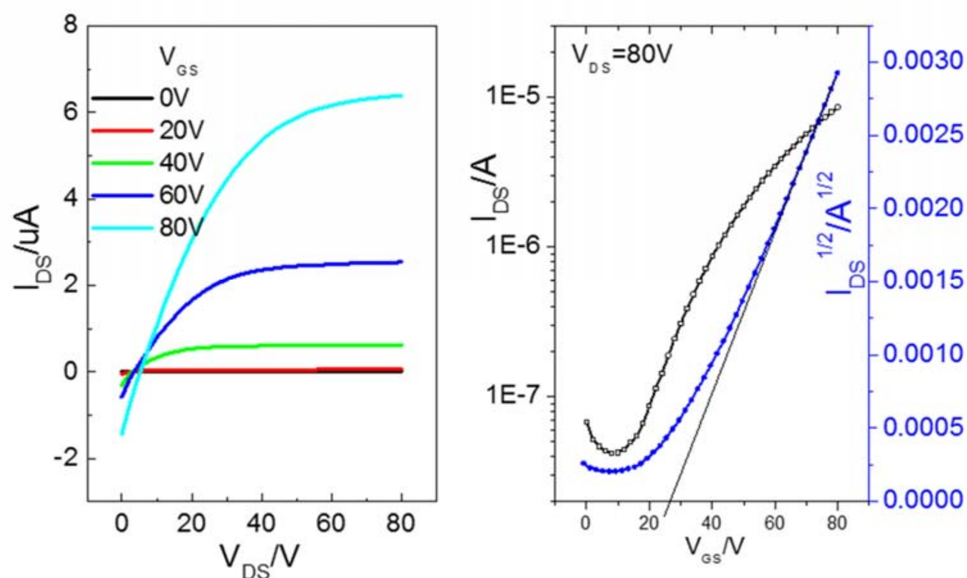

Figure S27. Output (left) and transfer (right) curves of representative unipolar n-channel OTFT devices of **P4-3** with PEI (3.9 nm) modified source and drain electrodes.

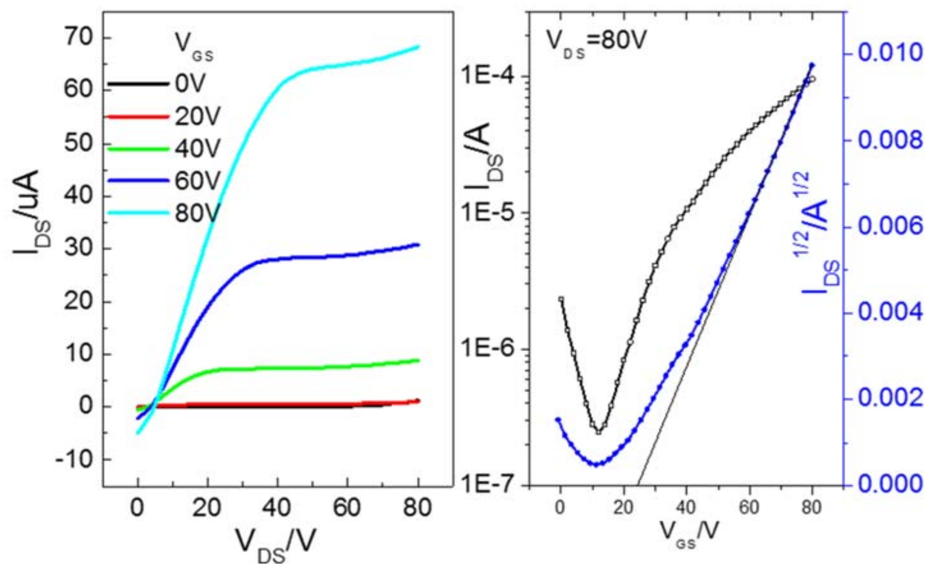

Figure S28. Output (left) and transfer (right) curves of n-channel OTFT devices of **P4-4** with PEI (1.5 nm) modified source and drain electrodes.

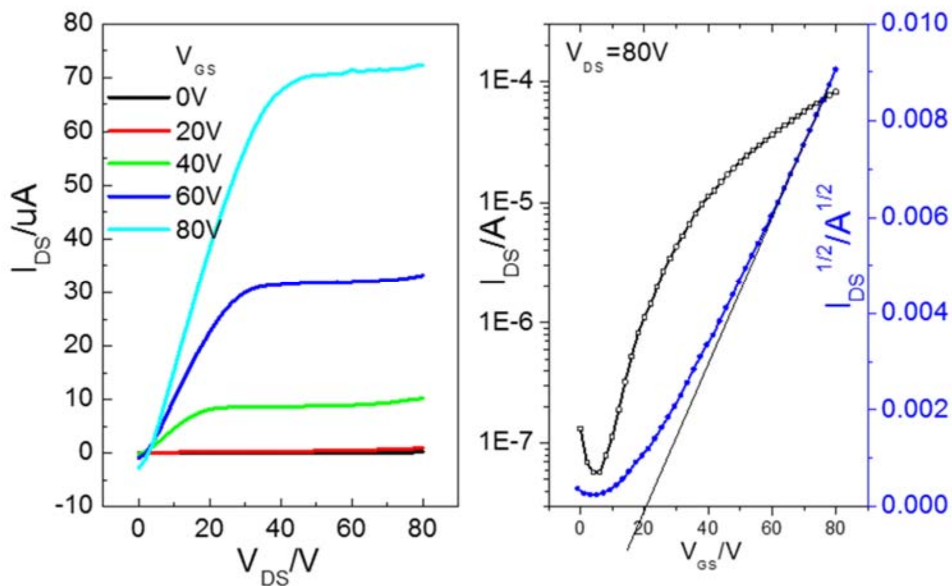

Figure S29. Output (left) and transfer (right) curves of n-channel OTFT devices of **P4-4** with PEI (2.2 nm) modified source and drain electrodes.

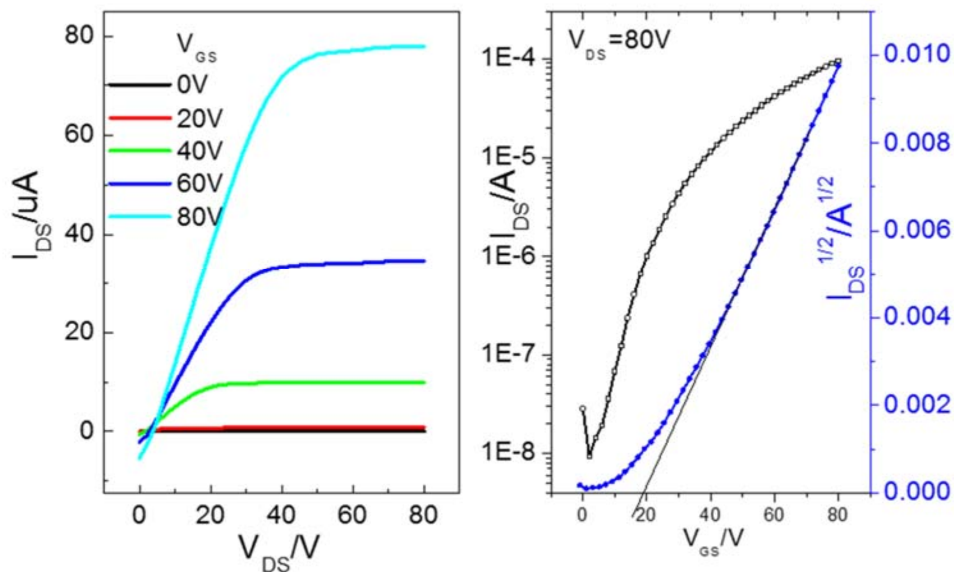

Figure S30. Output (left) and transfer (right) curves of n-channel OTFT devices of **P4-4** with PEI (2.9 nm) modified source and drain electrodes.

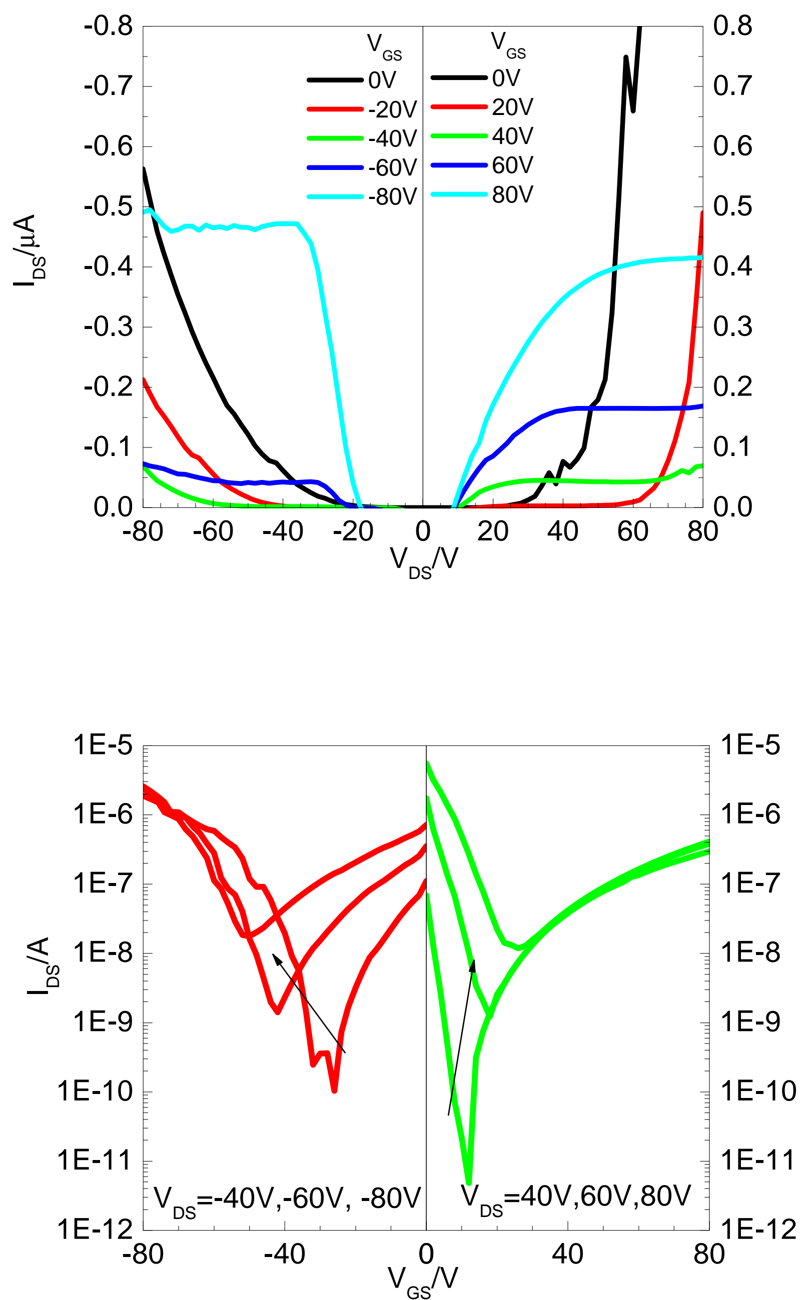

Figure S31. Output (left) and transfer (right) curves of ambipolar OTFT devices of **P4-5** with PEI (1.5 nm) modified source and drain electrodes.

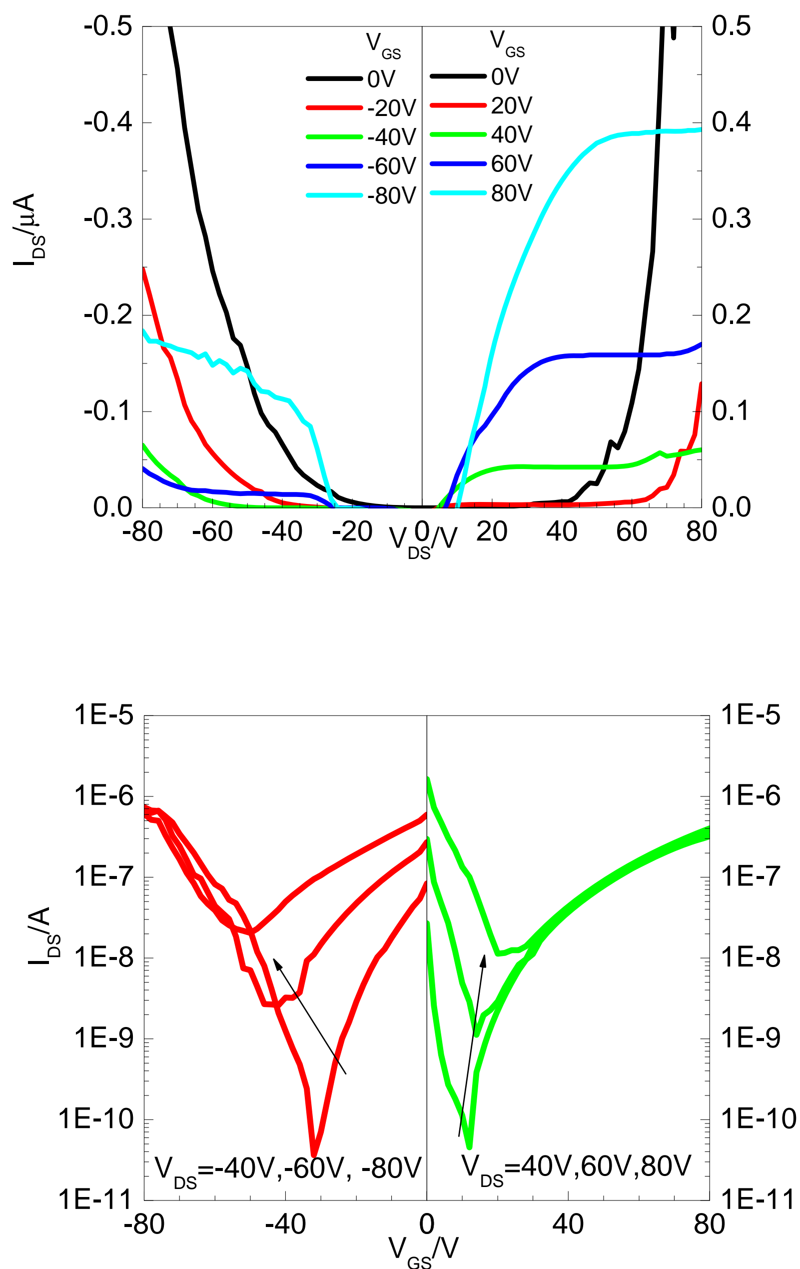

Figure S32. Output (left) and transfer (right) curves of ambipolar OTFT devices of **P4-5** with PEI (2.2 nm) modified source and drain electrodes.

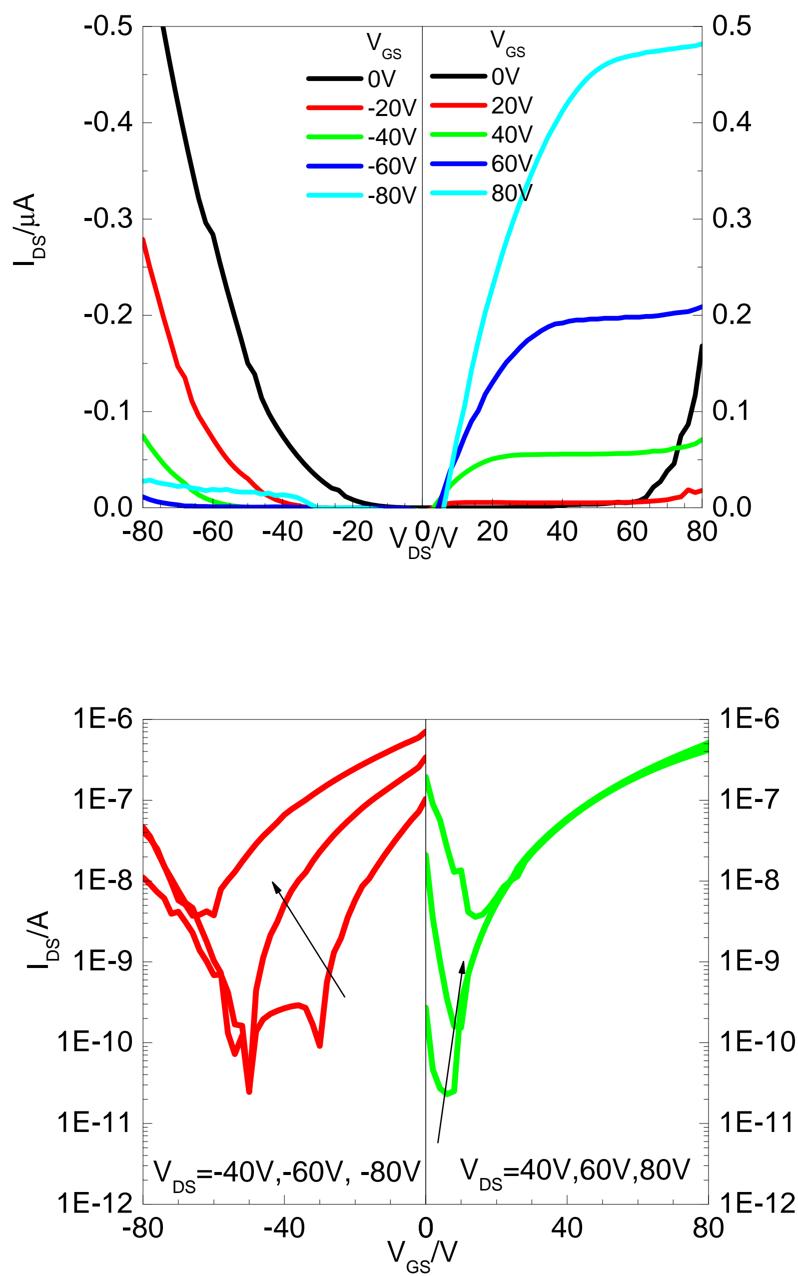

Figure S33. Output (left) and transfer (right) curves of ambipolar OTFT devices of **P4-5** with PEI (2.9 nm) modified source and drain electrodes.

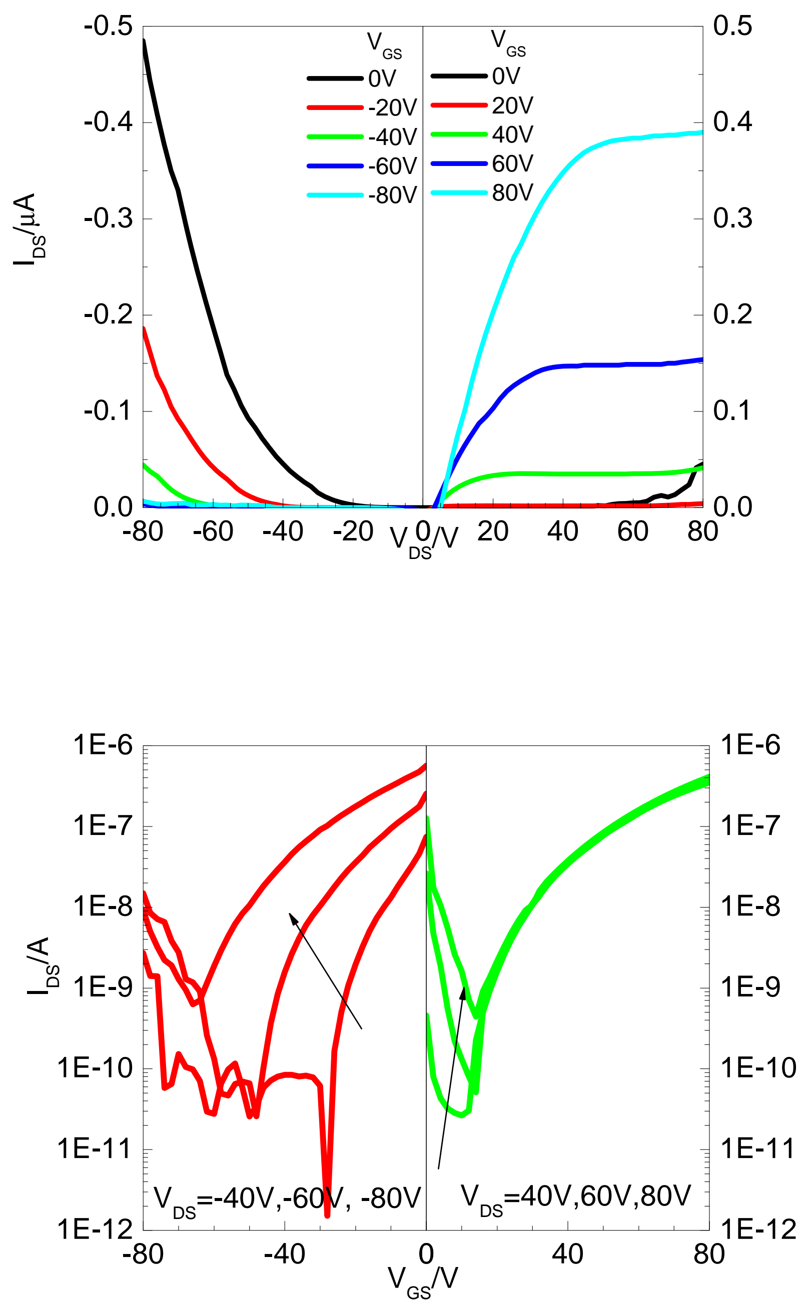

Figure S34. Output (left) and transfer (right) curves of ambipolar OTFT devices of **P4-5** with PEI (3.9 nm) modified source and drain electrodes.

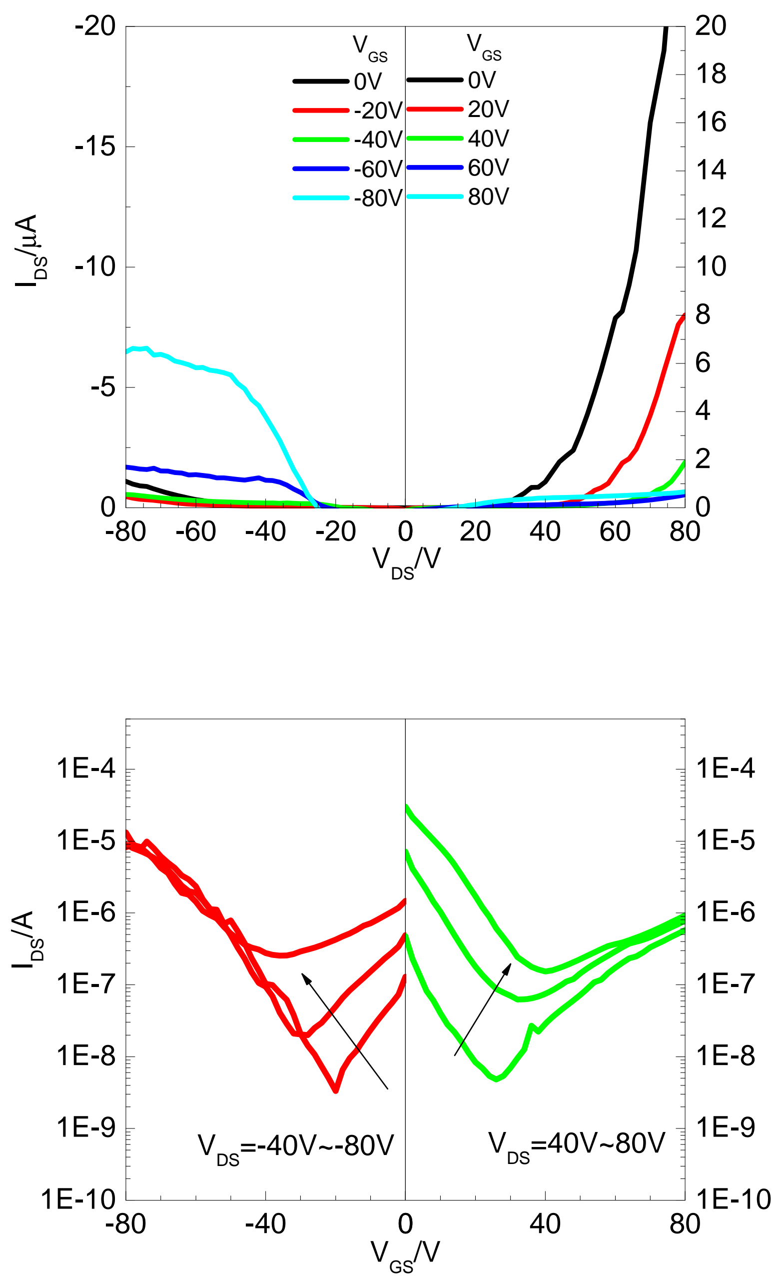

Figure S35. Output (left) and transfer (right) curves of ambipolar OTFT devices of **P4-6** with PEI (1.5 nm) modified source and drain electrodes.

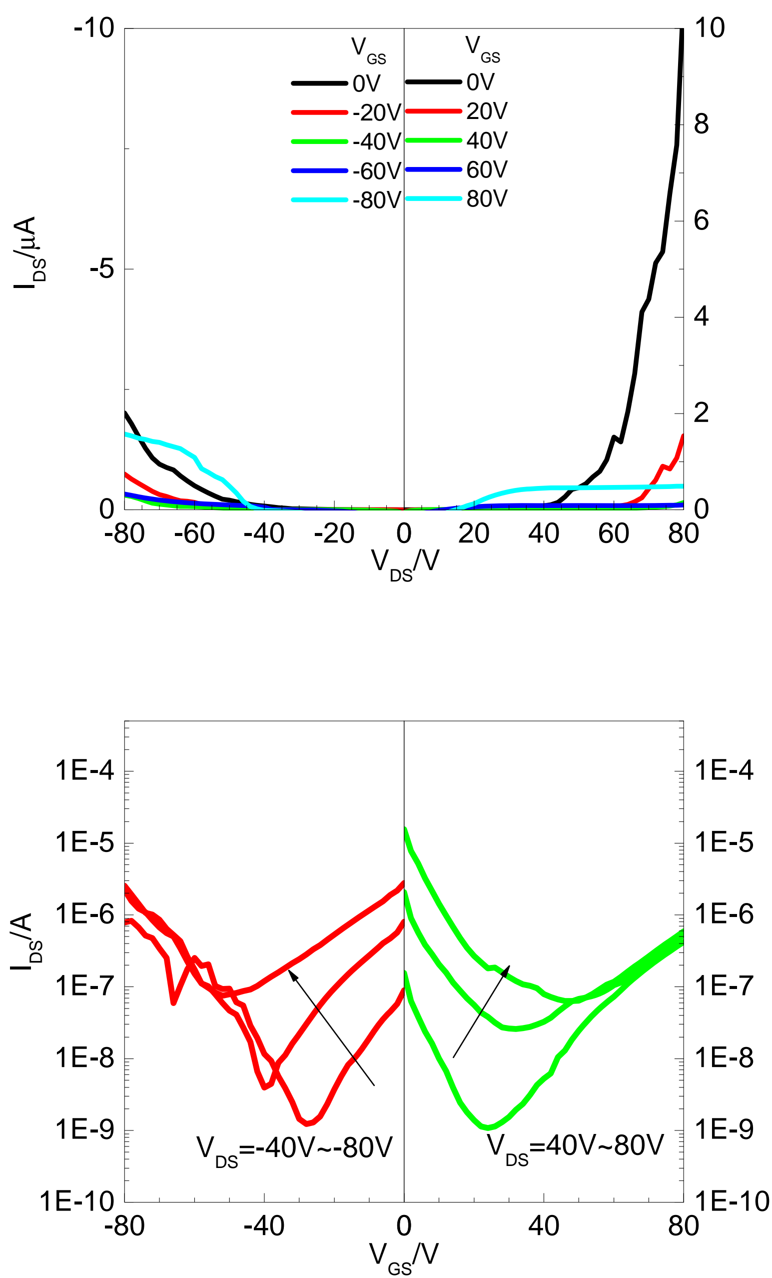

Figure S36. Output (left) and transfer (right) curves of ambipolar OTFT devices of **P4-6** with PEI (2.2 nm) modified source and drain electrodes.

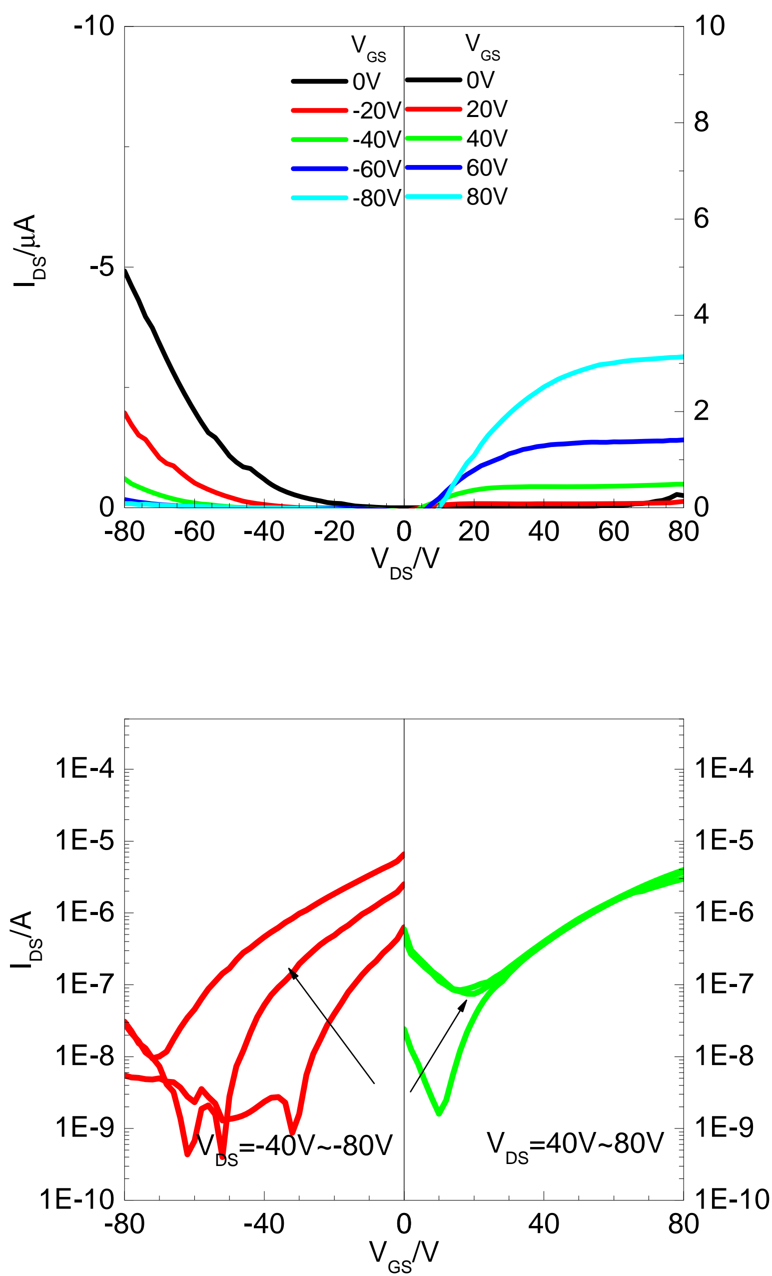

Figure S37. Output (left) and transfer (right) curves of ambipolar OTFT devices of **P4-6** with PEI (2.9 nm) modified source and drain electrodes.

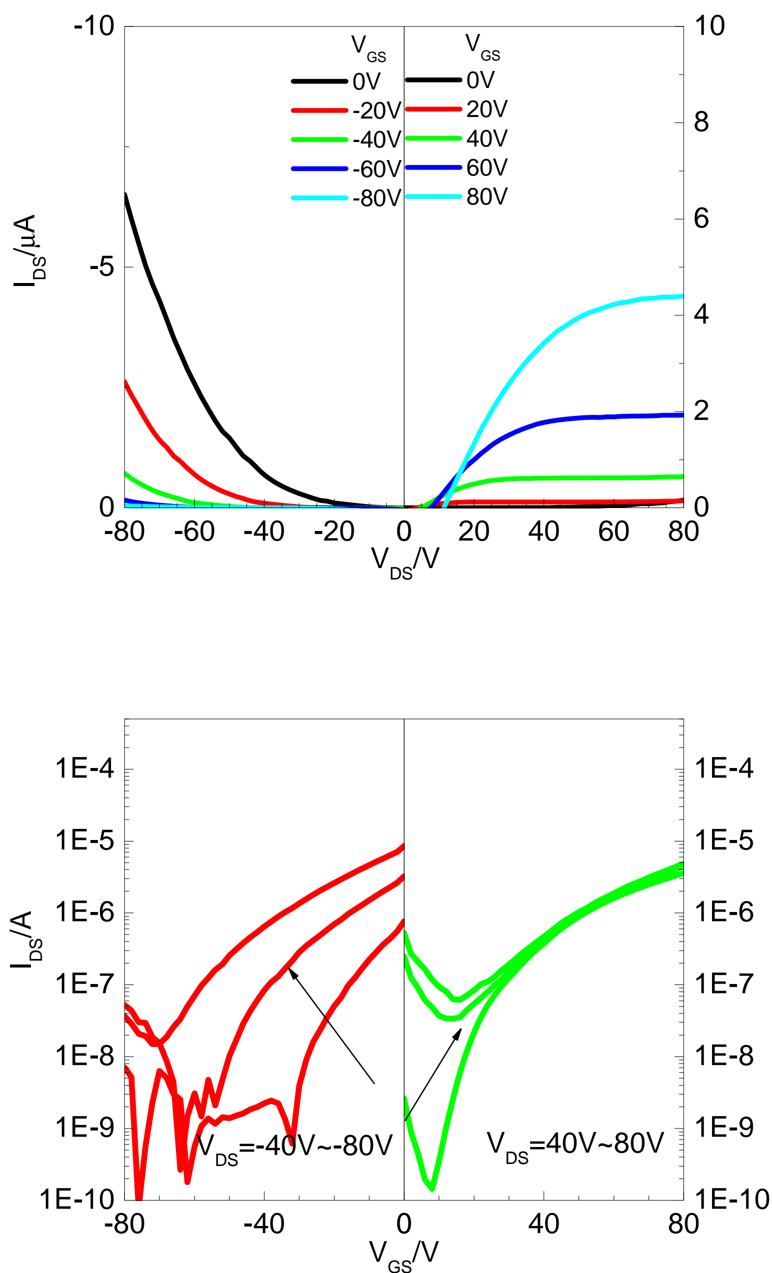

Figure S38. Output (left) and transfer (right) curves of ambipolar OTFT devices of **P4-6** with PEI (3.9 nm) modified source and drain electrodes.

Part 3. Output and transfer characteristics of OTFT devices in Chapter 5

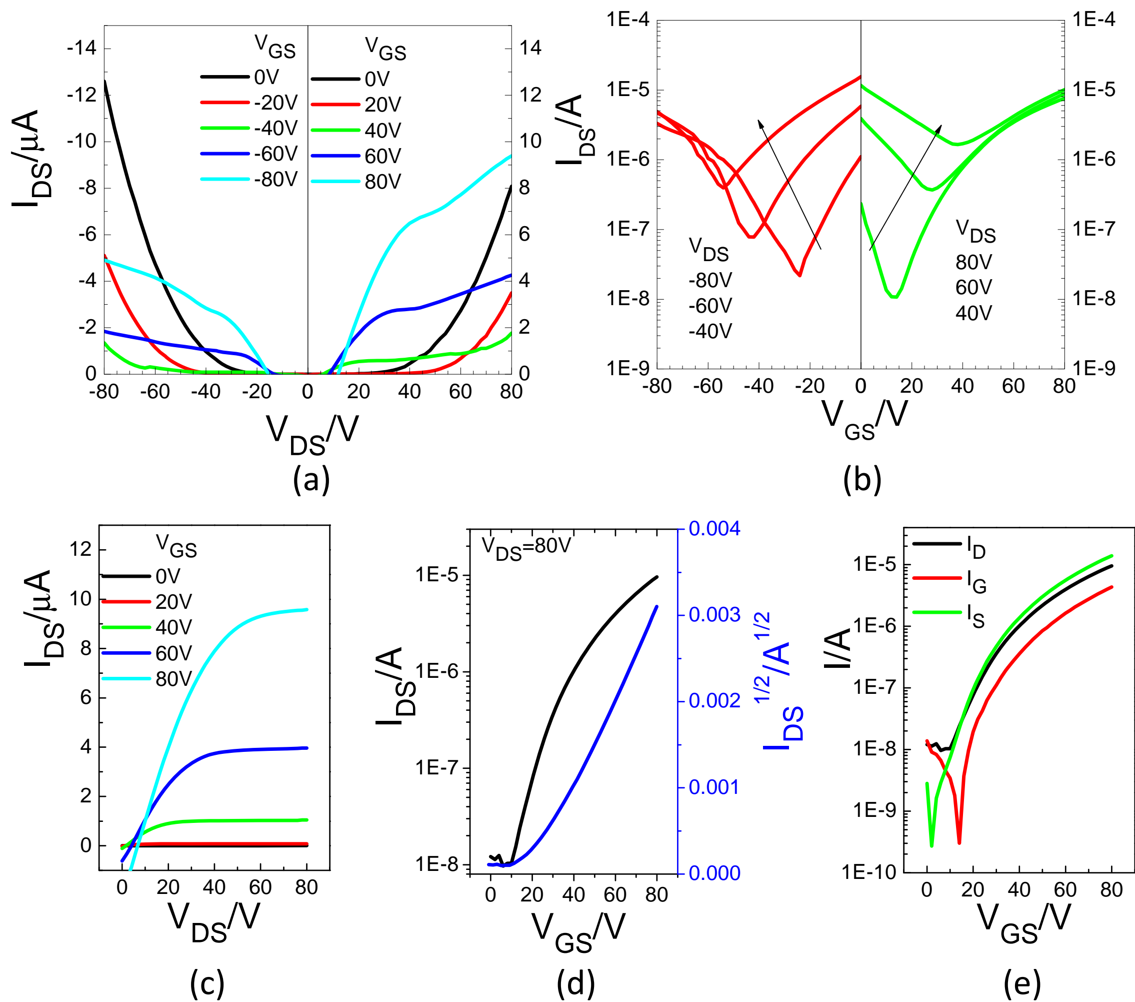

Figure S39. (a) and (b): Output and transfer curves of a typical TGBC OTFT device with a pure **P5-2** (0% PEI) thin film annealed at 150 °C, which shows a characteristic ambipolar charge transport performance. (c), (d), and (e): Output curves, transfer curves, and absolute drain (I_D), source (I_S) and gate (I_G) currents of a TGBC OTFT device with a **P5-2**:PEI (2% PEI) blend film annealed at 150 °C, which show a characteristic n-channel electron-only charge transport performance. Device dimensions: channel length L = 30 μm; channel width W = 1 mm.

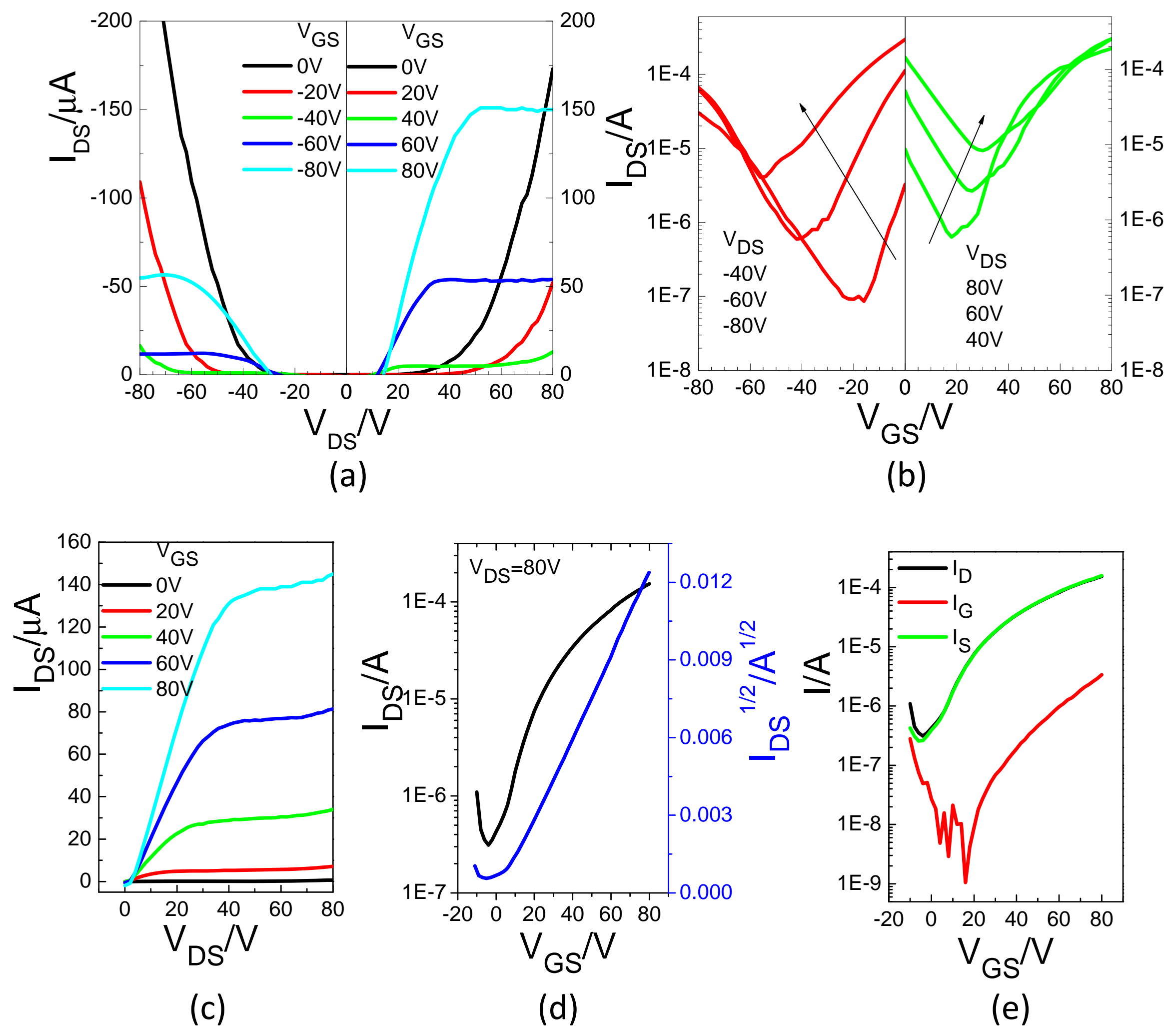

Figure S40. (a) and (b): Output and transfer curves of a typical TGBC OTFT device with a pure **P5-3** (0% PEI) thin film annealed at 150 °C, which show a characteristic ambipolar charge transport performance. (c), (d), and (e): Output curves, transfer curves of a TGBC OTFT device with a **P5-3**:PEI (2% PEI) blend film annealed at 150 °C, which show an n-channel electron-only charge transport performance. Device dimensions: channel length $L = 30$ μm; channel width $W = 1$ mm.

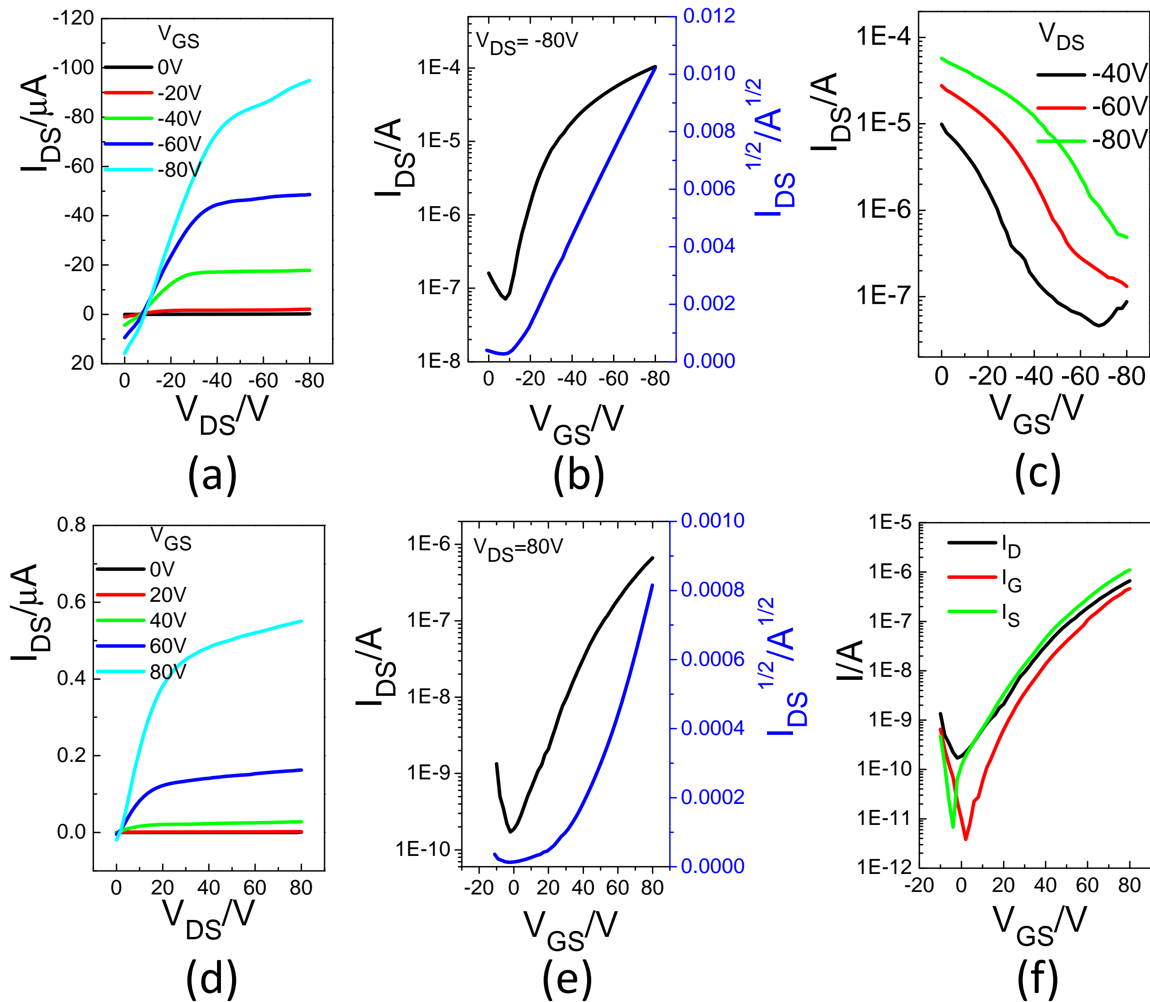

Figure S41. (a) and (b): Output and transfer curves of a typical TGBC OTFT device with a pure **P5-4** (0% PEI) thin film annealed at 150 °C, which show a characteristic p-channel hole-only transport performance. (c): Transfer curves of a TGBC OTFT device with a **P5-4**:PEI (10% PEI) blend film annealed at 150 °C, which show no p-channel charge transport performance. (d), (e), and (f): Output curves, transfer curves, and absolute drain (I_D), source (I_S) and gate (I_G) currents of the same OTFT device in (c). Device dimensions: channel length $L = 30$ μm; channel width $W = 1$ mm.

Part 4. Fabrication of Complementary Inverters in Chapter 6

Complementary inverters consist of two OTFTs, p-type and n-type. The BGBC configuration was utilized for OTFT fabrication, and heavily doped n^{++}-Si substrate was used as the substrate, with 300 nm of thermally grown SiO_2 as the dielectric. The substrate was patterned with gold

source/drain pairs by conventional photolithography methods, and then cleaned by air plasma, acetone, and isopropanol. After drying with nitrogen, the substrate was merged in a solution (10mg mL^{-1}) of DDTS in toluene for passivation of the dielectric surface for 20min. Then the substrate was rinsed by fresh toluene and dried by nitrogen. After this, the p-type and n-type polymer semiconductors, **PDQT-24** and **PIBDFTT**, were inkjet printed by Ceradrop's L-Series Inkjet printer, sequentially, followed by annealing in glove box at 150 ºC for 15 min. The PMMA encapsulation was formed by spin-coating a PMMA solution (7 mg mL^{-1}) in butyl acetate at 3000 rpm for 60 s. Finally, the devices were tested in air using a Keithley 4200-SCS analyzer.